The role of atmospheric forcing in the mass balance and evolution of a debris-covered Himalayan glacier

Anya Marie Schlich-Davies

Submitted in accordance with the requirements for the degree of Doctor of Philosophy

The University of Leeds

School of Earth and Environment

The Priestley International Centre for Climate

July 2021

Declaration

The candidate confirms that the work submitted is her own and that appropriate credit has been given where reference has been made to the work of others.

This copy has been supplied on the understanding that it is copyright material and that no quotation from the thesis may be published without proper acknowledgement.

The right of Anya Marie Schlich-Davies to be identified as Author of this work has been asserted by her in accordance with the Copyright, Designs and Patents Act 1988.

Acknowledgements

Firstly, I would like to thank my supervisors Andrew Ross and Duncan Quincey, for their continued support throughout my PhD. To Andrew, for always being so calm and encouraging during our meetings, and particularly for helping me with the meteorology aspects of the project. To Duncan, for being a fountain of knowledge on Himalayan glaciers and for always adding positive comments (and a few jokes) in my work. I am extremely grateful for the support and guidance from Ann Rowan on using iSOSIA, and on modelling debris-covered glaciers in general. All three of you have taught me a lot and your expert guidance and optimism, even during the challenges of COVID-19 working, has been greatly appreciated.

Secondly, thank you to fellow PhDs for their friendship over the past 4 years: Josie, Anne, Laura K, Charlotte, Sam G, Claudio, Niall, Beth, Craig and Dean. Particularly to Sarah and Laura A over the last few months.

I would like to thank those outside of Leeds for the insightful conversations and feedback, particularly Emily Potter and Tom Matthews. Also to Lindsey Nicholson and Anna Wirbel who provided some code and advice to get me started with some sub-debris ablation modelling used in Chapter 4, and to David Rounce for the debris thickness data. Thanks also to Franco Salerno and Patrick Wagnon for providing the high elevation weather station data that have been critical for this study, and more generally for our understanding of the climate of the Khumbu region. Thank you to the developers of the two models used in this thesis, Tobias Sauter and Anselm Arndt for COSIPY and David Egholm for iSOSIA.

Thanks go to staff in the University of Leeds computing team for providing a great high performance computing facility, ARC4, where the glacier mass balance and ice flow model simulations were run. I am very grateful for the help from the Centre for Environmental Modelling and Computation (CEMAC), particularly from Richard Rigby, for his perseverance with getting the early versions of the mass balance model working on the Leeds system despite the innumerous error messages. Huge thanks also go to those in the School of Earth and Environment who have been working hard for safe re-entry into the department for those who need it. Having access to a desk during the final few months made all the difference. Thank you to the convenors of the Shut up and Write sessions which were particularly useful during home working, but also more broadly to Francesco Cirillo who invented the pomodoro technique! My existence is now divided into 25-minute chunks.

Huge thanks to the EverDrill team, particularly Duncan, for the great opportunity to join the 2018 trip to Khumbu Glacier. This experience made me truly appreciate this amazing environment, and

all its complexity. To staff at the Himalayan Research Expedition for all your help, and to those at the Pyramid observatory and particularly Jo Hornsey for taking care of me when I became ill!

I feel lucky to have spent 6 months in the middle of my PhD in the international climate science team at BEIS. Working with such great colleagues in the climate science/policy interface and seeing how my research tied into the bigger picture meant I returned to my PhD with renewed enthusiasm. Particular thanks to Caroline who has encouraged me ever since. Also thanks to my Nan and Pam, who took me in during this time.

This PhD was funded by the University of Leeds and the Priestley International Centre for Climate. I am also appreciative of funding received to attend international conferences from the India-UK Water Centre and Leeds for Life.

On a more personal note, I would like to thank my family and friends for their continued encouragement. Special thanks to my sister, brothers, Dad and Bonnie.

To Sam, I cannot put into words how thankful I am for your love and support and, most importantly, for bringing me a coffee most mornings.

My final thanks go to my amazing Mum, to whom I owe my love for the outdoors and who has been greatly missed over the last few years. I will never forget stories of your hiking adventures in Nepal in the '80s and thought of these when I encountered my first yak.

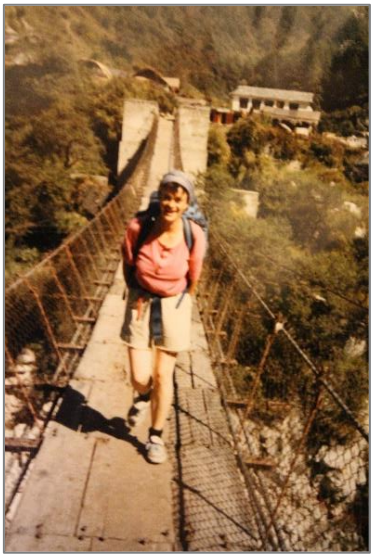

EverDrill field campaign on Khumbu Glacier May 2018

Abstract

The Hindu Kush–Karakoram Himalaya (HKKH) hold the largest ice mass outside of the poles. It is estimated that 1.9 billion people depend on the major rivers that are partially sustained by melt-water from these glaciers. Glacier mass loss has accelerated over the last decade and predictions indicate that this will continue over the next century, though vary widely and are based on relatively simplistic representations of climate and glacier behaviour.

The aim of this thesis is to investigate the impact of climatic drivers on glacier mass balance, and how a robust representation of mass balance influences longer-term evolution of debris-covered Khumbu Glacier in the Nepal Himalaya. A cross-disciplinary modelling approach is adopted, utilising meteorological observations and regional climate models to aid downscaling of present-day and future climate, which is used to force a distributed energy balance model. The distributed mass balance results are integrated into a 3D higher-order ice flow model to study glacier evolution under historical and future atmospheric forcing.

Energy balance modelling results demonstrate that the meteorological drivers of Khumbu Glacier mass balance vary substantially over space and time. The seasonality is more marked at lower elevations, where net shortwave radiation provides much of the energy available for melt, though net longwave radiation contributes appreciably during the monsoon. Despite temperatures remaining below freezing in the Western Cwm, ablation through sublimation is simulated. The calculation of a sub-debris ablation curve for Khumbu Glacier is applied to simulated clean-ice mass balance, improving glacier-wide and altitudinal ablation rates relative to observations.

By 2100, temperature is found to increase by 1.8°C to 3.9°C depending on the emission scenario, with highest warming in the winter. Over the coming 80 years, precipitation increases by 15%, though varies substantially between models, demonstrating the high uncertainty regarding future precipitation trends.

The value of forcing the ice flow model with distributed mass balance is seen in the simulated present-day velocities, particularly of the Khumbu icefall, which match closely with remote-sensing observations. The results indicate that the stagnant debris-covered tongue has already dynamically, and perhaps physically, detached from the active Khumbu Glacier. The significant recent warming means that the active section of Khumbu Glacier is committed to a 22% volume loss by 2100, and 34% by 2300. Future increased precipitation can act to offset the impact of moderate warming on glacier mass balance. However, under the most extreme warming scenario, mass loss is significant, particularly during the monsoon. Despite having the world's highest accumulation area, Khumbu Glacier may cease to exist by 2160.

Table of Contents

List of Figures

List of Tables

List of abbreviations and symbols

AAR	**A**ccumulation **a**rea **r**atio
AWS	**A**utomatic **w**eather **s**tation
CMIP5	**C**oupled **M**odel **I**ntercomparison **P**roject **P**hase **3**
CMIP5	**C**oupled **M**odel **I**ntercomparison **P**roject **P**hase **5**
CN	**C**hangri **N**up
CORDEX	**C**oordinated **R**egional Climate **D**ownscaling **Ex**periment
COSIPY	**Co**upled **S**nowpack and **I**ce Surface energy and mass balance model in **Py**thon
CS	**C**hangri **S**har
DADDI	**D**ynamic **A**blation **D**ue to **D**ebris from **I**ce model
DCG(s)	**D**ebris **c**overed **g**lacier(s)
DEM	**D**igital **E**levation **M**odel
DTR	**D**iurnal **t**emperature **r**ange
EBC	**E**verest **B**ase **C**amp
EBM	**E**nergy **b**alance **m**odel
EDW	**E**levation **d**ependent **w**arming
ELA	**E**quilibrium **l**ine **a**ltitude
ELR	**E**nvironmental **l**apse **r**ate
ERA-5	ECMWF Reanalysis 5th Generation
GCM	**G**eneral **c**irculation **m**odel
GIS	**G**eographic **i**nformation **s**ystem
GLIMS	**G**lobal **L**and **I**ce **M**easurements from **S**pace
GLOF	**G**lacial **l**ake **o**utburst **f**lood
HKKH	The **H**indu-**K**ush **K**arakoram **H**imalaya
HPC	**H**igh **P**erformance **C**omputing/**C**omputer
IPCC	**I**ntergovernmental **P**anel on **C**limate **C**hange
ISM	**I**ndian **s**ummer **m**onsoon
iSOSIA	**i**ntegrated **S**econd-**O**rder **S**hallow **I**ce **A**pproximation
KP	**K**ala **P**atthar
LIA	**L**ittle **I**ce **A**ge
LGM	**L**ast **G**lacial **M**aximum
LR	**L**apse **r**ate
LW_{in}	**L**ong**w**ave **in**coming radiation
LW_{out}	**L**ong**w**ave **out**going radiation
m.a.s.l.	**M**etres **a**bove **s**ea **l**evel
MB	**M**ass **b**alance

m w.e.	**M**etres **w**ater **e**quivalent
RCM	**R**egional **c**limate **m**odel
RCP	**R**epresentative **c**oncentration **p**athway
RH	**R**elative **h**umidity
SEB	**S**urface **e**nergy **b**alance
SIA	**S**hallow **i**ce **a**pproximation
SRTM	**S**huttle **r**adar **t**opography **m**ission
STF	**S**now **t**ransfer **f**unction (snow/rain partition)
SW_{in}	**S**hort**w**ave **in**coming radiation
SW_{net}	**Net s**hort**w**ave radiation
SW_{out}	**S**hort**w**ave **out**going (reflected) radiation
TP	**T**hird **P**ole
WCN	**W**est **C**hangri **N**up
WRF	**W**eather **r**esearch and **f**orecasting

α	albedo
$\alpha_{freshsnow}$	albedo of fresh snow
α_{snow}	albedo of snow
α_{firn}	albedo of firn
α_{ice}	albedo of ice
c_{ref}	Accumulation from refreeze of meltwater
c_{solid}	Accumulation from solid precipitation
L_M	Latent heat of melt
L_s	Latent heat of sublimation
F	All surface energy fluxes
u	wind speed
z_0	surface roughness length
κ	thermal diffusivity
λ	thermal conductivity
ρ	subsurface density (snow/firn and ice)

ρ_{air}	air density
ρ_{ice}	density of ice
ρ_{snow}	density of snow/firn
Q_G	Ground heat flux
Q_{lat}	Latent heat flux
Q_{liq}	Heat flux from liquid precipitation
Q_{melt}	Melt energy
Q_{sens}	Sensible heat flux
T_{air}	Air temperature
T_s	Surface temperature

Chapter 1 Introduction

1.1 Motivation

Glaciers are key indicators of atmospheric change and play an important role in the hydrology and climatology of a region. Himalayan glaciers act as seasonal buffers against drought (Wang et al., 2017) for densely populated, downstream communities (Wiltshire et al., 2014, Maurer et al., 2019; Pritchard, 2019). It is estimated that 1.9 billion people, 25% of the global population, are dependent on the Ganges, Brahmaputra, Indus, Yangtze, and Yellow rivers (Immerzeel et al., 2010), which are partially fed by meltwater from glaciers that are rapidly losing mass with climate change (Pritchard et al., 2019; Wester et al., 2019). The socioeconomic importance of glacial meltwater is particularly high for the agricultural and hydropower sectors; 129 million farmers in the Indus and Ganges depend on this water source (Biemans et al., 2019) and hydropower generates 90% of Nepal's electricity (Zarfl et al., 2014; Pritchard, 2019).

A substantial proportion of sea level rise to date has been driven by melting glaciers. Globally, glacier thinning rates have doubled from 2000 to 2019, contributing 0.74±0.03 mm yr^{-1} or 21% to global sea level rise for the same period (Hugonnet et al., 2021). The glaciers of the Hindu Kush–Karakoram Himalaya (HKKH) are the largest ice mass outside of the poles, often referred to as the Third Pole (Yao et al., 2012) or the Water Towers of Asia (Messerli et al., 2004, Immerzeel et al., 2010 and 2019 and Mishra, 2015). As such, understanding their future behaviour in response to climate change has global implications.

The development and expansion of glacial lakes that often accompanies mass loss poses a threat to downstream communities (Prakash and Nagarajan, 2018; Allen et al., 2019). Globally, over 12,000 deaths have been attributed to glacial lake outburst floods (GLOFs), with 6,300 deaths occurring in central Asia. Currently in the HKKH, the highest risk from GLOFs is in the eastern Himalaya, and Nepal and Bhutan experience the greatest socio-economic impacts from glacier floods (Carrivick and Tweed, 2016). This trend is likely to continue into the future with the development of new transboundary glacial lakes (Zheng et al., 2021). Alongside these emerging hazards, glacier loss will lead to steep terrain susceptible to landslides, therefore increasing the likelihood of GLOF triggers (Dadson and Church, 2005). More generally, the extensive cross-border flow of water across the HKHH has the potential to trigger social and political instability following periods of water scarcity or flooding (Schleussner et al., 2016; Pritchard, 2019).

Glacier and snowpacks are vital for communities in the Himalaya. Tourism, mostly from trekkers and mountaineers, is a vital source of income, particularly in Nepal. Safety concerns associated

with a rapidly evolving high-altitude environment will likely reduce footfall and therefore income in the region (Watson and King, 2018). The mountains hold immense spiritual and cultural value in high mountain communities (Becken et al., 2013), and the damage to human wellbeing caused by cryospheric change will be multifaceted (Allison, 2015).

Glacier change is closely associated with glacier mass balance. Himalayan glacier systems are a product of the mass of snow and ice received (mainly through snowfall and avalanching) and the mass lost to ablation (through melt and sublimation). There is now a wealth of observations confirming strong negative mass balances across the HKKH (Azam et al., 2018; Brun et al., 2019), including the Everest region, from remote-sensing (Bolch et al., 2011, King et al., 2017 and 2020, Wagnon et al., 2020) and *in situ* point measurements (Wagnon et al., 2013, Vincent et al., 2016, Sherpa et al., 2017; Bocchiola et al., 2020). However, the mechanisms driving this mass loss, and spatial and temporal variability in mass balance, are not fully understood. Changes in atmospheric forcing drive glacier mass balance change, and this is then mediated or enhanced through a variety of glaciological mechanisms. This thesis uses a cross-disciplinary modelling approach to consider both the climatic drivers of glacier change, and the key glaciological feedback mechanisms, with a focus on Khumbu Glacier.

The extreme orography of the Himalaya allows substantial variability in local meteorology over short spatial and temporal scales (Ueno et al., 2001; Potter et al., 2017). This variability in fundamental meteorological drivers of glacier change, namely temperature and precipitation, is not captured by coarse climate products that are often used to drive glacier models. Climate models fail to accurately simulate the meteorological phenomena that bring precipitation to HKKH glaciers; the westerlies in the west and the Karakoram, and the summer monsoon in the east (Scherler et al., 2011; Mishra, 2015). There exists an elevation bias in meteorological observations, and scarce high elevation *in situ* data are often fraught with uncertainties that can be almost as large as those of climate model simulations (Collins et al., 2013; Kannan et al., 2014). This creates challenges for climate model evaluation and downscaling and contributes to high uncertainty regarding future precipitation trends for the region. Improving accuracy of future climate projections is considered one of the greatest challenges concerning climate impacts on freshwater resources (Kundzewicz and Gerten, 2014).

A robust representation of the meteorological drivers of ablation and accumulation at the catchment-scale is required to obtain accurate calculations of glacier mass balance. Degree day models in their simplest form require only daily temperature, and as such have historically been applied more widely in glacio-hydrological modelling of Himalayan glaciers than other approaches. Yet these are not always suitable for glaciers that are “summer-accumulation type”, i.e. that receive a significant proportion of their precipitation via the summer monsoon and as such can experience

both ablation and accumulation over small spatial and temporal scales (Bollasina et al., 2002; Salerno et al., 2015). Energy balance models aim to resolve all meteorological drivers of glacier mass balance. Sensitivity analyses to ascertain the varying importance of these drivers are useful for explaining the spatial variability in glacier mass balance, the importance of fine resolution climate forcing, and the implications of future atmospheric change for glacier mass loss. However there are few studies using glacier-wide energy balance modelling approaches in the HKKH (Bonekamp et al., 2019; Che et al., 2019) and none for Khumbu Glacier.

Key factors controlling Himalayan glacier mass balance include the glacier elevation range and the slope of the glacier tongue, and the extent of supraglacial debris and the avalanche contributing area (Benn et al., 2012; Rowan et al., 2015, 2021; Brun et al., 2019). The presence of glacial lakes, particularly at the terminus, is also strongly related to highly negative mass balances across the HKHH (King et al., 2017; 2019, Brun et al., 2019; Watson et al., 2020). Resolving these elements of the glacier mass balance within glacier models is crucial for improving accuracy of future glacier evolution. Though there has been considerable progress in the understanding of these mass balance mechanisms, such as the influence of supraglacial debris on glacier melt (e.g. Brun et al., 2016; Buri et al., 2018; Nicholson et al., 2018), these have been studied in isolation in order to improve model parameterisations and quantify the significance of these controls on mass balance. Few studies have used a holistic modelling approach that have resolved these mass balance elements and their impact on individual glacier behaviour.

This uncertainty in future climate and the representation of glacier dynamics in models has resulted in widely varying predictions of glacier response to climate change for the region. End-of-century projections in ice volume change for the Everest region range from 70 to 99% under a moderate and extreme warming scenario respectively (Shea et al., 2015), up to 50% (Soncini et al., 2016) and as low as 8-10% (Rowan et al., 2015). Much of this discrepancy stems from substantial differences in approaches to modelling glacier change, including the representation of glacier mass balance within ice flow models. To date, there have been no ice flow modelling approaches that have used a robust representation of climate and glacier mass balance. This is particularly critical for debris-covered, summer-accumulation type glaciers of the HKKH.

1.2 Thesis Aims and Objectives

The overall aim of this thesis is to investigate the role that changing atmospheric forcing has on the historical and future mass balance and evolution of Khumbu Glacier. This is broken down into four central aims:

1. To investigate the complexities of catchment-scale meteorology using a network of weather stations and the implications for glacier modelling. The following questions are addressed:
    a) How do temperature lapse rates and other altitudinal dependencies vary over time?
    b) How can the valley-scale wind regime be characterised, and is this apparent in regional reanalyses products?
    c) What are the implications of the valley-scale meteorological complexities for glacier modelling?

2. To explore the sensitivity of Khumbu Glacier mass balance to atmospheric and glaciological forcings in the present day. The following questions are addressed:
    a) What are the meteorological drivers of ablation and accumulation?
    b) Is the energy balance model able to resolve the critical elements of Khumbu Glacier mass balance?
    c) How does the modelled spatial distribution of mass balance compare to observations?

3. To produce an ensemble of downscaled, hourly resolution present day and future climate scenarios for Khumbu Glacier from a selection of Regional Climate Models. The following questions are addressed:
    a) How are the key meteorological phenomena of the study region represented in the Regional Climate Models?
    b) How do the chosen downscaling and disaggregation approaches remove biases and improve the climatology relative to observations?

d) What does the future climate for Khumbu Glacier under two emissions scenarios look like?

4. To improve accuracy of simulated historical and future evolution of Khumbu Glacier through integrating a more robust representation of glacier mass balance into ice flow modelling.

   The following questions are addressed in the analysis of historical simulations:

   a) How does a more robust, distributed representation of glacier mass balance influence simulated historical glacier evolution?

   b) Which sub-debris ablation parameterisation is most accurate for present-day Khumbu Glacier? This builds on the work by Rowan et al. (2021) where a more simplistic, linear representation of mass balance is used for historical glacier change simulations.

   The following questions are addressed in the analysis of future simulations:

   a) How do projections of glacier mass loss change under future emission scenarios? This builds on the work by Rowan et al. (2015) by using an improved representation of future climate and distributed mass balance.

   b) What are the characteristics of future glacier behaviour?

   c) How does Khumbu Glacier respond to varying future atmospheric forcing?

1.3 Thesis Structure

The following chapter builds on the motivation in this chapter, whilst providing a detailed review of previous studies and identifying knowledge gaps in this area. As each of the results chapters (Chapters 3-6) addresses the above aims individually, a further review of the literature is given in each. The chronology of the results chapters link to each of the stages of the modelling chain, and so description of methods and models used fall within each results chapter.

The first aim and associated research questions are addressed in Chapter 3, which provides an analysis of the catchment-scale meteorology using a network of weather stations that span 3000 m in elevation. This meteorological analysis is conducted through a glacier mass balance lens, considering how this *in situ* data can be used to aid downscaling and distribution of meteorology

for glacier models, and how differing glacier modelling approaches can resolve the meteorological complexity of this high elevation catchment.

Chapter 4 focuses on the second aim, where a distributed glacier energy balance model is applied to Khumbu Glacier in the present day. Sensitivity analyses are conducted to reveal the meteorological drivers of melt. A sub-debris ablation component is applied to aid evaluation of the otherwise simulated clean-ice ablation rates.

The third aim is addressed in Chapter 5, where various statistical downscaling and disaggregation techniques are described in detail and applied to data from three Regional Climate models. Observations that were analysed in Chapters 3 and 4 are used to aid downscaling and validation of results. Future climate scenarios are described.

The final aim is addressed in Chapter 6, where the downscaled climates (Chapter 5) are used to force the energy balance model (Chapter 4) to produced simulated present-day and future glacier mass balance. The ice flow model is introduced, and the impact of the integration of the distributed glacier mass balance model on present-day and future glacier change and its implications are discussed.

The concluding chapter acts as a synthesis of the findings from the four results chapters, where the limitations and uncertainties of the approaches used in the thesis are described. Finally, the implications of these findings and opportunities for future work are discussed.

Chapter 2 Literature Review

2.1 The Hindu-Kush Karakoram Himalaya region

The Hindu Kush Karakoram Himalaya (HKKH) region is the largest and youngest mountain region in the world, encompassing an area of 4,192,000 km^2 across eight countries: Afghanistan, Bangladesh, Bhutan, China, India, Myanmar, Nepal, and Pakistan (Bajracharya and Shrestha, 2011 and Figure 2.1). It comprises the Hindu Kush, Karakoram, Kunlun Shan, Pamir Alai and Tian Shan in the northwest, and the Himalaya in the east.

The HKKH harbours the largest snow and ice deposits outside of the two poles (Mukherji et al., 2015 and Wester et al., 2019). The chain of mountains, spanning 2000 km in length, are termed the "Water Towers of Asia", as they supply ten major rivers that flow to growing downstream populations (Eriksson et al., 2009 and Pritchard, 2019 and Figure 2.1). All of these rivers are snow and glacier fed from the more than 54,000 glaciers that cover an area up to 81,140 km^2 and act as critical stores of water during periods of scarcity (Bajracharya et al., 2011, Nuimura et al., 2015, Arendt et al., 2015 and Pritchard, 2019).

Figure 2.1 The Hindu-Kush Karakoram Himalaya with the ten major river basins. Modified from Mukerji et al. (2015).

In this chapter, the climate and glaciology of the HKKH are outlined, and the impacts of glacier change discussed. The focus then shifts to the Everest region of Nepal Himalaya, where the impact of climate change on debris-covered glaciers are considered, with an emphasis on Khumbu Glacier. Projections of future climate and glacier change across the HKKH will then be discussed, with a background to glacier modelling, with some emphasis on the Everest region, then being provided . This is built on further in Chapter 4 (mass balance models) and Chapter 6 (ice flow models).

2.1.1 Regional climate

The HKKH region exerts a strong influence on the large-scale atmospheric circulation such as the upper tropospheric zonal jet and the Indian summer monsoon (Nan et al., 2009) and act as a source and sink of heat in summer and winter, respectively (Yanai and Li, 1994; Wu and Zhang, 1998).

The Indian summer monsoon generally occurs between June and September, contributing up to 80% of annual precipitation for the central and eastern Himalaya (Bookhagen and Burbank, 2006; Pokharel et al., 2019). This distinguishes glaciers in this region from those situated in other regions of the world as their accumulation and ablation seasons occur simultaneously, referred to as "summer-accumulation type" glaciers (Ageta and Higuchi, 1984). There is an east-west division in annual precipitation as precipitation increases farther east with the growing dominance of the summer monsoon.

Glaciers of the western Himalaya and Karakoram depend on the upper-level westerlies that provide winter precipitation (Archer and Fowler, 2004; Farinotti et al., 2020). Extratropical cyclones form over the Mediterranean, and are then transported via the sub-tropical jet to the western Himalaya. The heavy precipitation brought about by these disturbances are critical inputs to glacier and river systems, and plays a role in modulating the albedo of the mountain range, affecting atmospheric circulation and the monsoon (Dimri et al., 2015).

For the monsoon-dominated regions in the Himalaya, there is a significant south-north precipitation gradient, as the monsoon arrives from the south to the Himalayan foothills. The highest topography further north experiences less precipitation (Bookhagen and Burbank, 2006 and 2010). In recent years, positive precipitation trends in eastern and central Nepal have contrasted with negative precipitation trends towards the west (Wang et al., 2019). Warming air temperatures have likely driven the significant increase in extreme precipitation in Nepal since the end of the 20th century as warmer air can support increased atmospheric moisture (Krishnan et al., 2019; Pokharel et al., 2019).

Atmospheric warming has been observed across the HKKH over recent decades. For the 1901 to 2014 period, increases of 0.104°C per decade in mean daily temperature have been observed across the region (Figure 2.2, Table 2.1). Highest rates of warming (0.176°C per decade) are exhibited in daily minimum temperatures (T_{min}, Ren et al., 2017), leading to an overall negative trend in the diurnal temperature range (DTR and Figure 2.2). Increases in T_{max} were found to be greater than for T_{min} below 2,566 m.a.s.l. in Nepal, yet the reverse was true at Pyramid station at 5,050 m.a.s.l. in the Everest region of Nepal (Table 2.1). Spatially heterogenous and short-term deviations in warming occur due to altitudinal and latitudinal dependencies and decadal climate oscillations such as the Pacific Decadal Oscillation and the Indian Ocean Dipole (Krishna et al., 2006). A slight decrease in temperatures particularly during summer, have been seen in the Karakoram though this is highly anomalous (Forsythe et al., 2017).

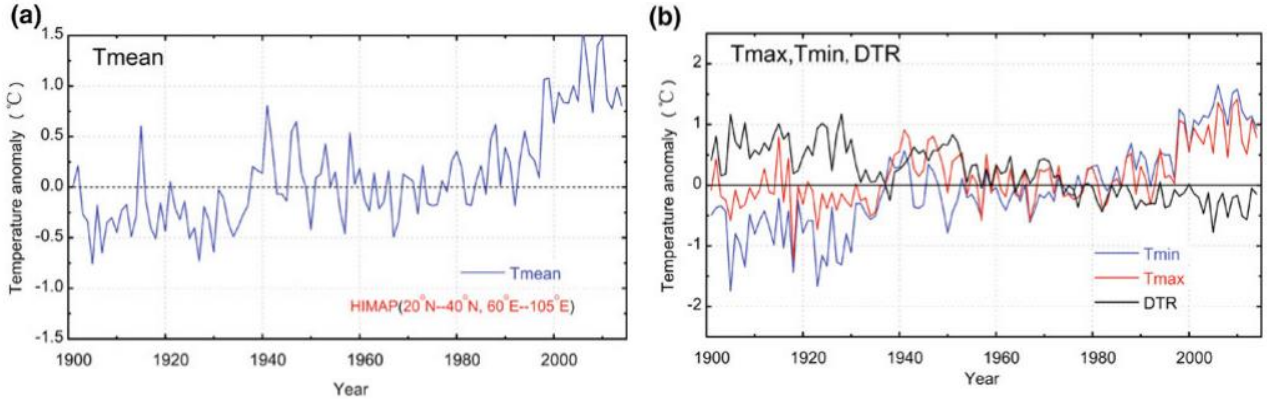

Figure 2.2 Annual mean temperature anomaly against the baseline period of 1961-1990 (a) Mean daily temperature (T_{mean}) and (b) Maximum (T_{max}), minimum daily temperature (T_{min}) and diurnal temperature range (DTR). Modified from Ren et al. (2017) and Krishnan et al. (2019). There is higher density of stations in eastern China and so removal of bias from uneven station density using the climate anomaly method was undertaken (see Annex 1 in Krishan et al., 2019 for further detail).

Globally, the climate warming signal generally increases with elevation as a result of a variety of complex feedback mechanisms that exacerbate warming (Wang et al., 2013; Pepin et al., 2015). Though warming rates are not linear with elevation, warming trends closest to the 0°C isotherm are highest. Here, snow and ice are particularly sensitive to temperature change, and melt reduces surface albedo which causes further warming (Pepin and Lundquist, 2008). Another positive feedback that is thought to be critical is through the increased moisture capacity of a warming atmosphere that amplifies latent heat release. This will also cause a rise in incoming longwave radiation, as is seen on a seasonal scale during the monsoon in Nepal (Bonekamp, et al., 2019). This will further enhance warming, particularly in dry high elevations (Mountain Research Initiative Elevation Dependent Warming Working Group 2015). This elevation dependent warming (Giorgi et al., 1997) means that, even if global warming is limited to 1.5°C, the HKKH will experience warming of 1.9°C (Krishnan et al., 2019) to 2.1°C (Kraaijenbrink et al., 2017, Table 2.3).

In the HKKH, the cryosphere is also vulnerable to short-lived climate forcings, namely black carbon and other aerosols. These aerosols are carried from cities in Asia and a small proportion of black carbon comes from cooking stoves (Duan et al., 2006; Wester et al., 2019). Black carbon causes localised warming of the lower atmosphere, which in the short term can be close to that of carbon dioxide (Ramanathan and Carmichael, 2008). Black carbon deposition on snow and ice lower surface albedo, particularly above 5000 m.a.s.l. during the pre-monsoon, and encourage further albedo decay of the glacier surface (Bonasoni et al., 2010; Ginot et al., 2014; Jacobi et al., 2015).

General Circulation Models (GCMs) are not always able to represent atmospheric drivers of glacier change, due in part to the coarse spatial resolutions that cover extreme elevation ranges within one gridbox. Although GCMs from the World Climate Research Programme's Coupled Model Intercomparison Project Phase 3 and 5 (CMIP3 and CMIP5, respectively) were found to simulate mean annual temperature and precipitation cycles over the last century across the HKKH, there still existed large deviation from weather station precipitation records. Panday et al. (2015) found that AOGCMs were unable to capture the negative trend in annual temperature in the Western Himalaya over the 20th century and suggested that higher resolution dynamical downscaling with regional climate models (RCMs) is necessary to resolve hydrometeorological dynamics that are key for glaciers, including the monsoon.

The high computational expense of dynamical downscaling limits its applicability for unravelling longer term historical or future climate trends, and thus bias correction or statistical downscaling of climate models is often the preferred method. Statistical downscaling methods are designed to correct and lessen biases in the mean and extremes of climate model data (Gudmundsson et al., 2012; Cannon et al., 2015b). A more detailed background to statistical downscaling is provided in Chapter 5.

There are few precipitation measurements at elevation across the HKKH and the length of observations is often too short to characterise the climatology and extract the climate change signal. The precipitation gauge at Biafo glacier in the Central Karakoram offers a rare insight into precipitation rates of the accumulation zone, with annual precipitation rates of 1000 mm and sometimes up to 2500 mm (Hewitt, 2014). When compared with valley measurements, strong positive precipitation gradients with height were revealed. This orographic enhancement of precipitation likely occurs elsewhere in this region, yet contrasts with other HKKH regions. Weak or absent gradients in the Everest region mean there is a lower likelihood that precipitation will fall as snow (Ageta and Higuchi, 1984). There, annual precipitation rates are also 400-500 mm lower and show less interannual variability (Bollasina, 2002).

Region	Temperature change per decade				Precipitation change per decade	Period	Reference
	T_{mean}	T_{min}	T_{max}	DTR			
HKKH	0.104°C	0.176°C	0.077°C	-0.101°C	-	1901-2014	Ren et al. (2017); Sun et al. (2017)
	0.195°C	0.278°C	0.156°C	-0.123°C	-	1951-2014	
	-	-	-	-	0.528%	1961-2013	
HKKH	-	-	-	-	0.284% (light precip days)	1961-2012	Zhan et al. (2017)
	-	-	-	-	0.515% (extreme precip days)	1961-2012	
East Karakoram	-0.18°C (annual) -0.042°C(winter) 0.16°C (summer)	-	-	-	0.332%	1985-2015	Negi et al. (2021)
	0.9°C (annual) 0.45°C (winter) 0.58°C (summer)	-	-	-	-0.293% (snowfall) 0.587% (rainfall)	2000-2015	
Nepal (below elevations of 2,566 m.a.s.l)	0.27°C	0.09°C	0.45°C (annual) 0.3°C (winter) 0.51°C (pre-mon) 0.63°C (monsoon) 0.69°C(post-mon)	0.34°C	-	1976-2015	Thakuri et al. (2019)
Southern Koshi basin, Nepal (158-5,050 m.a.s.l)	0.3°C	0.003°C	0.6°C	-	-11.1 mm (∼-1.5%)	1994–2013	Salerno et al. (2015)
Pyramid, Everest region of Koshi basin, Nepal (5,050 m.a.s.l)	0.44°C	0.72°C (annual) 0.151°C (post-mon)	0.09°C	-	-13.7 mm (-4.1%)	1994–2013	
Northern Koshi basin, Tibet (3,811-4,302 m.a.s.l)	0.37°C	0.39°C	0.34°C	-	-0.1 mm	1994–2013	

Table 2.1 Historical change in temperature and precipitation for several HKKH regions from observational datasets. For Pyramid station there is thought to be an underestimation of up to 5% of solid precipitation from the tipping bucket rain gauge (Salerno et al., 2015). This AWS and the rest of the Ev-K2-CNR network is described in detail in the following chapter. Only two stations are located in the Northern Koshi basin (Tibet).

2.1.2 Contrasting glacier signals

Observations of glacier change show overwhelming trends of ice mass loss since the 1970s across much of the HKKH (Wester et al., 2019), which appears to accelerate from 2000-2016 in response to climate change (Brun et al., 2018; Maurer et al., 2019; Hugonnet et al., 2021). This mass loss is likely strongly driven by the atmospheric warming seen across the HKKH.

Glacier length and area measurements indicate that glaciers of the HKKH have been receding since around 1850 (Bolch et al., 2012). *In situ* and geodetic mass balance studies show negative trends of glacier mass balance of −0.2 to −0.7 metres water equivalent per year (m w.e. a^{-1}), which have accelerated from the mid-1990s (Bolch et al., 2012; Gardner et al., 2013; Shean et al., 2020 and Table 2.2). Extrapolation of *in situ* measurements across the HKKH produced rates of −0.72 ± 0.22 m w.e. a^{-1}, though a sampling bias of relatively easy-to-reach lower elevation glaciers likely contributed to this especially negative value (Gardner et al., 2013). Brun et al. (2017) used ASTER DEMs to reaffirm findings of high spatial variability across the HKKH between 2000 and 2016. Glacier-wide mass balances of −0.33 to −0.42 m w.e.a^{-1} were found for the Himalaya, while glaciers in the Karakoram were stable (−0.03 ± 0.07 m w.e. a^{-1}), and Kunlun Shan were positive (+0.14 ± 0.08 m w.e. a^{-1}). For basins with negative glacier mass balances, excess glacier meltwater runoff represents ~12–53% of the total meltwater runoff (Shean et al., 2020).

The regional mass balance for the Karakoram between 1998 and 2008 was +0.11±0.22 m w.e. a^{-1} and was mirrored by a reduction of river runoff (Gardelle et al., 2013, Table 2.2). The so-called 'Karakoram anomaly' has persisted since observations began, and has also been found to reach the Pamir and Western Kun Lun. The two distinct precipitation regimes of the central/eastern Himalaya, and the west and Karakoram are likely strong drivers of the contrasting regional signals in glacier mass balance. Unlike the majority of glaciers of the HKKH which have exhibited sustained mass loss and glacier slowdown (Dehecq et al., 2018), the glaciers of the Karakoram that make up 30% of HKKH glaciers are balanced or somewhat gaining mass and velocity (Farinotti et al., 2019, 2020).

The mechanism that contributes a substantial proportion of precipitation to the western Himalaya and Karakorum are the westerly disturbances. These are extratropical cyclones that form in the Mediterranean, often during winter, which are then carried by the subtropical jet until they encounter the Himalaya (Farinotti et al., 2019). Westerly disturbances have increased in intensity and frequency in recent decades (Cannon et al., 2015a) indicating that increased accumulation could be a potential driver of observed stable and positive glacier mass balances in the region (Archer and Fowler, 2004, Fowler and Archer, 2006; Scherler et al., 2011a). Positive annual trends in snowfall occurred between 2000 and 2008, though began to decrease from 2008 (Negi

et al., 2021, Table 2.1). This contrasts with reduced solid precipitation seen over the past few decades in other HKKH regions (Kapnick et al., 2014). Growth in irrigation in Northwest China since the 1960s could have contributed to a rise in atmospheric moisture and summer snowfall, offsetting ablation, yet this remains uncertain (Cook et al., 2015; de Kok et al., 2018). In the central and eastern Himalaya, irrigation induced tropospheric cooling (and thereby reduced geopotential height) may have contributed to changes in atmospheric circulation here too with observed monsoonal weakening (Singh et al., 2018). Large-scale irrigation could therefore have altered circulation systems, that have opposing implications for glaciers in the west and east of the HKKH.

The year-round accumulation regime seen in the Karakoram (Farinotti et al., 2020), aided by the orographic enhancement of precipitation (Hewitt, 2004) reduces sensitivity to atmospheric warming, and limits radiative fluxes that favour warming. Glacier accumulation is known to be highly avalanche driven from the steep headwalls, and it has been shown by numerous studies that the thick debris cover on many glacier tongues in the Karakoram insulates the ice from atmospheric forcing (Hewitt, 2014). However, similar glacier characteristics are seen in the Everest region, where glaciers have thinned by 100 m since the 1960s (King et al., 2020). The glacier melt regimes in the Shimshal valley (the Karakoram) have been found to be controlled by net shortwave radiation, so observed summer snowfall and cooling and associated with higher albedos may also be responsible for glacier growth (Bonekamp, et al., 2019). Glacier melt in the Langtang valley in Nepal (Central Himalaya) is driven more by net longwave radiation, increased by low and high-level clouds in the melt season.

This so-called Karakoram anomaly contrasts strongly with glacier signals elsewhere across the HKKH and globe. Whether this will persist into the future is uncertain and there are early indications that it may be coming to an end (Hugonnet et al., 2021; Miles et al., 2021a). These contrasting glacier signals are demonstrative of the complex drivers and mediators of glacier behaviour; external atmospheric forcing and internal glacier dynamics.

Region	Mass balance (m w.e. a^{-1})	Debris cover	Period	Reference	Notes
HKKH		23% of glaciers	2000-2008	Scherler et al. (2011)	
				Bolch et al. (2012)	
	−0.72 ± 0.22[1] −0.24 ± 0.11[2] −0.16 ± 0.17[3]		2003-2009	Gardner et al. (2013)	[1]Extrapolation of *in situ* observations [2]ICESat altimetry [3]GRACE
		18% of glaciers		Kraaijenbrink et al. (2017)	
	-0.18 ± 0.04		2000-2016	Brun et al. (2017)	ASTER
	−0.19 ± 0.03		2000-2018	Shean et al. (2020)	ASTER and GeoEye-1 DEMs
Central Himalaya (or East Nepal)	-0.79 ± 0.52		2002-2007	Bolch et al. (2011)	
	-0.40 ± 0.25	36% of glaciers (Everest region)	2000-2008	Nuimura et al. (2012)	
	-0.26 ± 0.13		1999-2013	Gardelle et al. (2013)	SRTM
	-0.31 ± 0.14		2003-2008	Kääb et al. (2015)	
	−0.32 ± 0.18		1974-1999	Pellicciotti et al. (2015)	Langtang
	−0.21 ± 0.08 −0.38 ± 0.17		1974-2006 2006-2015	Ragettli et al. (2016)	Langtang
	-0.33 ± 0.20		2000-2016	Brun et al. (2017)	ASTER
	-0.52±0.22[1] -0.53 ± 0.21[2] −0.70 ± 0.26[3]		2000-2016	King et al. (2017)	SRTM [1]Everest region [2]Land-terminating DCGs of Everest region [3]Lake-terminating glaciers
West Himalaya (or West Nepal)	-0.32 ± 0.13		1999-2011	Gardelle et al. (2013)	SRTM
	-0.37 ± 0.15		2003-2008	Kääb et al. (2015)	
	-0.34 ± 0.09		2000-2016	Brun et al. (2017)	ASTER
Karakoram	+0.11±0.22				
	-0.13± 0.34			Kääb et al. (2015)	
	-0.06 ± 0.19		2000-2008	Brun et al. (2017)	ASTER
	0.05 ± 0.19		2008-2016		

Table 2.2: Historical annual regional averages of glacier-wide mass balance, and the percentage of DCGs relative to clean-ice glaciers.

2.2 The hydrological impact of climate change

Across the region, glacier discharge is expected to rise until the middle of the century in response to atmospheric warming, as the trajectory follows the rising limb of the peak water curve (Huss and Hock, 2018; Figure 2.3) until peak water is reached. Following this, there is a steady decline in runoff (falling limb). Even without further 21st century warming, the input of glacier melt into rivers will reduce by 28% by 2100 across the HKKH, due to current glacier-climate imbalance;

the region will therefore reach and surpass peak water in the next century (Miles et al., 2021a). This is of particular concern for mountain communities who often live above main rivers, and so directly depend on snow and glacier meltwater. The contribution of meltwater with increasing downstream distance still remains poorly constrained (Quincey et al., 2017a).

For the Indus river basin region, peak water is predicted to occur around 2070, and for the Ganges 2050. It is postulated that peak water has already been reached in the headwaters of the Brahmaputra. The western Himalaya and Indus river basin are particularly vulnerable to diminished meltwater, as they do not experience the mediating influence of the summer monsoon (Pritchard, 2019).

Monsoon-influenced river basins are projected to be able to sustain the increasing demands for water (Immerzeel et al., 2013). Currently in the Khumbu region, glacier meltwater supplies 65% of the water consumed by the local community during the pre-monsoon (Wood et al., 2020). Increased water stress with loss of melt from glaciers and snow melt will be exacerbated by the predicted delayed monsoon onset in the future (Panday et al., 2015; Sanjay et al., 2017b). The Dudh Koshi River, which flows through the Khumbu region, feeds into the Koshi river which holds 25% of Nepal's hydroelectric potential (Shea et al., 2015a).

Under extreme warming scenarios peak water will be delayed as excess glacier melt continues to rise, though streamflow patterns will become more unpredictable and limit time for adaptation for downstream communities. It is thought the slower rates of atmospheric warming under lower emission scenarios (RCP2.6 and 4.5, see section 2.4.1) will allow some glaciers to approach a new equilibrium and thereby reduce glacier runoff in the coming decades (Rounce et al., 2020).

Projected trends of unabated atmospheric warming will have the most significant impact on the region's glaciers, and will also influence precipitation trends. Precipitation is projected to increase as a result of the higher moisture capacity of warmer air masses. The summer monsoon is likely to become more unpredictable and intense into the future (Turner and Annamalai, 2012; Panday et al., 2015; Sanjay et al., 2017b). This could potentially counteract reduced river flow expected with snow and glacier mass loss. Atmospheric warming will shift the rain/snow balance, driving glacier mass loss and making downstream regions more prone to flooding, and ultimately drought with glacier shrinkage (glaciers act as a mediating water source) (Pritchard et al., 2021). The highest source of uncertainty in the region's future hydrology originates from future precipitation trends which will undoubtedly also prove critical for future glacier viability (Immerzeel et al., 2013).

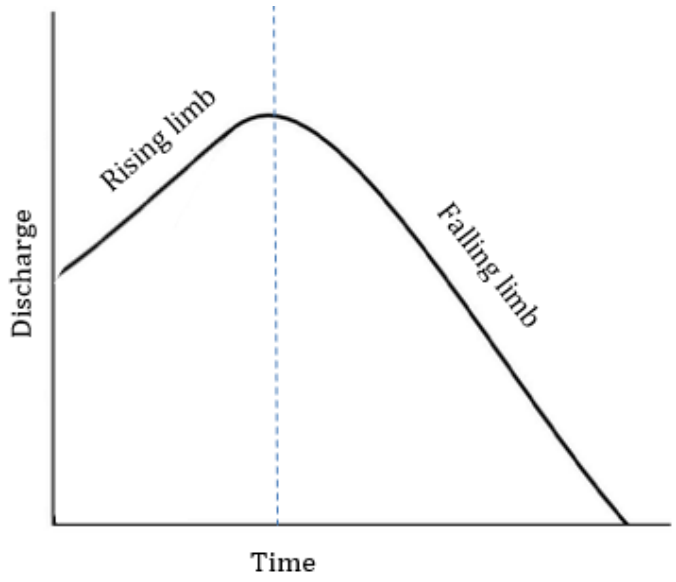

Figure 2.3 Schematic of concept of peak water, with peak water marked by blue dashed line.

More broadly, parts of the central Andes are already experiencing decreased stream flows in response to glacier loss (e.g. Migliavacca et al., 2015), which contrast strongly with increased flow for areas of the Nepal Himalaya (Ragettli et al., 2016). Reductions in discharge even at the highest elevations have been observed over the last few decades in the Italian Alps as glaciers and snow cover retreats (Bocchiola and Diolaiuti, 2010; Diolaiuti et al., 2012; Bocchiola, 2014).

Unlike other glaciers in the HKKH, glaciers in the Karakoram are prone to surging, with maximum velocities during surges being between one and two orders of magnitude higher than during periods of quiescence (Quincey et al., 2011; 2015). As glacier fronts advance during surges they form ice barriers in rivers that can evolve into lakes. The rate of accumulation of impounded water determines how quickly this ice dam will be breached, and the occurrence of such events in late spring and summer indicate temperature and therefore glacier melt plays a dominant role (Bazai et al., 2021).

Lake formation and expansion has accelerated more in the east than the west of the HKKH, mirroring the contrasting regional glacier signals (Gardelle et al., 2009). In the regions where downwasting dominates, increased retention of water in supraglacial lakes, supported by flat tongues with thick mantles of debris, has been observed. These can drain suddenly via the englacial drainage system as was observed on Changi Shar Glacier in the 2017 ablation season (Miles et al., 2018b). Although this lake was relatively small, the geomorphic impacts extended 11 km downstream, and three trails were destroyed.

Larger proglacial lakes can evolve behind moraine dams and in some instances can pose severe risks of glacial lake outburst floods (GLOFs). The likelihood of GLOFs depends on the lake and

dam geometry and vulnerability to trigger mechanisms such as rockfalls (Benn et al., 2012). The expansion of lakes in higher, steeper terrain that is more prone to avalanching may increase the frequency of GLOF occurrence, although as of yet there is no evidence of this occurring in the HKKH (Veh et al., 2019; Lala et al., 2020; King et al., 2020).

2.3 The Everest region

This section will discuss research to date on the climate and glaciology in the Everest region, where Khumbu Glacier is located.

2.3.1 Climate of the Everest region

The Everest region lies on the northern limit of the monsoon-dominated southern slopes of the Nepal Himalaya, with the drier lee-ward glaciers lying just north of Everest across the Nepal/Tibet border. Several studies estimate that up to 80% of the annual precipitation falls during the monsoon season (Burbank and Bookhagen, 2006) and 90% during June and September (Salerno et al., 2015). It is thought that below elevations of 2,500 m.a.s.l that synoptic-scale monsoon rains are the dominant driver of precipitation. At higher elevations the influence of the monsoon is still significant, but precipitation is also influenced by the daily convective precipitation caused by thermal valley winds (Yasunari and Inoue, 1978; Bollasina et al., 2002; Potter et al., 2019).

A network of automatic weather stations (AWS) in the Dudh Koshi valley of the Everest region provides an insight into atmospheric trends over the last decade. Greater warming of minimum annual temperatures (0.072°C) than of maximum temperature (0.009 °C) matches observations elsewhere across the HKKH region. Annual warming of mean temperatures of 0.044°C has decreased the likelihood of precipitation falling as snow by 10% (Salerno et al., 2015). The meteorology of this valley, where Khumbu Glacier sits at the northernmost limit, is described in detail with analysis of this AWS network in Chapter 3.

2.3.2 Debris-covered glaciers in the Everest region

Debris-covered glaciers (DCGs) are most often present in younger mountain ranges, where uplift provides ample sediment for erosion (Anderson and Anderson, 2016). There is therefore a high concentration of Earth's DCGs in the Himalaya (Bolch et al., 2011; Miles et al., 2017). In the Everest region, 36% of glaciers are debris-covered (Nuimura et al., 2012). This debris is transported to the glacier through rockfalls and landslides, through deformation of the bed, and from dust blown from hillslopes and moraines (Anderson, 2000; Gibson et al., 2017). Debris ablates from the ice

after being transported englacially, meaning debris thickness often increases towards the glacier tongue (Rounce and Mckinney, 2014, Rowan et al., 2015; Anderson and Anderson, 2018). As glaciers melt, surface debris layers develop and thicken, making DCGs a growing feature of the Himalayan cryosphere (Nicholson and Benn, 2006). DCGs typically lose mass through surface lowering and thinning rather than retreat of the tongue (Hambrey et al., 2008; Rowan et al., 2015).

A supraglacial debris layer alters the surface energy balance and therefore the ablation rates of the underlying ice (Østrem, 1959; Nicholson and Benn, 2006). Takeuchi et al. (2000) measured ablation under various thicknesses of debris on Khumbu Glacier between 21 May and 1 June 1999, using a positive degree day factor. They found that ice ablation was enhanced by the presence of surface debris at a thickness of ≤0.3 cm, with highest melt rates of 6.4 cm day^{-1} occurring at this thickness. A debris thickness above this value acted to insulate the ice surface from incoming solar radiation, thus retarding ablation (as in Figure 2.4). The critical thickness, the thickness at which the melt rate for a debris-covered glacier is the same as that of a clean glacier, was measured to be approximately 5 cm, with an average ablation rate of 4.7 cm day^{-1}. The neighbouring Ngozumpa glacier showed melt rates suppressed by 50% under 50 cm of debris (Nicholson and Benn, 2013). Given that Khumbu Glacier has a debris mantle with thicknesses that sometimes exceed several metres (Rounce and McKinney, 2014; Rounce et al., 2018), most of the debris acts to retard rather than enhance melt (Figure 2.4).

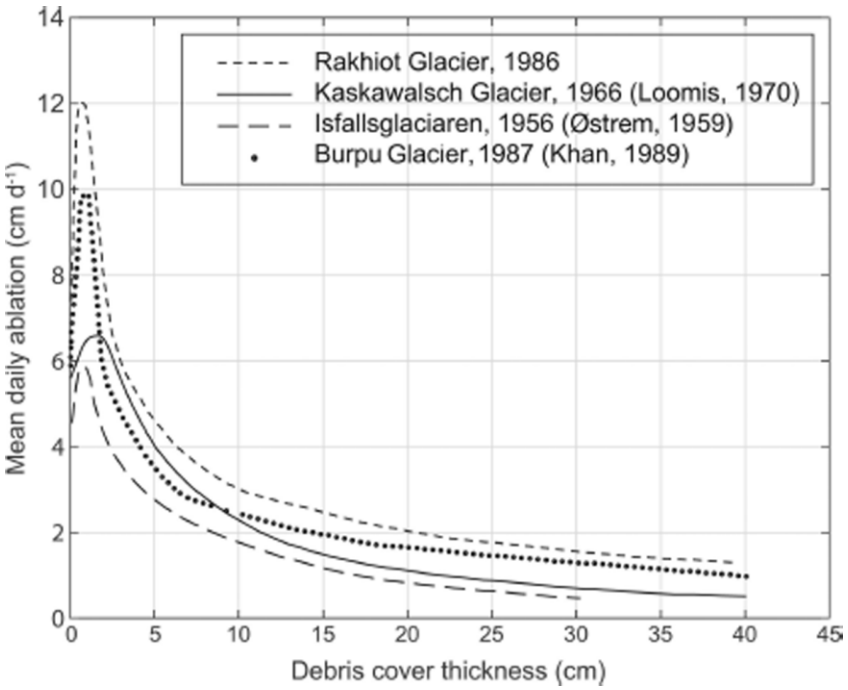

Figure 2.4 Østrem curves for measured melt rates under varying debris thickness. Source: Mattson et al. (1993).

Given this insulation effect, it could be theorised that DCGs are exhibiting lower mass loss relative to clean-ice glaciers. However, thinning rates for DCGs and clean-ice glaciers are similar across the Himalaya. Mass on DCGs is lost through melting of clean ice in the upper ablation areas, close to the Equilibrium Line Altitude (ELA) where accumulation and ablation rates are balanced. Melt also occurs beneath debris, but is more significant around ice cliffs and surface ponds that are able to develop on glaciers with thick mantles of debris (Benn et al., 2012). Melt around surface ponds is enhanced by up to ten times those below thick debris (Immerzeel et al., 2014a). DCGs in the Everest region are often characterised by an inverse mass balance profile, with highest ablation rates in the upper ablation area just below the ELA, and lower rates down-glacier on the debris-covered tongue.

This debris-cover anomaly (Pellicciotti et al., 2015) where DCGs are losing mass at similar rates to clean ice glaciers is seen across the HKKH but particularly in the Everest region (Kääb et al., 2012; Gardelle et al., 2013; Brun et al., 2019; Rounce et al., 2021; Rowan et al., 2021). This anomaly may be due to a combination of several factors:

a) An increasing presence of supraglacial ponds and ice cliffs in recent years that counter the insulating effect of debris. Ice cliff backwasting was found to be significant on the debris-covered tongue of the Changri Nup glacier, but was not able to compensate for the lowered ablation rates due to debris cover (Brun et al., 2018).

b) Reduced ice flux from higher elevations reducing emergence velocities (Vincent et al., 2016, Banerjee, 2017; Brun et al., 2018; Rounce et al., 2021) potentially due to weakening precipitation (Salerno et al., 2015).

c) This reduced ice flux is enhanced by the characteristic flat glacier tongues, that also predispose the geometry of DCGs to high climatic sensitivity, inverse mass balance gradients (Benn et al., 2012; Salerno et al., 2017) and even dynamic or physical detachment (Nakawo et al., 1986; Pellicciotti et al., 2015; Rowan et al., 2015).

d) The presence of continuous, thick debris allows DCGs to extend and persist well below the elevations that would be possible if they were in equilibrium with the climate (Anderson and Anderson, 2016). DCGs typically have lower accumulation area ratio (AARs) than clean ice glaciers (Scherler et al., 2011b). They are therefore climatically sensitive to increased ablation and reduced accumulation associated with atmospheric warming.

2.3.2.1 Khumbu Glacier

Khumbu Glacier flows down the southern flanks of Mount Everest. It is 16 km in length, and ranges in elevation from 4,900 to 7,500 m.a.s.l. (Figure 2.5). It has the world's highest accumulation area but is also characterised by its flat tongue with a thick debris mantle, and supraglacial ponds and ice cliffs that occupy 5% of its area (Nakawo et al., 1999; Rowan et al., 2015, 2021; Watson et al., 2016, 2017). Its location on the Everest Base Camp route and thus relative accessibility means that there are more observations compared to other glaciers of the HKKH, as such it is an ideal site for model development.

There are two sets of lateral and terminal moraines surrounding Khumbu Glacier, denoting the late Holocene advance and the Little Ice Age (LIA) advance, and thereby the glacier extent and thickness (Hambrey et al., 2008; Owen et al., 2009; Rowan et al., 2017). A variety of dating techniques indicate that the LIA advance likely occurred approximately 500 years before present, with strengthening westerly winter precipitation (between 1400 and 1800) in response to cooling across the Northern Hemisphere (Rowan et al., 2017). At some point between the LIA maximum until present, the tributary Changri Nup and Changri Shar glaciers detached from the west side of the tongue of Khumbu Glacier.

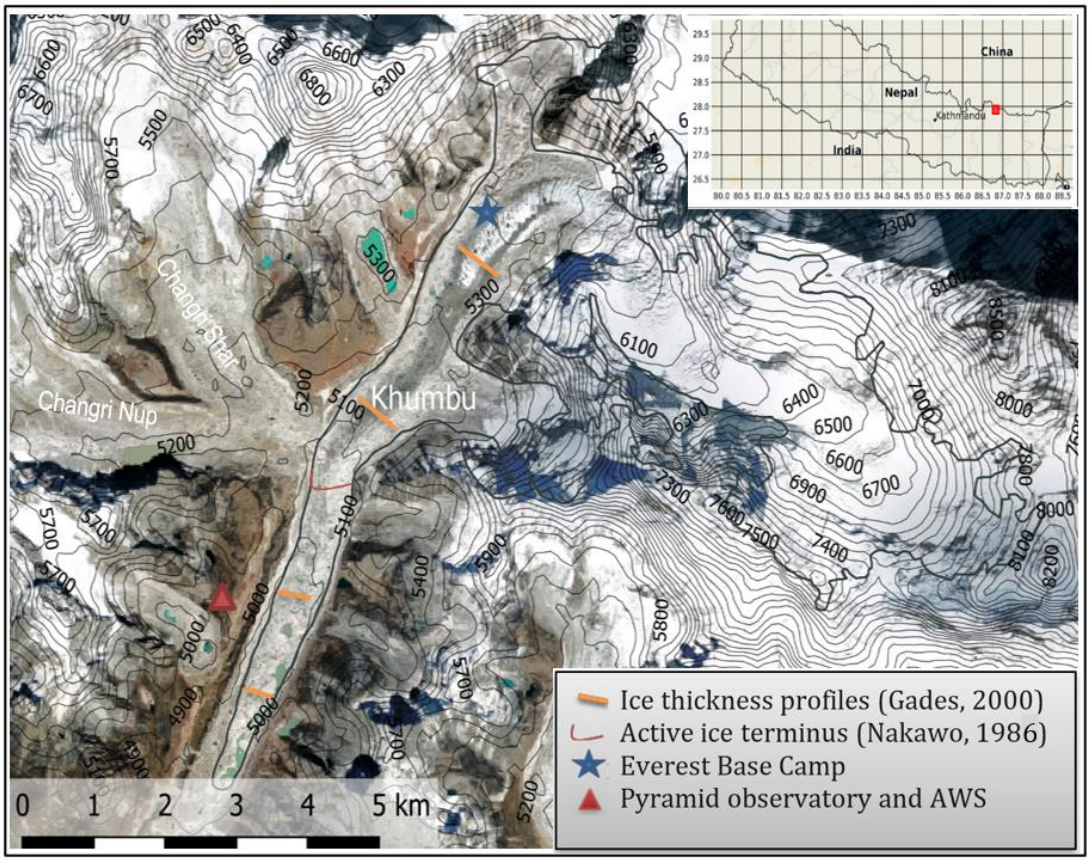

Figure 2.5 Khumbu Glacier with 100m contours, and its location in the Everest region of Nepal shown by red square in inset map (top right). Glacier outline from RGI Consortium (2017).

The Khumbu icefall is steep (Figure 2.5) and fast-flowing. Altena and Kääb (2020) determined icefall surface velocities of just over 1 m d^{-1}, using satellite imagery matching and validation from mountaineers' GPS devices. Cloudy monsoon days were omitted; icefall velocities are likely even higher during this period. The icefall is thought to somewhat act as a hydrological barrier between the accumulation and ablation zone (Harper and Humphrey, 1995; Armstrong et al., 2017; Altena and Kääb, 2020). The heavy crevassing associated with this fast-flowing ice allows percolation of surface water and advection of air down into the glacier ice (Gilbert et al., 2020).

Weak altitudinal precipitation gradients have been observed in this part of the Himalayas (Ageta et al., 1980). Observations from Inoue (1977) determined that accumulation on Khumbu Glacier is therefore independent of elevation, and that avalanching from the steep hillslopes must contribute significantly. Estimates of ELA heights have ranged from 5,300 m.a.s.l. to 6,000 m.a.s.l. (Fushimi, 1977; Inoue, 1977; Nakawo et al., 1987; Benn and Lehmkul, 2000; Kadota et al., 2000; Rowan et al., 2015). Highest thinning rates have been seen beneath the ELA in the upper ablation area, due to the absence of thick debris (Figure 2.6; King et al., 2020) where velocities can reach up to 20 m a^{-1} (Quincey et al., 2009). Previous estimates of velocities at the same location of 30 m a^{-1} in the 1960s indicate slowdown has occurred (Nakawo et al., 1999). Here, just below Everest Base Camp (EBC, Figure 2.5) maximum ice thickness estimated through ground-based echo sounding in 1999 was found to be 300 m (Gades, 2000). Maximum thickness halved to 160 m at a distance 3 km downglacier. Towards the terminus, melt is heavily suppressed below the several metres thick surface debris (Figure 2.6), where surface displacement is close to zero, indicating stagnant ice (Quincey et al., 2009) and a maximum ice thickness of 60 m (Gades, 2000).

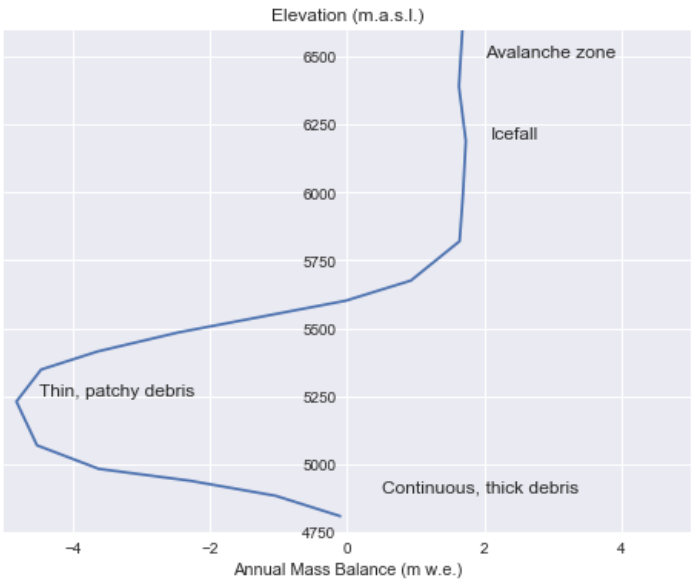

Figure 2.6 Mass balance curve of Khumbu Glacier from measurements by Inoue (1977) modified from Benn and Lehmkuhl (2000).

More recent fieldwork conducted on Khumbu Glacier (2017 and 2018) has involved hot water drilling to measure internal ice temperatures and debris content along the debris-covered tongue. Even the coldest glacier ice (at –3.3 °C) was found to be 2 °C warmer than the mean annual air temperature, often close to melting point (Miles et al., 2018a). This signals that despite its high elevation, the viability of Khumbu Glacier ablation area is at risk even with minimal atmospheric warming. Englacial debris was found to vary spatially and increased with depth (Miles et al., 2021b). The angle of the debris layers showed evidence of thrusting, which Miles et al. (2021b) suggested could stem from fast moving ice meeting stagnant ice at the base of the icefall or the tributary glaciers, or a significant topographic barrier or from a shift in thermal regime.

Nakawo et al. (1986) provided early empirical indications of contrasting behaviour between the clean-ice upper ablation area and accumulation area and the debris-covered tongue, delineating the active terminus. This differing behaviour of the active ice showing higher displacements than the almost-stagnant debris-covered tongue, the nonlinear mass balance curve and the absence of data above the icefall make Khumbu Glacier, and other large, debris-covered, avalanche-fed glaciers, particularly challenging to model.

2.4 Glacier change projections across the HKKH

Advances in remote-sensing, including the use of cold war-era spy satellite imagery (Maurer et al., 2019), have provided us with four decades of observations confirming that not only is mass loss across the HKKH significant, but that it is accelerating. These observations have been vital for a variety of reasons. They revealed that for the debris-covered glaciers that constitute up to 23% of the region's glaciers (Scherler et al., 2011a and Herreid and Pellicciotti, 2020), mass loss occurs through surface lowering rather than recession. Geodetic mass balance (e.g. King et al., 2017 and 2020, Shean et al., 2020), and remote-sensing derived measurements of glacier velocity (Luckman et al., 2007; Quincey et al., 2009; Heid and Kääb, 2012; Altena and Kääb, 2020) and of surface debris (Rounce and Mckinney, 2014; Rounce et al., 2015 and 2021) have aided calibration and validation of simulated historical glacier change. This has improved accuracy of future projections and quantification of uncertainties.

Many studies projecting the future evolution of mountain glaciers use approximate glacier models that rely on scaling of ELAs or AARs (e.g., Miles et al., 2021a), or statistical scaling relations between glacier volume and area/length (Banerjee et al., 2020). These regional-scale assessments have fed into studies of the contribution of HKKH glacier melt to global eustatic sea level (Hock et al., 2019, Kulp and Strauss, 2019; Marzeion et al., 2020) and river patterns (Zhao et al., 2014; Zhang et al., 2015; Kumar et al., 2019).

The 2015 ratification of the Paris Agreement by 195 countries, with the goal to limit global warming by 1.5°C relative to pre-industrial levels, has provided a framing for modelling efforts into future glacier change. Globally, sea level rise from glaciers could be halved if Paris Agreement targets are met (Edwards et al., 2021). If warming of global temperatures is limited to 1.5°C, meaning warming of 2.1°C for the HKKH due to elevation dependent warming, then 33% of glaciers will be lost by 2100 (Kraaijenbrink et al., 2017).

This growing array of regional and global studies predicting future glacier response to climate change relies on simplistic, computationally inexpensive modelling approaches. In reality, glaciers of the HKKH are exceptionally complex. The critical processes that govern the responses of individual glaciers to climate change are currently unrepresented in modelling approaches. These processers include mass accumulation due to avalanching, inverse mass balance gradients of DCGs and frontal ablation with the development or enlargement of marginal lakes (King et al., 2019; Rounce et al., 2020; Miles et al., 2021a). Representation of these processes requires energy balance and glacier dynamic models.

Understanding future glacier response to climate change requires a robust representation of local climate, and the processes that drive glacier change within glacier models. Glacier models can be categorised into glacier mass balance models and ice flow models. Mass balance models simulate ablation and accumulation rates, and are useful for understanding climate sensitivity (Immerzeel et al., 2014b; Bonekamp et al., 2019). Mass balance schemes are often integrated with glacio-hydrological models to simulate runoff (Soncini et al., 2016; Khadka et al., 2020). Calculated mass balance has also been used to force glacier dynamics models to reconstruct past and project future Himalayan glacier change (Shea et al., 2015a; Wijngaard et al., 2019). Ice flow models are required to simulate future glacier evolution, as glacier response to changing mass balance is not necessarily linear over time and space. Over the last decade, advances in high performance computing and a growing number of open-source packages and models mean there is now a variety of glacier models available (e.g. Maussion et al., 2019). There exists a hierarchy amongst both categories of models and the representation of spatial and temporal resolution vary greatly.

2.4.1 Projections of future climate

For future climate impact studies, representative concentration pathways (RCPs) are commonly used. These represent future trajectories of global greenhouse gas concentrations, and by proxy act as emissions trajectories (IPCC, 2014 and Figure 2.7). RCP4.5 refers to a moderate radiative forcing value that may occur in 2100 AD, so 4.5 W/m^2. Under RCP4.5, RCP6.0 and RCP8.5 HKKH glacier mass loss of 49%, 51% and 64% is projected (Kraaijenbrink et al., 2017). In this study glacier mass loss was found to be directly related to warming.

Predictions from RCMs from the Coordinated Regional climate Downscaling Experiment (CORDEX) found warming is to be higher in the winter in the Central and Southeast Himalaya than the summer (Sanjay et al., 2017b and Table 2.3). The reverse is projected for the Karakoram and Northwest Himalaya. These findings also predict warming of 2°C to 3°C under RCP4.5 and 3°C to 6°C under RCP8.5 at the end of the century in the central Himalaya. The predicted warming for the region indicates that EDW is not predicted to contribute to increased regional warming relative to the global land mean (Table 2.3 vs Figure 2.7), or, more probably, that the majority of GCMs and RCMs are unable to resolve this phenomenon.

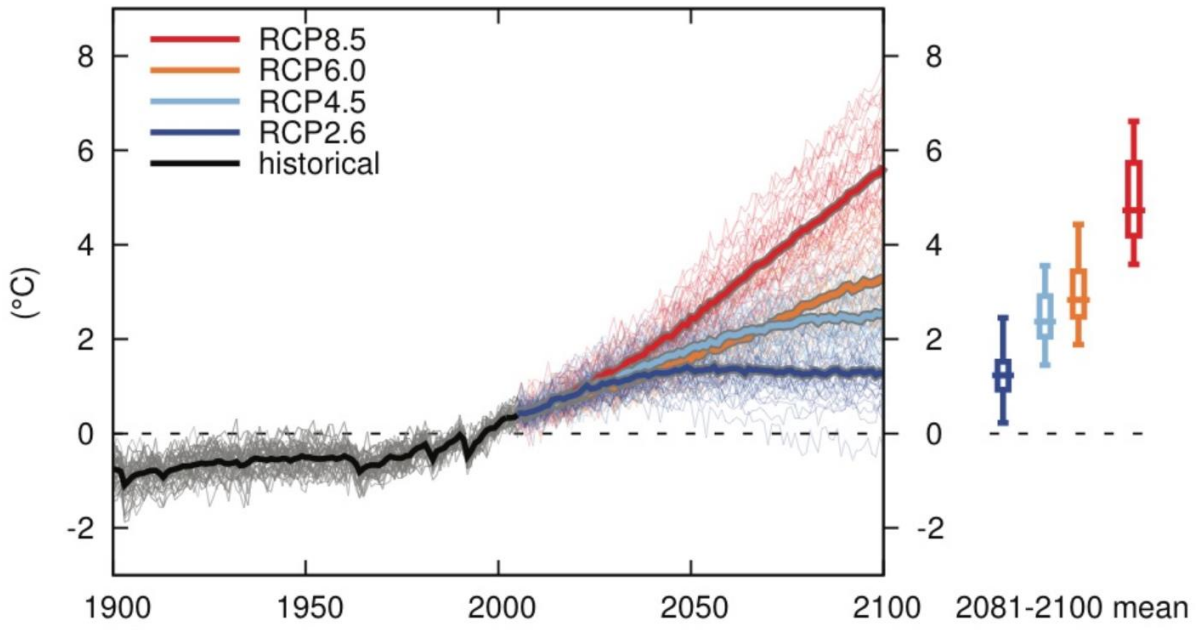

Figure 2.7 Global temperature change over land under each RCP (relative to 1986-2005 baseline). The thick lines show the multi-model mean, and the thin lines the trajectories from the CMIP5 members, with the end-of-century temperature box and whisker plots on the right. Source: IPCC, AR5 Supplementary Figure AI.SM2.6.4.

Previous studies have omitted future precipitation projections, and the interactions of precipitation with temperature and other key climate variables for glacier viability, such as incoming shortwave and longwave radiation. The uncertainty associated with precipitation and the emphasis on the relation between future glacier change and atmospheric warming means there are many more projections of temperature change over the 21st century than of precipitation (Table 2.3). The majority of precipitation projections indicate increases in annual rates, with an increase of up to 49% under RCP8.5 in the Koshi basin where Khumbu Glacier is situated (Kaini et al., 2019). Higher unpredictability in the summer monsoon is projected, combined with increased intensity and interannual variability (Turner and Annamalai, 2012; Panday et al., 2015; Sanjay et al., 2017b).

Climate projections from GCMs differ significantly, particularly for precipitation (Sanjay et al., 2017b; Watanabe et al., 2019). Differences between projections stem from future emission scenarios, but are also associated with model structure and parameterization of atmospheric processes that create biases that, if not considered or quantified, can then propagate to glacier models. Understanding and reducing these biases requires statistical downscaling of multiple models using an observational dataset. However, differences in downscaled climate between models will still remain. In this thesis, a multi-model approach is therefore used to drive simulations of future Khumbu Glacier evolution so as to cover future climate scenarios, particularly of precipitation.

Region	Emission scenario	Temperature change (°C)	Precipitation change (%)	Year	Data source	Reference
HKKH	RCP2.6	2.1	-	2071-2100	CMIP5 AOGCMs	Kraaijenbrink et al. (2017)
	RCP4.5	3.5	-			
	RCP6.0	4.1	-			
	RCP8.5	6.0	-			
Northwest Himalaya and Karakoram	RCP4.5	2.6 (summer) 2.1 (winter) *3.3 (summer)* *3.0 (winter)*	-3.5(summer) 14.1 (winter) *-0.3 (summer)* *6.2 (winter)*	1976-2005 to 2066-2095 *1976-2005 to 2066-2095*	CORDEX South Asia *CMIP5 AOGCMs*	Sanjay et al. (2017b)
	RCP8.5	4.9 (summer) 5.4 (winter) *5.7 (summer)* *5.1 (winter)*	5.0 (summer) 6.9 (winter) *3.9 (summer)* *12.9 (winter)*			
Central Himalaya	RCP4.5	2.2 (summer) 3.3 (winter) *2.7 (summer)* *3.6 (winter)*	10.5 (summer) 1.5 (winter) *11.8 (summer)* *-0.7 (winter)*			
	RCP8.5	4.3 (summer) 6.0 (winter) *4.7 (summer)* *5.8 (winter)*	19.1 (summer) -8.8 (winter) *19.1 (summer)* *-8.1 (winter)*			
Southeast Himalaya and Tibetan Plateau	RCP4.5	2.2 (summer) 3.1 (winter) *2.5 (summer)* *3.3 (winter)*	10.4 (summer) 3.7 (winter) *7.3 (summer)* *5.5 (winter)*			
	RCP8.5	4.2 (summer) 5.6 (winter) *4.4 (summer)* *5.4 (winter)*	22.6 (summer) 0.6 (winter) *9.7 (summer)* *6.0 (winter)*			
Koshi river Basin (Nepal/Tibet)	RCP4.5	1.6–2.8 (annual)	4–24 (annual)	2071-2100	CMIP5 AOGCMs	Kaini et al. (2019)
	RCP8.5	3.1–5.6 (annual)	13–49 (annual)			

Table 2.3 Projections of temperature and precipitation under future emission scenarios from published studies.

2.4.2 Mass balance modelling

Temperature is a critical driver of glacier mass balance and *in situ* measurements of temperature are more numerous than of other climate parameters. Therefore temperature-index approaches have been used to calculate glacier mass balance. The temperature-index or positive degree day (PDD) method assumes that the amount of snow or ice melt during a specific period is proportional to the number of days with a mean temperature above the melting point (although timesteps other than days are occasionally used) (Braithwaite et al., 1989; Hock, 2003 and 2005). This method is valuable for data-scarce regions such as the HKKH and has been used to force hydrological models or for large-scale studies due to the low relative computational expense (Ragettli et al., 2015; Shea et al., 2015; Khadka et al., 2020). Limitations include the low spatial and temporal resolution, with ablation rates often strongly related to the diurnal cycle of temperature in reality (Hock, 2003).

The addition of other meteorological variables that are known to be key drivers of melt has improved temperature-index melt calculations. These enhanced temperature-index models have been developed as a middle ground between PDD methods and sophisticated energy balance models, which have high input data and computational requirements. Shortwave radiation is globally one of the most significant drivers of glacier melt. The addition of a shortwave component to a temperature-index model, and parameterisation of snow/ice albedo over space and time which strongly controls absorption of incoming solar radiation, increased accuracy of modelled melt rates significantly (Pellicciotti et al., 2005).

Temperature generally correlates well with shortwave and longwave radiation at mid-latitude and low-elevation glaciers (Litt et al., 2019). The remote nature and high elevation of glaciers in the Himalaya means that validation is rare, and the meteorological drivers of melt are therefore less constrained than those of the European Alps, for example. However, it is known that for some Himalayan glaciers, shortwave radiation dominates the energy available for melt throughout much of the year (Azam et al., 2014; Litt et al., 2019; Bonekamp et al., 2019). For two glaciers in the Nepal Himalaya during the summer monsoon, melt was driven by temperature and shortwave radiation, and dominated net ablation (Litt et al., 2019). A temperature-index or enhanced temperature-index approach would suit these instances. However, outside of the monsoon when temperatures are below freezing, sublimation or other wind-driven processes likely dominate net ablation. This is also true throughout the year at high elevation sites such as at 6,325 m.a.s.l. on Mera glacier (Litt et al., 2019) and South Col at 7,945 m.a.s.l. on Khumbu Glacier (Matthews et al., 2020). Here, an energy balance modelling approach or coupled snow/atmosphere model is preferable (Vionnet et al., 2014; Sauter et al., 2015 and 2020; Gerber et al., 2018).

Where the meteorological drivers of ablation are unknown or poorly constrained yet there are data available for several parameters, such as at Khumbu Glacier, energy balance modelling should be performed. An energy balance model (EBM) usually requires hourly data of at least the radiation components, temperature, precipitation, pressure, relative humidity and wind speed to translate the energy balance at the glacier surface to ablation and accumulation rates. They are often forced by *in situ* measurements or bias corrected climate model data. These point-based measurements are distributed using gradients (e.g. Immerzeel et al., 2014b), and some mass balance models include radiation models that estimate radiation based on aspect and topographic shading (e.g. Klok and Oerlemans, 2002; Hock and Holmgren, 2005; Mölg et al., 2009; Sicart et al., 2011; Cogley et al., 2011; Gurgiser et al., 2013; Sauter et al., 2020). The radiative fluxes on ice are often calculated through a parameterisation of albedo and surface roughness of the glacier components (normally at least snow and ice) (Oerlemans and Knap, 1998; Mölg et al., 2012). This surface energy balance model is often coupled with a subsurface scheme that deals with percolation, meltwater re-freeze and subsurface melt (Sauter et al., 2020). The surface energy balance and subsurface models for the model used in this thesis, the open-source COupled Snowpack and Ice surface energy and mass balance model in PYthon (COSIPY), are described in detail in Chapter 4 (Sauter et al., 2020).

The high prevalence of DCGs in the HKKH, including Khumbu Glacier, requires mass balance models that resolve the impact of debris on melt. Both enhanced temperature-index and EBM approaches have been able to correct melt under varying debris layer thicknesses and even continuity (Nicholson and Benn, 2006; Reid et al., 2012; Lejeune et al., 2013; Evatt et al., 2015; Carenzo et al., 2016; Shaw et al., 2016) and reproduce the Østrem curve (Figure 2.5 and described later). A coupled atmosphere-glacier model found DCGs decrease local wind speeds (due to increased surface roughness) and temperature lapse rates relative to clean-ice glaciers (Collier et al., 2014 and 2015). Refined modelling of DCG surface features such as supraglacial ponds (Miles, et al., 2016) and ice cliffs (Buri et al., 2016 and 2021) and analysis of high-resolution imagery to quantify related loss (Brun et al., 2016 and 2018) has been critical for diagnosing potential drivers of the "debris cover anomaly" (Pellicciotti et al., 2015).

The majority of mass balance studies for DCGs generally assume a static surface. In reality supraglacial debris evolves over time and space through englacial debris transport and melt out. This latter process – the melt-out of englacial debris - is likely to increase under future warming. Debris transport is fundamentally linked to glacier dynamics, and therefore requires an ice flow modelling approach (Rowan et al., 2015, 2021).

This distributed mass balance approach captures the high spatial variability of glacier mass balance, that rare *in situ* point measurements are unable to. *In situ* measurements using ablation

stakes (Fujita et al., 1997, 2001, Wagnon et al., 2007; Sherpa et al., 2017) or snow pits (Bocchiola et al., 2020) are, however, valuable for validation of simulated mass balance. Geodetic mass balances from satellite imagery also aid validation, though the surface lowering measured in this way is a product of glacier ablation and the counteracting force of emergence velocity. This is a product of displacement from driving ice flux, and thus varies widely between glaciers, and remains poorly constrained (Vincent et al., 2021).

There have been several mass balance schemes used within Himalayan glacier evolution (ice flow) model studies. These mass balance representations include:

a) Temperature-index approaches with temporal resolutions that range from daily to monthly averages (Shea et al., 2015; Soncini et al., 2016; Wijngard et al., 2019; Rounce et al., 2020).

b) A mass balance gradient (linear function with height) (Racoviteanu, et al., 2013; Rowan et al., 2015, 2021)

c) Varying heights of the Equilibrium Line Altitude (ELA) with increased PDD under future climate scenarios (Rowan et al., 2015; Kraaijenbrink et al., 2017).

At the time of writing, there has been no study that has used a representation of distributed mass balance produced via an EBM (driven by hourly meteorology) to force an ice flow model.

2.4.3 Ice flow modelling

In this section, prognostic models that are used to explore glacier evolution over time are discussed. The challenges of accurately simulating glacier flow are enhanced in locations where the topography is extreme and highly variable on short spatial scales. There exists a hierarchy of ice flow models, some of which are more appropriate for such locations or for different points in a glacier's lifecycle.

Traditionally, the health of a glacier has been determined by locating the ELA from satellite imagery via the snowline (Braithwaite and Raper, 2009) which also helps to determine the AAR (Zemp et al., 2015; Miles et al., 2021a). For glaciers with avalanche driven accumulation regimes, such as Khumbu Glacier, the ELA can differ by several hundreds of metres from the snowline (Benn and Lehmkuhl, 2000; Rowan et al., 2015). For projections of DCGs, ELA placement or estimation of AARs have been achieved by delineating the debris-covered tongue from the snow-covered accumulation area (e.g. Miles et al., 2021a). However, the high ablation rates seen just below the ELA that are thought to considerably drive mass loss (Benn et al., 2012) may not be represented with these approaches. Observations of ablation above 6000 m.a.s.l. in the Everest

region (Sunako et al., 2019; Matthews et al., 2020) require approaches that resolve the finer detail.

Equally, as avalanching and supraglacial debris are ubiquitous across the HKKH, glacier projections that rely on scaling of ELAs or AARs over time will not produce accurate results. Both avalanche-fed and debris-covered glaciers are known to have very low AARs. For example, a flowline modelling approach indicated that for three glaciers located in the Central Himalaya and Western Himalaya, with AARs of < 0.2 (i.e. 80% of the glacier is the ablation area), avalanching could contribute up to 95% of total accumulation (Laha et al., 2017).

Approaches to estimating future glacier change include temperature-imposed changes to ELA heights (Fujita and Nuimura, 2011) and volume area scaling (Shi and Liu, 2000; Cogley, 2011). Both suggest further mass loss into the future, yet these approaches assume linearity in the mass balance signal and glacier response.

The response of 703 steady-state synthetic Himalayan glaciers to an ELA rise of 50 m was simulated over 500 years using scaling (Radic et al., 2007), linear-response and SIA models. The resultant projections of volume change differed by up to 20% (Banerjee, et al., 2020). All other parameters, including study sites and mass balance profiles, were kept constant and so this 20% difference stems from the varied representations of ice flow and velocity within the three models. Simulations using the scaling model showed lower climate sensitivities but shorter response times relative to results from a SIA model, indicating there are biases in existing regional-scale studies that use this method.

Flowline models simulate glacier flow along a centre-line, and as such do not represent cross-sectional variability, though valley-width is often used to resolve conservation of mass down glacier. They have been described as "1.5D" as although ice flow is only possible in one direction, this valley-width restriction means they can respond to width changes with thickness change. The Open Global Glacier Model flowline model is an example of this, where four basal types are available, each of which has a knock-on influence for shear stress (Maussion et al., 2019). In flowline models, velocity does not vary with depth, but this approach has still generated accurate results for Alpine glaciers (Oerlemans et al., 1998; Huss et al., 2007; Banerjee and Shankar, 2013) and regional or even global applications (Zekollari, et al., 2019; Huss and Hock, 2015, respectively), particularly when basal sliding is included (Banerjee, 2017).

One and two-dimensional models of glacier dynamics have been applied previously to the Everest region e.g. Khumbu Glacier (Naito et al., 2000), East Rongbuk Glacier (Zhang et al., 2013), and the wider region (Shea et al., 2015a). Glacier redistribution models are useful for region-wide studies (e.g. due to the lower computational expense relative to Full Stokes or even Shallow Ice

Approximation (SIA) models (Shea et al., 2015; Kraaijenbrink et al., 2017)). Ice flow is parameterised for each elevation band and driven by thickness and surface slope.

SIA models assume that vertical shear stress at the ice/bed interface perfectly counteracts the gravitational driving stress. They offer a clear improvement, especially for ice masses with small aspect ratios (i.e. "shallow" relative to their horizontal extension such as ice sheets; Pattyn, 2002 and Le Meur, et al., 2004). However, the SIA overlooks the more complex stresses that describe lateral and longitudinal drags which are of particular importance in steep terrain (Le Meur et al., 2004; Adhikari and Marshall, 2013). In these settings, the accuracy of SIA approaches reduces as the contribution of basal slip to ice velocity increases. In the Himalaya, glacier flow is forced through steep, confined valleys that complicate the patterns of stress.

Also, in this terrain, basal sliding likely contributes more significantly to glacier velocity than ice deformation (Pattyn, 2003; Egholm et al., 2011). To resolve these complex stress gradients on glacier flow, higher-order or second-order models are required. The integrated second-order shallow-ice approximation (iSOSIA) (Egholm et al., 2011) accounts for the transverse and longitudinal stresses that govern mountain glacier flow, and as such is a better representation of mountain glacier dynamics than the SIA. Further improvements to iSOSIA include debris transport, where debris is passively transported through the ice via a Eulerian scheme and the majority melt outs to form the supraglacial debris layers seen on many Himalayan glaciers today (Rowan et al., 2015).

Many glacier evolution studies initiate simulations of future glacier change from the present day, or from the start of the satellite era (1979) to enable evaluation of historical glacier evolution. However, these approaches rely on the assumption that glaciers are in a hypothetical steady state. The response time of mountain glaciers, i.e. the time taken for glacier volume to adjust to a new equilibrium following an atmospheric perturbation, is thought to be around 50-100 years (Jóhannesson et al., 1989). Therefore projections that use spin-up simulations from, for example, the Himalayan LIA maximum, are preferable (Rowan et al., 2015).

2.4.4 Future glacier response to climate change

The extent of future change of Himalayan glaciers is an evolving area of research, yet discrepancies between studies remain. End-of-century glacier volume loss projections under RCP4.5 (RCP8.5) are 46-49% (64-67%; Table 2.3). Committed volume loss across the HKKH, i.e. the loss that will occur even if warming stops in the present day, ranges from 14 to 27% (Kraaijenbreik et al., 2017; Zemp et al., 2015, respectively). For the Everest region, predictions of change until 2100 range from 8-10% (Rowan et al., 2015), 50% (Soncini et al., 2016) and 70 to 99% for RCP4.5 and 8.5, respectively (Shea et al., 2015a).

Region	Future climate scenario	Projected glacier volume change	Year	Projection approach	Reference
Asia South Central	No further warming	-27%	Committed	Extrapolation of field observations	Zemp et al. (2015)
HKKH	No further warming	-14%	2100	Mass balance gradient and ice redistribution model	Kraaijenbrink et al. (2017)
	1.5°C or RCP2.6 (~2.1°C with EDW)	-33%			
	RCP4.5	-49%			
	RCP6.0	-51%			
	RCP8.5	-64%			
HKKH	RCP2.6	-29%	2100	OGGM Python Glacier Evolution Model (PyGEM) and geodetic MB	Rounce et al. (2020)
	RCP4.5	-46%			
	RCP6.0	-50%			
	RCP8.5	-67%			
HKKH	No further warming	-21% (25% of glaciers would lose 50% of current volume)	2100 *2200*	AAR/ELA scaling	Miles et al. (2021)
Koshi basin (six glacierised sub-basins), Nepal/Tibet	RCP4.5	-76%	2071-2100	OGGM Glacio-hydrological Degree-day Model (GDM)	Khadka et al. (2020)
	RCP8.5	-86%			
Everest, Nepal	RCP4.5	-70% (-39%)	2100 (2050)	Glacier redistribution model	Shea et al. (2015a)
	RCP8.5	-99% (-52%)			
Khumbu and Changri Nup glaciers of Everest region, Nepal	0.9°C (ELA increase of 225 m)	-8%	2100	iSOSIA with MB as a function of ELA and continuous debris cover	Rowan et al. (2015)
	1.6°C or RCP4.5 (ELA increase of 400 m)	-10%			
Khumbu Glacier (Nepal)	No further warming	-53% (-32%)	2100 (2050)	Degree day glacio-hydrological model	Soncini et al. (2016)
	RCP2.6	-54% (-34%)			
	RCP4.5	-59% (-35%)			
	RCP8.5	-67% (-38%)			
Langtang (Nepal)	RCP4.5	-37%	2071-2100	Glacio-hydrological model (degree-day and redistribution)	Immerzeel et al. (2013)
	RCP8.5	-54%			

Table 2.4 Projections of glacier volume change under future emission scenarios from published studies.

The variations in projections seen in Table 2.4 stem from our uncertainty of the key climatic and glaciological processes responsible for glacier change, in part from a lack of *in situ* data due to the remoteness and inaccessibility of the region. It also stems from the representation of glacier dynamics within models, and the representation of future climate and glacier mass balance as previously discussed.

Extrapolation of observed climate, mass balance or glacier response into the future is not appropriate for many reasons, in part as glaciers do not respond linearly to atmospheric change. It is possible that under moderate warming scenarios, glaciers will adapt to a new geometry or elevation and an equilibrium that allows them to persist. Equally, projections of increased precipitation into the future may compensate for warming to some extent.

Numerical models must be suitable for the chosen glacier. Previous studies (e.g. Shea et al., 2015a) have used models intended for clean-ice glaciers which explains the much higher predicted mass loss (70 to 99%) compared to other studies. Debris-covered glaciers are dynamically distinctive, thus representation of the feedbacks between mass balance, debris transport and ice flow in the modelling approach are critical for quantifying glacier evolution (Rowan et al., 2015).

Despite being a focal point for research over the last few decades and the availability of *in situ* meteorological data, there have been no previous EBM studies of Khumbu Glacier and as such the spatial distribution of mass balance remains poorly constrained. Thorough analysis of the meteorological complexity of the catchment and sensitivity analyses to determine the meteorological drivers of mass balance are used to establish downscaling and disaggregation routines of historical and future daily climate model data to a local-scale, sub-daily resolution.

Hourly climate is not traditionally used to force glacier models (all climate-driven approaches in Table 2.4 use monthly or daily climate inputs of temperature and, more rarely, precipitation). Representation of the finer climatic detail, including these diurnal trends in radiative fluxes, temperature and precipitation, will improve accuracy of mass balance calculations and thereby projections of glacier evolution for this summer-accumulation type glacier. At the time of writing, integrating a robust representation of distributed mass balance in a higher-order ice flow model has not yet been conducted. The relation between supraglacial debris, mass balance and glacier change is also explored. Using this cross-disciplinary approach to simulate historical and future evolution of Khumbu Glacier is the central aim of this thesis.

Chapter 3 Catchment-scale, high elevation meteorology in the Everest region of Nepal, 2009-2012, and implications for glacier modelling

3.1 Introduction

Meteorological observations across the HKKH rarely exist above 3,000 m.a.s.l. because of the logistical challenges associated with installing and maintaining equipment in such remote areas. In recent years, our understanding of present-day meteorology has improved through high resolution atmospheric simulations (e.g. Collier and Immerzeel., 2015; Potter et al., 2018), but forecasts of atmospheric change in the region are still largely based on coarse resolution (50-100 km) climate model outputs. While valuable, these modelled data fail to capture the complexities of catchment-scale terrain, which are key for driving altitudinal temperature gradients, localised wind and precipitation fluxes (Immerzeel et al., 2014). Finer resolution studies are able to capture the small-scale variability associated with complex terrain, though often still exhibit mean biases that stem from the driving global model or reanalyses (Collier and Immerzeel, 2015). Field-based meteorological observations are therefore crucial to aid validation and downscaling of coarse climate models (Maussion et al., 2014). They are equally essential when reconstructing and understanding glacier mass balance changes in response to the past and current climate (Shea et al., 2015b).

In recent years, Himalayan glaciers have been under particular scientific scrutiny because of their importance for human livelihoods and the uncertainties associated with ice volume change. Glaciers act as water reservoirs, providing downstream areas with a crucial supply of water, particularly during the dry season. However, in the eastern Himalaya, recent work has shown that 'peak-water' is imminent, or has even passed for some catchments (Huss and Hock, 2018). Many studies have shown that the glaciers in this region have been in recession in recent years, and possibly decades (e.g. Bolch et al., 2012; King et al., 2017), likely as a result of warming temperatures and reduced snowfall (Immerzeel et al., 2010). These glaciers are highly dependent on the monsoon for summer accumulation (Benn et al., 2012). It has been suggested that the monsoon is weakening through warming of the equatorial Indian Ocean, reducing the meridional sea-surface temperature gradient from the equatorial region to the coast (Yao et al., 2012). A weaker monsoon leads to reduced snow accumulation and clearer skies, both of which promote negative glacier mass balance. This improved understanding of the monsoon through observations and modelling is useful for explaining glacial behaviour, though is hindered by the poor spatio-temporal coverage of instrumental data in the region (Ramesh and Goswami, 2007).

The first meteorological observations for the Nepal Himalaya were collected during the 1970s and 1980s, and found a characteristic pattern of diurnal precipitation on ridges and nocturnal precipitation in valley bottoms (Ageta, 1976), most likely reflecting cloud development from orographic convection during the day. It was not until the 1990s that continuously recording Automatic Weather Stations

(AWSs) were installed in the region, the first of which was at the Pyramid Observatory near Lobuche. Bollasina et al. (2002) analysed meteorological observations from this station collected between 1994 and 1999, focussing on features of the monsoon. The onset of the monsoon was distinguished by higher daily precipitation totals, mean relative humidity and atmospheric pressure and a reduced diurnal range in atmospheric temperature. They identified two daily profiles in precipitation and wind direction, thought to be related to the monsoon. In addition, 5-day and 10-day periodical precipitation cycles were observed, which were linked to oscillations in the Tibetan High. A new AWS was installed at Pyramid in September 2000, as well as a network of AWSs along the Dudh Koshi valley. This network, run by Ev-K2-CNR and available through the SHARE project, ranges from 2,680 to 5,700 metres elevation, and some stations have ten years of measurements available. Only a handful of studies have attempted to bring together multiple meteorological datasets in a single analysis in the Himalaya (e.g. Shea et al., 2015b; Salerno et al., 2015), revealing the seasonal variation in key parameters across the study area, as well as a diurnal variability in vertical temperature gradients.

Glacier energy balance models distributed across the ice surface are highly dependent on several key meteorological parameters. For example, air temperature dictates ablation (melt and sublimation), and precipitation amount and type determine accumulation. Wind influences vapour gradients, turbulent transfer and the redistribution of snow (Hock et al., 2005). Cloud extent and type impact radiation at the ice surface, which drives melt (Bonekamp et al., 2019).

Dynamical downscaling involves using a high-resolution model to downscale a low resolution (often global) climate model (Bienek et al., 2016). This high spatial resolution improves the representation of topography, and consequently, the orographic enhancement of precipitation (Maussion et al., 2011). Though, when used to force glacier mass balance models, corrections to link these simulations to local conditions at the glacier surface are required, unless the spatial resolution is sufficiently high (~1 km) (Collier et al., 2013). Though, a 1 km spatial resolution would still remain insufficient for very steep terrain e.g., Khumbu icefall. This dynamical approach is usually computationally expensive, and so it is often not feasible to run models at a sufficiently high resolution to capture critical, intricate processes over the timescales required to study glacier evolution. This approach is therefore valuable for seasonal timescales, but less useful for long term hydro-glaciological studies.

Statistical downscaling, using relationships such as linear regression and quantile mapping to predict local climate variables from large-scale variables (Tang et al., 2016) is less computationally expensive, though often relies on the availability of *in situ* data for calibration and validation. It is possible to distribute air temperature to the site of interest through it being a function of elevation. This dependency is often considered linear, though in reality is highly spatially and temporally variable, particularly in areas of complex topography (Petersen and Pellicciotti, 2011).

Two previous studies have analysed these weather station data, the aforementioned study by Bollasina et al. (2002) and that of Salerno et al. (2015). The latter uses 17 years of data from Pyramid AWS to

attempt to extract precipitation and temperature signals to link to glacier change within the region. The work here focuses on a shorter timescale (3 years) but includes all weather stations in the catchment. It is a more exploratory analysis of all meteorological variables that are used to force energy balance models from the six weather stations spanning the Dudh Koshi catchment, located in the Everest region of the Nepal Himalaya. This catchment comprises a north/south oriented valley, and some of the more well-studied glaciers in the Nepal Himalaya, such as Khumbu Glacier (Rowan et al., 2015, 2021), Ngozumpa Glacier (Benn et al., 2017) and Imja-Lhotse Shar Glacier (Rounce et al., 2015). An on-ice AWS, located on Changri Nup Glacier, is included in this analysis as it contributes an additional dataset in a data-scarce region, but also gives an opportunity to investigate whether a glacier cooling signal is apparent. This chapter aims to characterise and compare the meteorology from these weather stations, ranging from 2,680 to 5,700 m.a.s.l. of the glacierised Dudh Koshi catchment in order to i) identify variability in temperature lapse rates and other altitudinal dependencies; ii) explore the valley-scale wind regime through comparison with ERA-5 wind data; iii) highlight the need for valley-scale climatology as an input to glacier and glacio-hydrological modelling experiment.

3.2 Study Area

The upper Dudh Koshi valley is located in the Sagarmatha National Park which ranges from 2,400 to 8,848 m.a.sl. (Mount Everest) in elevation (Amatya et al., 2010). As the major trekking route to Everest Base Camp, the catchment is well-populated, with local communities relying on rainfall and meltwater for drinking, sanitation and irrigation (Watson and King, 2018). The treeline is at approximately 4,100 m.a.s.l. (Gaire et al., 2014 and 2017) and most glaciers are situated between 5000 and 6000 m.a.sl. (Bajracharya et al., 2014; Salerno et al., 2015). As these glaciers rely on accumulation from the monsoon, they are referred to as "summer-accumulation type" glaciers, and the ablation and accumulation seasons largely coincide. Thirty-six percent of glaciers in the Everest region are debris-covered (Nuimura et al., 2012) and glaciers in the region are known to be losing mass at an accelerating rate (Maurer et al., 2019).

The weather stations used here are part of the SHARE network from the Ev-K2-CNR project (Locci et al., 2014) and all data were downloaded from Ev-K2-CNR SHARE network website. The stations are located over a 40 km stretch in the south/north oriented valley (Figure 3.1). The station at Lukla is west-facing, located near to the bottom of a steep valley, along which the Dudh Koshi river runs, and the station at Namche Bazaar is located on a south-facing slope 1 km above the valley floor. Pyramid station is situated on the crest of the slope above the Pyramid observatory structure, between the main tributary of Khumbu Glacier to the east and the smaller Lobuche glacier tongue to the west. Pheriche station is sited in the flat base of the pro-glacial valley that was previously occupied by Khumbu Glacier at the Last Glacial Maximum. Kala Patthar station is located immediately south of the ridge of Pumori, in an exposed position though surrounded by peaks on all sides. It is in close proximity to the Khumbu icefall to the northeast, the tongue of Changri Nup Glacier to the southwest and the valley sloping down towards the

village of Lobuche to the south. Changri Nup station is located on a flat, debris-free section of Changri Nup Glacier, a former tributary of the larger Khumbu Glacier, and on a gradually sloping valley side.

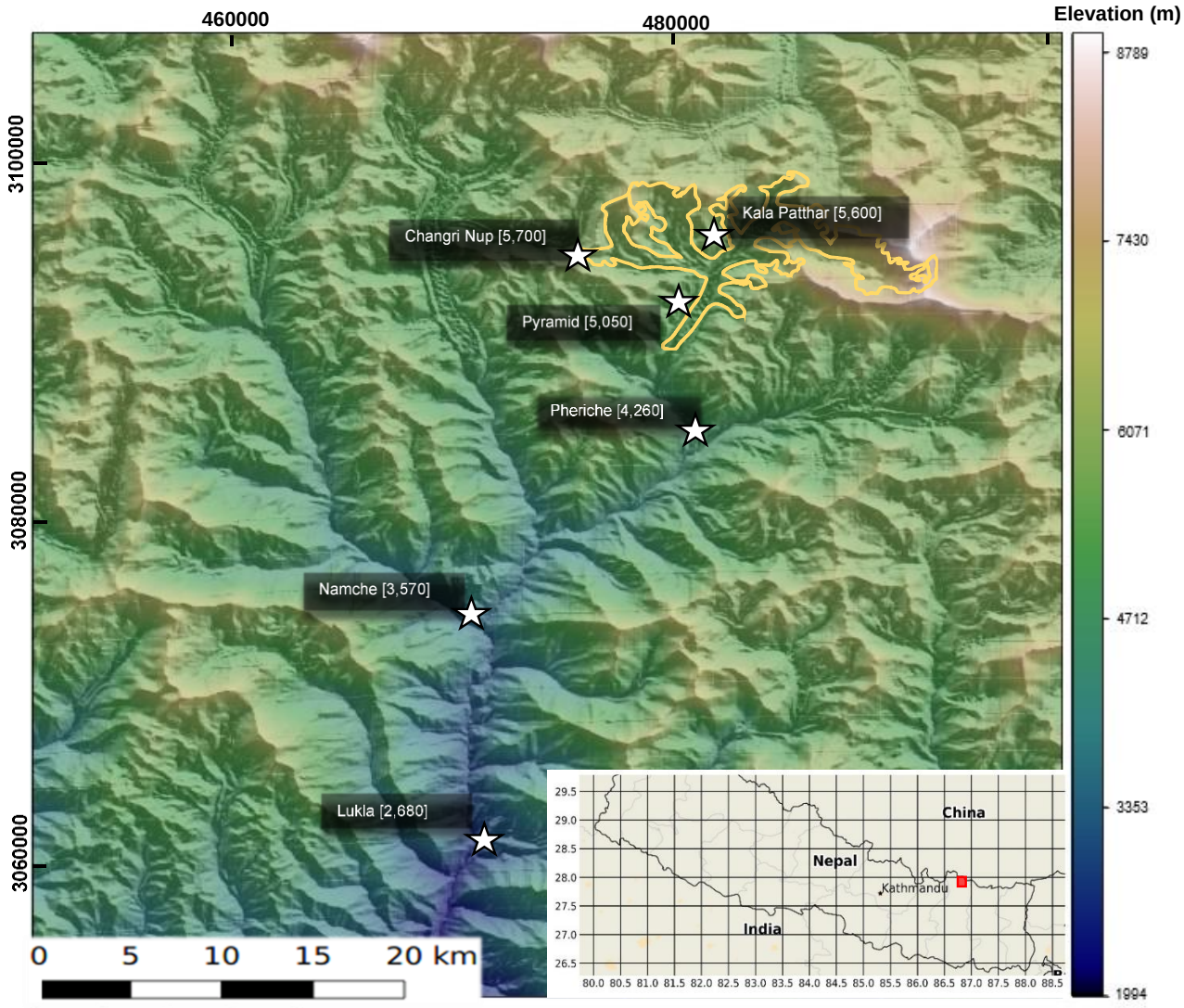

Figure 3.1 Elevation map of the six weather stations (elevations marked in metres) in the Dudh Koshi catchment in UTM45N projection and national context map of Nepal with network location marked by red box. Khumbu Glacier outline in yellow taken from the Randolph glacier inventory (Arendt et al., 2012) and imagery from the shaded relief map from a resampled SRTM DEM (30m).

3.3 Data pre-processing and analysis

The study focusses on the 2009-2012 period as measurement at Kala Patthar began in 2009, giving three full years of data for comparison. Table 3.1 includes the abbreviations for all variables used throughout. For the purposes of this study, the monsoon period is defined as June to October, post-monsoon (October–November), winter (December–February), and pre-monsoon (March–May) (Ueno et al., 2008), though much of the study compares the monsoon against the non-monsoon period. This definition of the monsoon dominates in the literature, though it should be noted that the monsoon can significantly

vary in onset/cessation. Throughout, periods used for the day are 8am until 4pm and for night 8pm until 4am (local time) to account for changing sunrise/sunset times throughout the year, and the influence of topographic shading for valley sites. Centred-means were used for some variables in order to remove local noise associated with daily frequencies. For sub-hourly measurements, hourly averages were calculated using data from the previous hour.

In order to measure the strength of the relationship between air temperature and elevation, temperature measurements from all stations are used (Heynen et al., 2016). The regression of the mean temperature values split by season and time of day is conducted, and the strength of the altitudinal dependence (estimated via linear regression) is shown with the R^2 coefficients (e.g. Bravo-Lechuga et al., 2019).

LRs of temperature and mixing ratios between pairs of stations were also calculated to investigate spatial variability using

$$LR = \frac{V1 - V2}{z1 - z2} \tag{3.1}$$

adapted from Immerzeel et al. (2014) and Thayyen and Dimri (2018). V1 refers to the measured variable at the highest elevation (z1) and V2 at lowest elevation (z2). Precipitation gradients were calculated as a regression using the same equation taken from Immerzeel et al. (2014), and converted to percentages. Here precipitation measurements from stations/years with lowest incidence of missing data were used.

All stations suffered from periods of error and missing data, which is perhaps unsurprising given the challenges of regularly maintaining equipment in such an environment. Daily averages were calculated when 83% (equating to 20 hours) of observations were available. For calculation of LRs for time periods (e.g. monsoon day), distributions of missing data across these periods were analysed. For example, Lukla had almost 45% of temperature observations missing during the monsoon, but as these were equally distributed between day and night LRs could still be calculated with confidence. Data gaps in the precipitation datasets were found to be most common, particularly during the onset of the monsoon. This led to several monsoon seasons at some weather stations having little or no data. Given that the aim of this study was to analyse *in situ* trends, gap-filling through interpolation was not conducted.

The tipping bucket precipitation gauges (Table 3.1) mean that precipitation may be underestimated following heavy snowfall events. Equally, during light rain events, droplets can fall on the bascule and evaporate without being measured. Pyramid has a snow depth sensor installed, but the data are discontinuous and inconsistent between 2009 and 2010, and the measurement period ends in December 2010.

The mechanisms driving the valley winds were investigated using the approach from Whiteman and Doran (1993) and Jemmett-Smith et al. (2018). In the absence of a weather station at the top of the valley to deduce ambient wind as in their studies, ERA-5 250 hPa pressure level were used to represent the

free atmosphere upper-level winds, where there is minimal influence of the >8000 m peaks. ERA-5 10 m surface wind speeds were also compared with observations for consideration as an approach to downscaling. The elevation of the ERA-5 data point is 4,608 m.a.s.l., and as ERA-5 has a spatial resolution of 31 km, this gridpoint is the same for Pheriche and Pyramid.

The mixing ratio (MR), the ratio of the mass of water vapour to the mass of dry air (kg/kg^{-1}), was calculated to obtain an absolute measurement of atmospheric water vapour independent of temperature or pressure. This was calculated using

$$MR = \frac{0.622\, e}{p - e} \tag{3.2}$$

where e is vapour pressure, p is pressure, RH is relative humidity, and 0.622 refers to the molecular weight ratio of water to dry air (Glickman, 2000). The maximum vapour pressure value for a given temperature, was first calculated using Teten's expression (Murray, 1967)

$$e_s(t) = 6.11 * 10(\frac{7.5t}{t + 237.3}) \tag{3.3}$$

Actual vapour pressure was then calculated from e_s with

$$e = e_s RH \text{ (4)} \tag{3.4}$$

from Bolton (1980).

The on-ice location of the Changri Nup station, and the availability of incoming and outgoing shortwave radiation data provided an opportunity to determine the glacier surface albedo. Half-hourly surface reflectivity, or albedo (α), was calculated with

$$\alpha = \text{SWin} * \text{SWout}^{-1} \tag{3.5}$$

for daytime hours (8am – 4pm), where SW_{in} is outgoing shortwave and SW_{out} incoming shortwave radiation.The albedo values for different snow/ice surfaces were taken from Paterson (1994) for comparison. Measurements of SW_{in} below 30 W/m^2 were discounted to prevent sensor noise being included in the calculation of albedo. One hundred and sixty-five days of albedo measurements were missing from the two years which is common given the exposure of the sensor location. Given that the on-ice location of this sensor means there was no suitable nearby surrogate, no interpolation to fill the data gaps was attempted.

Station (m.a.s.l.)	**Latitude**	**Longi-tude**	**Data start/end**	**Resolu-tion**	**Parameter**	**Instruments**
Changri Nup (5,700)	27.958	86.812	2010-2012	30 min	T, RH SW_{in}, SW_{out}, LW_{in} LW_{out}	Thermohygrometer DMA 572 (0.1°C accuracy) Pyranometer CM6B
Kala Patthar (5,600)	27.9818	86.764	2009-2012	10 min	T, RH Pressure Precip u, wind direction SW_{in}, SW_{out}, LW_{in} LW_{out}	Thermohygrometer DMA 572 (0.1°C accuracy) CX115P Lsi-Lastem Tipping bucket rain gauge - DQA030 Lsi-Lastem (on ground, 0.2mm resolution CombiSD DNA022 Lsi-Lastem (5 m pole, accuracy 0.1 m/s and 1%) Radiometer CNR1
Pyramid (5,050)	27.990	86.829	2002-2012	1 hour	T, RH Pressure Precip u, wind direction SW_{in}, SW_{out}, LW_{in} LW_{out} Snow Depth	Thermohygrometer DMA 570 (2 m pole, 0.1°C accuracy) CX115P Lsi-Lastem DQA035 Lsi-Lastem (1.5 m pole, resolution 0.2 mm) CombiSD DNA022 Lsi-Lastem (5 m pole, accuracy 0.1 m/s and 1%) Pyranometer CM6B 2m Snow Depth SLU4/20 Micros
Pheriche (4,260)	27.894	86.820	2002-2012	1 hour	T, RH Pressure Precip u, wind direction SW_{in}, SW_{out}, LW_{in} LW_{out}	Thermohygrometer DMA 572 (0.1°C accuracy) CX115P Lsi-Lastem DQA035 Lsi-Lastem (1.5 m pole, resolution 0.2 mm) CombiSD DNA022 Lsi-Lastem (5 m pole, accuracy 0.1 m/s and 1%) Pyranometer CM6B
Namche (3,570)	27.802	86.714	2002-2012	1 hour	T, RH Pressure Precip u, wind direction SW_{in}, SW_{out}, LW_{in} LW_{out}	Thermohygrometer DMA 570 (2 m pole, 0.1°C accuracy) CX115P Lsi-Lastem Tipping bucket rain gauge - DQA035 Lsi-Lastem (1.5 m pole, 0.2 mm) CombiSD DNA022 Lsi-Lastem (5 m pole, accuracy 0.1 m/s and 1%) Pyranometer CM6B
Lukla (2,680)	27.691	86.723	2002-2012	1 hour	T, RH Pressure Precip u, wind direction SW_{in}, SW_{out}, LW_{in} LW_{out}	Thermohygrometer DMA 570 (2 m pole, 0.1°C accuracy) Digital barometer – PTB330 Tipping bucket rain gauge - DQA035 Lsi-Lastem (1.5 m pole, 0.2 mm) Wind Set WA15 by Vaisala (accuracy 0.4 m/s and ±3°) Pyranometer CM6B

Table 3.1 Station and instrument details, with variables referring to atmospheric temperature (T), relative humidity (RH), atmospheric pressure (Pressure), precipitation (Precip), wind speed (u), wind direction, incoming shortwave, outgoing shortwave, incoming longwave, and outgoing longwave radiation (SWin, SWout, LWin LWout).

3.4 Results

3.4.1 Seasonal variations in meteorology

Atmospheric temperature (T) at all sites showed a strong seasonal cycle (Figure 3.2a-f) with the monsoon characterised by higher temperatures, and weaker day-to-day variability. The winter period (Nov-Feb) exhibited lowest temperatures, on average 13°C lower at Lukla (2,680 m.a.s.l.,) than during the height of the monsoon and high variability. Changri Nup (5,700 m.a.s.l.) showed a strong seasonal cycle with a daily mean minimum of -21.8 °C and a maximum of 4.17°C (Figure 3.2a). At Kala Patthar (5,600 m.a.s.l.), the daily T_{mean} exceeded 0°C for several weeks of the monsoon. Lukla had a daily average minimum of -3.1°C and a maximum of 17°C, only dropping below freezing for several days during the winter of 2010. Changri Nup, Pyramid, Pheriche and Namche stations all exhibited rising incoming shortwave radiation (SW_{in}) trends during pre-monsoon and a decrease in the post-monsoon, but with high day-on-day variability.

There was a strong seasonality in Precip, with the majority occurring during the monsoon (Figure 3.2), and a positive correlation between Precip and T. There was an increasing prevalence of high rainfall events with decreasing elevation. Monsoon Precip was of a low intensity at all stations, with infrequent occurrence of intense rainfall events. This was seen by the high frequency of 'drizzle type' Precip (<1 mm in two hours, Bollasina et al., 2002).

Wind speed (*u)* and wind direction showed strong seasonality, and were also controlled by diurnal cycle, valley axis and synoptic conditions. Highest *u* measurements were observed at Kala Patthar and Pheriche and were most frequent during the pre-monsoon. Southerly (up-valley) winds dominated at Pyramid, Pheriche and Namche (Figure 3.3 a-b, e-f). For all sites, *u* reduced during the monsoon and variability decreased. Most stations showed a strong southerly component during the monsoon (Figure 3.3a), though wind direction remained constrained by valley orientation (Figure 3.3 a-b, e and g). The monsoon reduced variability in the south-westerly wind direction at Kala Patthar (Figure 3.3c-d) which was less constrained to valley axis, coming from Changri Nup Glacier and Lobuche West peak.

Relative humidity (RH) was close to 100% at all stations during the monsoon with reduced variability. Whilst variations of RH with height were indistinguishable during the monsoon, due to decreasing air temperature the mixing ratio (MR) decreased with height. MR (derived from RH, pressure and T) showed a strong seasonality with a marked rise with monsoon onset at all stations (Figure 3.4) and decreased variability. The MR pattern was strongly correlated between sites throughout the year. Winter MR values were <0.006 kg/kg at all sites and 0.0015 kg/kg at Kala Patthar overnight, and 0.0047 kg/kg at Namche.

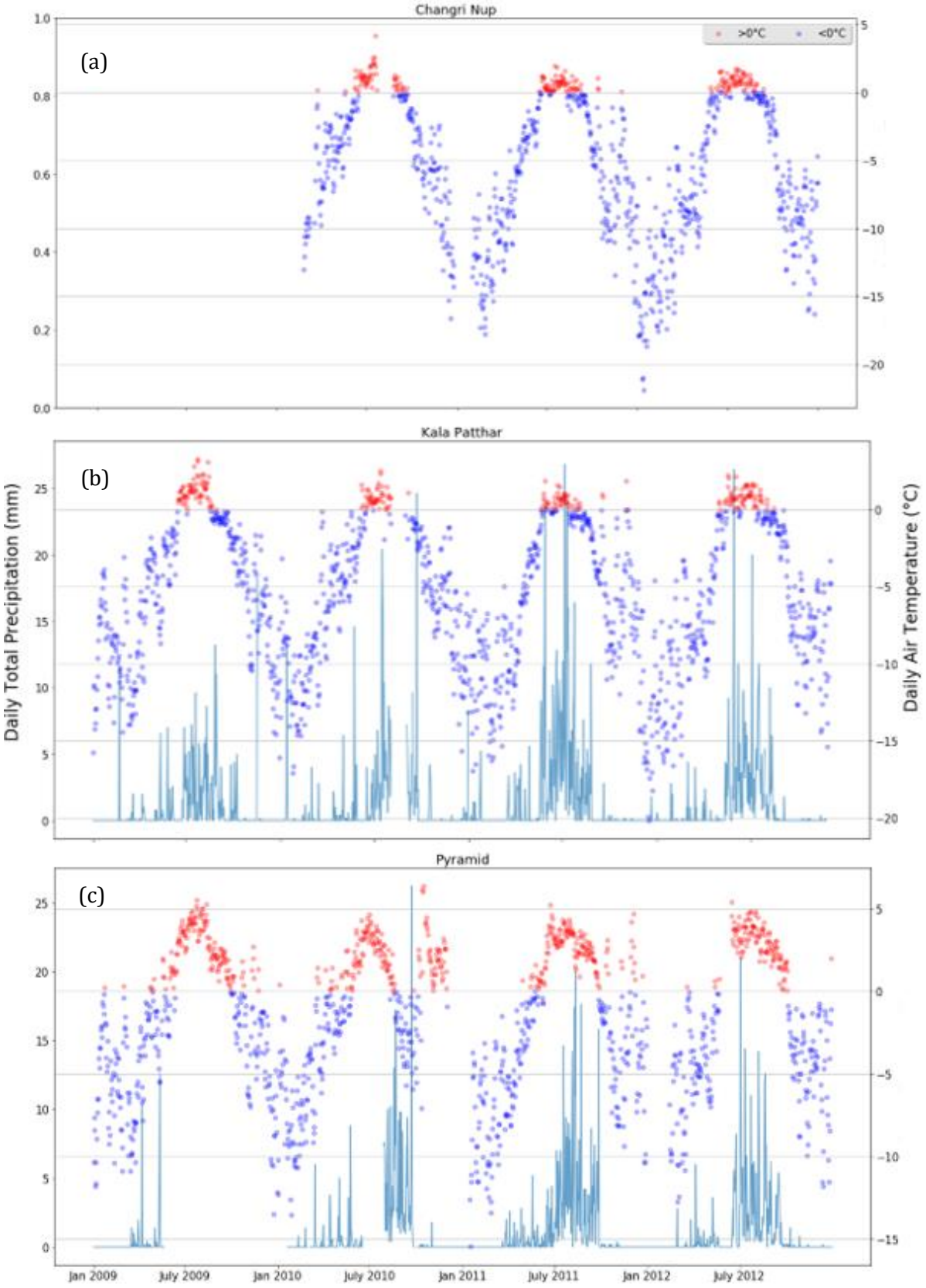
Changri Nup
(a)
>0°C
<0°C
Kala Patthar
(b)
Daily Total Precipitation (mm)
Daily Air Temperature (°C)
Pyramid
(c)
Jan 2009
July 2009
Jan 2010
July 2010
Jan 2011
July 2011
Jan 2012
July 2012

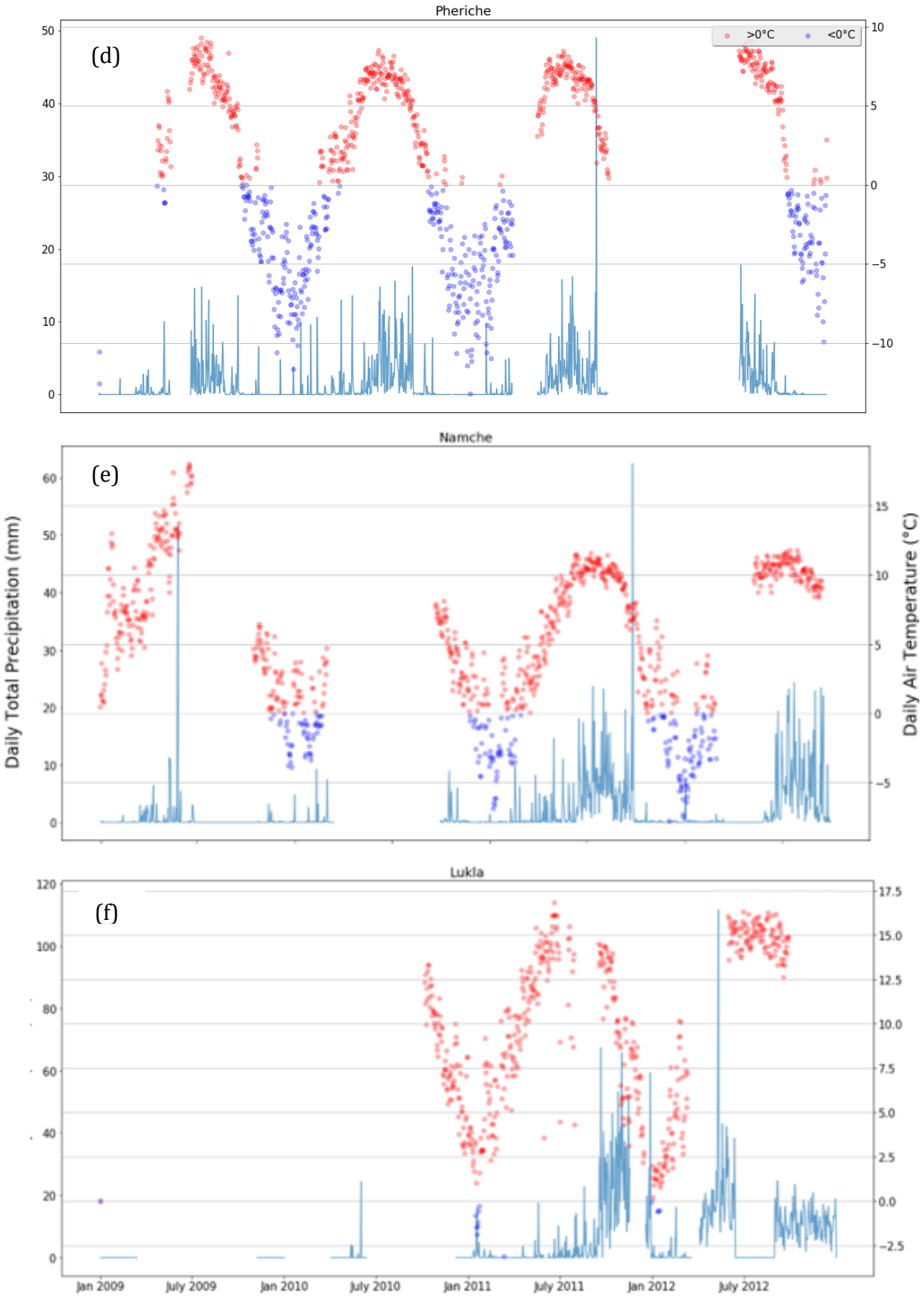

Figure 3.2(a-e) Daily Total Precip and Average T 2009-2012 (2010-12 for Lukla, and 2010-12 Daily Average T for Changri Nup), for all stations in Dudh Koshi. Note that y-axis scales differ. There is an increased concentration of Precip during the monsoon, and prevalence of high rainfall events with lower elevations.

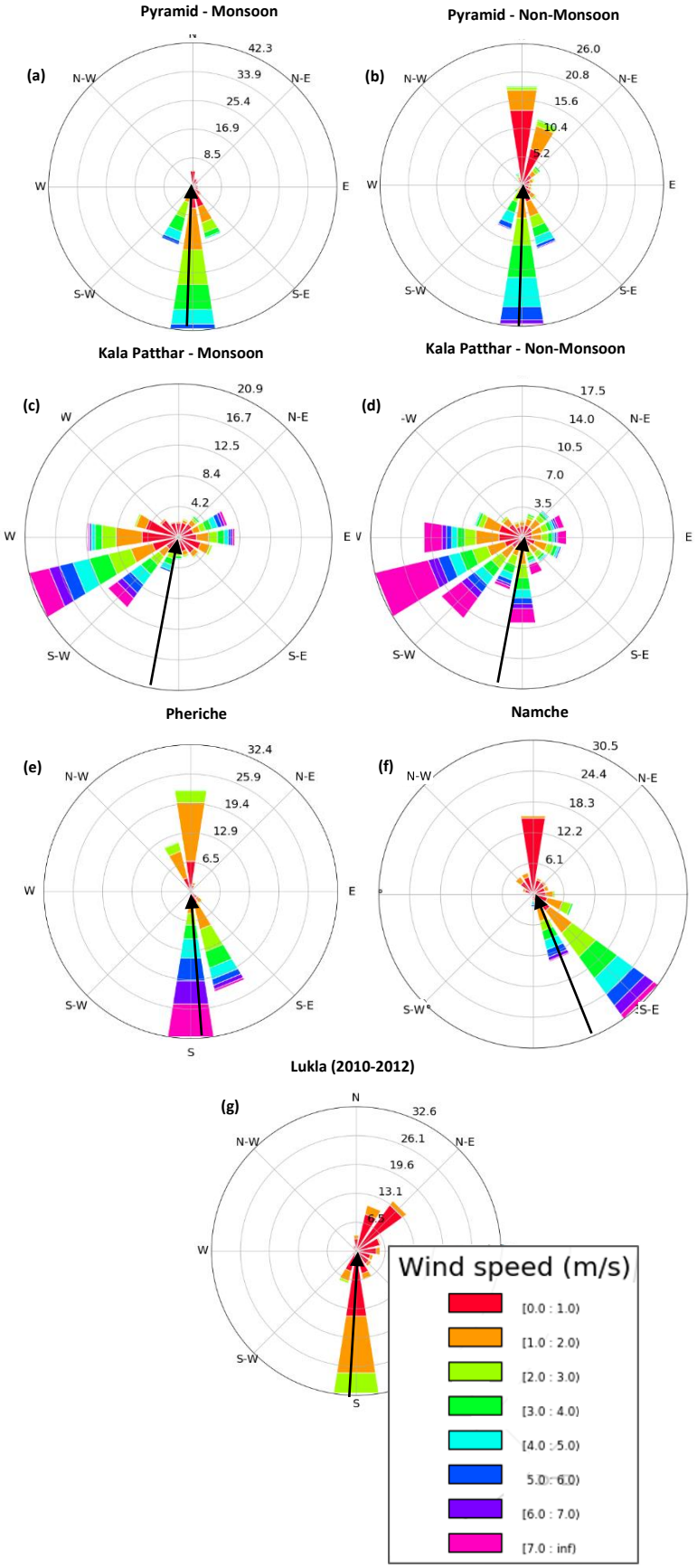

Figure 3.3(a-g) Wind direction and speed for Dudh Koshi sites for 2009-2012 period (2010-2012 for Lukla), split by monsoon/non-monsoon for Pyramid and Kala Patthar, with percentages of occurrence and up-valley wind directions shown by arrows.

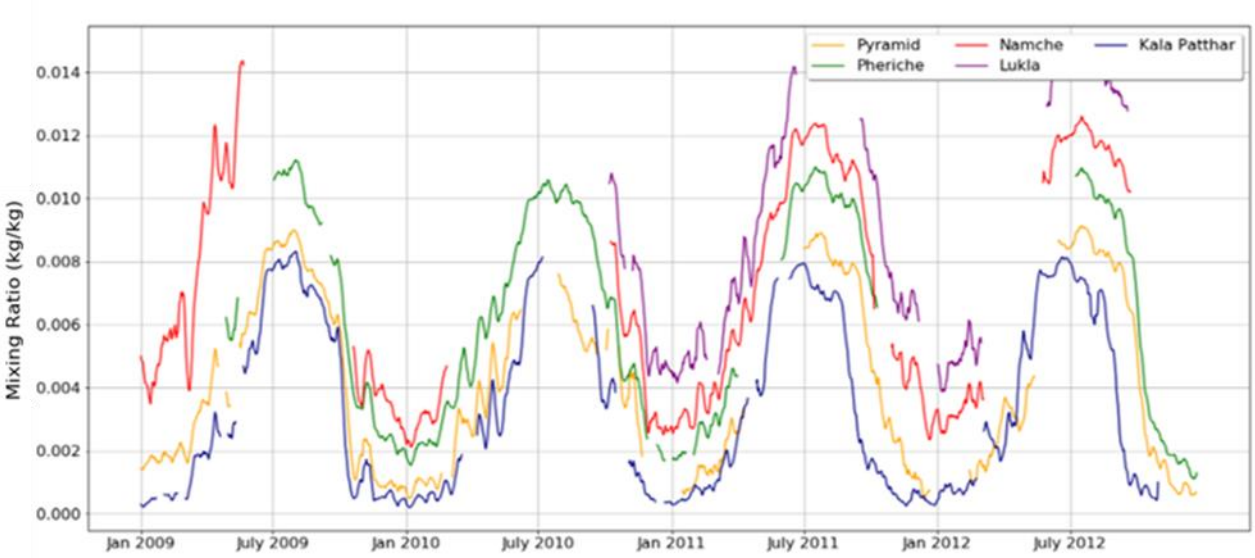

Figure 3.4 10-day mean of mixing ratio for each station.

3.4.2 Diurnal variations in meteorology

A strong diurnal cycle in T was seen at most sites outside of the monsoon (Figure 3.5b), with Pheriche and Lukla showing the largest diurnal T range. Temperature minima of -5.4°C and 3.9°C occur at 11pm and 6am, and maxima of 2.8°C and 14.7°C at 11am. There was a dampened diurnal temperature range during the monsoon months (Figure 3.5a), particularly at the Pyramid station, with a temperature low of 1.2°C and high of only 3.3°C. The monsoon not only reduced the diurnal temperature range, it altered the timing of the temperature maxima and minima, which always followed several hours after the SW_{in} peak unlike during the non-monsoon (not shown). The temperature maxima occurred later in the day during the monsoon for many sites. There are no data for SW_{in} at Kala Patthar, and data for Pheriche and Namche were only from 2010, and for Lukla prior to 2011.

There was a strong diurnal wind regime at Pyramid, with up-slope (southerly) wind flow during the day and higher *u* (Figure 3.6a), and a lighter downslope wind flow (though with higher variability) at night (Figure 3.6b). At Kala Patthar the wind direction was not oriented to the main valley. Here, there was increased variability in wind direction at night (Figure 3.6c), and a slightly a less apparent difference in *u* between day and night.

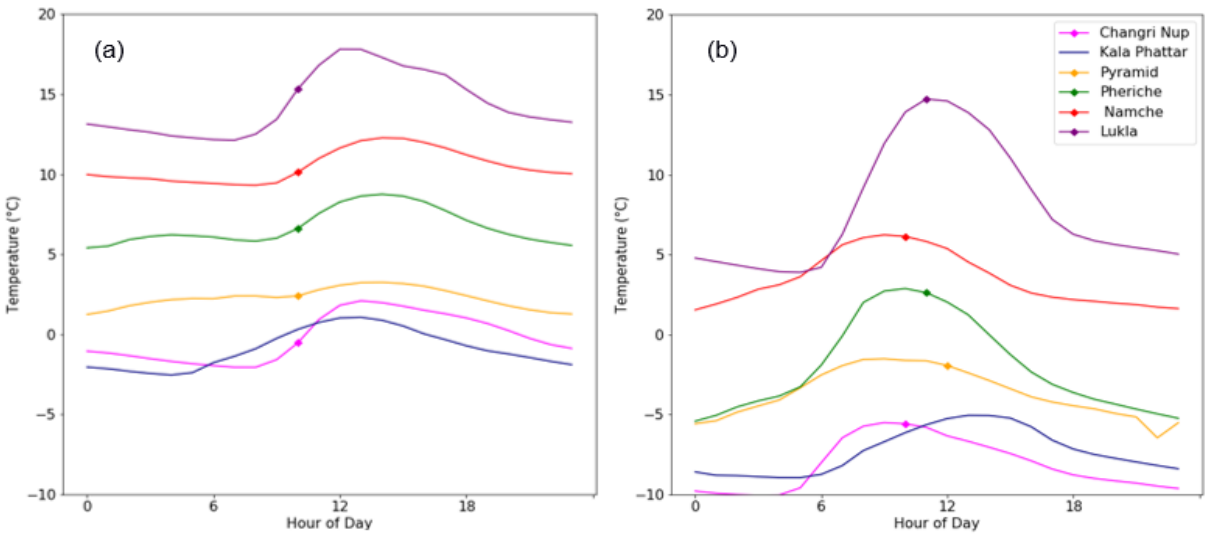

Figure 3.5 (a, b): Diurnal cycle of temperature for (a) monsoon (b) and non-monsoon 2009-2012 (local time) with diamonds marking peak SW_{in} timing. Note Kala Patthar has no SW_{in} data.

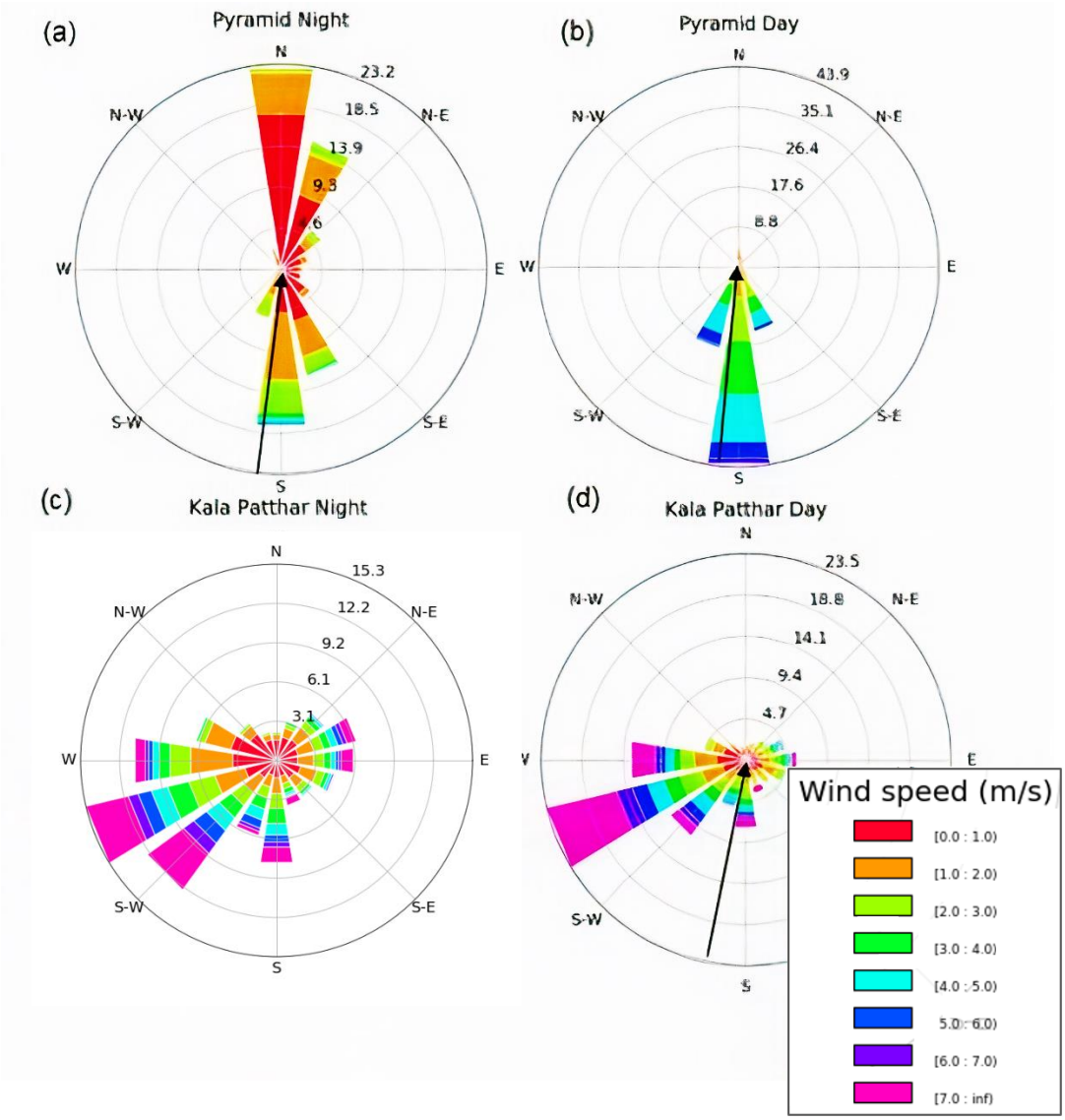

Figure 3.6 (a-d) Wind roses for Pyramid and Kala Patthar by time of day.

3.4.3 Comparison with ERA-5 reanalysis wind data

The mechanisms driving wind regimes at Pyramid and Pheriche were investigated by comparing hourly AWS wind directions with the hourly 250 hPa wind direction from ERA-5 (Figure 3.7). During the non-monsoon there was a strong diurnal cycle in wind regime, with directions oriented to the valley axis, and with strong up-valley flow dominating during the day, and down-valley flow during the night. The diurnal cycle was dampened during the monsoon as more consistent overnight cloud cover, seen by the increased overnight variability in wind directions with reduced wind speeds. Pheriche exhibited less variability at night during the monsoon, and in general the wind directions were fitted more closely to the valley axis. There was little evidence of coupling between the free atmosphere 250 hPa wind and the valley wind, and the strong up/down-valley regime indicates that temperature-induced density gradients drive the wind regime, and this is constrained by topography. The two major synoptic influences, the Indian summer monsoon and the upper-level westerlies, are visible in Figure 3.7, yet it is clear that the monsoon affects the diurnal cycle far more significantly than the westerlies do in the winter.

The absence of coupling between the AWS winds and the 250 hPa level winds suggests that ERA surface wind speeds might be more appropriate as a downscaling tool or glacier model forcing. ERA-5 surface wind speeds were generally well correlated with observations, particularly during the monsoon day. ERA-5 had a lower range than observations at Pheriche and Pyramid, though the diurnal patterns were comparable, with much reduced wind speeds at night (Table 3.2 and Figure 3.9). Seasonal patterns were also well represented. There was a reduced range in wind speeds during the monsoon day, particularly at Pyramid, though AWS wind speeds were more variable and sometimes several times higher.

	AWS wind speed (m/s)		**ERA-5 wind speed (m/s)**	**ERA-5 wind speed corrected to 5m (m/s)**		**Linear scaling factor after height-correction**	
	Pyramid	Pheriche	ERA-5	Pyramid	Pheriche	Pyramid	Pheriche
M_D	2.94 (±1.42)	4.34 (±2.21)	1.21 (±0.51)	0.84	0.84	3.5	5.17
M_N	1.09 (±0.85)	1.52 (±1.2)	0.64 (±0.37)	0.44	0.44	2.47	3.45
NM_D	2.97 (±1.74)	4.56 (±2.68)	1.51 (±0.71)	1.05	1.05	2.82	4.34
NM_N	1.14 (±1.11)	1.55 (±1.14)	0.48 (±0.31)	0.33	0.33	3.45	4.69

Table 3.2 AWS wind speed and ERA-5 10-m wind speed (Pyramid/Pheriche have same ERA-5 grid point) with standard deviation, and height corrected ERA-5 values using the logarithmic wind profile equation and a linear scaling factor between AWS and height corrected ERA-5 data. N = night, D = day, M = monsoon and NM = non-monsoon.

The ERA-5 surface winds (10 m height) were corrected to the AWS anemometers height (5 m) to allow for direct comparison using the logarithmic wind profile

$$u(z_5) = u(z_{10}) \frac{\ln(z_5 - d)/z_0}{\ln(z_{10} - d)/z_0} \tag{3.6}$$

(Holmes, 2015). Here z_5 and z_{10} are the 5 m AWS and 10 m ERA-5 heights respectively, d is the zero-plane displacement in metres (i.e. the height at which zero wind speed is reached due to flow obstacles e.g. boulders, trees), and z_0 is surface roughness (both in metres). For Pheriche and Pyramid we chose d as 0 m, given that measurements in this region are lacking (Miles et al., 2017). z_0 values for Pheriche and Pyramid were 0.3 m and 0.1 m approximated from surface characteristics. The height correction resulted in a wind speed reduction of 30.13%.

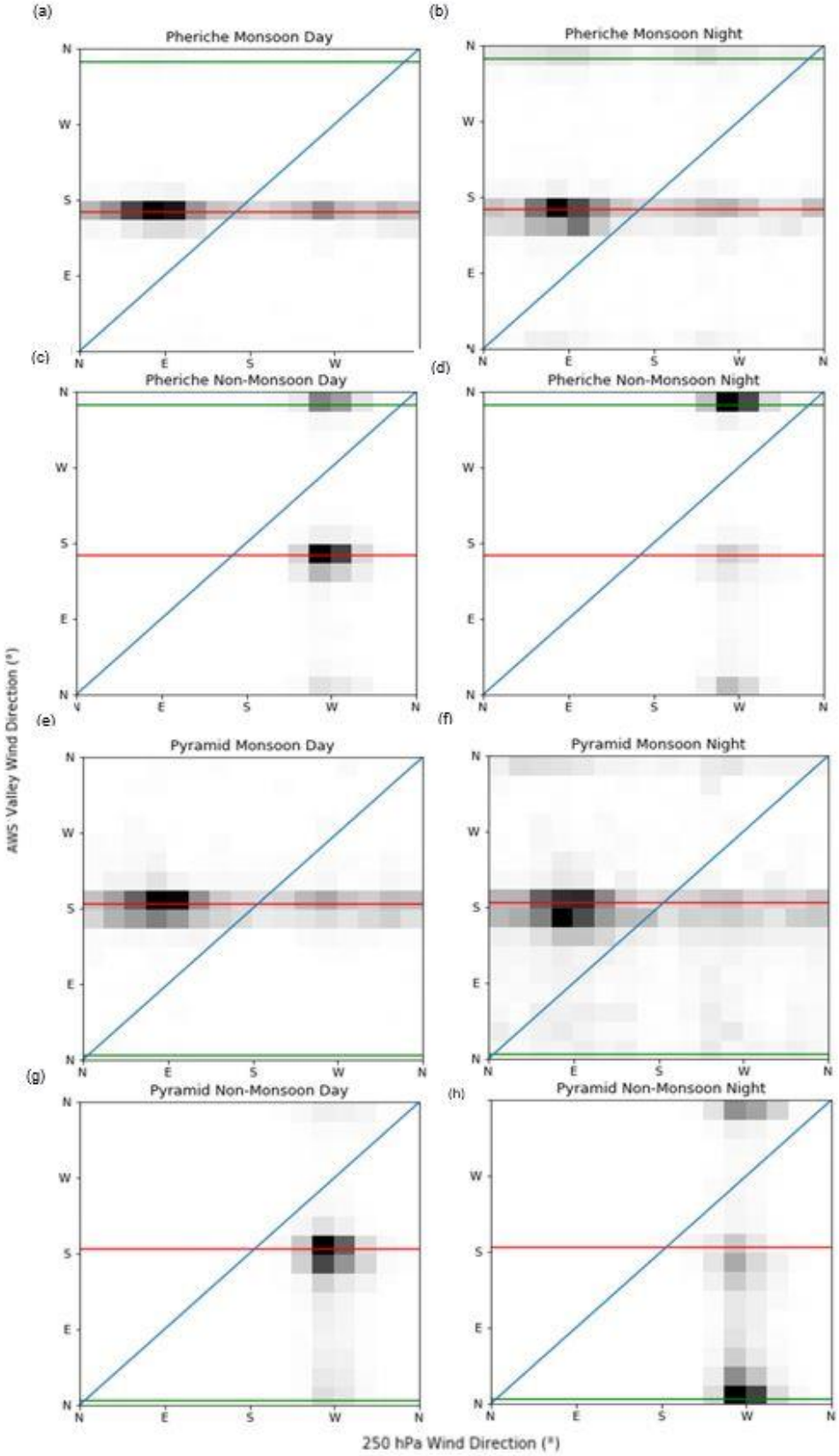

Figure 3.7 (a-h): Probability distribution of ERA-5 hourly 250hPa wind directions against the AWS valley wind at Pheriche (a-d) and Pyramid (e-h). The blue diagonal line represents coupled flow, the green line shows down-valley (northerly) flow, and the solid red line shows up-valley (southerly) flow. Wind direction is sliced into 22.5° width bins.

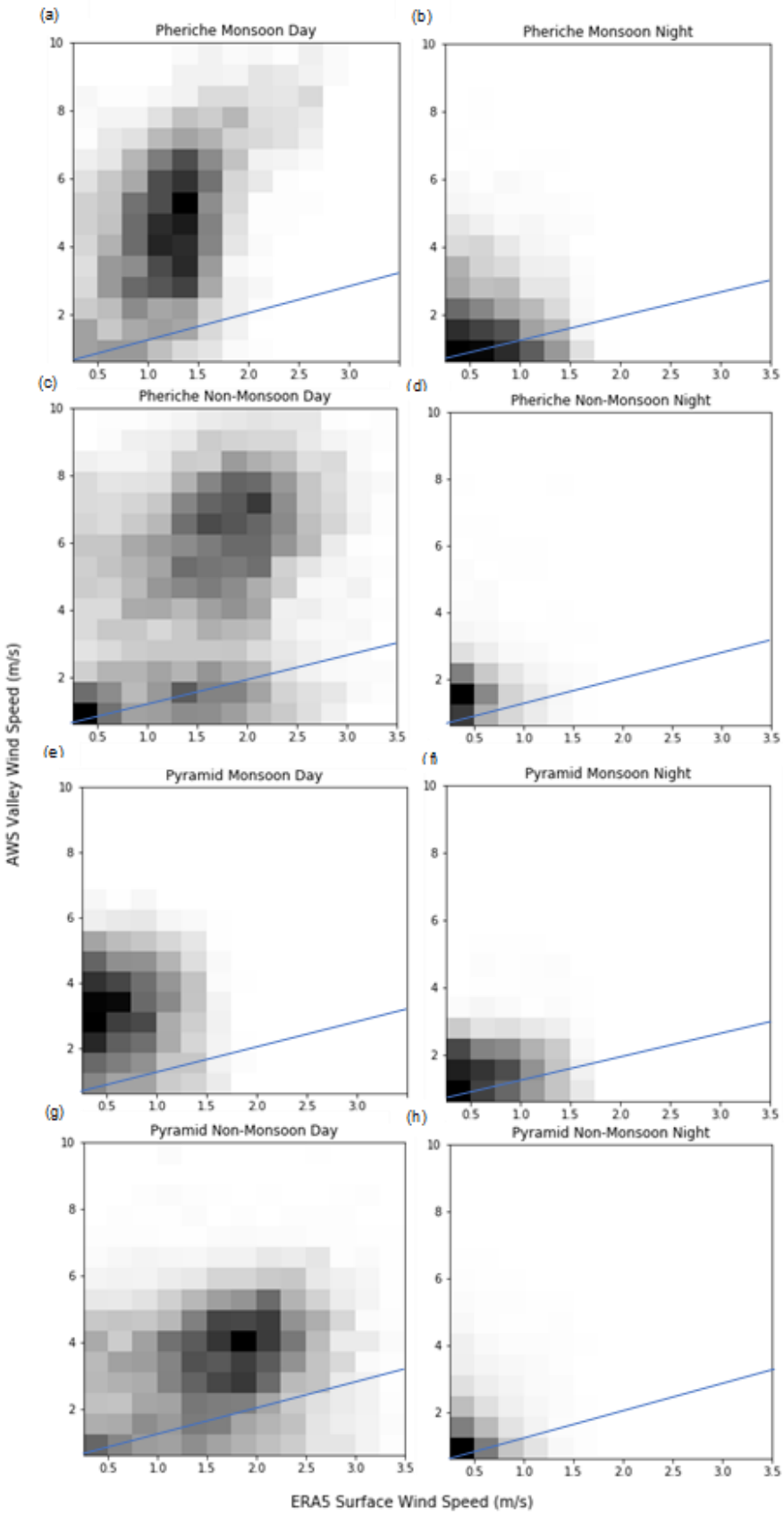

Figure 3.8 Probability distribution of ERA-5 hourly 10-m wind speeds against the AWS valley wind at Pheriche (a-d) and Pyramid (e-h). ERA-5 wind speeds are sliced into 0.2 m/s width bins, and AWS wind speeds into 0.625 m/s bins. The 1:1 line is shown in blue.

3.4.4 Altitudinal variations in meteorology

There was strong spatial variation in T across the weather stations, and T was shown to be largely a function of height. The highest temperatures occurred during the monsoon day. There was also the lowest variability in T during the monsoon (particularly during the monsoon night) (Figure 3.9). There was evidence of 'monsoon lowering' (Thayyen and Dimri, 2014) with shallower LRs relative to the non-monsoon. In general lowering of LRs at night was marked regardless of season. The strength of the altitudinal dependency of temperature was highest during the monsoon and lowest during the non-monsoon night (R^2 values, Table 3.3). There was also lowest variability in temperatures during the monsoon, particularly at night and highest during the non-monsoon during the day.

Several stations are shown in Table 3.3 to capture spatial variability in LRs. Changri Nup and Pyramid are included as station pairs located at glacierised elevations, where shallower LRs and less clear seasonal and diurnal patterns were seen. The on-glacier location of Changri Nup did not seem to have a glacier cooling effect relative to temperatures at Kala Patthar, perhaps as temperatures rarely surpass 0°C where this would become evident.

Stations used for LR calculation	**M_D**	**M_N**	**NM_D**	**NM_N**
All stations (R^2)	-5.5 ± 0.81 (0.99)	-4.55 ± 0.59 (0.99)	-5.79 ± 1.63 (0.98)	-5.05 ± 1.59 (0.91)
Changri Nup/Lukla	-5.32	-4.74	-5.15	-4.93
Kala Patthar/Lukla	-5.78	-5.03	-5.99	-5.48
Pyramid/Lukla	-5.73	-4.16	-5.83	-5.27
Changri Nup/Pyramid	-3.15	-4.18	-2.87	-3.35

Table 3.3 Temperature lapse rates (ºC per km) calculated using linear regression for all stations, (with standard deviation from hourly LRs, and the coefficient of determination (R^2) in brackets beneath) and equation 3.1 (for station pairs). N = night, D = day, M = monsoon and NM = non-monsoon.

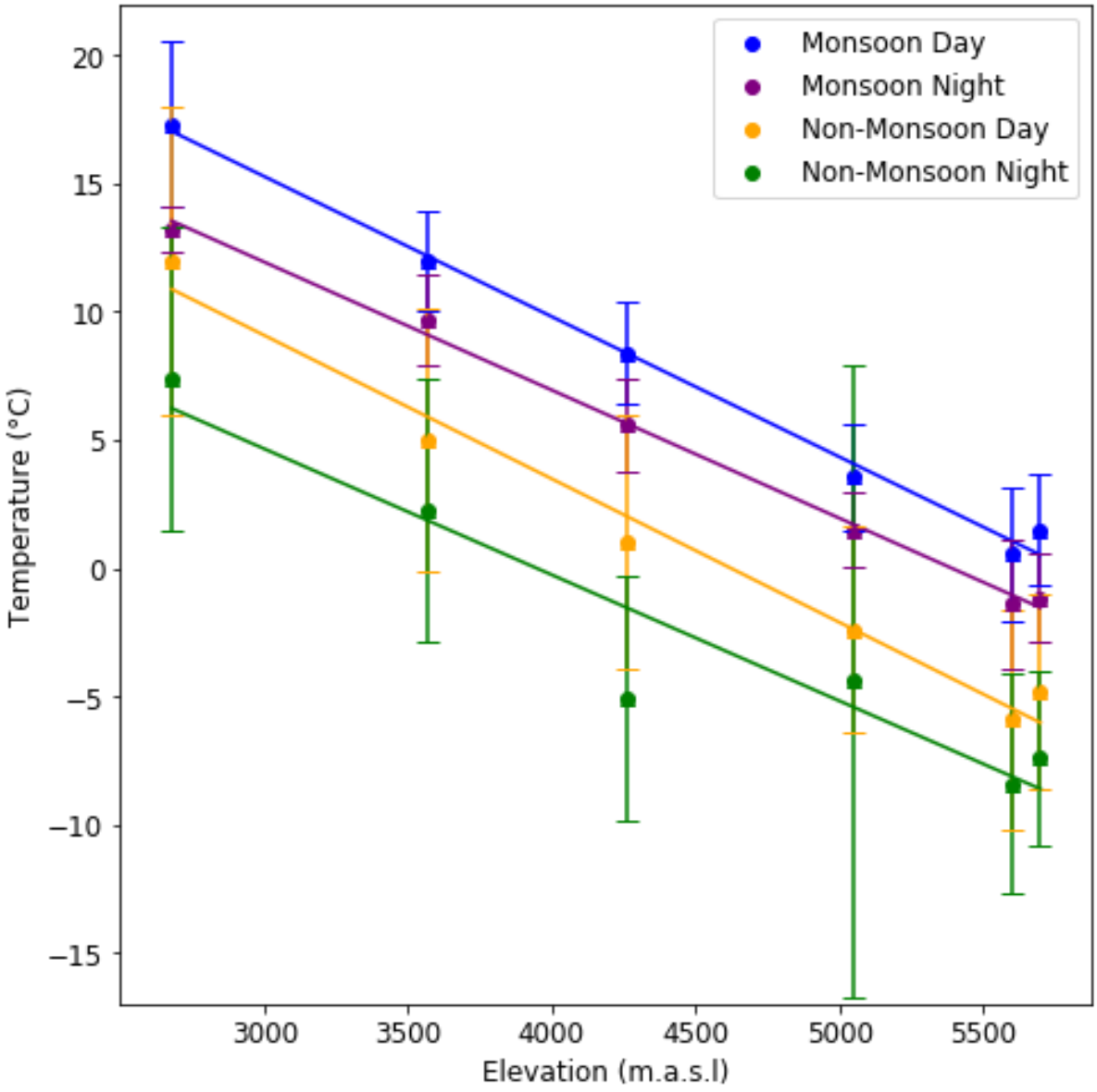

Figure 3.9 Mean temperature and standard deviation (whiskers) split by season and time of day at each station. These are split between day and night to avoid overlap of standard deviation bars.

Mixing ratios were higher during the monsoon (Figure 3.10), on average 0.0052 kg/kg higher at Kala Patthar and Pyramid, and 0.0063 and 0.0062 kg/kg at Pheriche and Namche, respectively. Between Kala Patthar and Namche, mixing ratio LRs (per km) were -2.78 $x10^{-6}$ for monsoon day, -2.25 $x10^{-6}$ for monsoon night, -2.12 $x10^{-6}$ for non-monsoon day and -1.50 $x10^{-6}$ for non-monsoon night. Mixing ratio LRs were higher between station pairs during the monsoon than outside of the monsoon and were lower at night in both seasons compared to the day. There was reduced variability during the monsoon relative to the non-monsoon, especially at lower elevations. The diurnal cycle was dampened during the monsoon at the two stations above 5,000 m.a.s.l., relative to the lower stations, particularly during the monsoon. Lukla was excluded due to unequal distribution of RH data throughout the measurement period.

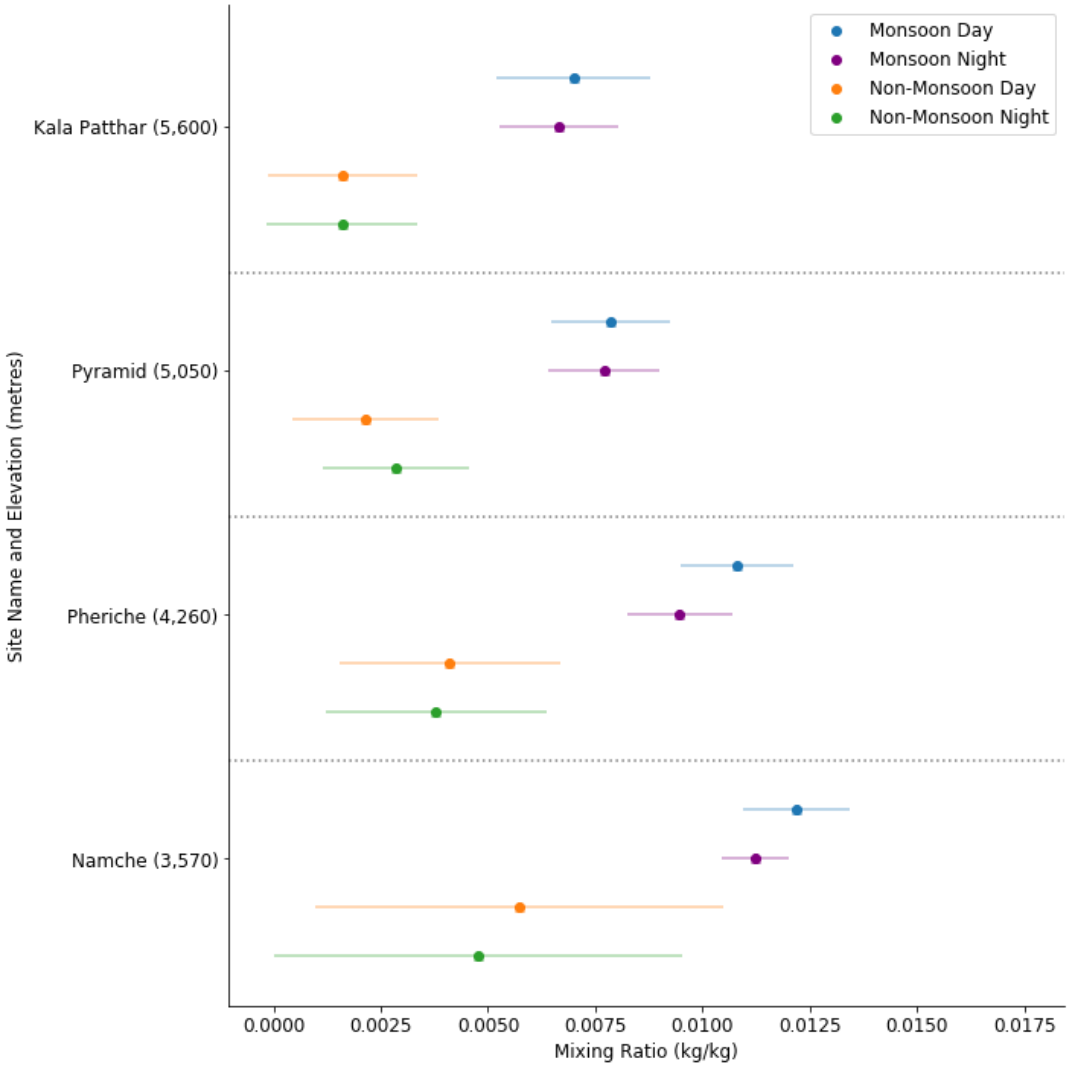

Figure 3.10 Mean mixing ratio and standard deviation (whiskers) calculated from hourly values of RH, pressure and T.

There were significant data gaps for precipitation, particularly during the monsoon (e.g. at Namche 45% of all points were missing) meaning the altitudinal dependency of precipitation could not be fully characterised using the same method as for temperature (Figure 3.9). The vertical LRs were therefore calculated using the station pairs. Vertical LRs (Table 3.4) were all weak and negative. For Kala Patthar/Pheriche and Pyramid/Pheriche in 2009, and Kala Patthar/Namche during 2011, it is clear the LRs were greater (more negative) during the monsoon than during the non-monsoon.

Station pairs	Time period	Precip lapse rate
Kala Patthar/Pheriche	2009	-0.0092
Kala Patthar /Pheriche	2009 Non-Monsoon	-0.0039
Kala Patthar /Pheriche	2009 Monsoon	-0.011
Kala Patthar/Pyramid	2009 Monsoon	-0.0001
Kala Patthar/Namche	2011 Non-Monsoon	-0.0043
Kala Patthar/Namche	2011 Monsoon	-0.0094
Pyramid/Pheriche	2009 Monsoon	-0.018

Table 3.4 Calculated precipitation LR as percentage change in total precipitation per metre of elevation (% m^{-1}) between station pairs.

3.4.5 Observations of Changri Nup Albedo

At Changri Nup, the mean albedo between February 2011 and December 2012 was 0.61, which is indicative of firn/clean ice. The albedo was highly variable although some seasonal trend was evident. There was a frequent presence of snow throughout the year. The incidences of the lowest albedo values (dirty ice) almost all fell during the monsoon. The variability was slightly reduced (around values characterised by firn) in the November of each year. Mean albedo for April 2010 and 2011 was 0.67, for June 0.37, and July 0.62. The decay of albedo in late May/early June corresponded with increasing SW_{in} and T, triggering snow melt.

Sub-daily data showed a high degree of noise on cloudy days, so incoming shortwave radiation values included in the albedo calculation were limited to > 30 W/m^2 to minimise this potential error. Figure 3.11(b) demonstrates that values considered to be within the snow/firn albedo range (0.65) occurred during the winter and the monsoon, yet ice albedo values (0.3) were during the monsoon only.

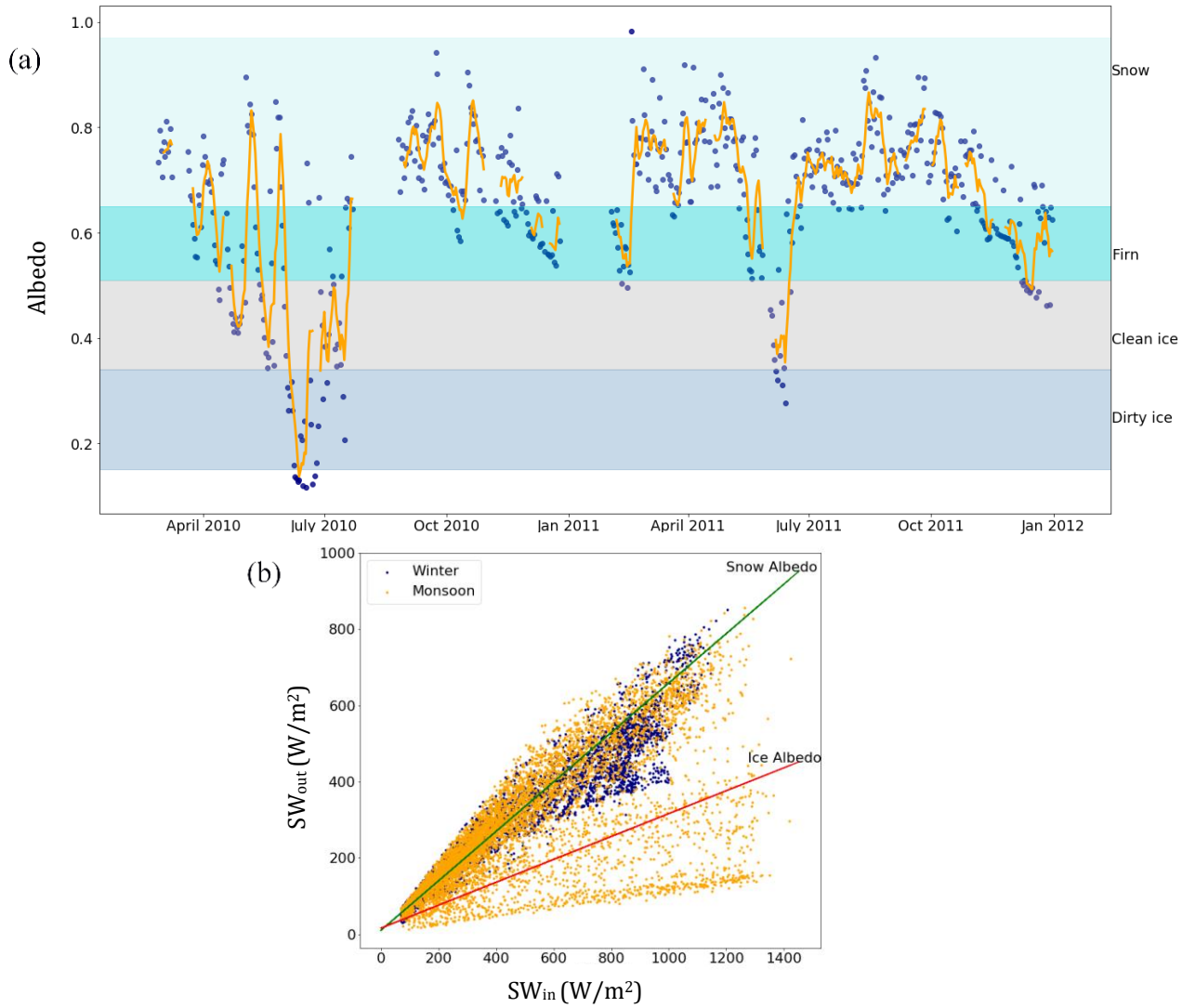

Figure 3.11 (a) Daily glacier surface albedo at the Changri Nup AWS with measurements from February 24th 2011-December 31st 2012, calculated from SW_{in} and SW_{out} with orange line showing five-day mean. (b) half-hourly incoming/outgoing shortwave radiation coded by season. The points for the winter fall close to the values that correspond with the snow albedo (0.65), whereas for the monsoon the values are for both snow and ice (0.3).

3.5 Discussion

Atmospheric temperature plays a critical role in determining processes that are key for glacier viability, such as ablation (melt and sublimation) and accumulation (snowfall and refreeze of meltwater), particularly when mean temperatures are close to freezing. In particular, the Khumbu and Changri Nup glaciers lie along the freezing point isotherm during the monsoon, thereby experiencing both melt and accumulation over short timescales. However, in the absence of *in situ* meteorology, temperature gradients are often assumed in glacier mass balance studies, meaning the position of this 0°C isotherm is poorly represented.

Glacier energy balance models (EBMs) requiring hourly input data that resolve all major energy fluxes to and from the glacier surface offer an improvement to temperature-index approaches for summer-accumulation type glaciers. EBMs distributed across the glacier surface are traditionally forced by extrapolating *in situ* temperature measurements using lapse rates relevant for the free atmosphere (e.g. the Environmental Lapse Rate, ELR, of 6.5°C per 1 km). This study demonstrates that LRs in the Dudh Koshi catchment are significantly lower than the ELR (as much as 2.5°C per 1 km lower). This is largely due to the complex boundary layer meteorology of this mountainous and glacierised catchment, enhanced by airflows such as katabatic winds and cold-pooling in valleys (Minder et al., 2010), and the ice-albedo effect on the radiative balance (Ayala et al., 2015). This difference from the standard LR, also found in the Langtang region (Immerzeel et al., 2014; Steiner and Pellicciotti, 2016; Heynen et al., 2016), the Tibetan Plateau (Shaw et al., 2021) and the Canadian Arctic (Gardner et al., 2009), demonstrates the necessity of using site-specific LRs in glacio-hydrological models, particularly for glaciers that span large elevation ranges meaning errors can propagate. These processes (e.g. cold air pooling) also point to the challenge of assuming a linear relationship of temperature with elevation, and the need for dynamic downscaling to resolve these complexities.

The temperature LRs during the monsoon were shallow, a phenomenon termed 'monsoon lowering' for the Dingad catchment of the Garwhal Himalaya (Thayyen and Dimri, 2014). Reduced LRs in the monsoon arise from the decreased diurnal temperature cycle with monsoon cloudiness, and latent heat release from precipitation warming higher elevations (Kattel et al., 2012; Heynen et al., 2016). The monsoon lowering of LRs found here for the Everest region is less marked than in the Langtang region where the monsoon influence is more significant (5°C vs 4.2°C per 1 km, respectively; Heyen et al., 2016). Diurnal LRs with season vary substantially, with shallow LRs overnight. This seasonality of diurnal cycles is more apparent than in the Langtang, where the relative increased strength of the monsoon means persistent cloud cover reduces incoming shortwave radiation, dampening diurnal variability (Kattel et al., 2012; Heynen et al., 2016). Incorporation of these diurnal LR differences with season would have a significant impact on distributed glacier melt calculations, particularly for glaciers that have large sections lying along the 0°C isotherm and summer-accumulation type glaciers.

Corrections to LRs for glacierised locations have been found to be necessary elsewhere, e.g. the Swiss Alps (Petersen et al., 2013), Italian Alps (Caturan et al., 2014), Chilean Andes (Pellicciotti et al., 2014), Chilean Patagonia (Bravo-Lechuga et al., 2019) and Tibetan Plateau (Shaw et al., 2021). On-glacier bias correction combined with variable LRs were found to produce the most reliable estimates of melt (Bravo-Lechuga et al., 2019). The analysis here found no evidence of "glacier cooling" from the on-ice Changri Nup records, with measured temperatures often higher than

those seen at Kala Patthar situated 100 m lower. Kala Patthar likely experienced greater topographic shading than Changri Nup, from Mount Everest in the morning, and Kala Patthar ridge in the afternoon (Figure 3.5). Glacier cooling was also found to be occasionally absent on the termini of Tibetan glaciers, with boundary layer divergence, warm up-valley winds, and debris cover/valley floor heating proposed as potential causes (Shaw et al., 2021). Here, LRs were also not lower between higher elevation station pairs in the nival-glacier regime (>4,260 m.a.s.l.) than other pairs, except between Changri Nup and Pyramid (Table 3.3). Local dynamics (such as cold-air pooling or katabatic winds) and the siting of stations with regards to topographic shading should therefore be considered when deriving LRs from measurements.

Distributed EBMs often assume a linear relationship between relative humidity with elevation (Klok and Oerlemans, 2002), which is not the case in reality, particularly in this region during the monsoon. To address this, and given the large altitudinal range (and therefore atmospheric pressure and temperature range) of the weather station network, the mixing ratio was calculated. The higher daytime MR seen in both seasons at Namche could potentially result from evapotranspiration, and may explain the absence of this trend for stations well above the treeline (approximately 4,100 m.a.s.l. for this region, Gaire et al., 2014, 2017). For Pyramid and Kala Patthar, the absence of a diurnal cycle during the monsoon means that seasonal LRs that disregard time of day could be used for distribution of meteorology; saving computational expense.

It is also worth considering diurnal patterns outside of the monsoon at glacierised heights. Though *in situ* measurements are lacking, the drier air at the elevation of Khumbu Glacier indicates that sublimation could be a significant component of the glacier mass balance budget, particularly outside of the monsoon in the ablation zone and all seasons in the accumulation zone. As temperature-index models do not resolve sublimation, distributed EBMs that account for this process and its spatial variability (driven by wind and MR) are preferable, particularly outside of the monsoon (Litt et al., 2019). Mixing ratio LRs rather than RH LRs are perhaps preferable for distribution of atmospheric moisture in glacier models, particularly for glaciers that have a large altitudinal range and therefore atmospheric pressure and temperature range.

Weak negative precipitation lapse rates were found in the Dudh Koshi (also found by Salerno et al., 2015 and Yang et al., 2017), perhaps due to a combination of monsoon precipitation weakening with elevation and latitude (aided by the north/south valley orientation) and undercatch of solid winter precipitation and due to high winds by the tipping buckets of higher elevation stations. Kala Patthar will be particularly prone to both given its high elevation and exposure, meaning winter precipitation will be particularly underestimated. The signal of the precipitation LR can depend on the dominant precipitation mechanism; winter westerly dominated regions often have positive LRs (Steinegger et al., 1993) and monsoon dominated regions often have negative

LRs (Seko, 1987, Bookhagen and Burbank, 2006 and Yang et al., 2017). The Tropical Rainfall Measuring Mission (TRMM) dataset also exhibits a decrease in precipitation above 2,100 m.a.s.l. (Bookhagen and Burbank, 2006). The lack of precipitation observations above 5,600 m.a.s.l. means that it is not possible to verify whether the direction/strength of precipitation LRs into glacier accumulation areas, and precipitation at this elevation is not well resolved in climate reanalysis, satellite or model products.

Precipitation LRs using observations have been found to work well for glacier modelling of some catchments, and save considerable computational expense (e.g. Immerzeel et al., 2014). However the spatial heterogeneity of precipitation with topography makes it likely that the weak LRs found in this study will not apply everywhere in the catchment, and so could produce erroneous melt calculations if used to distribute precipitation for a glacier model. To capture this variability more complex distribution approaches, with reduced computational expense relative to dynamical downscaling, could include kriging (Kumari et al., 2017) and linear orographic precipitation modelling (Smith and Barstad, 2004 and Weidemann et al., 2018), where precipitation is estimated by the orographic uplift of air (assuming stable conditions). For longer-term glacier evolution studies, as opposed to high-resolution seasonal studies, cumulative solid precipitation is of most importance and so LRs derived from *in situ* measurements could play a key role. Precipitation distribution in this region poses multiple challenges, many of which would be resolved with multi-year, well-maintained precipitation gauges that deal with solid precipitation and cover a range of elevations.

The monsoon wind regime was characterised by a weakened diurnal cycle, consistent southerly direction of flow, and lower and more consistent wind speeds (Figure 3.4a) which may be attributed to the retarding effect of glacier cooling on daytime up-valley winds (Yang et al., 2017 and Potter et al., 2018). There was no coupling between the upper-level wind and the valley wind, and the dominant mechanism was clearly driven by the pressure gradient, created by differential heating during the day and causing up valley flow, largely constrained by valley orientation (Figure 3.4 and 8).

Kala Patthar is the exception to this pattern, with wind direction and speeds indicative of either a frequent katabatic flow from the Changri Nup glacier (from the direction of the Changri Nup AWS) or perhaps the prevailing winds of the free atmosphere given the exposure of the site. The wind direction is more consistent during the day, perhaps as the orientation adjusts with sunrise (Figure 3.7c) (Bollasina et al., 2002). The katabatic wind may be triggered by the consistently lower temperatures over the clean ice sections of Changri Nup glacier relative to the surrounding land (Ayala et al., 2015). Higher resolution models capture persistent katabatic and föhn winds that affect near-surface air temperature and fluxes, thus inhibiting or enhancing glacier melt,

respectively (Cape et al., 2015). It was found that ice masses dampen up-valley flow in the Dudh Koshi when modelled with the Weather Research Forecasting model at 1 km resolution, and when removed up-valley flow strengthened (Potter et al., 2018). Incorporating this feedback on the local wind regime with future change in ice volume would be a highly valuable and novel area of research.

The diurnal and seasonal patterns of surface wind speeds were fairly well resolved by ERA-5 (Figure 3.8) but wind speeds were markedly lower than observations. The gradient was steeper for monsoon daytime (Figure 3.8a and e) than the non-monsoon daytime (Figure 3.8c and g) relative to a 1:1 relationship, potentially due to the AWS being sheltered. Downscaling of ERA-5 to the valley-scale could feasibly be carried out through extrapolation of this line.

Surface roughness is likely to increase the wind speed variability seen at weather stations, which will not be resolved by ERA-5 given the low spatial resolution (31 km) demonstrating the risks of using coarse resolution datasets which have not been downscaled or bias corrected. A correction factor was applied to the ERA-5 10 m wind data to match the height of the observations (here 5 m) using the logarithmic wind law method. This resulted in a reduction of the ERA-5 wind speeds by 31%, widening the discrepancy between observations and ERA-5 even further.

The wind correction carried out here is also limited in several ways. For example, it does not account for valley terrain enhanced winds, or weakened winds through sheltering, and assumes a logarithmic wind profile in neutral flow. Locations that have temperature measurements at different heights could apply an additional temperature stability correction to this logarithmic profile (Quincey et al., 2017). Wind can redistribute snow and alter turbulent heat fluxes, particularly on glacier surfaces with high surface roughness from crevassing or heterogeneous debris cover (e.g. Khumbu Glacier, Quincey et al., 2017). Recent modelling work for the Tien Shan indicates this could be significant, with a mean annual glacier mass balance increase (decrease) of 32% (24%) following a 54% increase (decrease) in mean hourly wind speed (Che et al., 2019). The resolved seasonality of ERA-5 surface winds but marked difference in absolute values relative to observations, suggests bias correction may be adequate, with linear scaling factors needed between 2.47 and 5.17 following height correction (Table 3.2).

The albedo on Changri Nup Glacier was highly variable throughout the measurement period, and indicative of frequent snow presence, including at times during the monsoon (Figure 3.11), though snow melt (albedo decay) and presence of dirty ice is higher between June and September. The high variability is likely the result of the snow cover remaining well below 0.35 m during the measurement period (Figure A2) making it susceptible to melt, exposing the darker underlying ice. There is an asymmetric pattern, with a rapid rise in albedo following snowfall, and a subsequent slower darkening with ageing of snow. There is evidence of two seasons of high albedo

straddling either side of the monsoon. The low albedo measured in mid-June was likely triggered by increased melt (and melt-out of englacial debris) and ageing of snow though rising albedo in July 2010 and 2011 suggests precipitation was falling as snow at points during the monsoon. The darkening observed in March 2010 also followed high concentrations of atmospheric black carbon (Vuillermoz et al., 2015).

Accurate estimates of glacier albedo are essential for glacier modelling (Schmidt et al., 2017), and to assess the contribution of the snow-ice-albedo feedback mechanism on elevation-dependent warming (Sharmer et al., 2019). However, they are rarely available at appropriate temporal or spatial resolutions. *In situ* measurements, such as those presented here, can account for processes that satellite imagery (e.g. MODIS snow albedo products) are unable to capture because of their relatively coarse spatial resolution, persistent cloud cover, and the limited sub-daily products that are available. They offer a vast potential improvement over using a single albedo value, and would be improved further by the installation of several further AWS to capture the spatial variability more robustly. This approach would still be limited, however, by not capturing the low albedo zones associated with surface meltwater ponds (Watson et al., 2016) and conversely, high albedo zones associated with exposed ice cliffs (Buri et al., 2016).

3.6 Conclusion

High elevation meteorology observations are required to force glacier models and for dynamical/statistical downscaling, as well as to calibrate and validate results from both. The high elevation network examined here, with an altitudinal range of 3020 metres, is unique in High Mountain Asia, and thus provides a critical insight into the intricacies associated with the complex orography. Lower elevations observations that are often used as substitutes would fail to capture the complex meteorology in the glacierised zones. This analysis has revealed key diurnal, seasonal and spatial patterns in meteorological variables in the Dudh Koshi catchment of the Nepal Himalayas, using data from 6 weather stations. The analysis of this dataset has also made steps towards bridging the inter-disciplinary gap between the use of *in situ* meteorology for glacier modelling.

Following this analysis, the following several key concluding remarks are made:

- The Indian summer monsoon has a profound impact on the Everest region of Nepal, bringing increased and more consistent temperatures and mixing ratios to all elevations.
- Temperature lapse rates vary seasonally and according to the time of day. For station pairs with >1 km elevation difference, daytime LRs during the monsoon (non-monsoon)

were 0.58-1.57°C (0.22-0.57°C) per km relative to night-time LRs. The approach used to split LRs by time period used in this study would produce more accurate results than using a mean LR for the whole year, and would be less computationally intensive than use of variable lapse rates.

- The wind regime was clearly driven by temperature-induced density gradients, controlled by topography, with no coupling with the upper-level winds. This was apparent throughout the year but dampened with the arrival of the monsoon. Wind speeds were significantly underestimated by ERA-5, although seasonal and diurnal patterns were captured. ERA-5 is therefore not a suitable substitute for observations in this region, and at the very least height and bias correction should be conducted.
- Precipitation reduced slightly with elevation, although the relationship with height is less clear than that of temperature and mixing ratio. The signal is likely a combination of monsoon weakening with elevation and latitude, and undercatch of snowfall at high elevations, or total precipitation under high winds. Precipitation remains one of the greatest uncertainties of mountain glacier modelling with few *in situ* high elevation sensors. Precipitation inputs for future glacier predictions pose even greater challenges.
- The Ev-K2-CNR weather station network provides a rare insight into the meteorological complexity of this region and how this can be effectively captured for glacier modelling. For multi-year glacier modelling studies, statistical downscaling is particularly valuable and saves considerable computational expense relative to dynamical downscaling. The sensitivity of the glacier model to different input variables should be analysed to help determine which variables need particular focus, and inform more complex downscaling approaches (often required for precipitation in particular). *In situ* meteorological and glaciological records are invaluable both for the first steps of ascertaining LRs, bias correction and the final steps of validation of model output.

Chapter 4 Investigating the sensitivity of Khumbu Glacier mass balance in the present day

4.1 Introduction

The previous chapter analysed the local meteorology of the Everest region, and discussed the implications of using *in situ* data for glacier modelling. Here COSIPY (version 1.3; Sauter et al., 2020), currently considered a leading open-source method for estimating glacier mass balance, is used to investigate the present-day mass balance of Khumbu Glacier and explore the sensitivity of the glacier to differing meteorological inputs. Khumbu Glacier is located on the southern flanks of Mount Everest, and has the world's highest accumulation area, sitting at an elevation of around 7,500 m.a.s.l.. It terminates at approximately 4,900 m.a.s.l. and the flat tongue has a highly heterogenous surface of thick mantles of debris, supraglacial ponds and ice cliffs (Rowan et al., 2015, Watson et al., 2016 and Quincey et al., 2017).

Khumbu Glacier experiences cold and dry winters, warm summers, and the strong influence of the monsoon means it is classified as summer-accumulation type. The monsoon onset is generally in June, although this is highly variable from year-to-year, and some studies estimate that it brings 90% of the annual precipitation (Salerno et al., 2015). Snow melt begins in the pre-monsoon (May), and ice melt peaks during the monsoon (July) at the lower elevations of the glacier (Bocchiola et al., 2020). Changri Nup (5,700 m.a.s.l.) and Kala Patthar (5,600 m.a.s.l.) weather stations see temperatures around freezing throughout the monsoon (Chapter 3), and so it is likely that solid precipitation dominates above these elevations. A network of stations installed in 2019 as part of a National Geographic expedition reveal that during the monsoon of 2019 at Camp II (6,464 m.a.s.l.) temperatures rarely went above freezing (Matthews et al., 2020). Preliminary analysis of this meteorological data has revealed that ablation (largely sublimation) of up to 60 mm a^{-1} is possible in the upper reaches of the glacier primarily as a result of the significant incoming shortwave radiation, despite temperatures being well below freezing (Matthews et al., 2020).

Mass balance measurements of Khumbu Glacier were conducted in August 1974 by the Glaciological Expedition of Nepal (Mae et al., 1975) to aid the first study on the mass budget of a Himalayan glacier (Inoue, 1977). Thermal drilling at Base Camp (5,550 m.a.s.l.) revealed an annual melt rate of -3.74 m w.e. and ablation stakes elsewhere found rates of -0.9 m w.e. at Lobuche (~5,000 m.a.s.l.) and -0.45 m w.e. at the terminus (4,800 m.a.s.l.). The inaccessibility of the upper reaches of the glacier meant accumulation rates were not measured, but it was observed that

accumulation could not just be from precipitation falling directly onto the glacier as accumulation rates would otherwise be less than one third of the measured ablation rates. Therefore, mass gain of snow from the steep surrounding walls is thought to contribute between 66% and 75% to accumulation rates. Thick debris towards the terminus of the glacier is known to insulate the underlying ice, to the extent that peak ablation occurs several kilometres up-glacier, around the position of Everest Base Camp (EBC, 5,550 m.a.s.l.). However, given that the debris is punctuated with areas of clean-ice around ponds and ice cliffs, local ablation rates are highly variable. This surface heterogeneity may partly explain the "debris cover anomaly" (Pellicciotti et al., 2015), with debris-covered glaciers displaying similarly high ablation rates to clean-ice glaciers in response to atmospheric warming (Brun et al., 2018).

This ablation pattern was confirmed by satellite imagery studies (Nakawo et al., 1999) that found ablation and downwasting peaked just below the ELA (near EBC) where debris is thin or absent, and then decreased towards the terminus (Bolch et al., 2016). The velocity reduced linearly from EBC to the terminus. The area around EBC is likely the transition zone between the active parts of the glacier, and the stagnant debris-covered tongue (Bolch et al., 2016 and King et al., 2020). These observations are all associated with a glacier in negative mass balance (Kirkbride and Deline, 2013). Most of what is understood of the mass balance of Khumbu Glacier is via these types of proxy-based approaches. Traditional methods of determining glacier mass balance (e.g. from accumulation area ratios or measuring ELA variations) are not appropriate for Khumbu Glacier, in part because of the inaccessibility of the accumulation area, but also as the surface debris cover and non-uniformity of the ablation gradient complicates matters. Equally, the ELA can differ by several hundreds of metres from the snowline due to the proposed significance of avalanching for accumulation (Benn and Lehmkuhl, 2000).

Geodetic techniques have confirmed more recently that Khumbu Glacier is losing mass through thinning rather than terminus recession, which contrasts with clean-ice glaciers. Differencing of DEMs from 2002-2007 found area averaged mass balance rates of −0.45 ± 0.52 m w.e. a^{-1} for Khumbu and −0.29 ± 0.52 m w.e. a^{-1} for Changri Shar/Nup (Bolch et al., 2011). The same approach was used with higher resolution DEMs from 2000 and 2015 (King et al., 2017), finding a spatially averaged mass balance of −0.58 ± 0.19 m w.e. a^{-1} for Khumbu Glacier.

Ice flow modelling studies on Khumbu Glacier have been used to simulate past change and future evolution of the glacier (e.g. Rowan et al., 2015, discussed in further detail in Chapter 5). These approaches are great improvements compared to ice redistribution models (e.g. Shea et al., 2015a) as they capture the ice dynamics that are integral to studying glacier change, and can resolve a spatially/temporally evolving debris layer which is of particular importance for Khumbu Glacier (Rowan et al., 2015). However, traditionally these models are solely driven by

temperature (and sometimes precipitation; Shea et al., 2015a) or by the height of the ELA (Rowan et al., 2015).

Although temperature and precipitation are critical for glacier mass balance, Khumbu Glacier's extreme elevation range and location on the northern limit of the monsoon-dominated southern slopes mean the meteorological drivers of mass balance are less well constrained. Here, sensitivity analyses will aid quantification of the EBM to the quality and quantity of the input data. Despite the presence of *in situ* data that can aid model calibration and evaluation, to the best of our knowledge, there have been no mass balance modelling studies of this kind on Khumbu Glacier, particularly above the ELA. Addressing this specific knowledge gap forms the basis of this chapter.

Glacier mass balance models calculate glacier-wide ablation rates from local meteorological conditions. Distributed mass balance models are most commonly driven by meteorological variables that are distributed from point-based observations using elevation-based lapse rates, to allow catchment-wide melt calculations to be performed. The glacier surface energy balance (SEB) links the glacier surface layer with atmospheric processes, with the ice surface acting as an interface within which energy cannot be stored (Cogley et al., 2011). The exchange of energy fluxes at the ice-atmosphere interface are illustrated in Figure 4.1. If the energy balance is positive and air temperature is at or above 0°C, melt will occur. The subsurface processes are also critical for determining runoff and refreeze, and thereby glacier mass balance.

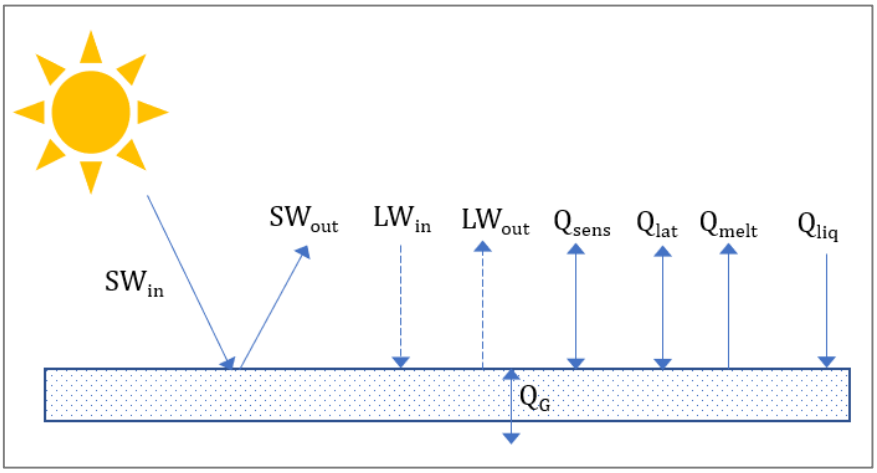

Figure 4.1 Glacier surface energy balance where SW_{in} and SW_{out} (LW_{in} and LW_{out}) are incoming and outgoing shortwave (longwave) radiation, Q_{sens}, Q_{lat}, Q_g and Q_{liq} are sensible, latent and ground heat fluxes and the heat flux from rain, and Q_{melt} the energy available for melt.

In this chapter the drivers of mass balance are investigated using energy flux and melt component analysis. The sensitivity of Khumbu Glacier mass balance to changing temperature and precipitation is then assessed. Perturbations to meteorological parameters (varying temperature lapse

rates and precipitation partitioning schemes) and glaciological variables (surface roughness and albedo) are also performed. As all perturbations are within the range of real measurements (as defined by *in-situ* AWS data or measurements from other studies), the results of these sensitivity studies are useful to determine uncertainty in mass balance calculations.

Studies using the former COSIMA model and COSIPY have focused on smaller Austrian and Tibetan glaciers (e.g. Zhadang glacier; Huintjes et al., 2015b). This open-source mass balance model has not yet been applied to a glacier of this scale, both in terms of size and elevation range, which both lead to increased computational requirements. For example, Khumbu Glacier has an elevation range of 3,010 m and an area and length of 32 km^2 and 16 km respectively (Nakawo et al., 1999, Benn and Lehmkuhl, 2000; Rowan et al., 2015). This is significantly larger than Zhadang Glacier which has an area of 2 km^2 and length of 2.2 km (Huintjes et al., 2015b, Zhang et al., 2017; Sauter et al., 2020). The impact of spatial resolution on mass balance results is also investigated to assess the viability of applying COSIPY to large, complex mountain glaciers or even regional scale mass balance studies. This would be an improvement on regional studies that derive mass balance from ELA or accumulation area ratios.

The model was originally written for application to clean-ice glaciers (no surface debris layer). While this is clearly a poor representation of the heavily debris-covered tongue of Khumbu Glacier, the intention is to measure the impact of changing meteorology on glacier mass balance in isolation. In the final section of this chapter, the impact of supraglacial debris on mass balance model is calculated using a debris thickness dependent modification of ablation calculated specifically for Khumbu Glacier using the model by Evatt et al. (2015). This will allow comparison of mass balance results to observations or simulations from other studies to assess its suitability to generate mass balance forcings for future ice flow modelling (Chapter 6).

4.2 Model description

The coupled snowpack and ice surface energy and mass balance model in Python (COSIPY) is an open-source, distributed model (Sauter et al., 2020) that is applied here to Khumbu Glacier. The model is developed and modularised in Python from its earlier version (COSIMA), which has previously been applied to the Purogangri ice cap (Huintjes et al., 2015a), to Zhadang Glacier (Huintjes et al., 2015b) of the Tibetan Plateau, and to Grey and Tyndall Glaciers of Patagonia (Weidemann et al., 2018), amongst others.

COSIPY integrates a SEB model with a multi-layer snow and ice model (Weidemann et al., 2018). It thereby resolves all energy fluxes *(F)* at the ice surface that contribute to surface melt *(Q_{melt})*

$$F = SW_{in} \cdot (1 - \alpha) + LW_{in} + LW_{out} + Q_{sens} + Q_{lat} + Q_g + Q_{liq}. \quad (4.1)$$

Where SW_{in} is incoming shortwave radiation, α is albedo, LW_{in} and LW_{out} are incoming and outgoing longwave radiation and Q_{sens}, Q_{lat}, Q_g and Q_{liq} are the sensible, latent and ground heat fluxes (Oerlemans et al., 2001), and the heat flux from liquid precipitation. The latter is often neglected in melt models (Cuffey and Paterson, 2010), but is of particular importance here as the Indian summer monsoon brings a significant amount of liquid precipitation to the lower reaches of Khumbu Glacier.

If Q_{lat} is negative, ablation will occur through sublimation even in instances where surface temperature (T_s) and/or air temperature (T_{air}) are well below melting point (0°C). The resultant F is equal to the energy available for surface melt (Q_{melt}, Figure 4.1 and equation 4.2 below) when T_s is at melting point (0°C). T_s is used to calculate LW_{out}, Q_{sens}, $Q_{lat,}$ Q_G and partition solid and liquid precipitation (section 4.1.3). When T_s exceeds the melting point it is reset to 0°C (273.15 K) and the residual F fluxes equal Q_{melt}. In this instance, subsurface melt is triggered when the energy fluxes, e.g. penetrating SW_{in} warm the ice layer so that T_s exceeds the melting point of ice (Sauter et al., 2020).

The exchange processes at the surface, including energy release and consumption with phase changes, control temperature distribution and phase changes within the glacier (comprised of horizontal ice and snow layers). The coupling of the SEB component with a multi-layer subsurface snow and ice model accounts for meltwater refreeze and percolation, with the meltwater produced from the surface melt calculations, acting as an input. The mass balance *(MB)* is calculated at an hourly resolution, with the accumulation rates coming from this refreeze of meltwater *(c_{ref})*, and the accumulation of solid precipitation *(c_{solid})* on the ice surface (Figure 4.2), as well as deposition of water vapour (Sauter et al., 2020). Ablation is by subsurface and surface melt and sublimation.

This is described as follows

$$MB = \frac{Q_{melt}}{L_M} + \frac{Q_{lat}}{L_s} + c_{solid} + c_{ref} \quad (4.2)$$

where Q_{melt} is the energy available for surface melt, L_M and L_S are the latent heat of melt (3.34×10^5 J kg^{-1}) and sublimation (2.849×10^6 J kg^{-1}), respectively. T_s links these surface and subsurface model components.

Accumulation can also occur through avalanching onto the glacier. This is known to be a significant process for Khumbu Glacier (and indeed many other Himalayan glaciers) via the steep hillslopes of the Western Cwm accumulation area (Benn and Lehmkuhl, 2000). Accumulation by avalanching is generally not accounted for by mass balance models, but is resolved with the iSOSIA ice flow model and discussed further in Chapter 6.

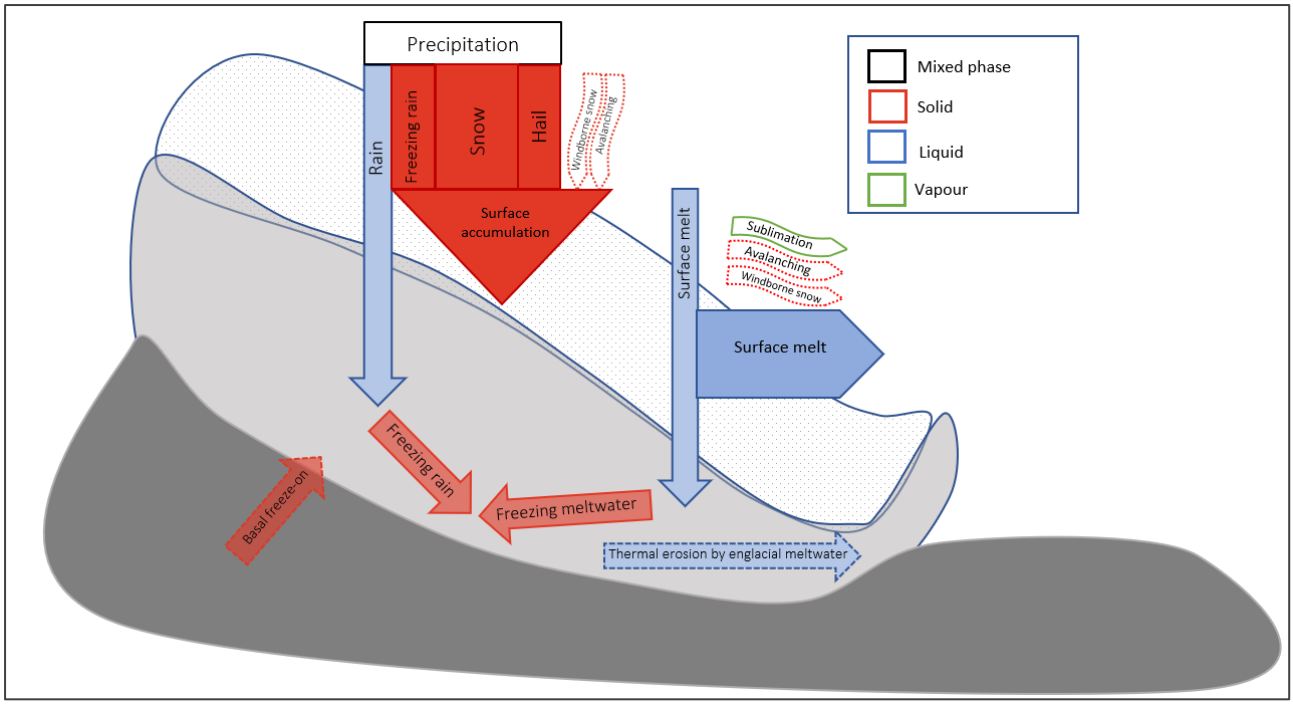

Figure 4.2 Schematic of processes that contribute to ablation and accumulation on a land-terminating glacier. Dashed lines demonstrate processes that are not treated by the model. Modified from Cogley et al., 2011.

Surface albedo *(α)* at a given hour *(i)* is parameterised following Oerlemans and Knap (1998), first through assuming that $a_{snow}{}^{(i)}$ depends on the age of the snow; a function of snowfall frequency and snow depth with

(4.3)

$$\alpha_{snow}{}^{(i)} = a_{firn} + (\alpha_{freshsnow} - a_{firn}) \exp\left(\frac{t_{snow}{}^{(i)}}{t^*}\right)$$

where $t_{snow}{}^{(i)}$ is the time since last snowfall at a given hour *(i)* and t^* is the time taken for snow to decay to firn. The transition to α_{ice} when snow depth is low is calculated as follows

$$a^{(i)} = a_{snow}{}^{(i)} + (a_{ice} - a_{snow}{}^{(i)}) \exp\left(\frac{-h}{d^*}\right) \quad (4.4)$$

where h is the snow depth, and d^* the constant for the effect of snow depth on albedo. Albedo values for each of these components are pre-determined in the model, and the values chosen for the reference run are outlined in Table 4.4.

The turbulent fluxes comprise sensible (Q_{sens}) and latent heat (Q_{lat}) fluxes, which are determined through the bulk aerodynamic method (Hock et al., 2005 and Brock et al., 2010). The temperature difference between the glacier surface and overlying boundary layer determines the direction of the sensible heat flux. When the T_{air} is higher than the glacier surface temperature (T_s), Q_{sens} heat is transferred from the boundary layer to the glacier surface. The direction of Q_{lat} is dominated by the vapour pressure gradient. If atmospheric vapour pressure is higher than that at the glacier surface, there is a transfer of moisture from the boundary layer to the glacier, releasing latent heat.

The turbulent heat fluxes were calculated following Oerlemans (2001) between the glacier surface and the instrument height (~2 m)

$$Q_{sens} = \rho_{air} \cdot c_p \cdot C_{se} \cdot u \cdot (T_{air} - T_s) \quad (4.5)$$

$$Q_{lat} = \rho_{air} \cdot L_{E/S} \cdot C_{lat} \cdot u \cdot (q_{air} - q_s) \quad (4.6)$$

where ρ_{air} is air density, derived from air pressure *(P)*, T_{air} and specific humidity at a height of 2 m, c_p is the specific heat capacity of air (1004.67 J kg^{-1} K^{-1}), L_E is the latent heat of evaporation (2.514×10^6 J kg^{-1}), and L_S of sublimation (2.849×10^6 J kg^{-1}). Q_{air} and q_s refer to specific humidity at instrument height (2 m) and at the surface, calculated from RH, P and saturation water vapour pressure.

The bulk transfer coefficients for sensible (C_{se}) and latent heat (C_{lat}), or the Stanton and Dalton numbers respectively, are calculated as follows

$$C_{se} = k^2 \left[\ln\left(\frac{z}{z_0}\right)\right] \cdot \left[\ln\left(\frac{z}{z_{0t}}\right)\right] \quad (4.7)$$

$$C_{lat} = k^2 \left[\ln\left(\frac{z}{z_0}\right)\right] \cdot \left[\ln\left(\frac{z}{z_{0q}}\right)\right] \quad (4.8)$$

where k is the von Karman constant (0.41), z the instrument height (2 m) and z_{0t} and z_{0q} the roughness length for sensible heat and for moisture ($z_0/10$). COSIPY uses the typical values of $z_0/100$ and $z_0/10$ for these roughness lengths, respectively, though in reality these are fairly poorly understood.

A linear scale for z_0 is used, from 0.24 mm for fresh snow to 4 mm for firn (aged snow). This scales over 60 days according to the method from Mölg et al. (2012). If there is no snow present, the z_0 is that of clean ice (1.7 mm; Table 4.4). The roughness length is updated depending on the hours since last snowfall and snow height.

The model uses a vertical structure that is defined here as being 30 m thick, comprising layers that are 0.5 m thick. As this chapter focuses on the interaction of meteorology and glacier MB, a description of the subsurface model is not included. Information regarding the schemes used for percolation, penetrating shortwave radiation, refreeze and densification can be found in Huintjes et al. (2015b).

COSIPY was selected as it is one of very few open-source distributed EBMs available, and also calculates sublimation (unlike those designed by Reid and Brock, 2010 and Lejeune et al., 2013); an important ablation process for high elevation glaciers particularly outside of the monsoon (Bonekamp et al., 2018). The absence of mechanisms that represent avalanching and the impact of supraglacial debris on ablation is a limitation of this model for Khumbu Glacier. However, a mass balance model that includes both mechanisms does not currently exist. Integration with the ice flow model, iSOSIA (Chapter 6), which includes mechanisms that transport avalanched snow and debris from hillslopes supraglacially and englacially, and parameterises the impact of supraglacial debris on ablation, means that, though these limitations are apparent in this Chapter, these will not have implications for the glacier change projections (Chapter 6).

4.2.1 Meteorology inputs and distribution

The model is forced by hourly 2 m air temperature (K), total precipitation (mm), relative humidity (%), air pressure (hPa), wind speed (m/s), incoming shortwave radiation (W m^{-2}) and either incoming longwave radiation (W m^{-2}) or cloud cover fraction. Snowfall (m) is also an optional input, and when not given the total precipitation is partitioned to estimate snowfall. The default snow/rain partition scheme, or snow transfer function (STF), means the proportion of solid precipitation linearly transitions from 100% at 0°C to 0% at 2°C (Figure 4.3) as in Hantel et al. (2000) and Weidemann et al. (2018).

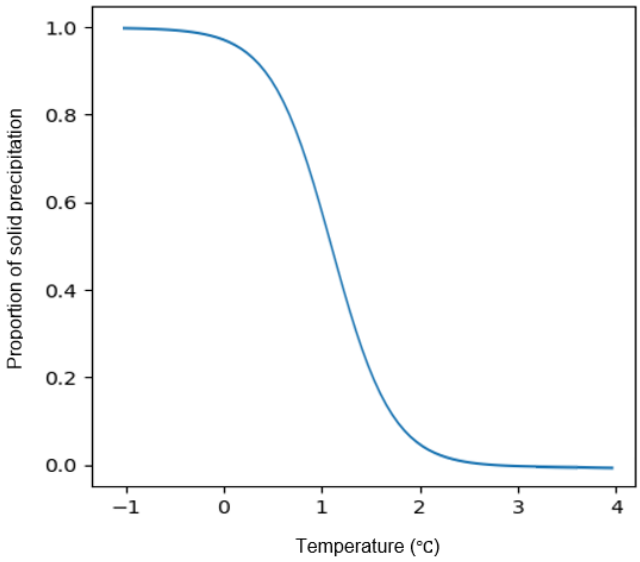

Figure 4.3 Default snow transfer function (STF) used to partition rain and snow.

Temperature, precipitation, snowfall and relative humidity are all interpolated across the domain through linear lapse rates

$$V_{interp} = (V) + (pixelAlt - stationAlt) \cdot LR\_V \quad (4.9)$$

where V_{interp} is the variable to be interpolated, V is the hourly variable in question (e.g. temperature or precipitation), *pixelAlt* is the elevation (m.a.s.l.) of the target pixel in the domain, *stationAlt* the elevation (m.a.s.l.) of the station (e.g. Pyramid rain gauge at 5,035 m.a.s.l.) and *LR_V* is the specified LR. For the majority of simulations, the same temperature LR is used across the simulation period. However, the MB sensitivity to LRs that differ depending on season or time of day is examined later in this chapter. Also note that the distribution is from a prescribed elevation, not from the exact location (latitude/longitude) of the AWS.

The radiative and turbulent fluxes are critical determinants of the SEB. In reality, SW_{in} is modified through local cloud cover and atmospheric structure, topography, and the seasonal cycle. In COSIPY, the temporal radiation cycle is calculated by considering the day of year, solar zenith and azimuth angle, solar radiation measured horizontally and the zenith threshold. The direct radiation across the domain is corrected by the slope, azimuth (Figure 4.4) and shadowing potential of each pixel across the domain (Ham, 2005, Wohlfahrt et al., 2016 and Sauter et al., 2020). A footprint weighted correction is also applied to horizontal measurements of net radiation. The fraction of diffuse SW_{in} is estimated by using the ratio of total shortwave (global) radiation and potential shortwave radiation to define a clearness index (Wohlfahrt et al., 2016). This clearness index is used to calculate diffuse radiation, which is calibrated with data from Neustift, an eddy

covariance station in the Austrian Alps (Wohlfahrt et al., 2008). In this chapter, the distributed radiative fluxes are compared with high elevation stations in 2019 to assess the efficacy of this method across the domain.

Pressure *(P)* is first distributed by calculating sea level pressure *(SLP)*

$$SLP = P\left(1 - \frac{0.0065 * stationAlt}{288.15}\right)^{-5.255} \quad (4.10)$$

where 0.0065 is the environmental lapse rate, 288.15 the standard sea level temperature (Lente and Osz, 2020). *P* is then interpolated (*P_interp*) across the domain with the barometric equation

$$P_{interp} = SLP.(1 - 0.0065\,.pixelAlt)/(288.15)^{-5.255}. \quad (4.11)$$

4.2.2 Sub-debris ablation correction

The thick debris mantle which is ubiquitous across the 7 km tongue of Khumbu Glacier acts to insulate the ice from atmospheric forcing. This relationship between debris thickness and melt is well conceptualised (Østrem, 1959), though this is not uniform over space and time. Kayastha et al. (2000) measured ablation beneath debris thicknesses of ≤40 cm, yet thicknesses greater than this dominate on Khumbu Glacier. In the absence of recent *in situ* measurements of ablation under thick debris, a sub-debris ablation model was used to produce a Khumbu specific Østrem curve for the study period (as seen in Figure 2.5). The dynamic ablation due to debris from ice model, or "DADDI", model resolves distributed temperature within the debris layer by estimating debris skin temperature and using prescribed debris conductivity. Evatt et al. (2015) provides an in-depth description of the DADDI model. In the absence of observed melt rates under thick debris on Khumbu Glacier or neighbouring glaciers, the model is used to produce a Khumbu specific melt reduction curve to be applied to the simulated clean-ice mass balance produced by COSIPY.

Although the majority of ablation occurs in the summer months (Wagnon et al., 2013), the MB modelling showed evidence of ablation occurring in the pre-monsoon and post-monsoon. Therefore mean temperature and relative humidity for the mean elevation of the debris-covered tongue for the months of May until October for 2013-2015 were used to force the DADDI model (0.24°C and 74%, respectively). Ice surface temperature was assumed to be 0°C as with COSIPY. SW_{in} and LW_{in} were 241 and 253 W/m^2 and wind speed 1.7 m/s. The thermal conductivity of the debris layer was 0.98 W m^{-1} K^{-1}, taken from Rowan et al. (2017) which is also the mean of measurements taken across Khumbu Glacier by Conway and Rasmussen (2000). The albedo of debris and ice were 0.15 and 0.4, respectively (Inoue and Yoshida, 1980; LeJeune et al., 2013).

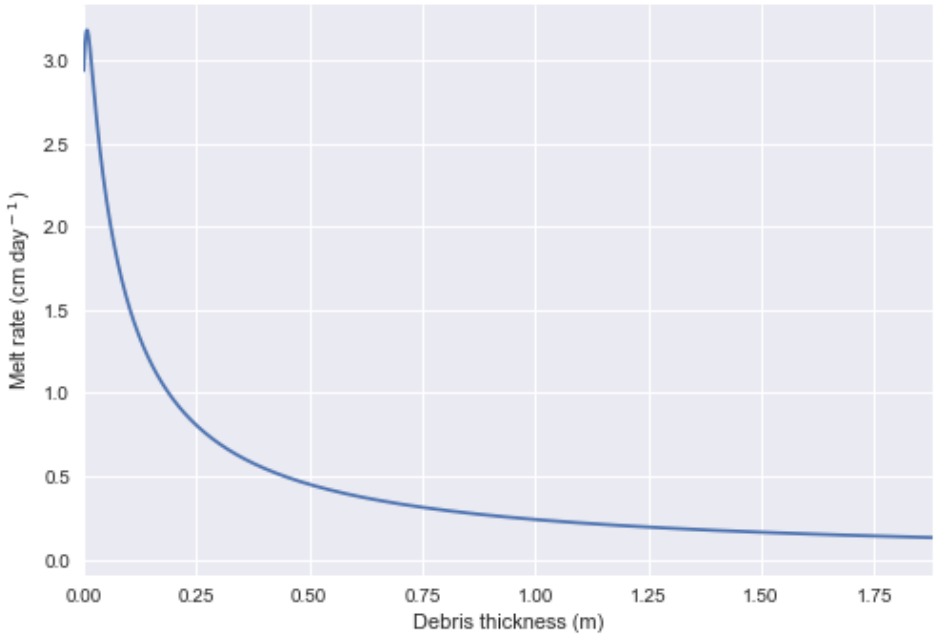

Figure 4.4 Modelled sub-debris ablation curve for Khumbu Glacier 2013-2015 using the "DADDI" model from Evatt et al. (2015).

4.3 Application to Khumbu Glacier

4.3.1 Weather station data

The period for the reference and sensitivity experiments is January 1st 2013 until December 31st 2015 (Figure 4.5). All meteorological data excluding precipitation used for the reference simulation were from the West Changri Nup (WCN) on-glacier AWS at 5,363 m.a.s.l; part of the glacioclim network (Table 4.1). WCN is mostly debris-free, but the AWS is located on a small area of debris that is 21-26 cm thick, within the range of thicknesses measured on the upper tongue of Khumbu Glacier (Rounce et al., 2014, 2018; Rowan et al., 2015). The data are less intermittent than other nearby weather stations. The precipitation data were from the Pyramid precipitation gauge installed at 5,035 m.a.s.l.. This gauge provided a longer period of continuous data than the gauges used in the previous chapter, and so was used in place of this dataset and study period.

The data were acquired from the glacioclim website run by Dr Patrick Wagnon (https://glacioclim.osug.fr/). For these stations there is clear explanation of the post-processing applied to the data, which is particularly important for interpreting patterns of precipitation. The temperature was adjusted to match the height of the Geonor precipitation gauge (5,035 m.a.s.l., that is also part of the glacioclim network) using hourly LRs that averaged 0.00554°C/m. The model was run for both elevations using the non-adjusted temperature data (for 5,336 m.a.s.l.) and the adjusted

temperature data (for 5,035 m.a.s.l.) and it made little impact on model results. Up to 13% of the WCN temperature records were missing. Missing data were replaced by interpolating Pyramid AWS data from the SHARE network (http://geonetwork.evk2cnr.org/) and the same LR as above. The interpolated results were compared with preceding/succeeding periods from the same AWS and months. Data available from November 2014 from the debris-covered north Changri Nup AWS (5,470 m.a.s.l., also from the glacioclim website) were also used for comparison with the interpolated data. Higher elevation distributed data are compared with measurements from Camp II (6,464 m.a.s.l.) and South Col (7,945 m.a.s.l.) (Matthews et al., 2020, available via https://www.nationalgeographic.org/projects/perpetual-planet/everest/weather-data/). Measurement periods in Table 4.1 show the data that had been released at the time of writing.

Precipitation was measured using a Geonor T-200BM sensor mounted 1.8 m above the surface, and logging at 15-minute intervals. Evaporation from the bucket is supposedly blocked by a layer of oil but still occurs, as evidenced by values below 0 mm. Noise from wind and evaporation were corrected by compensating any negative change over the 15-minute time step with the neighbouring positive value (and so accumulated precipitation was unchanged). Periods with prolonged evaporation were set to zero. Undercatch due to snowfall was corrected through precipitation phase partitioning and mostly through wind speed (Forland et al., 1999; Wagnon et al., 2009). Snowfall can be given as an input to the model, yet given the high degree of uncertainty both from *in situ* data and climate reanalysis and modelled products for this region, the total precipitation was partitioned using the scheme shown in Figure 4.3 instead.

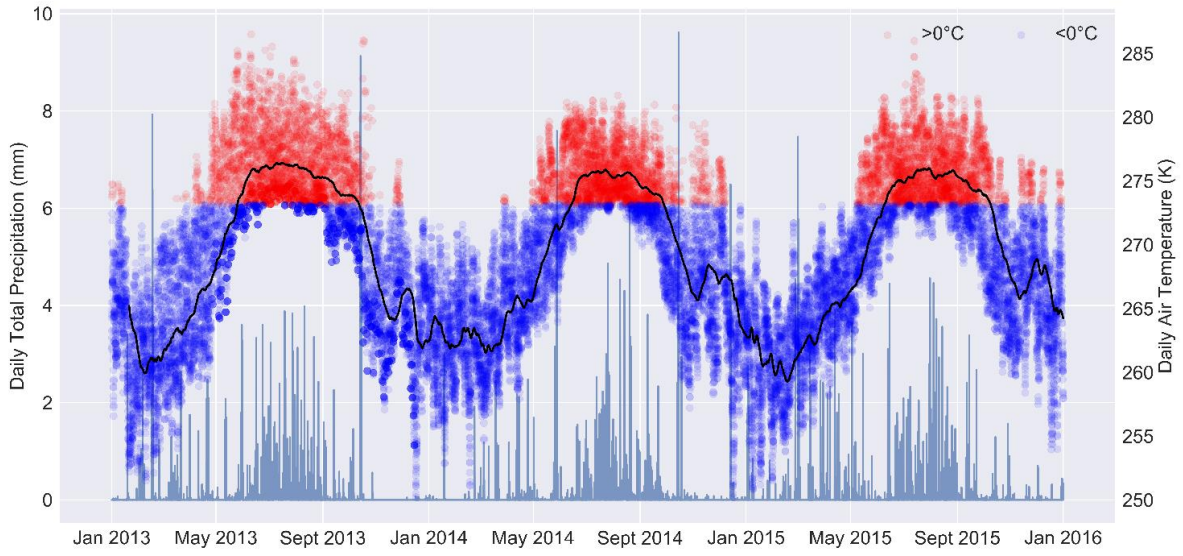

Figure 4.5 Daily total precipitation and hourly temperature with 20 day running mean in black, and of period for reference run. Temperatures above freezing (273.15 K) are coloured red, and those below coloured blue. Other meteorological forcings for this reference period are shown in Figure A1.

AWS	Elevation (m.a.s.l.)	Lat/Lon	Measurement period	Parameters	Purpose	Source
Pyramid_1	5050	27.990°N 86.829 °E	2002-2019 (intermittent)	T, RH, Pressure, u, wind direction, Prec. Snowfall K↓, K↑, L↓, L↑	LR calculation to match WCN T to Pyramid_2 Infilling of WCN temperature records	http://geonetwork.evk2cnr.org Salerno et al. (2015)
Pyramid_2	5035	27.95888 °N 86.81361°E	Dec 2012 - Nov 2016	Prec	Model input for reference simulation	https://glacioclim.osug.fr/Donnees-himalaya Wagnon et al. (2013) Sherpa et al., (2017)
West Changri Nup	5363	27.983237°N 86.7791°E	Dec 2010 - Nov 2019	T, RH, Pressure, u, wind direction, K↓, K↑, L↓, L↑	Model input for reference simulation	https://glacioclim.osug.fr/Donnees-himalaya Wagnon et al. (2013) Sherpa et al., (2017)
Camp II	6464	27.9810°N 86.9023°E	May 2019 - Nov 2019	T, RH, Pressure, u, wind direction, K↓, K↑, L↓, L↑	High elevation validation	https://www.nationalgeographic.org/projects/perpetual-planet/everest/weather-data/ Matthews et al. (2020)
South Col	7945	27.9719°N 86.9295°E	May 2019 - Nov 2019	T, RH, Pressure, u, wind direction, K↓, K↑, L↓, L↑	High elevation validation	https://www.nationalgeographic.org/projects/perpetual-planet/everest/weather-data/ Matthews et al. (2020)

Table 4.1 AWS data used as inputs of reference simulation and interpolated meteorology.

4.3.2 Static surface data

A 30 m digital elevation model (DEM) was acquired from the Shuttle Radar Topography Mission (SRTM) (Farr et al., 2007). The DEM was degraded for experiments with coarser spatial resolution. Aspect and slope were calculated from the DEM using Python programming packages gdal, rasterio and xarray. Glacier outlines were from the Global Land Ice Measurement from Space (GLIMS) Randolph Glacier Inventory (RGI) version 6.0 released in 2017 (Arendt et al., 2015). The outline of Khumbu Glacier represents ice extent in 2018 and has an area of 26 km^2. It clearly shows the detachment of the glacier from the debris-covered terminus of the tributary Changri Nup glacier.

The Changri Nup and Changri Shar outlines were from the same source with a combined area of 13.95 km^2 and marked in grey (Figure 4.6). The mass balance of these two glaciers was also modelled to assess the performance of COSIPY compared to observations (Figure A4), though focus is on Khumbu Glacier. It should be noted that the Changri Nup/Shar glacier outlines are known to be erroneous for this period. In reality, the debris-free West Changri Nup is disconnected from the debris-covered Changri Nup glacier (Vincent et al., 2016 and Sherpa et al., 2017). However, several studies (Bolch et al., 2011 and Bocchiola et al., 2020) have used this GLIMS outline and so for comparitive reasons this outline is used. Equally, as the simulations are included only briefly, simply to aid model evaluation through comparison with point measurements, the total glacier area is not important. The outlines are treated as boolean masks within the model.

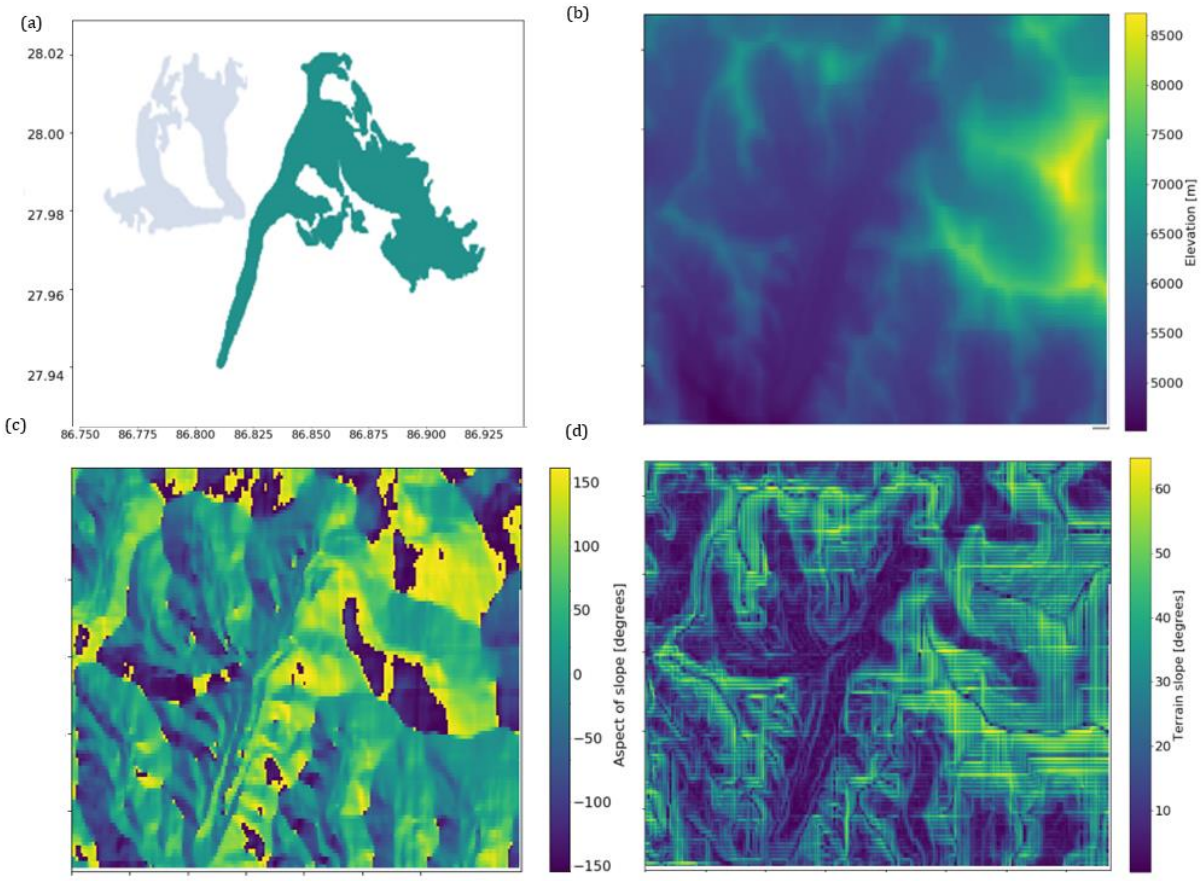

Figure 4.6 Static surface files for distribution of meteorology: (a) Khumbu Glacier mask (green) and Changri Nup and Changri Shar (grey), (b) height of terrain, (c) aspect of slope and (d) slope of terrain).

4.3.2.1 Debris thickness data for sub-debris ablation correction

Debris thickness estimates on Khumbu Glacier include those made manually (Soncini et al., 2016), those simulated by ice flow models such as iSOSIA (Rowan et al., 2015, 2021) and those using a combined thermal satellite imagery and melt modelling approach (Rounce and McKinney, 2014 and Rounce et al., 2018). Debris thicknesses derived by Rounce and McKinney (2014) were found to be under-estimated when compared with *in-situ* measurements (Nakawo et al., 1986), due to difficulties parameterising fluxes and temperature gradients within the debris layer. Also, ice cliffs and/or meltwater ponds can exist within the same pixel as thick debris, thereby reducing the surface temperature and the measured debris thickness. For this reason, debris thicknesses estimated using an inverted sub-debris ablation model and elevation change derived from DEM differencing were used (Rounce et al., 2018; Figure 4.7). The sub-debris ablation correction using these 600 m bands will not produce high resolution mass balance estimates, but the improved

consistency of this dataset relative to that of Rounce and McKinney (2014) will aid validation of COSIPY following the clean-ice mass balance sensitivity analysis.

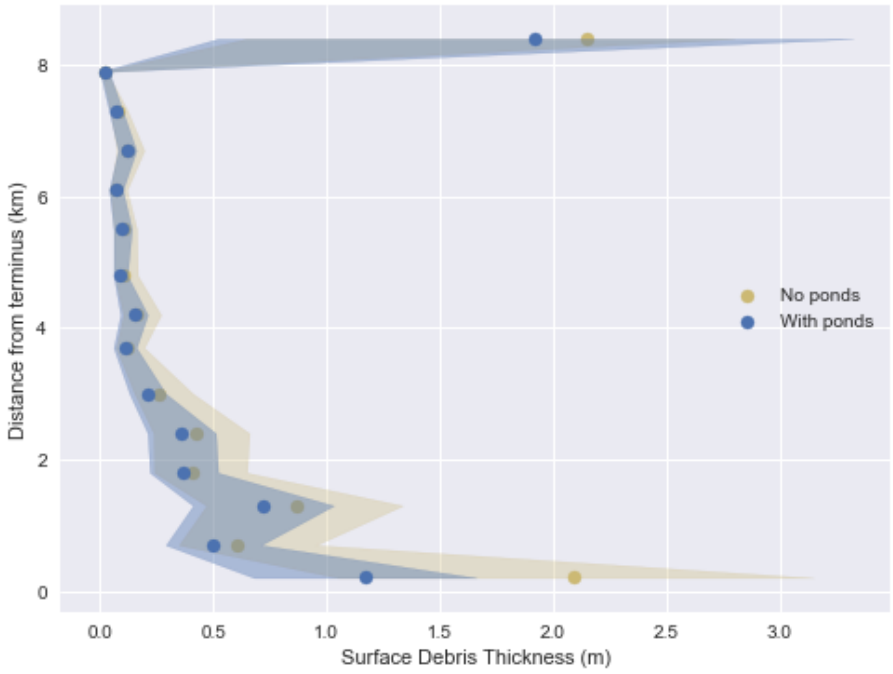

Figure 4.7 Mean and standard deviation of estimated debris thickness of centrepoint of each band as a function of distance from the glacier terminus (yellow) and the same but including supraglacial ponds and ice cliffs (blue). Data from http://doi.org/10.5281/zenodo.120620.

4.4 Sensitivity experiments

4.4.1 Reference Simulation

The reference simulation is run from 2013-2015. Temperature and precipitation are distributed from the elevation of the Pyramid gauge (5,035 m.a.s.l.; section 4.3.1) using linear LRs for distribution across the domain (Table 4.2). The temperature LR represents the calculated mean from all stations in the Ev-K2-CNR network, as in Figure 3.9 (Chapter 3) but for the measurement period used within this Chapter.

For the purpose of model evaluation for this Chapter, the precipitation LR (0.00001% per km) was calculated from observed accumulation rates from Sherpa et al. (2017) and Inoue (1977). This method is of course based on the assumption that the sole source of accumulation is through direct precipiation onto the glacier surface. In reality, avalanching is estimated to contribute to accumulation rates by 66-75% (Benn and Lehmkuhl et al., 2000; Rowan et al., 2015). This process is not represented in COSIPY and is challenging to quantify (Laha et al., 2017). The distribution of

precipitation in this simplistic, linear way was purely conducted to aid validation of the spatially-averaged simulated mass balance, though the precipitation LR used is very weak, which is the case for those found across this region (Ageta and Higuchi, 1984). Validation of precipitation LRs for the elevation range of Khumbu Glacier is not possible, with precipitation observations above 5050 m.a.s.l. absent. It is therefore assumed that precipitation LRs remain weak, and for the purpose of the modelling studies for this Chapter, slightly positive with elevation.

The glaciological constants used in this reference simulation are included in Table 4.3.

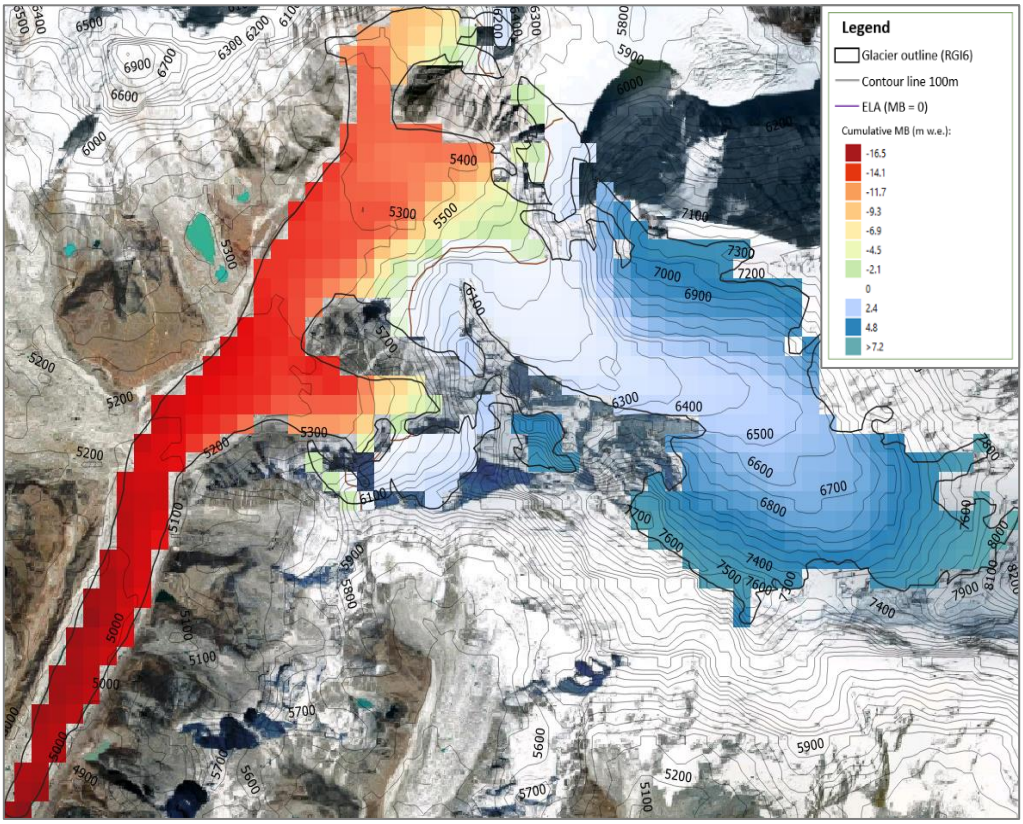

Figure 4.5 Reference run at 200m spatial resolution.

The glacier-wide clean-ice mass balance across Khumbu Glacier for this period is -3.4 m w.e which equates to -1.13 m w.e a^{-1}. The area of maximum ablation located on the tongue of the glacier show cumulative melt rates of up to 16.23 m w.e. for the reference period. Ablation is set in motion in May (the pre-monsoon) (Figure 4.9 and 4.10). High precipitation events (Figure 4.6) can be seen in the accumulation record, and if they occur outside of the summer months can offset some of the ablation (as in October 2013 and May 2014; Figure 4.10). Higher minimum temperatures in the winter of 2013/14 relative to the other winters did not influence accumulation rates, which are similar to those of 2014/15. The reduced precipitation in the monsoon months of 2015 (286 mm total compared to 330.8 mm and 333.9 mm for 2013 and 2014, respectively) led to

lower accumulation in the upper reaches of the glacier. The 2015 monsoon was 10% drier than the average monsoon total for the 2009-2015 period of 329 mm (using data from Sherpa et al., 2017 and Chapters 3 and 5).

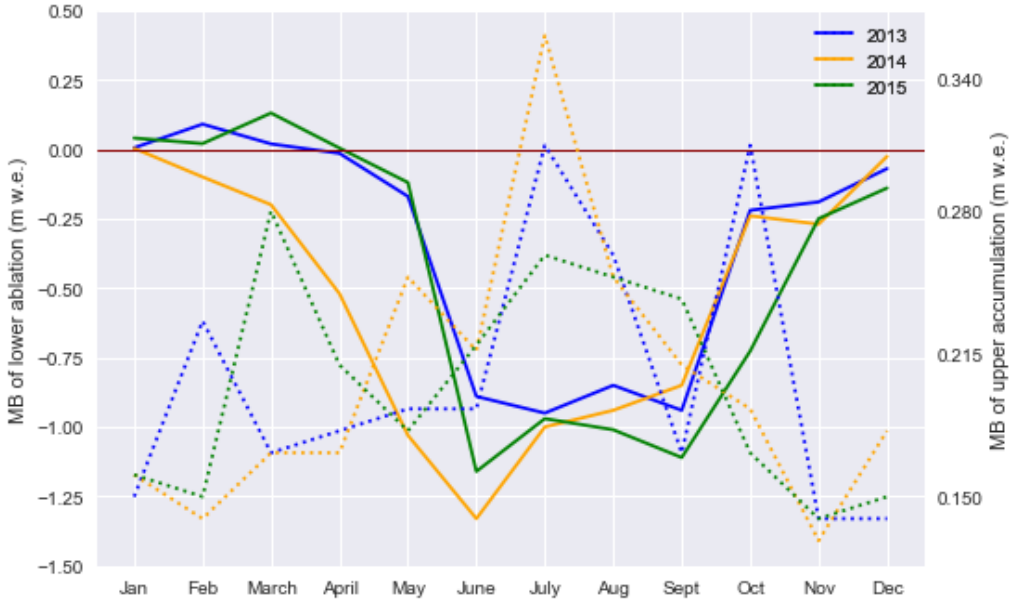

Figure 4.6 Monthly mass balance sums of lower ablation area (solid line) and of the upper accumulation area (dotted line). The threshold between ablation and accumulation (0 m w.e.) for the lower ablation zone is marked with a dark red line. Note different y axes scales for ablation vs accumulation.

Lapse Rate	Value	Unit	Source
T	-0.00554	K per m	Ev-K2-CNR network
Precip	0.00001	% per m	Accumulation measurements of Mera (Sherpa et al., 2017) Inoue (1977)
RH	-0.002	% per m	Calculated from Ev-K2-CNR network and validated with Nat Geo network

Table 4.2 Lapse rates for meteorology distribution for reference run.

Parameter	Value	Unit	Source
$\alpha_{freshsnow}$	0.85	-	Mölg et al. 2012 and Changri Nup measurements (Chapter 3)
α_{firn}	0.6	-	Oerlemans and Knap, 1996 and Mölg et al. 2012
α_{ice}	0.3	-	Mölg et al. 2012
t^*	20	days	Mölg et al. 2012
d^*	1.0	cm	Mölg et al. 2012
Z_{0snow}	0.24	mm	Gromke et al., 2011
Z_{0firn}	4.0	mm	Brock et al., 2006
Z_{0ice}	1.7	mm	Brock et al., 2006 and Cullen et al., 2007
Z_0 ageing length (linearly from z_{0snow} to z_{0firn})	60	days	Mölg et al. 2012

Table 4.3 Glaciological constants used for reference run. The albedo values are widely used within the literature. Z_0 values are less well parameterised, and in reality there is high spatial variability on clean-ice but particularly debris-covered glaciers (discussed further in section 4.4.4).

4.4.1.1 Initial conditions

Simulated mass balance is highly sensitive to initial snow depth conditions, shown by three sensitivity experiments using initial snow depths of 0, 0.5 and 1 m (Figure 4.10). The cumulative mass balance and absolute values are similar until May 2013 where the increased temperatures with the pre-monsoon bring significant mass loss for the experiment with 0 m of initial snow depth. The maximum ablation difference is 1.05 m w.e. a^{-1} between experiments with initial snow depths of 0 and 1 m. The impact of differing initial snow depths on the maximum accumulation are minimal yet is considerable for ablation rates and glacier-wide cumulative mass balance. Despite the overall high sensitivity of glacier mass balance, the temporal and spatial variability of snow depth remains poorly constrained in the Himalaya.

Figure 4.7 Cumulative mass balance of three experiments using three different initial snow conditions.

As with total precipitation measurements across the HKKH, there is a paucity of snow depth measurements. The Pyramid AWS measures snow depth though measurements are highly intermittent. Fig A1 shows snow depth data from Pyramid for 2009-2015 taken from Rounce et al. (2018). Assuming the January 2013 measurement is correct, the initial snow depth was low, at least for the lower glacier elevations. The first 6 weeks of 2013 received considerably higher snowfall than the preceding and succeeding years (Figure A2). The sum of total precipitation in January/February 2013 was also 105 mm at Pyramid, compared with 45 mm in the same months of 2014, and 26 mm of 2015. The few snow depth measurements that are available include those taken from a snow pit located at 5,601 m.a.s.l. on West Changri Nup Glacier on 4 May 2014, where snow depths of up to 0.2 m were measured (Bocchiola et al., 2020). Therefore 0.5 m is considered a reasonable estimate of initial snow depth that would also account for greater snow depths at higher elevations. An initialisation period of up to 1 year is found to be required for the subsurface module to adapt to local conditions. Therefore the first MB year (2013) is interpreted with caution, and focus is on the cumulative mass balance over the measurement period rather than specific years.

4.4.1.2 Spatial resolution

The simulated maximum accumulation rate does not change significantly with resolution (Table 4.5). The accumulation area located from 6,500 to 7,000 m.a.s.l. saw rates of 2.1 to 3.9 m w.e. over the study period. The 27 glacier points of the 1 km resolution simulation do produce a similar spatial mean MB to the finer resolution experiments (Table 4.5 and Figure 4.11). However, there are obvious gaps across the glacier, affecting the height of the ELA and significantly reducing the calculated maximum accumulation.

The 30 m resolution experiment produces remarkably similar results to the 50 m resolution experiment. Both of these finer resolution experiments capture greater spatial variability in mass balance relative to the 200 m resolution experiment, particularly below the ELA between 5200 and 5400 m.a.s.l. (Figure 4.8 against Figure 4.12). The coarser resolutions fail to capture variability that does not result from elevation. However, given that the height of the ELA and the modelled maximum and minimum mass balances are not significantly different, the 200 m resolution experiment is adopted for use in the sensitivity studies, benefitting from much reduced computational expense.

Experiment resolution (m)	ELA height (m.a.s.l.)	Max Accumulation (m w.e.)	Max Ablation (m w.e.)	Spatial average MB (m w.e.)	Simulation time (hours)
30	5838	7.221	16.33	-2.09	62
50	5835	7.221	16.29	-2.02	33.5
100	5810	7.31	16.25	-2.22	11.5
200	5790	7.477	16.23	-2.12	2.7
1000	6050	3.7	14.57	-2.2	0.61

Table 4.4 Glacier mass balance characteristics with different spatial resolutions. Simulation time is the sum of the pre-processing (the distribution of meteorology across the domain) and the core mass balance simulation.

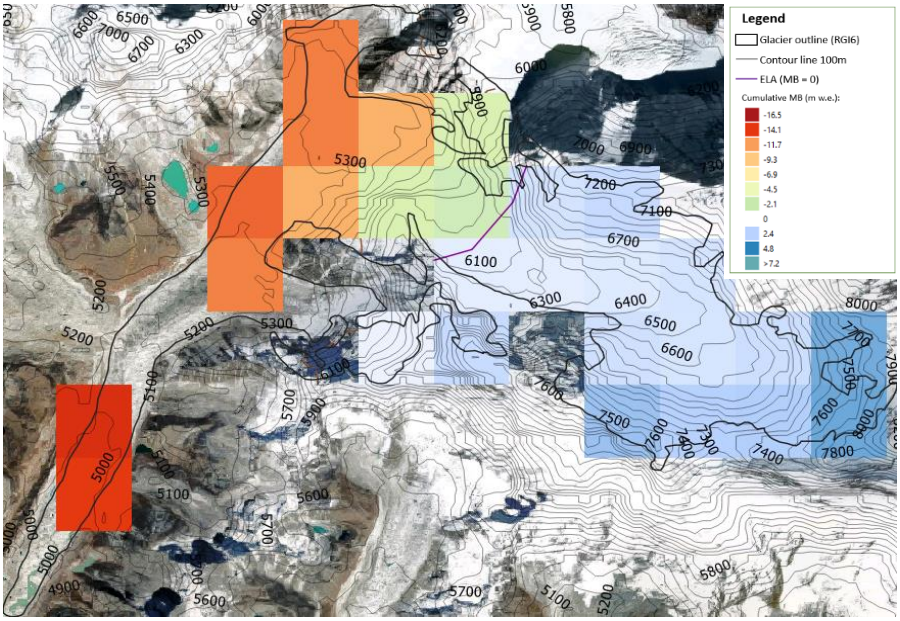

Figure 4.8 1km resolution reference simulation

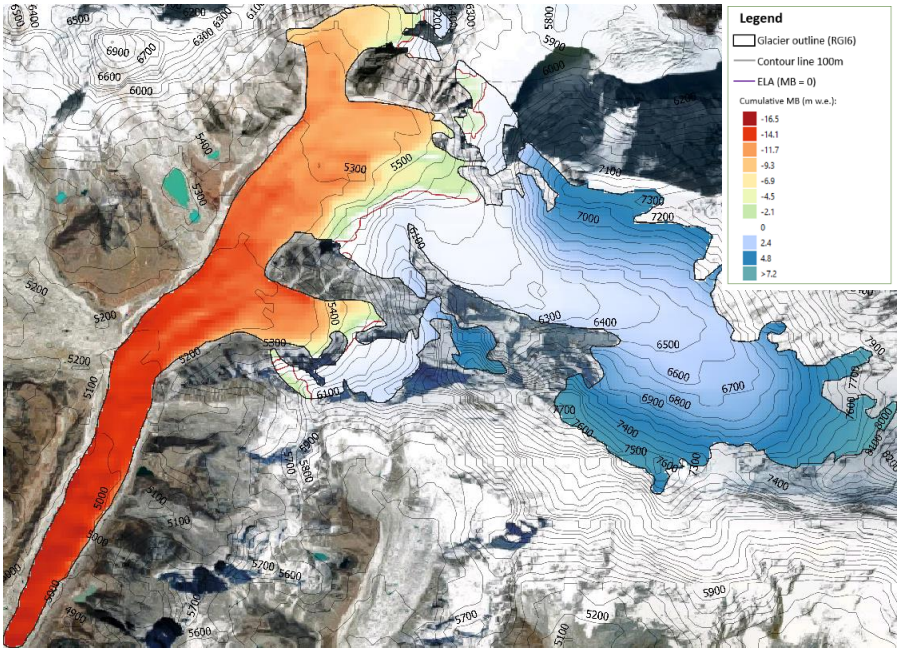

Figure 4.9 30 m resolution reference simulation

4.4.1.3 Energy flux and melt components

The contribution of the components to the SEB is investigated at five points along the glacier centreline (Figure 4.13a) and varies substantially in both absolute values and seasonality. Net shortwave radiation (Q_{SW}) contributes the largest energy input to the surface at the lower elevation sites, and is the SEB component that correlates most strongly with Q_{melt} (with a mean correlation coefficient of 0.79). The high temporal variability relates to varied cloud cover exhibited in the hourly SW_{in} forcing and fluctuating albedo during the warmer months with the melting of the snowpack. Q_{SW} is especially low at higher elevations. The high SW_{in} in the upper reaches indicate this low Q_{SW} is not through topographic shading. Q_{SW} is correlated with albedo (r=0.86, not shown), and the persistence of snow throughout much of the year will reduce Q_{melt}. Modelled SW_{in} matches closely to observations (Figure A3) indicating the radiation model performs fairly well despite the extreme terrain. Net longwave radiation (Q_{LW}) also contributes to Q_{melt} as the pattern of both fluxes correspond. At EB5950, EB6480 and EB7910 (Figure 4.13a), Q_{LW} sometimes rises above zero during the monsoon, most likely from heavy cloud cover and increased temperatures relative to the glacier surface. Q_{lat} is almost zero at the lower elevation sites as the arrival of the monsoon brings higher RH, and this pattern is similar but dampened at the higher elevations. At site EB7910, Q_{melt} correlates exactly (r=1) with the sensible heat flux.

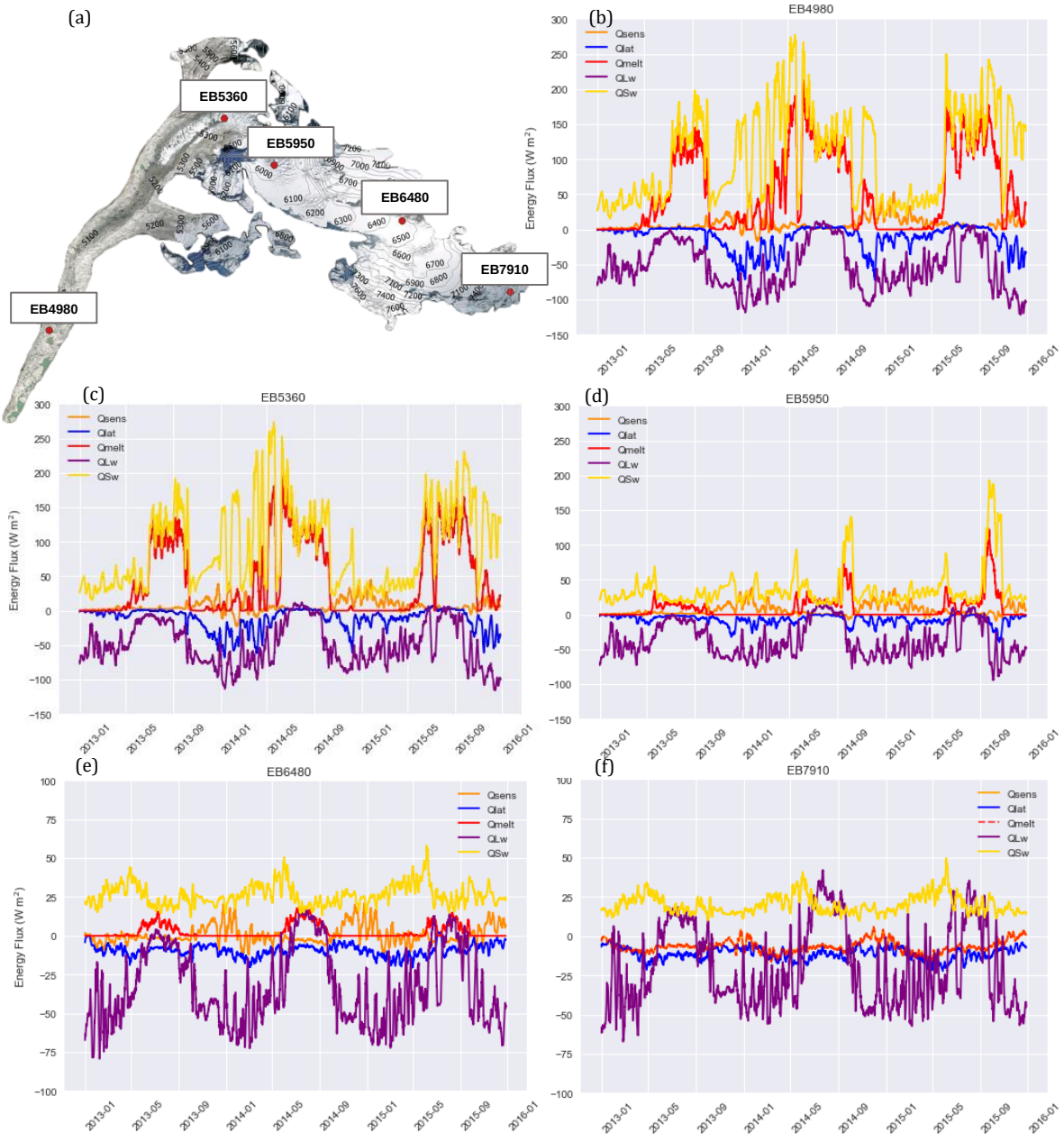

Figure 4.10 (a) Locations of energy balance (EB) points used for energy flux and melt components analysis (named after corresponding altitude e.g. EB6480) and (b-f) 5-day average of energy fluxes across study period for each site. Note that scales are different for (e) and (f) compared to (b)-(d) due to the marked difference in absolute values.

The energy available for ablation peaks in the pre-monsoon and monsoon, bringing higher rates of sublimation and subsurface melt (Figure 4.14a, b). Modelled sublimation occurs at all elevations, with the highest cumulative loss at EB7910 near to South Col where sublimation dominates (Figure 4.14a). Sublimation rates are increasingly tied to seasonality down-glacier, with rates at site EB4980 located on the lower section of the tongue increasing from April until the start of the monsoon in July. At EB7910 sublimation only slightly slowed from December until May. Subsurface melt at or above the ELA (5,950 m.a.s.l) is negligible. At the lower elevations sub-surface melt dominates, with a stronger seasonal cycle related to surface temperatures. The interannual variability in subsurface melt is tied to surface temperatures, though low simulated subsurface melt rates in the first year are likely largely due to the initial snow cover persisting, shielding the subsurface from surface temperatures until the subsurface adapts to local conditions (as discussed in section 4.4.1). Refreeze (Figure 4.14c) occurred at all sites and the onset was staggered with increased elevation, though for all sites absolute values were low. The higher Q_{lat} with the monsoon brings higher deposition to the glacier at the lower elevations, with negligible rates at higher elevations. Similar absolute values and patterns are seen for condensation (not shown).

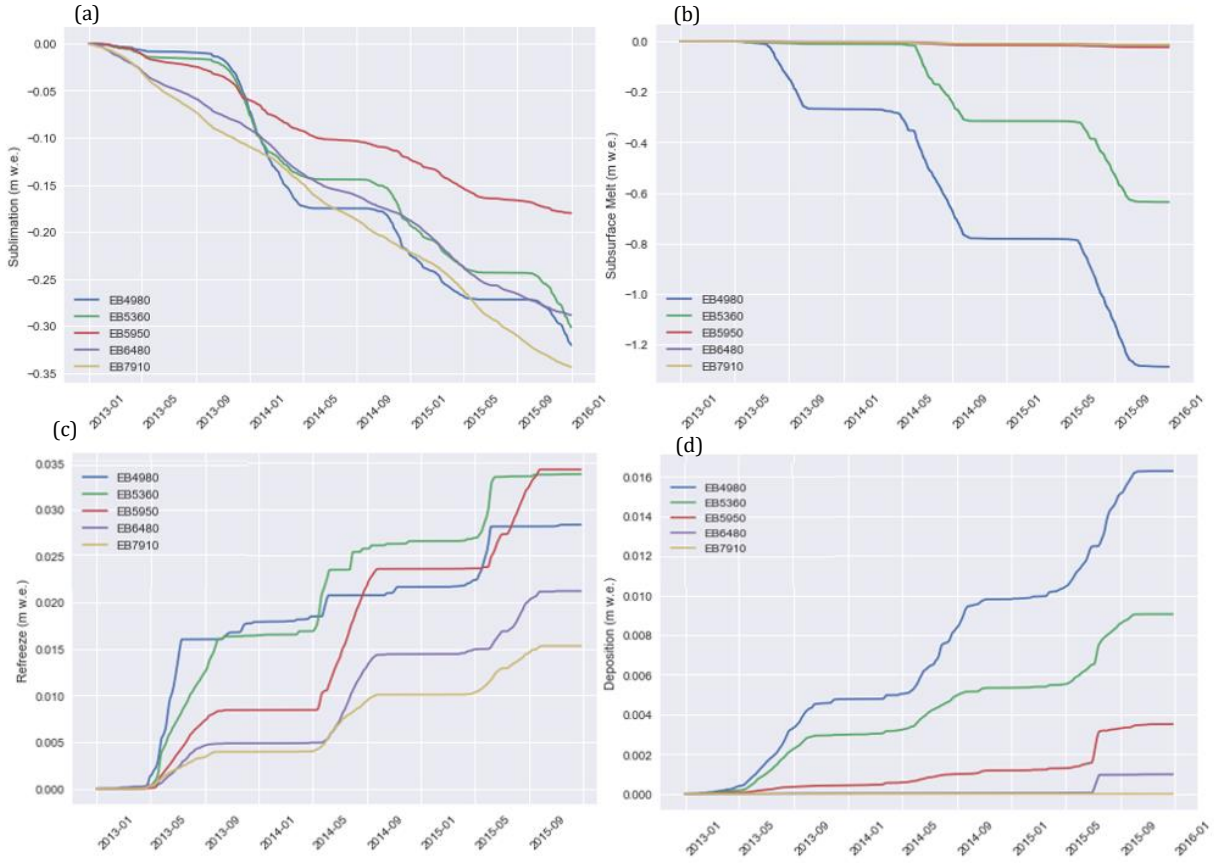

Figure 4.11 5-day averages of (a) Sublimation, (b) subsurface melt, (c) refreeze and (d) deposition for the 5 EB sites across Khumbu Glacier. Note different y-axis scales.

4.4.2 Atmospheric forcing perturbations

4.4.2.1 Parameter perturbation

The coupled parameter testing (Figure 4.15) involved perturbing precipitation and temperature simultaneously. Perturbations are within the range of possible uncertainty that may stem from a combination of observations, climate models, downscaling approach or distribution of meteorology. The temperature and precipitation positive perturbations are comparable in magnitude to possible future climate forcings (Table 2.3; Kraaijenbrink et al., 2017; Sanjay et al., 2017b; Kaini et al., 2019; Chapter 5). The most significant change in spatially averaged MB follows a 3°C increase in temperature and 20% decrease in precipitation, which is not reflective of current end-of-century climate projections for the region (Table 2.3). The perturbation that best matches the scenarios outlined in Table 2.3 (1.5°C increase in temperature and 10% increase in precipitation) leads to a MB change of -0.6 m w.e. (38% higher mass loss than the reference simulation). The ablation following an increase in temperature of 1.5°C is fully compensated by the accumulation from 20% higher precipitation. The implications of this are discussed further in Section 4.6.2.

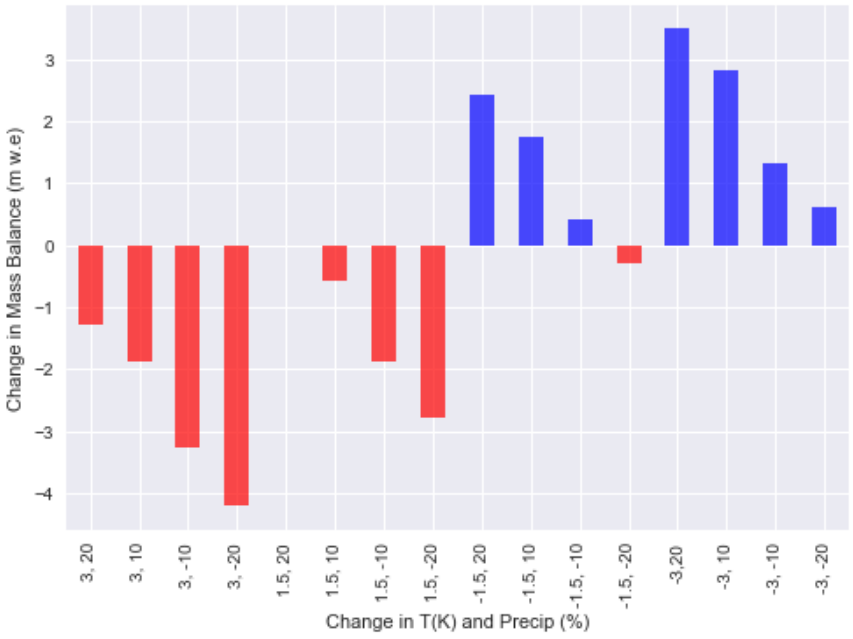

Figure 4.12 Coupled parameter testing of temperature and precipitation for reference period.

4.4.2.2 Snow/rain partitioning

Accurate estimation of precipitation phase is of great importance for summer-accumulation type glaciers. Threshold values of air temperature are often used to separate liquid and solid precipitation. Previous work has calculated threshold temperatures across 6883 stations in the Northern Hemisphere, finding an average threshold value of 1°C, and 95% of observations falling between 0.4 and 2.4°C (Jennings et al., 2018). Although there remains a lack of data for the HKKH, this study also found that high mountain areas have the highest thresholds (up to 4.5°C on the Tibetan Plateau). Other studies have used 2°C for Patagonian glaciers (Rivera, 2004, Koppes et al., 2011; Bravo-Lechuga et al., 2019).

The impact of two different precipitation partitioning schemes on glacier MB is investigated. Here, threshold temperatures of 0.5, 2 and 3.5°C are chosen and compared with the default STF (outlined in section 4.1.1.), and a final scheme that smoothly scaled from 100% solid precipitation at -1°C to 0% solid precipitation at 4°C was also tested.

Scheme	Temperature (°C)	MB change (m w.e.)
Threshold	0.5	-2.51
	2	-0.77
	3.5	+1.01
Smooth scale	-1 to +4	+0.22

Table 4.5 Snow/rain partitioning schemes, median temperatures and resultant MB change for the study period.

The marked impact of snow/rain partitioning schemes on glacier-wide MB is also found for Patagonian glaciers (Bravo-Lechuga et al., 2019) where point-based calculations diverged by up to 3.5 m w.e. depending on the chosen scheme. This highlights the need for future work to investigate the appropriate scheme for the HKKH (which are currently lacking) to ensure that mass balance calculations are accurate to allow comparisons between studies. In the absence of this data, the original scheme by Weidemann et al. (2018) is used for mass balance modelling both within this Chapter and Chapter 6.

4.4.3 Temperature distribution

The sensitivity of the cumulative MB to different LRs is tested at 200 m resolution (Figure 4.16) using the LR values given in Table 4.6. These LRs are calculated using the same method in Chapter 3 (Figure 3.9) for all available stations in the Ev-K2-CNR network for the 2013-2015 study period,

and with the same seasonal/diurnal split (i.e. 8am until 4pm and for day and 8pm until 4am for night to account for changing sunrise/sunset times and topographic shading).

Experiment	LR (K per km)		Source
Reference	-5.54		AWS network (2013-2015)
ELR	-6.5		Meteorological standard (Thayyen and Dimri, 2018)
Diurnal	Day	- 5.9	AWS network (2013-2015)
	Night	-5.18	
Seasonal	Monsoon	-4.84	AWS network (2013-2015)
	Non-monsoon	-5.78	
Dayseas	Monsoon Day	-5.5	AWS network (2013-2015)
	Monsoon night	-4.16	
	Non-monsoon day	-5.99	
	Non-monsoon night	-5.37	

Table 4.6 LRs used to distribute temperature across the model domain, and sources from which they were calculated. These are close to those measured in Chapter 3 but for the study period used in this Chapter.

The seasonal LR yields a spatially averaged mass balance that is -5.6% relative to the reference, and the diurnal LR mass balance is only -0.45% (as the reference LR is close to the mean of the day/night LRs; Table 4.6). The experiment where temperature is distributed by time of day and season (dayseas) produces a MB 5.98% lower than the reference, whereas the MB for the simulation using the ELR was 1.24% higher. This is likely due to the high elevation of the accumulation area being below 0°C for much of the year, meaning the effects of the steeper LR do not propagate to these upper reaches. The tongue of Khumbu Glacier is at an elevation close to that of the reference station (Pyramid) from which the meteorology is distributed, and so experiences less change with varying LR.

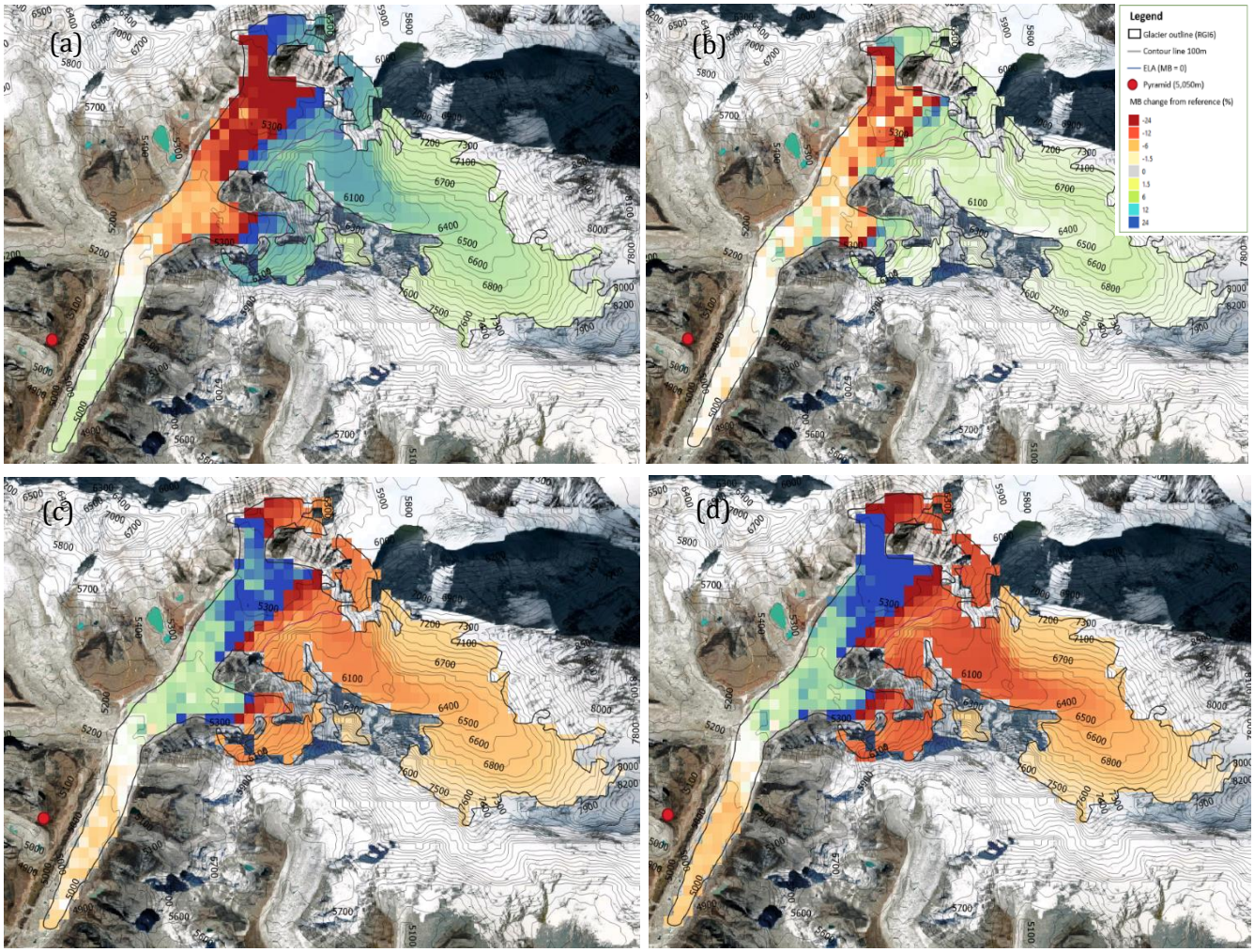

Figure 4.136 : Percentage difference of modelled glacier mass balance using (a) the ELR, (b) diurnal, (c)seasonal and (d) diurnal/seasonal lapse rates. The Pyramid AWS is shown by the red circle, though the temperature is interpolated from this elevation (5,035 m.a.s.l.), not necessarily this location.

For all LR experiments, the largest difference from the reference measurement is located just below the ELA (up to ±24%). The position of the ELA between experiments does not change with different LR forcing, most likely as the horizontal deviation in ELA position is no greater than the 200m grid-spacing.

The height of the 0°C isotherm during months that experience significant ablation (May - September) fluctuates around 5,125-6,250 m.a.s.l. (Figure 4.17), which correlates with the elevations that also experience the greatest MB change with different LR forcings. Though LRs used to distribute temperature do not have a significant impact on glacier-wide MB, the elevation of the 0°C isotherm from the pre-monsoon until the end of the monsoon is highly sensitive to temperature distribution.

The installation of the National Geographic weather stations in 2019 provided an opportunity to examine temperature LRs at higher elevations of the glacier. For the period (April to November 2019) the LR measured between Camp II and South Col (5.36°C km) is similar to the LRs used here (5.38°C per km). LRs measured between Phortse (3,810 m.a.s.l.) and Basecamp (5,315 m.a.s.l.) were 4.68°C per km. The LR measured between the two highest weather stations (South Col and Balcony), are on average 1.2°C per km higher than those measured between stations below 5,600 m.a.s.l.. This indicates that LRs in high elevation, glacierised sections may be better represented by LRs suitable for the free atmosphere (the ELR).

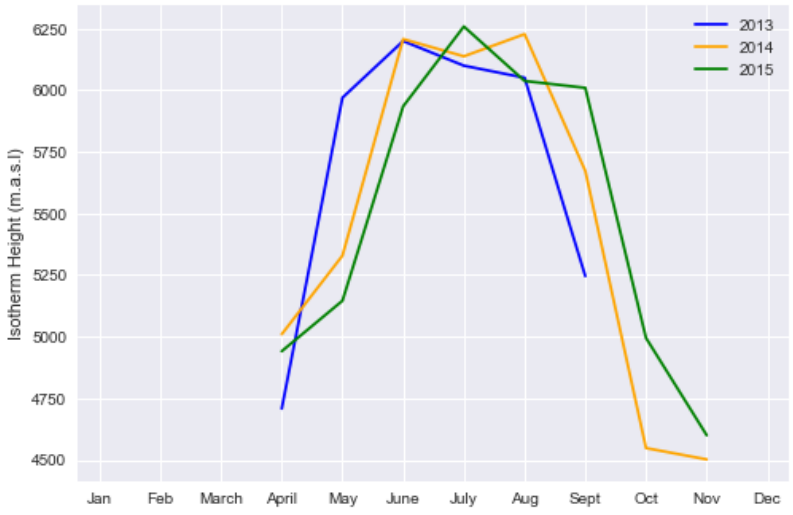

Figure 4.147 Height of freezing isotherm (monthly mean) over measurement period. During the winter the isotherm is located outside of model domain (at lower elevations).

The low sensitivity of modelled mass balance to varying temperature lapse rates contrasts with findings for Yala glacier in the Langtang region where different LR forcings caused differences in simulated glacier ablation of up to 400% (Immerzeel et al., 2014). As Khumbu Glacier spans a large elevation range with a smaller section along the 0°C isotherm relative to glaciers like Yala, the lower sensitivity of the glacier-wide mass balance to temperature LRs is perhaps not surprising.

4.4.4 Glacier parameter perturbations

The glacier ice surface roughness (z_0) is defined as 1.7mm for the reference simulation (Table 4.4), which is a reasonable estimate for clean-ice glaciers (Mölg et al., 2012). The z_0 values reported within the literature vary widely even for clean-ice glaciers, and so two substantially different z_0 values are used. Values of 0.1 mm were measured at Midtre Lovénbreen, Svalbard (Irvine-Fynn et al. 2014) and August-One glacier, China (Guo et al., 2018), and of 6.9mm on the clean-ice section of the Haut Glacier D'Arolla (Brock et al., 2006) and Laohugou Glacier No. 12 (Sun et al., 2018). These values are adopted as endmembers of the likely range in z_0 values. Overall, adjusting z_0 has minimal impact on glacier mass balance (Figure 4.18), though a higher (lower) z_0 did result in slightly increased (decreased) mass balances. The response is not proportional to the change in z_0, with a z_0 1.6 mm lower than the reference value leading to a similar mass balance change than that of the experiment with a z_0 5.2 mm higher than the reference value.

The albedo values of the three glacier components are perturbed by ±0.05 from that used in the reference experiment (e.g. 0.85 for fresh snow, used widely within the literature). There is a strong response of the glacier mass balance to changing snow albedo. Reducing snow albedo by 0.05 led to a 65% reduction in MB of 2.21 m w.e. (Figure 4.18). Ablation (accumulation) rates were 3.7 m w.e. (1.75 m w.e.) higher relative to the reference simulation for this perturbation. This further supports the importance of Q_{SW} to ablation rates. Varying albedo values for firn and ice revealed a lower sensitivity of glacier MB relative to snow albedo.

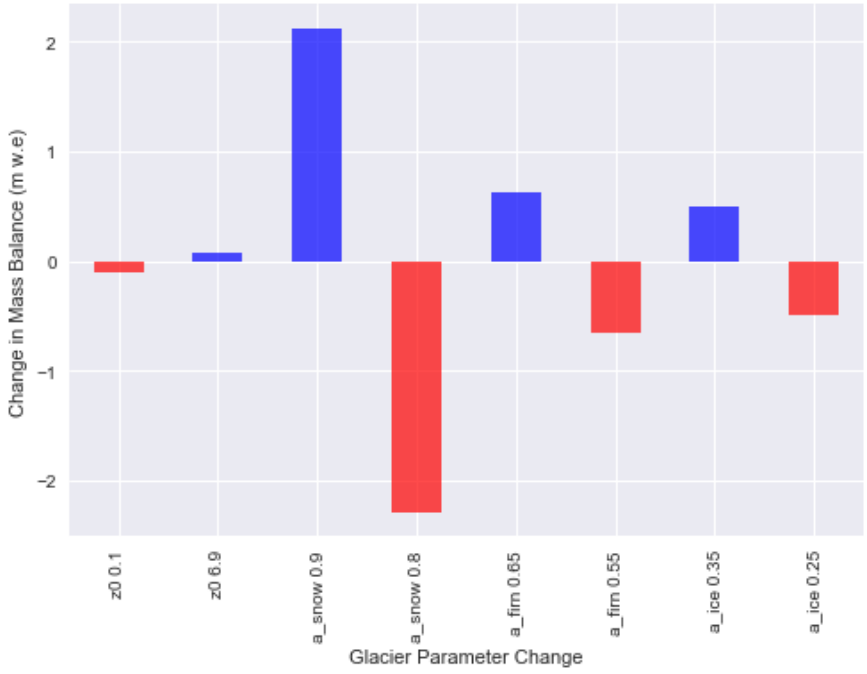

Figure 4.158 Sensitivity of mass balance for the reference period to changing glacier parameters (surface roughness, and albedo of snow, firn and ice).

4.5 Model validation

Model evaluation is a necessary step to ensure that COSIPY is appropriate for Khumbu Glacier MB calculations prior to integration with the ice-flow model in Chapter 6. This is challenging as COSIPY does not resolve two glacier components that are critical for Khumbu Glacier mass balance: sub-debris ablation and avalanching.

Khumbu Glacier is split into two sections to aid validation of this complex glacier. Changri Nup Glacier is also considered to assess the performance of COSIPY for the tributary glacier (A2).

4.5.1 Mass balance below the ELA

The clean-ice melt rate simulated with the DADDI model for May to October 2013-2015 is 3.2 cm/day (Figure 4.7). This agrees well with measurements made by Kayastha et al. (2000) of 3.1 cm/day (from 21 May until 1 June 1999) and 2.6 and 2.5 cm/day from August 1956 (Inoue, 1977) and August 1978 (Inoue and Yoshida, 1980), respectively. The melt reduction curve (Figure 4.19) is similar to those measured on Khumbu Glacier by Kayastha et al. (2000) and from other HKKH glaciers, though direct measurements of melt beneath debris layers thicker than 50 cm are absent.

Following integration of the sub-debris ablation correction with the clean-ice MB model, the ablation rates across Khumbu Glacier are much improved, particularly when using the debris thickness estimates with ponds from the Rounce dataset (Figure 4.20) though differences between the two datasets are not substantial (not shown). The observed inverse mass balance with elevation is simulated, with the thick debris towards the terminus suppressing ablation by up to 90% (Figure 4.20). With the addition of the sub-debris ablation correction, the glacier-wide MB is -1.64 m w.e. for the study period, which equates to -0.546 m w.e. a^{-1}. This agrees well with measurements derived from DEM differencing from King et al. (2017) of −0.58 ± 0.19 m w.e. a^{-1} for 2000 and 2015. Modelled mass balance is slightly higher than those using lower resolution DEMs of −0.45 ± 0.52 m w.e. a^{-1} for the 2002-2007 period by Bolch et al. (2007).

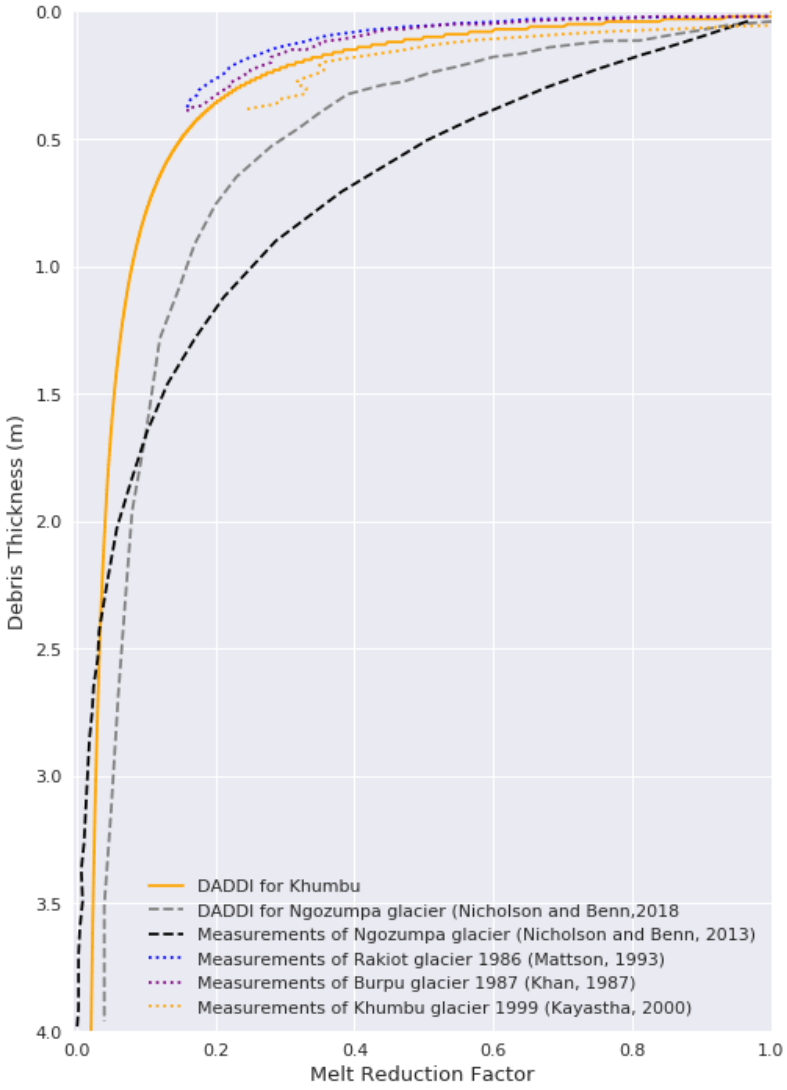

Figure 4.19 Comparison of simulated melt reduction from varying debris thickness produced here (solid orange line) with findings from other studies for other HKKH glaciers. Note measurements on Ngozumpa Glacier are extrapolated from observed suppression of melt of 50% under 50 cm of debris (as in Rowan et al., 2015).

The spatial distribution of ablation matches point measurements well, though it is likely that these ablation rates and the spatial distribution and thicknesses of debris have changed since the measurements in 1979 and 2000. The high ablation rates in the debris-free area just below the ELA were well replicated by COSIPY. The representation of these high ablation rates is important, as mass loss here is considered a critical component for present-day DCG mass loss (Benn et al., 2012). Experiments where temperature is distributed using the reference LR and the diurnal LR best matched observations. On-ice temperature measurements to improve estimates of LRs would be beneficial and may reveal that different LRs are required for temperature distribution across the debris-covered tongue compared with the clean-ice areas. This would likely improve simulated mass balance, particularly below the ELA where temperatures circulate around 0°C.

Figure 4.160 Simulated mass balance with correction for sub-debris ablation using the DADDI model as a function of elevation. Point observations from Inoue (1977) and Benn and Lehmkuhl (2000) are included to aid validation.

It is possible the ablation correction from the DADDI model is too significant, particularly compared to other curves such as those from Nicholson and Benn (2013, Figure 4.19). Ablation rates could differ by 40% under 0.25 m between these two corrections. When this curve was used to correct simulated mass balance with COSIPY, glacier-wide mass balance was -0.712 m w.e. a^{-1}.

Maximum debris thickness measurements by Rounce et al. (2018) match field measurements made by Nakawo et al. (1986). Debris thickness also increases with decreasing elevation as is seen in observations. However, it is possible that absolute debris thicknesses are underestimated in places (Rounce et al., 2018). This excludes the area immediately below the icefall (8.4 km from the terminus) where debris is ~1.5 m thick, an overestimation of ~1 m (Nakawo et al., 1986 and Rounce; McKinney et al., 2014). The anomalously thick debris here is considered by Rounce et al. (2018) to be an artifact of the flux divergence calculations through an absence of surface velocity data upglacier. This dataset was chosen as previous efforts substantially underestimate debris thickness (Rounce and McKinney, 2014) and debris thickness simulated using ice flow modelling is known to be slightly overestimated (Rowan et al. 2015). Despite these uncertainties associated with this dataset and the sub-debris ablation correction, the addition of this debris component to COSIPY has enabled validation of the simulated mass balance in the present day, which is critical for ensuring accurate initial conditions for future glacier modelling.

4.5.2 Mass balance above the ELA

Matthews et al. (2020) modelled total sublimation of 0.05 m.w.e. and 0.12 m.w.e. with data from Camp II (6,464 m.a.s.l.) and South Col (7,495 m.a.s.l) from May until November 2019. If these rates are extrapolated to a 3-year period, and assuming little seasonality as with the EB7910 sublimation rates shown here (Figure 4.14a), sublimation rates at South Col are twice as high as those modelled by COSIPY.

This is likely due in part to the assumed uniformity of wind speed across the domain in COSIPY. Wind speeds at high elevations will therefore be significantly underestimated; South Col AWS measured wind speeds of up to 21 m/s (Matthews et al, 2020). Simulated Q_{melt} was between 1-2 times higher at Camp II than the respective grid point in these simulations (Figure 4.13) and Q_{melt} was also 25 W/m^2 higher at South Col, whereas at EB7910 it remained close to zero. Different parameterisations of snow and ice albedo and decay were also likely responsible for these discrepancies.

The radiation model performs well (Figure A3) which is perhaps surprising given the extreme topography and solar insolation (>1,250 W/m^2 at times) of the upper reaches of the glacier, only recently revealed through the National Geographic weather station network.

Despite the low relative contribution of sublimation at high elevations to total glacier mass loss, the ability of COSIPY to parameterise this MB component is valuable and is an improvement to existing models that assume ablation can only occur if $T_{air} \geq 0$°C. The contribution of refreeze to overall MB has not been investigated for Khumbu Glacier prior to this study. Simulated refreeze is lower than expected, particularly given the significant subsurface melt at lower elevations (Figures 4.14b; 4.14c) and the anomalously high internal ice temperatures measured via borehole drilling that are indicative of latent heat release via refreeze (Miles et al., 2018a).

A weak precipitation gradient has been applied to Khumbu Glacier to match the few accumulation measurements available (1979 and 2000, Figure 4.20), and as avalanching is not treated by COSIPY which is thought to contribute substantially to accumulation. This approach enabled model evaluation, though it should be noted that accumulation high above the icefall is potentially overestimated with this method, though no observations exist to confirm this.

4.6 Discussion

4.6.1 Sources of uncertainty

The topographic and climatic complexity of the catchment produces high spatial variability in atmospheric forcings that are critical for glacier viability. Spatially distributed high-resolution climate data can give an insight into those variations, in a way which is not possible from individual weather stations. Distributing the meteorology with LRs is a simplistic approach, but is necessary in the absence of high resolution data that covers more than several months. Varying LRs did not significantly impact the spatially-averaged melt rates, though significantly affected rates around the 0°C isotherm. New high elevation weather station data supports use of a bespoke LR that accounts for the extreme atmospheric conditions (i.e. different to free atmosphere not affected by topography). As more data is released from this network, including from Balcony AWS (8,430 m.a.s.l) we will learn whether this is true for LRs at this elevation.

Ablation is perhaps overly suppressed in the lower reaches of the ablation area when simulated with the debris component compared with other measurements from nearby Ngozumpa Glacier (Figure 4.19). The coarse resolution of the debris thickness data from Rounce et al. (2018) means that the observed surface heterogeneity is not represented using this approach. Different parameterisations of differential ablation resulting from the increasing presence of ice cliffs and meltwater ponds are investigated in Chapter 6 (Brun et al., 2018; King et al., 2020).

It should be noted that geodetic mass balance observations used for model evaluation represent surface lowering which is a function of ablation (and/or reduced accumulation) and emergence velocities; the speed of ice uplift due to ice flux convergence (Nuimura et al., 2010; Vincent et al., 2021). Glacier-wide mass balance could therefore be more negative than these geodetic measurements, though emergence velocities are poorly constrained.

4.6.2 Implications

The varying spatial resolution experiments revealed that some detail was lost when modelling at 200 m (though this was necessary due to available computational resource). There was no added value for resolutions below 100 m, and so this was the chosen resolution for coupling with the ice flow model in Chapter 6.

Analysis of glacier mass balance seasonality demonstrates that melt is triggered in May, prior to the onset of the monsoon (Figure 4.11). Future climate projections indicate an increased likelihood of delayed monsoon onset, which would mean melt could continue unabated without any

mediating accumulation. With the 0°C isotherm reaching heights of 6,250 m.a.s.l. in the present day (Figure 4.10), it is likely that monsoon precipitation will more frequently fall as rain along the flat glacier tongue, even if warming is limited to 1.5°C. For this reference period, heavy precipitation events outside of the monsoon were seen in the simulated mass balance. Increased frequency of extreme precipitation events, inside and outside of the monsoon (Panday et al., 2015; Sanjay et al., 2018) may partially offset increased pre-monsoon and monsoon melt. However future precipitation trends are a significant source of uncertainty for future glacier viability (Immerzeel et al., 2013).

The potential of increased future precipitation acting to compensate for the Himalayan glacier mass loss from warming has been proposed in numerous studies (e.g. Immerzeel et al., 2013; Kraaijenbrink et al. (2017); Rounce et al., 2020) and is shown here in a simplistic way (Figure 4.15). Changing seasonality will complicate this however, with predictions of increased precipitation through prolonged monsoons and increased sporadicity in the drier (often colder) seasons in Nepal complicating predictions of glacier change (Dhaubanjar et al., 2019). Uncertainty of the direction of precipitation trends is considerably higher than that of temperature in the Central Himalaya (Sanjay et al., 2017b). The impact of future temperature and precipitation trends for glacier viability is explored in later Chapters following this analysis, by selecting varying precipitation scenarios for downscaling. These downscaled climate scenarios will then be used to force COSIPY. The future distributed simulated mass balance will be integrated with iSOSIA to investigate whether compensation of atmospheric warming induced glacier mass loss from increased precipitation can occur even with committed mass loss from historical warming.

Although a somewhat crude approximation, this sub-debris ablation component has added value to COSIPY and was computationally inexpensive. Further work to fully integrate this debris cover correction into future versions of COSIPY is underway (Sauter et al., 2020) to enable users studying debris-covered glaciers to produce more accurate simulated mass balance.

The high sensitivity of the EBM to perturbations in albedo values, particularly of fresh snow, highlights the importance of *in situ* albedo, rain/snow threshold and snow depth measurements, and has implications for real-world melt rates (Litt et al., 2019). Darkening of snow and ice across HKKH has been observed for several years (Yasunari et al., 2015; Kang et al., 2020), including from surface snow samples in the upper Khumbu valley (Jacobi et al. 2015). Increased albedo decay times have also been observed over the 21st century from industrial black carbon deposition (Maurer et al., 2019) particularly in the pre-monsoon, though observations on the south side of the HKKH are lacking (Gertler et al.., 2016). Future predictions of these parameters are non-existent given the immense challenge of predicting future industrial activity in the region and trajectories of atmospheric circulation.

4.7 Conclusion

This analysis of simulated Khumbu Glacier mass balance is the first of its kind. The extreme elevation range of Khumbu Glacier makes simulating mass balance challenging. Unlike other glaciers of the HKKH that have more distinct meteorological drivers of glacier mass balance (Bonekamp et al., 2018), the meteorological drivers of Khumbu Glacier mass balance fluctuate significantly over space and time. Therefore EBM is the preferred approach for simulating mass balance. Though ablation is likely underestimated in these upper reaches, the ability of COSIPY to simulate ablation in these dry conditions that are well below freezing is encouraging.

There are three critical elements of Khumbu Glacier mass balance: accumulation through avalanching and ablation from just below the ELA and beneath the thick supraglacial debris on the tongue. The results for each of these elements are summarised here:

- Few mass balance models resolve avalanching including COSIPY, and therefore a weak precipitation gradient, that would otherwise have been kept constant (Inoue, 1977), was used to roughly match observed accumulation rates. The role of avalanching in the spatial distribution of accumulation and rates is investigated in Chapter 6.
- The high ablation rates (approximately 5 m w.e. a^{-1}) observed just below the ELA, are well replicated by COSIPY.
- The inverse mass balance of DCGs such as Khumbu Glacier makes mass balance simulations challenging, but the addition of the Khumbu specific, computationally inexpensive sub-debris ablation correction (calculated using the DADDI model) has enabled this inverse mass balance to be replicated. This debris component improved accuracy of calculations of melt across the debris-covered tongue and glacier-wide mass balance is close to geodetic calculations. However, the DADDI model assumes a uniform supraglacial debris cover. The high ablation rates seen around ice cliffs and supraglacial ponds are key sources of ablation. In Chapter 6, the role that differential ablation plays in mass balance and historical glacier evolution will be explored.

Chapter 5 Downscaling of present and future Regional Climate Model data for glacier mass balance modelling

5.1 Introduction

The use and development of General Circulation and Regional Climate Models (GCMs and RCMs, respectively) has grown significantly over the last decade with a consequent rise in the number of climate change related studies across disciplines. There have also been great advances in computational and scientific knowledge, vastly enhancing the quality and quantity of climate models, as well as improved collaboration as part of the Coupled Model Intercomparison Project (CMIP). Despite this, there still exist significant systematic biases of climate variables between GCM and RCM outputs relative to observations. These biases result in significant differences in absolute values, as well as seasonal and inter-annual trends and can be attributed to several sources. These include, though are not limited to, the poor representation of large-scale climate variability and forcing in GCMs, that can further propagate when dynamically downscaled to RCMs, such as those from the Coordinated Regional Downscaling Experiment (CORDEX) project.

Biases can also occur due to poor resolution of sub-grid scale processes, such as atmospheric convection, which can significantly alter local climate (though parameterisations of such processes are a key and growing area of research (Sherwood et al. 2013, de Rooy et al. 2013, Yano 2014 and Morrison et al., 2020)). Coarse resolution GCMs (falling between 70 and 400 km resolution) are unable to resolve synoptic-scale interactions between weather systems and complex topography (Cannon et al., 2016), which is of utmost importance for the HKKH given the extremes in terrain at the sub-grid scale. Downscaling or bias correction prior to application in climate change studies is therefore required.

The RCMs used to force the present day (2014-2019) and future (2095-2100) mass balance of Khumbu Glacier and subsequent ice flow modelling are from the World Climate Research Programme initiative CORDEX. The CORDEX project is a co-ordinated worldwide effort to generate an ensemble of RCMs and climate change projections at a higher spatial resolution (50 km) than their driving parent GCM. Sanjay et al. (2017a) assessed the CORDEX RCMs for their skill in simulating general climate characteristics over South Asia, and found that performance is highly dependent on the chosen RCM and boundary conditions (i.e. the parent AOGCM). Future climate across the HKKH has also been assessed using multiple CORDEX models and emission scenarios until 2095 (Sanjay et al., 2017b). This study found a multi-model approach provided greater consensus than the single driving GCM in projecting increased monsoon precipitation for the foothills

of the southeastern Himalaya and the Tibetan Plateau (by 22% under RCP8.5). However, poor consensus over projected monsoon and winter precipitation dynamics remained for the central Himalaya and Karakoram among the multiple RCMs.

This poor consensus for the Central Himalaya between RCMs (Sanjay et al., 2017b) means a similar multi-model approach is taken for this study. RCMs are firstly selected based on their ability to simulate present day temperature and precipitation seasonality, and the selected number is reduced based on future temperature and precipitation projections to ensure several future climate scenarios that are not limited to emission scenarios are covered, and to assess uncertainty. Given the higher uncertainty regarding precipitation change relative to temperature, the RCMs were selected to cover a range of future precipitation scenarios.

Dynamical downscaling involves high resolution atmospheric simulations linked dynamically to large-scale climate patterns, often through nesting within the coarse climate model boundary conditions. A convection permitting resolution of 10 km resolution was able to reproduce summer precipitation patterns in the Himalaya (Norris et al., 2017), however ≤ 6.7 km was found to be necessary for accurate representation of nocturnal precipitation patterns (Norris et al., 2017) when dynamically downscaling the Climate Forecast System Reanalyses with the Weather Research Forecasting (WRF) Model. Although there are clear advantages of dynamical downscaling that are particularly apparent in complex terrain (Potter et al., 2018), it is often not computationally feasible, especially for long-term climate change modelling studies.

Initially, the delta change method was considered for bias correction, as it is computationally inexpensive, and has been widely applied to temperature and precipitation for future climate change studies, including projections of glacier evolution (Akhtar, M. et al., 2008, Immerzeel et al., 2012, Shea et al., 2015a and Zhang et al., 2015), winter and monsoon precipitation patterns (Rajbhandari et al., 2016 and Kaini et al., 2019) and hydrological change (Li et al., 2017) in the HKKH. The future climate change signal (delta) is calculated through comparison between the reference period and future scenarios (Bosshard et al., 2011). Delta is applied to observations from the present day into the future. However, there exist several assumptions behind this method, the first being that it is effective for all quantiles of the distribution: the mean and the extremes. Equally future temporal patterns are assumed to remain identical to observations.

Statistical downscaling addresses the latter assumption from the delta change method, as in place of the observations being adjusted, the climate model data is corrected towards the reference observations, thereby partially eliminating systematic biases. For this reason, statistical downscaling is common practice in climate change modelling studies, and is a more viable alternative to dynamical downscaling. It is therefore used in this Chapter. There now exists a plethora of statistical algorithms designed to correct and lessen biases in mean, variance and extremes of

climate model data (Gudmundsson et al., 2012 and Cannon et al., 2015b). They are effective in improving the representation of fine scale processes, and so in theory bias between RCMs and observations should be reduced relative to GCMs, although several studies show that the 0.25° spatial resolution of CORDEX RCMs still contain systematic bias when compared to observational data. This is particularly true for this region in the Central Himalaya, where an elevation range of 7000 m could exist within one single RCM grid box. This does however mean that pointwise downscaling can be used for this study, and so the chosen downscaling method does not need to accurately resolve spatial variability, only temporal variability and trends.

Removal of systematic biases as sources of error is of particular importance for climate change studies that involve successive modelling chains. The efficacy of the method is dependent on the climate model data, the length and quality of observations, and the parameter in question. Quantile mapping (QM) has been found to produce more accurate results in terms of the mean and variance for most climate variables relative to delta change or simpler bias correction methods such as linear regressions (Gudmundsson et al., 2012 and Chen et al., 2013). This is particularly true for precipitation, with previous simple methods assuming linearity or normal distribution which would lead to erroneous corrected precipitation. Two-state gamma distribution QM performs particularly well for precipitation (Teng et al., 2015) and so is used here. Many downscaling approaches are designed for monthly or daily temporal resolutions (Maurer et al., 2008 and Li et al., 2010), to force hydrological or crop models for example. Given the importance of the diurnal trend in temperature and radiative fluxes for glacier melt, downscaled daily data are further disaggregated from daily to hourly resolution when modelling energy exchanges and ultimately, glacier mass balance.

The previous chapter examined the sensitivity of glacier mass balance to changing atmospheric forcing using the COSIPY model, and assessed the suitability of this model for Khumbu Glacier. The analysis of meteorology and glacier mass balance is used here to inform the CORDEX model selection and downscaling, through QM. This will be used in the final chapter of the thesis to force present day (PD) and future mass balance, which will be used to drive an ice flow model to explore future evolution of Khumbu Glacier. There is emphasis on temperature and precipitation downscaling given their strong influence on glacier mass balance, though the full range of COSIPY atmospheric forcings are considered and subject to downscaling. The efficacy of the downscaling methods is assessed through comparison with the raw RCM data, but mainly with the observations used to conduct the downscaling.

5.2 Climate model selection and downscaling

5.2.1 CORDEX data

Many research institutions around the world have contributed to CMIP5 (Taylor et al., 2012). Several modelling centres have dynamically downscaled CMIP5 data from the coarse resolution atmosphere-ocean coupled GCMs to 50 km spatial resolution RCMs over the South Asia domain (19.25°-116.25°E; 15.75°S - 45.75°N) through the CORDEX project. The Centre for Climate Change Research (CCCR) at the Indian Institute of Tropical Meteorology led on this for CORDEX South Asia, and hosts an archive of data (http://cccr-dx.tropmet.res.in:8000/cccrindia/) to aid users conducting climate change research in the region. Daily data were downloaded from this website for the grid box nearest to Khumbu Glacier (27.9065056°N, 86.4352951°E). These data include the climate variables used to force the COSIPY mass balance model. As the CCCR website did not provide SW_{in}, LW_{in} and RH, these were downloaded from the ESGF portal (https://esgf-index1.ceda.ac.uk/search/cordex-ceda/).

5.2.2 Future climate scenarios

Climate data from two different future emission scenarios were used: RCP4.5 and RCP8.5. CORDEX only conducted dynamical downscaling of these two RCPs. An RCP refers to a greenhouse gas concentration trajectory, and by proxy an emissions trajectory, and was used in the Intergovernmental Panel on Climate Change (IPCC) 5th Assessment Report (AR5) in 2014. These two RCPs represent the intermediate and high-end radiative forcing values that are possible for 2100 AD (so 4.5 and 8.5 W/m^2, respectively).

At the time of writing, the next generation of climate model simulations had just been released through CMIP6. These state-of-the-art experiments use shared socioeconomic pathways which allow simulations of a wider variety of future climates that are based on economics and demographics (Eyring et al., 2016). It was decided that these should not be used as they were not all yet available. Equally there had been few studies assessing the biases of these climate models or employing them to perform dynamical downscaling such as CORDEX or to assess glacier change, particularly for the HKKH.

Analysis since AR5 has suggested that global emissions are following the trajectory of the middle range scenarios, and that RCP8.5 should be described as “low-possibility, high-impact” (Pedersen et al., 2020). Both observations and predictions indicate that high elevations warm much faster than lower elevations. This elevation dependent warming (Pepin et al., 2015) is brought about by several feedback mechanisms, including surface albedo feedbacks with snow cover and ice mass shrinkage and water vapour changes and latent heat release. Kraaijenbrink et al. (2017)

estimated that the extent of atmospheric warming in mountain regions could in fact exceed those widely used RCPs relevant for global climate change scenarios. Therefore, a higher emissions scenario (RCP8.5) future climate could be more plausible for these high elevations, and in fact could even still underestimate warming.

It is recommended that at least 10 years (and ideally 30 years) of observations are used for downscaling to ensure the reference period is not in an extreme phase of natural variability. Many studies that necessitate PD downscaled climate data sourced from the CMIP5 or CORDEX projects use historical experiment data (1951-2006). Given that the first high elevation observations in this region (Pyramid) began in 2001, there would be insufficient (5 years) of reference observations for the same time period. Therefore for PD downscaling, climate data from the RCP4.5 experiment (from 2006) across the historical period was used in place of the historical experiment data.

Observational data from January 2006 until November 2019 were gathered from the Ev-K2-CNR and glacioclim networks (Chapter 3 and 4) with gaps filled with interpolated data from neighbouring stations where possible (Figure 5.11). December 2019 climate data were not available and so the mean from each day of the December months in 2001-2005 were used for interpolation. Daily means (or sums for precipitation) were calculated from hourly observations to produce the reference dataset. These reference data were used for both calibration (or training) of the statistical downscaling method that will be used on the RCM data.

In theory the choice of RCP should not significantly impact climate in the PD, but this was specifically assessed prior to choosing RCP4.5 for the PD climate. This approach of using the RCP experiment data over historical experiment data for both the present day and the future also ensures greater confidence in future downscaling, as the bias between RCM data and observations in the present day is better understood. Equally the MB simulations forced with PD climate can effectively and legitimately be compared with remote sensing and *in situ* MB measurements.

5.2.3 Model selection

A single RCM approach was not considered sufficient for representing both PD climate and potential future climatic extremes. A multi-model mean approach, which is widely used elsewhere, was also not considered as this gives equal weighting to models with poor and good performance in their ability to reproduce climate (Pierce et al., 2009). Therefore three RCMs were chosen and downscaled separately in order to force separate COSIPY simulations. The selection of the three RCMs was a combination of two approaches.

Firstly, RCMs were assessed on their fidelity to present day climate, also known as hindcasting (Biemans et al., 2013), with the emphasis on temperature seasonality and seasonal precipitation

dynamics given the importance of these parameters for glacier viability. The resolution of the monsoon even in RCMs is poor (Kaini et al., 2020), with much reduced seasonality relative to observations mostly due to a significant overestimation of winter precipitation, and the known challenges associated with the representation of complex orography at the sub-grid scale. This analysis also found that RCP PD experiments have an even poorer representation of seasonality relative to the historical experiments. Given the high elevation of the study area, it was expected that there would be a strong warm bias, however the wet bias was also significant. A drawback of this approach is the assumption that climate models that perform well for past climates will also represent future climate well (Lutz et al., 2019). Nevertheless, several CORDEX models were discounted purely on their performance in the historical period, such as the absence of monsoon signal (e.g. the RCM driven by the CSIRO GCM; Figure B1.2).

The second stage comprised analysis of possible future climate scenarios. The potential of future precipitation trends acting to either exacerbate or compensate for atmospheric warming was demonstrated simply in the coupled parameter perturbation experiments. It was therefore important that future projections that represent contrasting temperature and precipitation scenarios were used for glacier model forcing. This envelope-based selection approach is often used to ensure a variety of possible future climate extremes are selected. The quadrilateral approach is used by Kaini et al. (2019) for the entire Koshi river basin spanning the China/Nepal border, where future climate scenarios can be considered as being four corners of a quadrilateral representing warm/wet, warm/dry, cold/wet and cold/dry scenarios or indices. These extremes were found to vary in time and space for each model and for each RCP, with a clear knock-on effect for future glacier evolution.

A three-model approach was used instead of the quadrilateral approach for this study (Figure 5.1), in part because there were not four future climate scenarios that fitted the above indices for the Khumbu region, and also for computational efficiency with the expensive modelling efforts of the final chapter in mind. The future precipitation projections of the six CORDEX models that were downscaled by the Indian Institute of Tropical Meteorology were compared (Figure B1.1), and three discounted based on the future precipitation scenario, or fidelity to precipitation seasonality in the present day (e.g. B1.2). Given the higher uncertainty on future precipitation trends in comparison to temperature trends, and the interplay of changing precipitation with atmospheric warming for glacier evolution, three models that represented three discrete precipitation scenarios were chosen (Figures 5.2 a-b). These RCMs represent wet, moderate and dry climates in 2080-2100 for at least one of the two future emission scenarios.

CORDEX South Asia RCM	Driving CMIP5 GCM	CMIP5 Modelling Centre	Name referred to in this chapter
IITM-RegCM4	CCCma-CanESM2	Canadian Centre for Climate Modelling and Analysis (CCCma), Canada	CCCma
IITM-RegCM4	NOAA-GFDL-GFDL-ESM2M	National Oceanic and Atmospheric Administration (NOAA), USA	NOAA
IITM-RegCM4	IPSL-CM5A-LR	Institut Pierre-Simon Laplace (IPSL), France	IPSL

Table 5.1 Chosen models and information regarding their GCM. Further information on the driving GCMs as part of the CMIP5 can be found here: https://verc.enes.org/data/enes-model-data/cmip5/resolution.

Figure 5.1 Schematic of future precipitation scenarios of three chosen models.

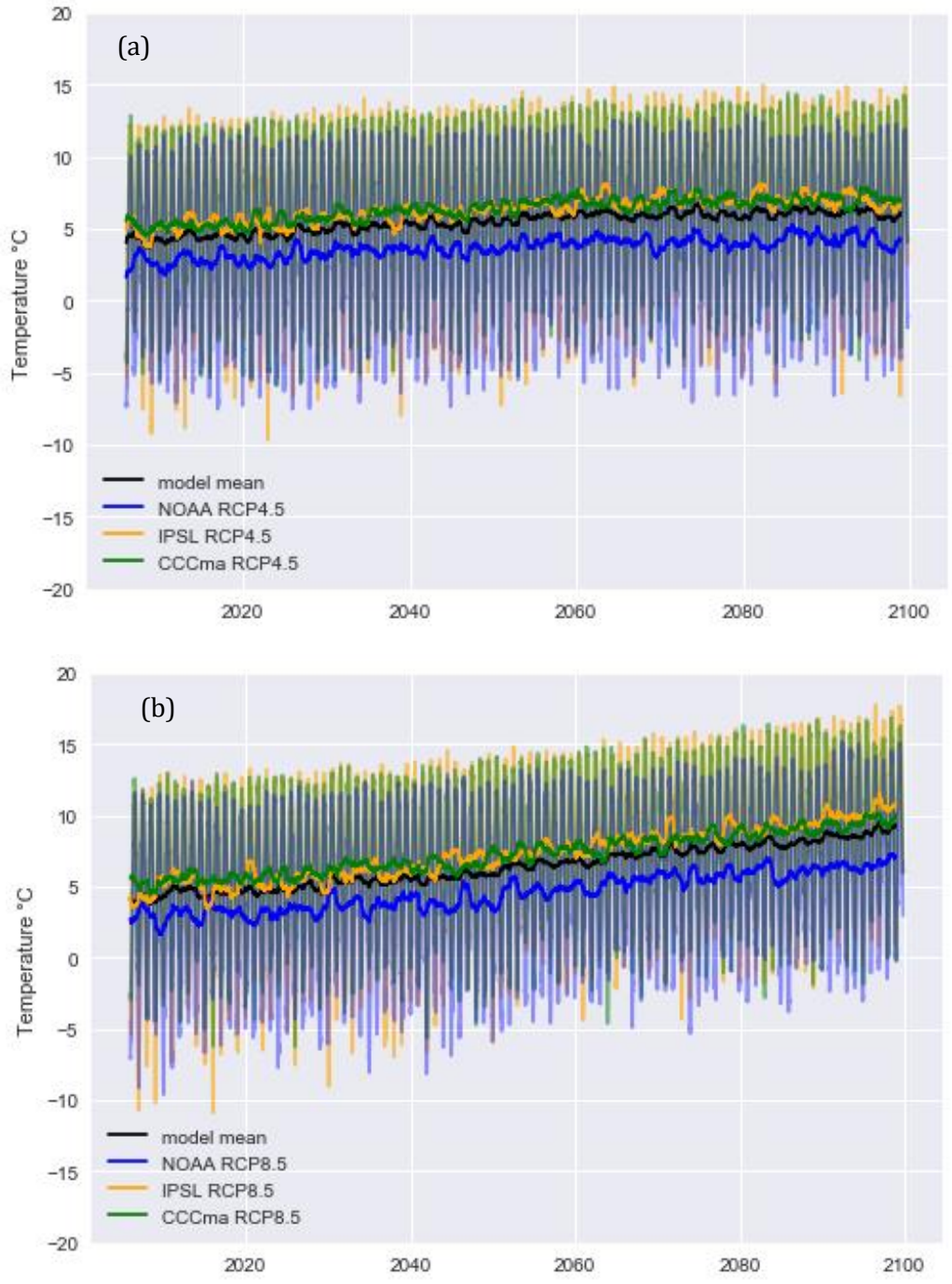

Figure 5.2 (a,b) Annual temperature (thick coloured lines) with monthly means (shaded) from the start of the RCP experiments (2006) until the end (2100). This is for each of the selected CORDEX models, and multi-model mean in black, for RCP4.5 (a) and 8.5 (b).

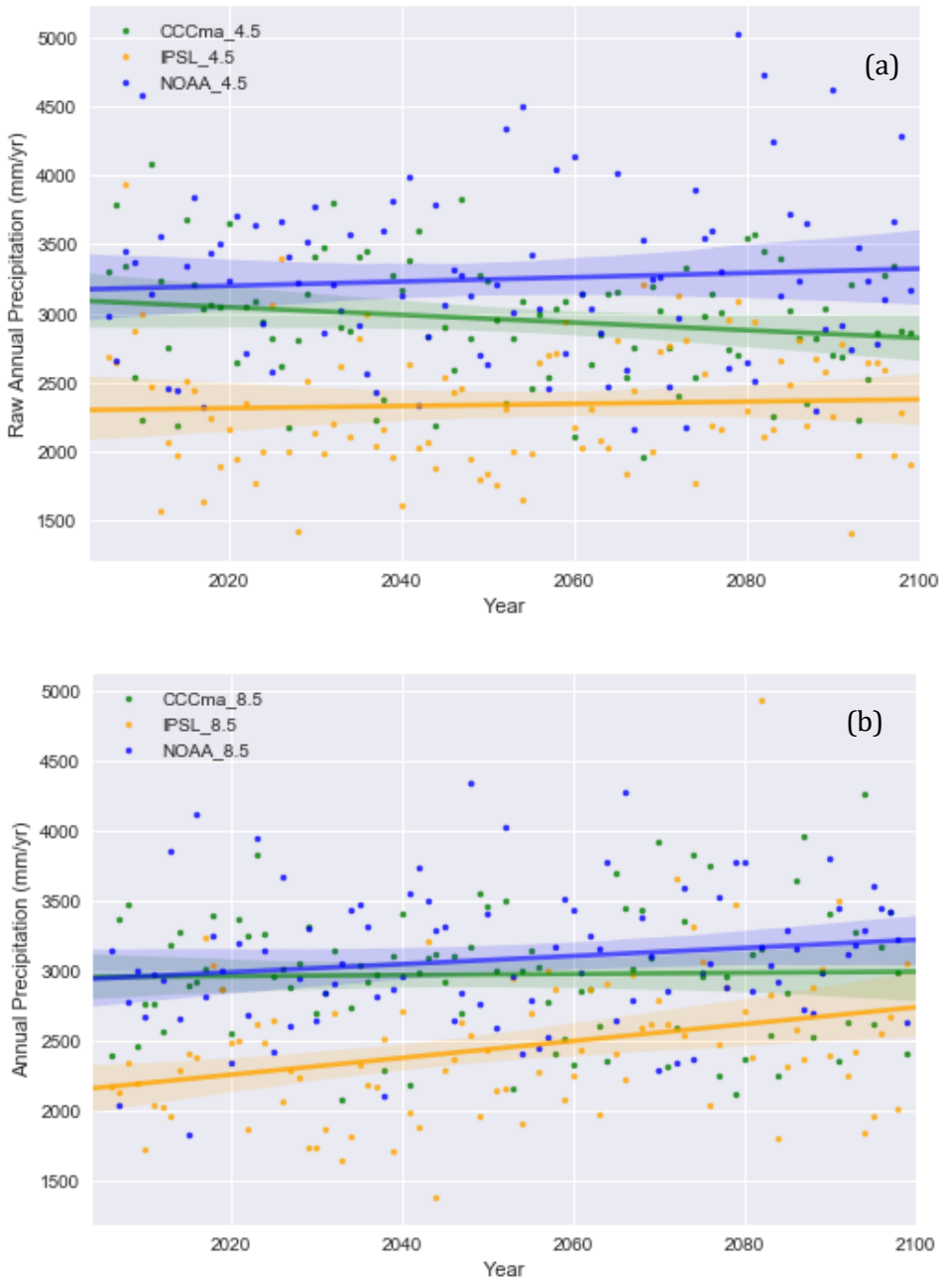

Figure 5.3 Annual precipitation sums (dots) with fitted trend line from the start of the RCP experiments (2006) until the end (2100) for each of the selected CORDEX models for RCP4.5 (a) and 8.5 (b).

The climate time-slice for the period 2095-2100 is used to force the future MB simulations which drive the ice flow model from the present day into the future, and is referred to hereon in as the future time-slice. Five year time-slices were chosen to reduce computational expense associated with COSIPY. To ensure the selected 5 years were reflective of the climate of that period, the preceding decade was also used for comparison with the time-slice climate data, though the downscaling method using 14 years of reference data should limit the influence of any natural

variability. This comparison was particularly important for the future time-slice where uncertainty arises between models and with no observations for validation of downscaled climate or mass balance. A midway point time-slice (2059-2064) was selected for two of the experiments (CCCma under RCP4.5 and NOAA under RCP8.5), and were downscaled and disaggregated in the same way as in this chapter. This was used to force a mid-century MB simulation to assess the response of the ice-flow model to this mid-way MB forcing.

5.2.4 Statistical downscaling of daily climate data

Quantile mapping, also known as "distribution mapping", corrects for biases in the distribution of a modelled variable (e.g. precipitation) through "training" against the distribution of observations. The raw climate model output is downscaled through determining a correction or transfer function from observations that will differ depending on the quantile. This quantile-dependent correction is applied to the raw data to produce a third downscaled dataset, which should better match the observations, though will not be identical (Figure 5.4).

The quantiles from both observations and the climate model can be derived from a full empirical distribution, so will not differ depending on the climate variable (non-parametric QM; Déqué et al. 2007, Lafon et al., 2013; Themessl et al., 2012). The alternative is to use a theoretical distribution for each variable (parametric QM; Piani et al., 2010). In this instance, a statistical relationship between the raw climate data and the observations is formed by substituting the climate model data with observations at a cumulative density function (CDF) of the prescribed distribution. For example, if temperature data were being downscaled, a normal distribution would be used. The distributions and equations for each of the key variables are shown in Table 5.2.

The climate variables listed in Table 5.2 were downloaded for the calibration periods for all time-slices for the three CORDEX RCMs. Though T_{min} and T_{max} are not required to force the MB model, these were downloaded and statistically downscaled using QM with normal distribution (equation 5.2) to aid disaggregation to an hourly time step (section 5.2.3). Table 5.2 does not include wind speed or pressure, which are both required for MB modelling, which were not subject to QM, the approaches used for these are discussed later. Prior to downscaling, the precipitation data were converted from precipitation flux ($kg/m^2/s$) to mm/day by multiplying daily sums by 86,400.

For future downscaling, the same method was used as for present day. However, RCM data for the same historical period used for the PD downscaling were also used to ensure any changes in parameters into the future were preserved following downscaling (Cannon et al., 2015). The PD

RCM data were for the same RCP as the future data that were being downscaled, given that there was some difference in absolute values between the two RCPs evident even in the present day.

Distribution Model	Climate Variable	Equation	Reference
Gamma	Precip	$\bar{x}_{ms.corr} = \{ \frac{F_{oh}^{-1}(F_{mh}(x_{ms})), x_{ms} \geq x_{th}}{0, \quad x_{ms} \geq x_{th}}$ (5.1)	Vrac et al., 2007; Piani et al., 2010
Normal / Gaussian	T_{mean} T_{min} T_{max}	$\bar{x}_{ms.corr} = x_{ms} + F_{oh}^{-1}(F_{ms\,(x_{ms})}) - F_{mh}^{-1}(F_{ms}(x_{ms}))$ (5.2)	Li et al., 2010, Gupta et al., 2016; Luo et al., 2018
Beta	SW_{in} LW_{in} RH	$\bar{x}_{ms.corr} = F_{oh}^{-1}(F_{mh}(x_{ms}))$ (5.3)	Ruane et al., 2015

Table 5.2 Distribution models and cumulative density function equations (1-3) used for each climate variable. Where x is the climate variable, $x_{ms.corr}$ is the downscaled climate model data. categories between the wet and the dry day threshold value x_{th}, *F* is the cumulative density function, and F^{-1} is its inverse. *o* refers to observations observed, *m* is model, *h* is historical period, and *s* is simulation period.

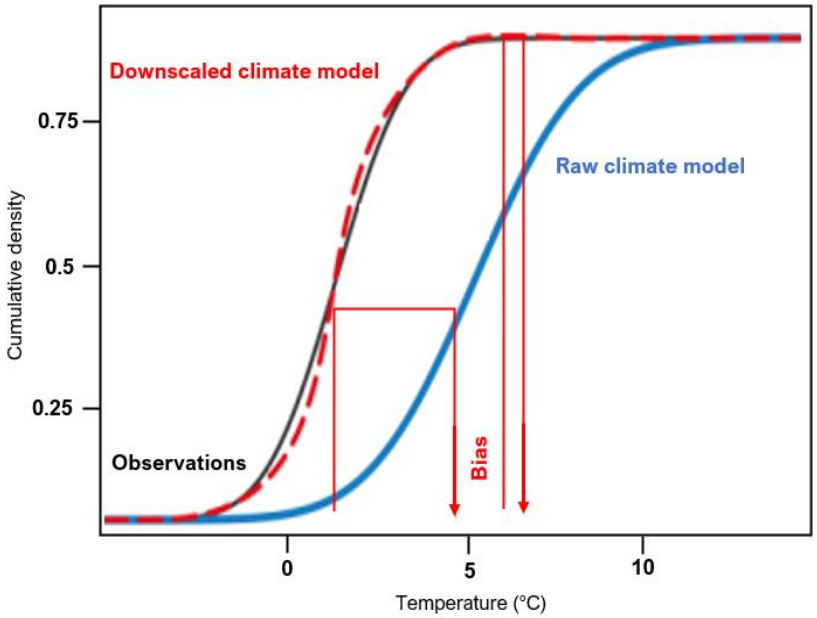

Figure 5.4 Schematic of quantile mapping using temperature as an example though this would be appropriate for other variables (e.g., precipitation as in Figure 1 of Lafon et al., 2013). A quantile of the observed distribution is used to replace the quantile of the observed distribution is used to replace the quantile of the raw climate model data. Modified from Maraun (2016).

Piani et al. (2010) developed the QM method for precipitation data using a gamma distribution. This was based on annual precipitation, but it was recommended that seasonal distinctions would improve results. Given the extreme precipitation seasonality in the Khumbu region, this seasonal approach was adopted here, supported by the work of Li et al., (2010), where daily values of each month were fitted to a gamma distribution.

The parametric QM method for precipitation has been compared with two forms of bias correction (linear and non-linear) and another form of QM (empirical) for their efficacy in downscaling RCM derived precipitation in Great Britain (Lafon et al., 2012). Error reduction in mean precipitation using gamma QM was slightly lower than for other methods (86% compared to 88%, 86% and 88% for linear, non-linear and the empirical method, respectively). However, the gamma distribution method outperformed all other methods in terms of reducing error in standard deviation, coefficient of variation and skewness of distributed values and so was generally considered the most accurate and robust option. Alternative methods for precipitation downscaling were assessed for this study, including Random Forest Regression, linear regression and Generalized Analog Regression Downscaling (GARD) and though the prediction of mean values was sometimes better than for QM, QM was found to outperform these methods for other variation and distribution statistics, as with the study by Lafon et al. (2012).

Solar radiation for each month was converted so as to range from 0 to 1; the range of beta distribution (Ruane et al., 2015). Beta distributions were fitted to the daily mean of the two radiation components (LW_{in} and SW_{in}) for the simulated and observed datasets. The monthly maximum from the 14 years of observations was used as the upper limit for the distribution of each month and zero as the lower limit, and then the distribution was adjusted using QM.

QM for the CORDEX wind data was found to be ineffective when analysing the time series output against observations, both for the absolute wind speed as well as the reduced day-on-day variability seen during the monsoon. Therefore, GARD was used instead (https://github.com/NCAR/GARD). This is a simple statistical analogue regression downscaling method appropriate for pointwise downscaling.

The RCM simulated atmospheric pressure performed well in terms of seasonality with a peak in pressure in the post-monsoon matching observations and reduced variability during the monsoon. However, there was a systematic bias evident in the absolute values of 140 hPa likely due to the elevation difference between the RCM grid box and observations. Given the low sensitivity of MB modelling to pressure change, this bias was subtracted from the CORDEX pressure variable for all RCMs and time periods to improve the match to observations.

5.2.5 Disaggregation to hourly resolution

The requirement of glacier energy balance models to be forced with hourly resolution climate data necessitated further disaggregation of the daily downscaled data. This was conducted on a variable-by-variable basis by training downscaled data with hourly observations from the 2006-2019 period. The primary focus was on disaggregating temperature, precipitation and the two radiation components, given their particular importance for energy balance modelling.

The hourly reference data and the downscaled daily data were both subdivided into a calibration period (2006-2014), and a validation period (2015-2019). The validation period is used hereon in to assess the downscaling method and to compare downscaled present day and future climate (2095-2100). The future downscaled daily climate was disaggregated in the same way as the present day. For all variables excluding temperature, this relies on the assumption that the diurnal cycle in climate variables will be the same into the future, the validity of which will be discussed in more depth later.

Temperature

Daily temperature on a given day (T_i) was upsampled to hourly (T_j) using equation 5.4, a cosine function defined by Debele et al. (2007)

$$T_{i,j} = T_{min,i} + \frac{T_{min,i}T_{max,i}}{2} \cdot \left(1 + \cos\left(\frac{\pi \cdot (t_j + a)}{12}\right)\right) \quad (5.4)$$

where daily T_{min} and T_{max} define the cosine amplitude and *a* refers to the time difference between midday (12 - approximately maximum SW_{in}) and the occurrence of maximum temperature (T_{max}) that is calculated from the hourly time series as previous analysis has found this to vary seasonally. Simple statistics (R^2 and r values) between hourly observations and the disaggregated output were calculated and random sampling of the time series was conducted to check seasonality and day-on-day variability of diurnal cycles. The former is illustrated with the NOAA PD example in Figure 5.5a, showing good agreement between modelled and observed data particularly during the monsoon, though the timing of T_{max} occurred after midday in observations in contrast to the modelled data. The day-on-day variability (shown as standard deviation in Figure 5.5b) also matched better to observations during the monsoon (i.e. reduced variability, especially overnight) though was underestimated in the disaggregated data outside of the monsoon.

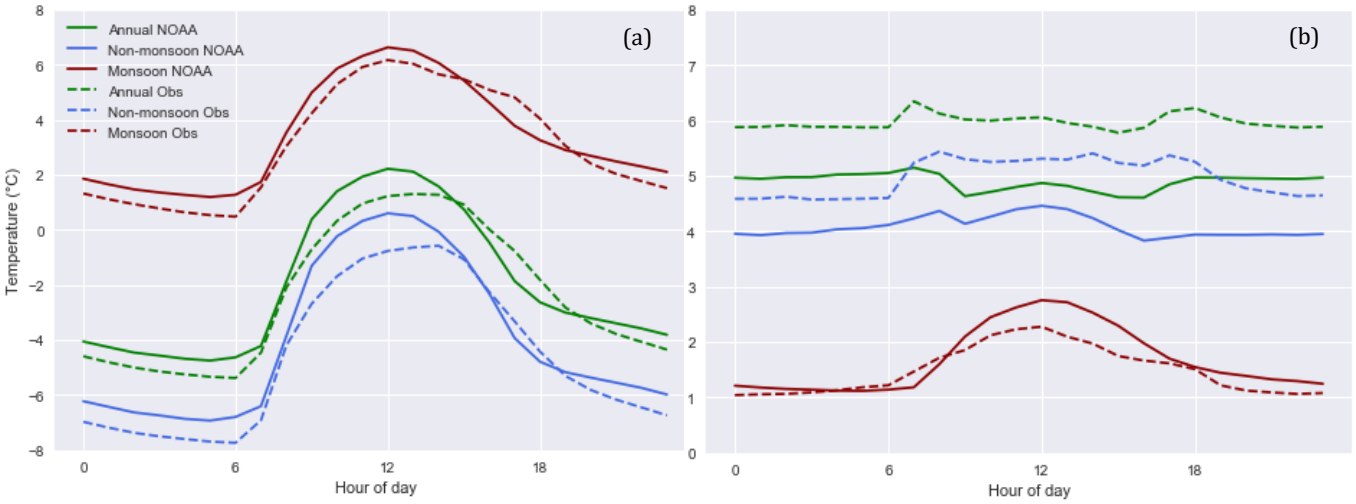

Figure 5.5 (a) Temperature mean diurnal trend for the NOAA PD time-slice following disaggregation using equation 4 observations split by season (b) and the diurnal standard deviation. Note the different scales on the y axis.

Radiation components

For disaggregation of the radiation components the open-source MEteoroLOgical observation time series DISaggregation Tool MELODIST (Förster et al., 2016 and gathered from the site:

https://github.com/kristianfoerster/melodist) was used. A variety of methods were tested and those with the best R^2 values were chosen.

For SW_{in} hourly values of potential (clear-sky conditions) radiation is calculated using

$$R_0 = 1370\ \mathrm{Wm}^{-2}, \cos \mathrm{Z}\,.\,(\psi\ \mathrm{dir} + \psi\ \mathrm{dif}) \tag{5.5}$$

where the solar constant (1370 W/m^{-2}) was scaled according to the solar zenith (Z) which was calculated using time of year, hour since solar noon and latitude (Liston and Elder, 2006). The division of direct (dirψ) and diffuse radiation (difψ) over time is also outlined in the study by Liston and Elder (2006). Potential radiation was calculated for an assigned location. The longitude, latitude and time zone of Pyramid were used, and statistics derived with the same hourly dataset used for temperature. The CCCma results exhibited diurnal cycles that match well with observations (Figure 5.6a) and were able to represent the seasonal variation in diurnal cycles. This seasonal variation was underestimated with a more extreme diurnal amplitude in SW_{in} during the monsoon, for example. The peak in SW_{in} in the disaggregated data was an hour earlier (later) in the non-monsoon (monsoon) compared to the observations. The variability in SW_{in} was higher during the monsoon in both disaggregated data and observations than outside of the monsoon (Figure 5.6b).

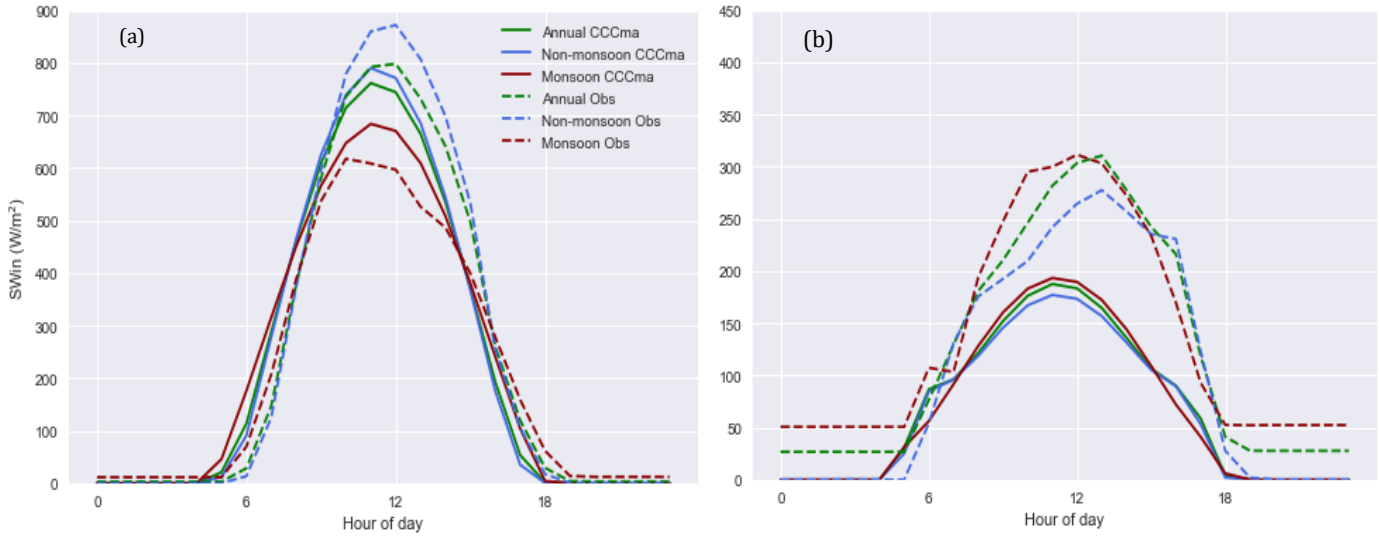

Figure 5.6 (a) SW_{in} mean diurnal cycle for the CCCma PD time-slice following disaggregation using equation 5 and observations split by season (b) and the diurnal standard deviation. Note the different scales on the y axis.

The seasonal variation of LW_{in} was slightly underestimated in the disaggregated output e.g. for the IPSL data (Figure 5.7a). The stability of the high LW_{in} values during the monsoon were captured (Figure 5.7b) though the variability in the diurnal trend was not so well represented during the monsoon and across the year.

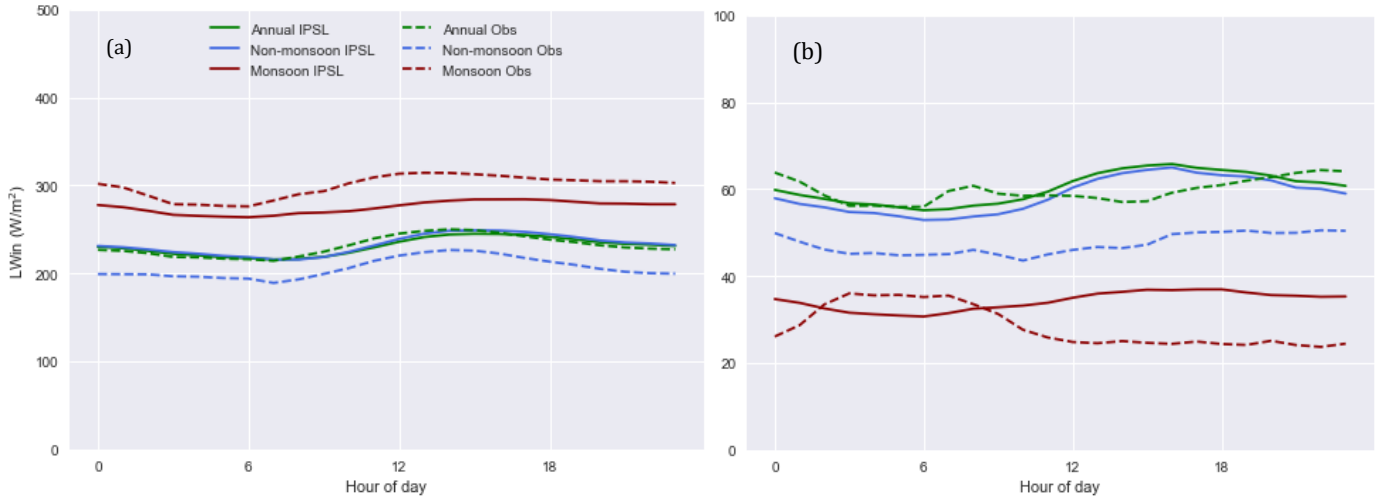

Figure 5.7 (a) LW_{in} mean diurnal cycle for the IPSL PD time-slice following disaggregation, and observations split by time of year (b) and the diurnal standard deviation. Note the different scales on the y axis.

Precipitation

The cascade method (Olsson, 1998 and Gunter et al., 2001) of MELODIST was used to test the disaggregation of the downscaled daily precipitation. It is a probabilistic method, and as such is useful for realising extreme, stochastic precipitation events, but it was unable to reproduce the midnight peak in precipitation that is characteristic of the Central Himalaya, particularly during the monsoon (Ueno et al., 2001, Barros and Lang, 2003 and Bhatt and Nakamura, 2005 and Figure 5.8). It also produced low R^2 values (<0.3) compared to hourly observations. Therefore, the diurnal curve (Figure 5.8) was applied to disaggregate daily precipitation sums for the monsoon/non-monsoon and to ensure the "nocturnal peak" of precipitation was taken into account.

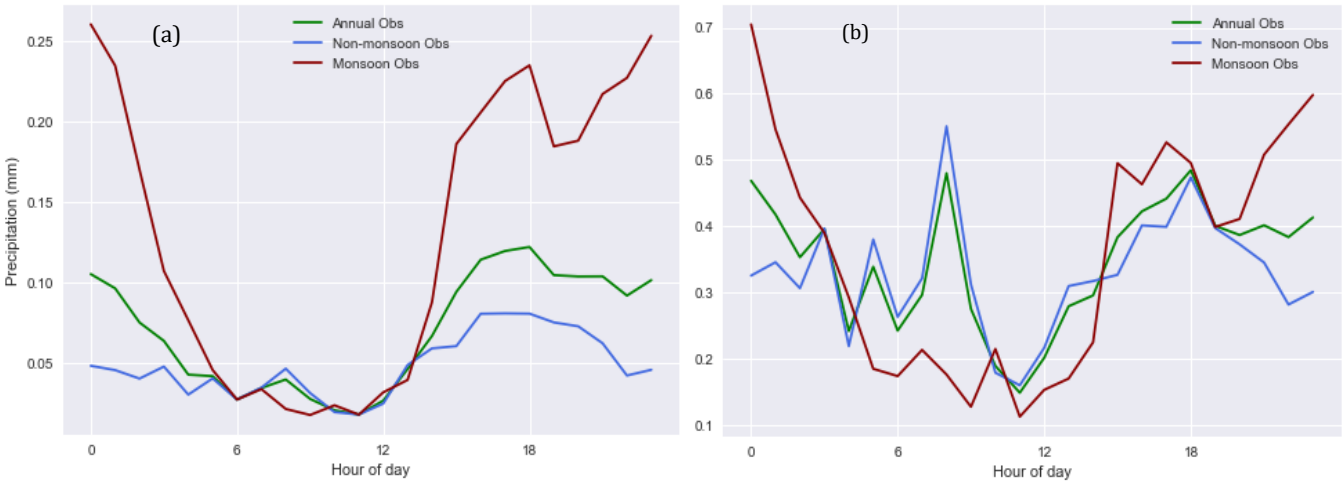

Figure 5.8 (a) Precipitation mean diurnal cycle from observations for 2006-2019 period. (b) The seasonal diurnal cycle was applied to the downscaled daily data to disaggregate to an hourly time step. The standard deviation of the diurnal precipitation curve. Note the different scales on the y axis.

RH

Though the parameter perturbation study revealed a low sensitivity of glacier MB to changing RH (Figure 4.14, Chapter 4), there is a strong diurnal cycle in RH that should be represented at the hourly time step. The method uses equation 5.6

$$T_{\text{dew,day}} = \alpha T_{min} + \text{b} \tag{5.6}$$

where a =1 and b=0, and thus relies on the assumption that the dew point temperature (T_{dew}) is assumed to be equal to daily T_{min}. This was found to be sufficient in representing the mean diurnal cycle for each season, with a good match in timing of minimum RH during the monsoon, though in the early morning hours until sunrise RH is overestimated.

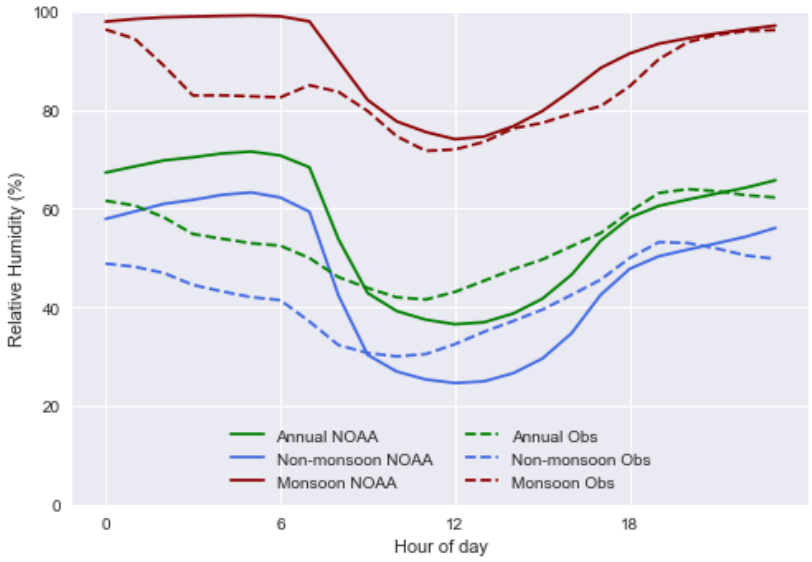

Figure 5.9 RH mean diurnal cycle for the NOAA PD time-slice following disaggregation using equation 6 and observations split by season.

Wind

Wind speed is spatially and temporally variable, particularly in complex terrain (Stull, 2009). There is ample evidence of thermally driven winds in the Khumbu valley producing a distinct diurnal wind regime in both wind direction and wind speeds (as discussed in more depth in Chapter 3). In wind speeds the diurnal pattern is characterised by decreasing wind speeds overnight to a minimum at 7am that was persistent in all seasons, and maximum wind speeds between midday and 2pm (Figure 5.10a). Given this phenomenon and that the glacier MB was found to be moderately sensitive to wind speed change, equally distributing wind speed (i.e. applying one unique value for each hour as in Waichler and Wigmosta (2003)) was not considered sufficient. The diurnal trend in wind speed is persistent regardless of season or synoptic conditions (Figure 5.5) and so a cosine function similar to that used for temperature from Debele et al. (2007) was used:

$$v_{i,t} = a_w \,.\, v_i \,.\, \cos\left(\frac{\pi \,.\, (t - \Delta\, t_w)}{12}\right) + b_w \,.\, v_i \qquad (5.7)$$

where the wind speed for dIy i is upsampled to $v_{i,t}$ for hour t. Parameters a_w b_w and $\Delta\, t_w$ are site-specific parameters determined when creating the station object (Förster et al., 2016).

This cosine function was fitted to observed hourly data and then applied to daily data for disaggregation. The results did not match observations as well as for temperature as there was not

minimum and maximum wind speed to force the diurnal amplitude, and the amplitude was reliant on calibration of the cosine function from hourly observations. The amplitude was overestimated, with wind speeds too low overnight (Figure 5.10a) though with a good match to observations following sunrise. The assumption of this method is that there is higher variability during the day as is often the case for temperature (Green and Kozek, 2003; Debele et al., 2007) which is not realistic for wind speed at this location as shown by Figure 5.10b. This method is thought to work well for locations that have a local wind circulation that endure for the majority of the time period, such as land-sea or mountain-valley system. It is likely that this method will not work as well when a dominant synoptic weather system overwhelms the local wind system (Oke, 1987), such as a winter westerly disturbance or a typhoon though, these are fairly rare in this region.

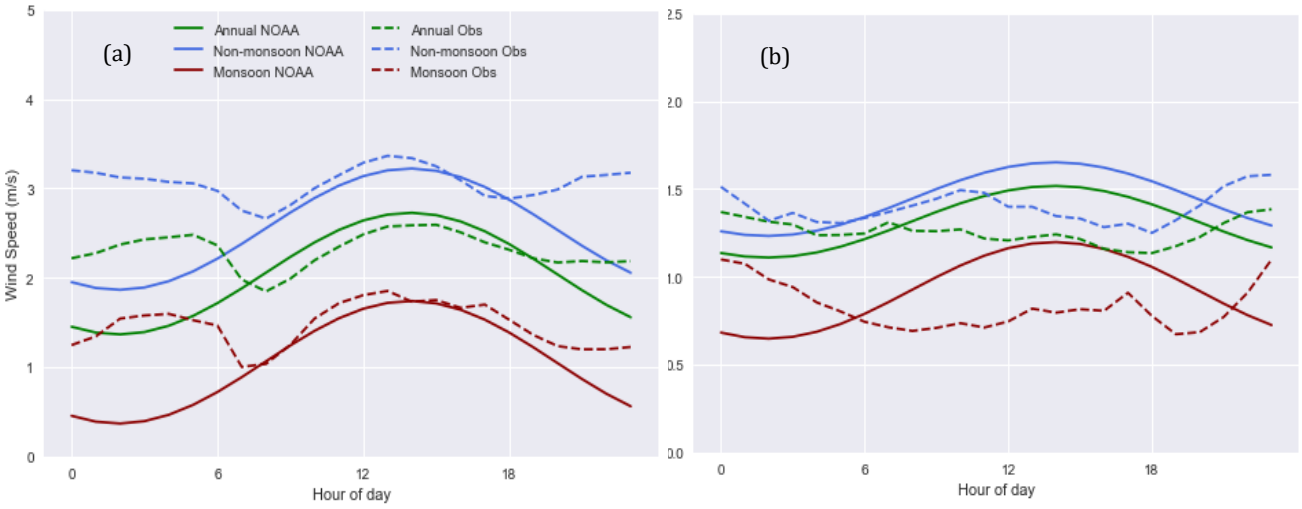

Figure 5.10 Wind mean diurnal cycle for the NOAA PD time-slice following disaggregation using equation 7 and observations split by season (5.10a) and the diurnal standard deviation (5.10b). Note the different scales on the y axis.

Pressure

Pressure was redistributed from the daily mean following the prescribed course calculated from the hourly observations using equation 5.7.

5.3 Downscaling results

5.3.1 Present day downscaling with observations

The Pyramid station that neighbours the debris-covered tongue of Khumbu Glacier experiences mean annual air temperatures of -2.1°C and receives up to 600 mm of precipitation per year. With this in mind, the raw RCMs significantly overestimate absolute mean annual air temperature by up to 7°C (Figure 5.2a and 5.2b) and annual total precipitation by at least a factor of 5 (Figure 5.3a and 5.3b) for the selected gridpoint. The annual precipitation matches measurements in the southern Dudh Koshi catchment at 2000 m.a.s.l. (Asahi, 2010 and Figure B2.2). Simulated seasonal temperature and precipitation trends from the raw RCMs are seen in Figure 5.12. There is a much larger proportion of temperatures above 0°C than in observed temperatures, due to the altitudinal range within one gridbox.

Notwithstanding the clear differences in absolute values, RCM temperature seasonality (Figure 5.12) follows a similar pattern to observations (Figure 5.11) with warmer temperatures in the summer months. However, the stabilising effect of the monsoon (i.e. the reduced day-on-day variability in temperatures) is not seen in the raw RCM temperatures. Temperature seasonality is also more extreme in the CORDEX temperature dataset for all three RCMs. The most marked weakness in the raw RCM data is their inability to simulate monsoon precipitation as the significant proportion of annual precipitation, with a considerable overestimation of winter precipitation both in frequency and magnitude. The absence of the monsoon signal in the RCM precipitation data means that a simple bias correction to resolve the difference in absolute values would be inadequate.

The QM with normal distribution for t_{mean} significantly improved absolute temperatures and seasonality. However in comparison to the raw CORDEX data (Figures 5.12a-c) and to a lesser extent the observations (Figure 5.11) there was much less noise. Temperature extremes not tied to seasonality are of particular importance for glacier melt when temperatures go above freezing in winter and below during the monsoon. This issue is improved when disaggregating daily temperatures to an hourly time step.

Following correction to the CORDEX precipitation using gamma distribution QM, the issues of overestimation of winter precipitation and relative underestimation of monsoon precipitation amounts were substantially improved, with a much clearer monsoon signal (Figure 5.13). When comparing with the observations from the PD time-slice, the downscaling perhaps over-corrected the seasonal precipitation pattern, with an underestimation of winter precipitation or at least extreme winter events.

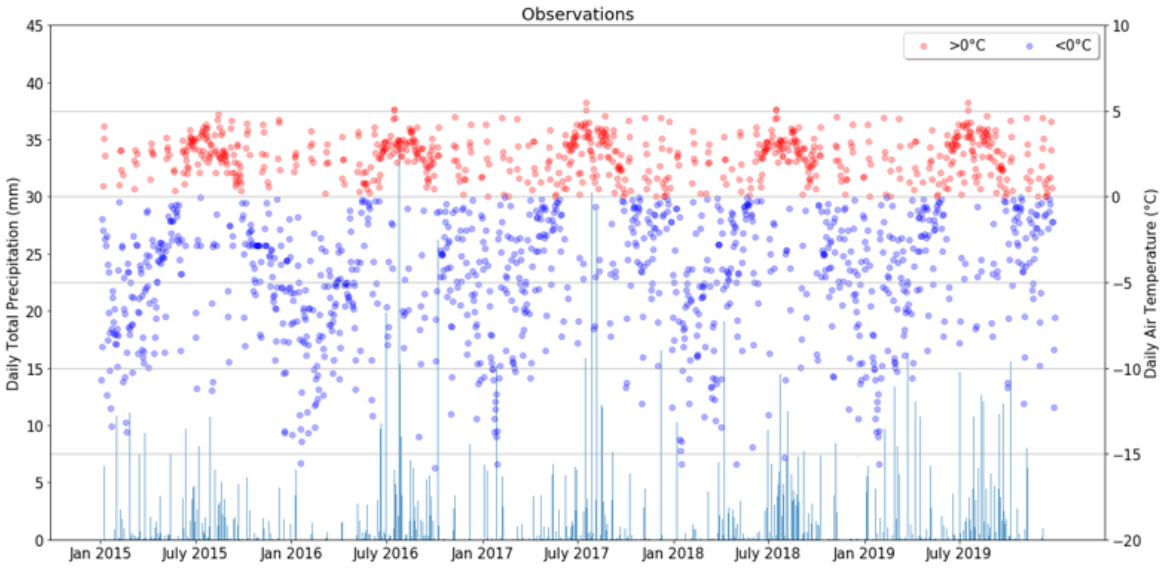

Figure 5.11 Daily mean temperature (split by above/below freezing) and total precipitation over the PD time-slice used for comparison with downscaling efforts later in the Chapter.

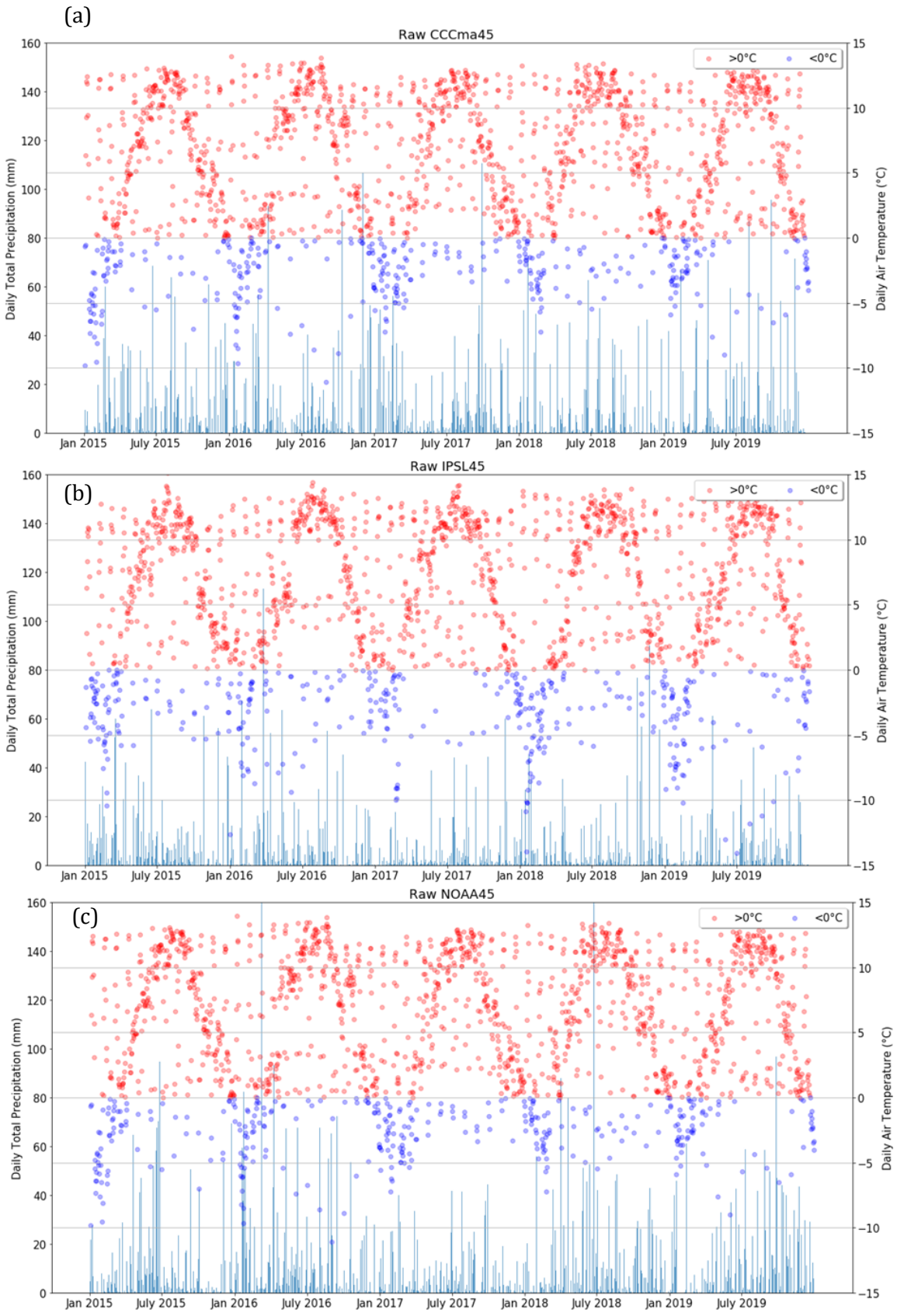

Figure 5.12 (a-c) Daily mean temperature and daily total precipitation prior to downscaling for PD time-slice for three RCMs, with temperatures categorised into above (red) and below (blue) freezing.

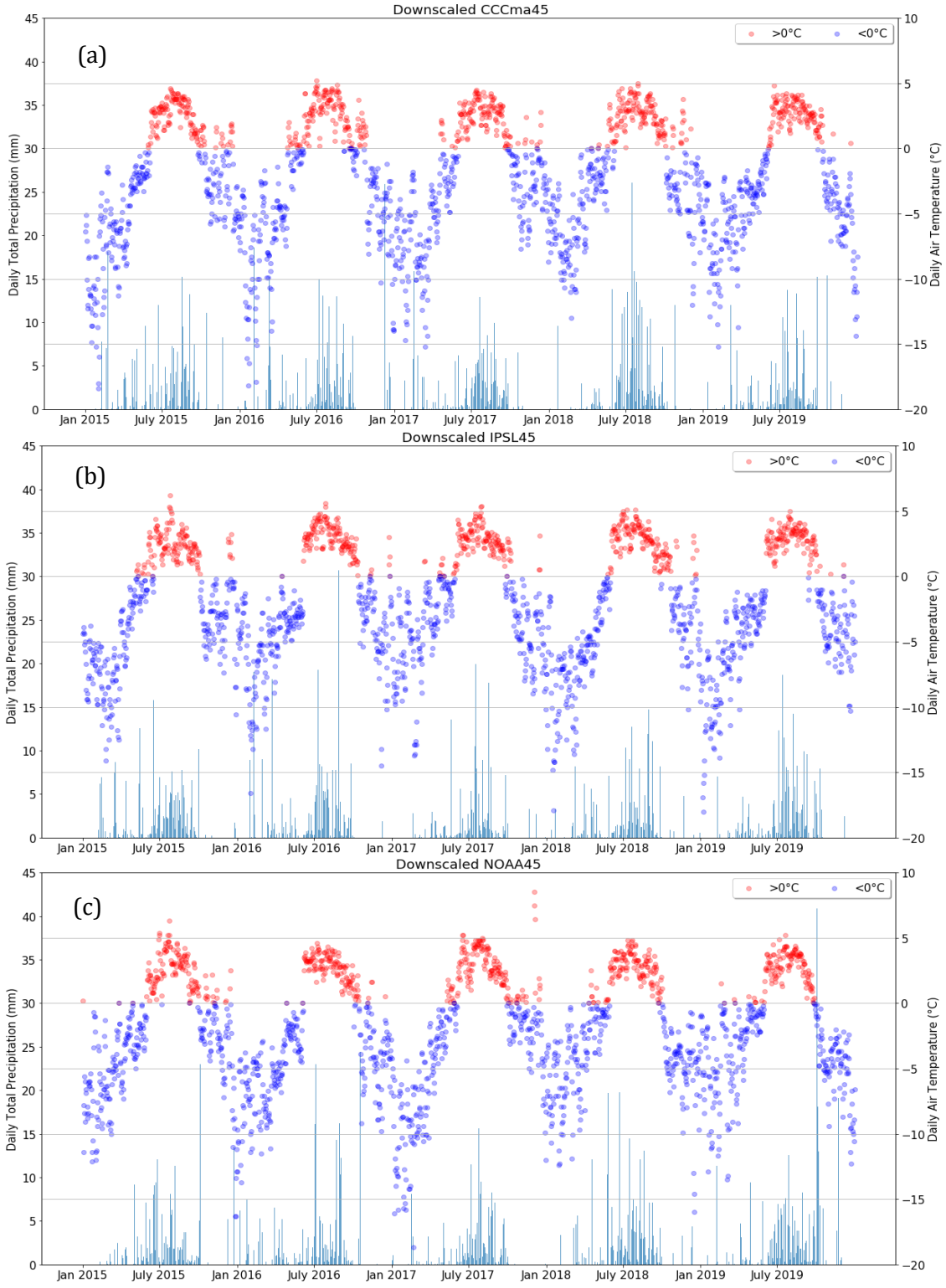

Figure 5.13 (a-c) Daily mean temperature and daily total precipitation following downscaling by QM for PD time-slice for three RCMs, with temperatures categorised into above (red) and below (blue) freezing.

For the entire 14 years of observations used for calibration and validation, monsoon precipitation accounted for 62% of total annual precipitation. For the 2015-2019 period, 58.5% of annual precipitation fell during the monsoon period (Figure 5.14). This figure is lower than those reported elsewhere of annual sums of ~450-475 mm and 80% of annual precipitation occurring between June and October (Bertolani et al., 2000; Bookhagen and Burkan, 2006; Ueno et al., 2008; Shea et al., 2015; Benn et al., 2016), compared to 67.5% of precipitation falling between June and October in the reference observations. This discrepancy partly stems from the interannual variability in the strength of the monsoon and of heavy precipitation events from winter westerly disturbances (as seen by the standard deviation bars; Figure 5.14). The winter and pre-monsoon of 2015 was unusually wet with the monsoon only accounting for 55% of the annual precipitation. The higher proportion of monsoon precipitation (and lower annual sums) reported elsewhere likely are derived from precipitation quantities calculated from tipping bucket measurements, such as the one located at the Ev-K2-CNR run Pyramid observatory. These known to systematically underestimate solid precipitation, particularly during high winds (Sherpa et al., 2017).

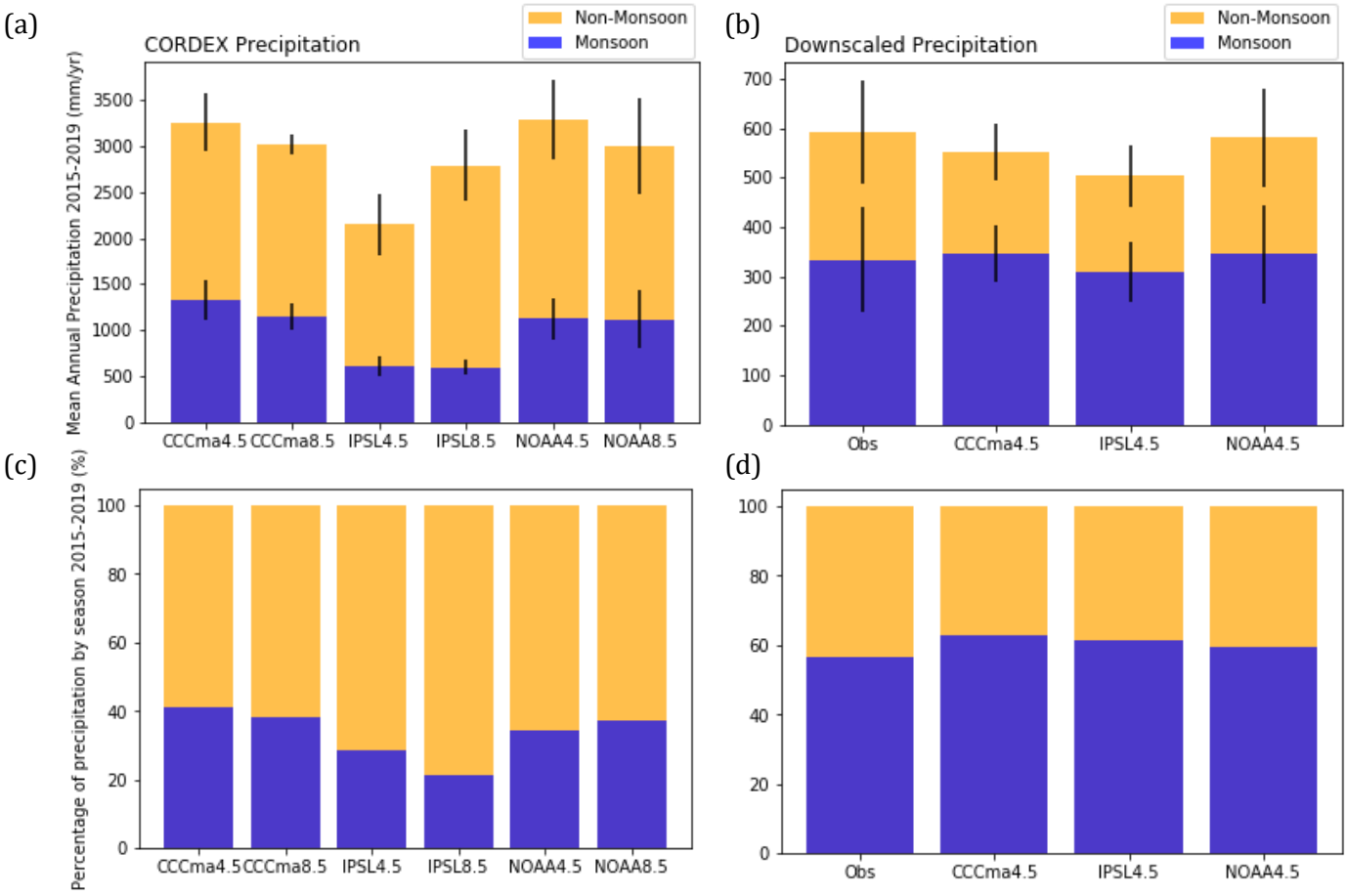

Figure 5.14 Annual precipitation totals for non-monsoon and monsoon months pre and post downscaling with standard deviation between selected years shown by black bars (a and b) and as their seasonal percentages (c and d). Only the downscaled data for RCP4.5 is used for the present day.

The distribution of downscaled temperatures from the CCCma climate data in comparison to observations show that a good match (Figure 5.15). Though vastly improved both in absolute values and distribution of temperatures in both seasons, there is still a slight warm bias in the downscaled data, mainly seen in the higher minimum temperatures compared to observations. The three downscaled RCMs show good agreement in the mean annual air temperature (-2.15 ±0.05°C; Figure 5.16). Temperature seasonality is well resolved following downscaling, with monthly T_{mean} and T_{min} generally matching observations well across the PD time-slice (Figure 5.16). There is a tightening in the range between T_{min} and T_{max} during the monsoon, which would translate to a decreased diurnal temperature range following disaggregation, agreeing with observations (Figure 5.5a). Downscaled T_{max} is often too high during the post-monsoon and winter relative to observations, and T_{max} from NOAA is too high in the pre-monsoon and monsoon. There is a warm bias of up to 3.9°C for the downscaled IPSL $T_{mean,}$ T_{min} and T_{max} in January, though temperatures have a better match with observations in the pre-monsoon and month of usual monsoon onset (June) compared to the downscaled CCCma and NOAA temperatures.

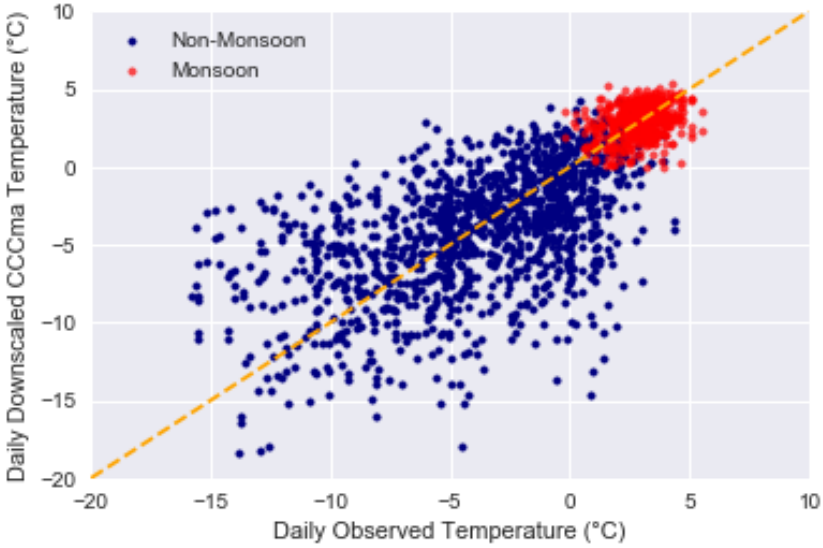

Figure 5.15 Daily downscaled temperature for CCCma against observations for 2015-2019, split by monsoon/non-monsoon with 1:1 line to aid analysis of temperature distributions (dashed orange line).

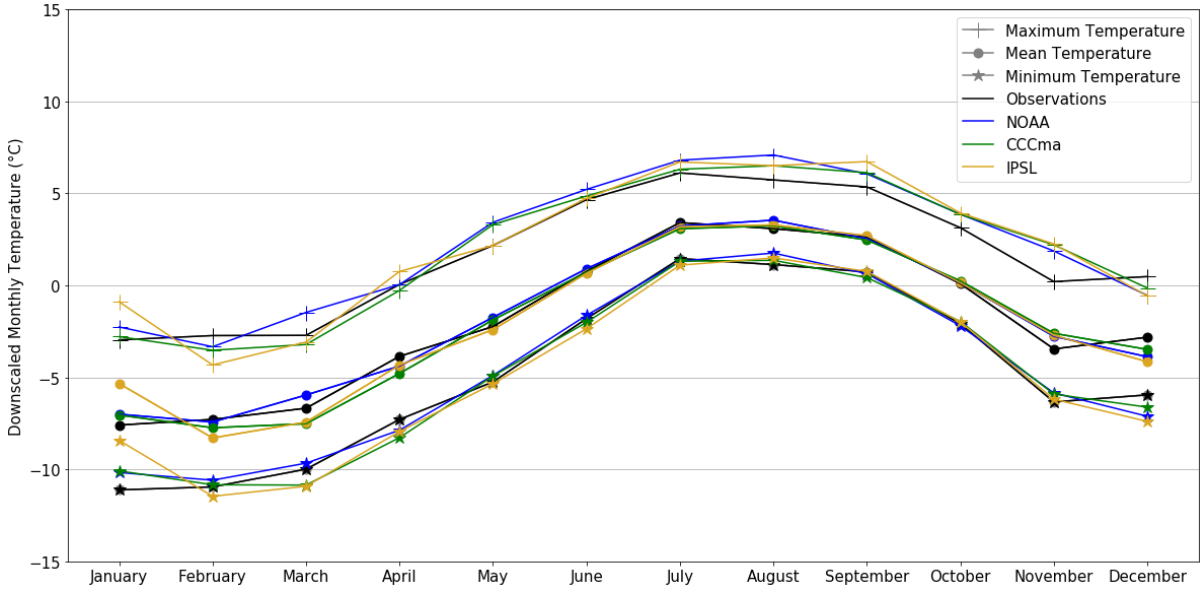

Figure 5.16 Downscaled monthly mean, maximum and minimum temperature calculated for the PD time-slice. T_{min} and T_{max} are used to disaggregate daily downscaled temperatures in equation 5.4. For the observations, T_{min} and T_{max} are calculated from hourly data and then the monthly mean is calculated.

Hourly disaggregation of precipitation means that, although rare, extreme precipitation events are spread throughout the day. The maximum hourly precipitation recorded in the observational reference period is 6 mm, in comparison to 3.4 mm, 3.3 mm and 2.6 mm for the disaggregated precipitation from NOAA, IPSL and CCCma, respectively. In the 5 years of observations (Figure 5.17a) there are 9 hours during which >3 mm of precipitation fell, whereas this did not occur in the CCCma downscaled data (5.17b) and the precipitation is instead spread across several hours. The temperature seasonality is much improved following disaggregation, yet hourly maximum temperatures is often higher than observations during the monsoon. The incidences of extremely low temperatures (i.e. less than -10°C) occurring during the monsoon are lower in the hourly temperatures from the downscaled CCCma data (Figure 5.17b). However, the proportion of temperatures above and below freezing are well resolved following QM with normal distribution (Figure 5.21).

The seasonality of modelled wind speed is fairly well represented in the raw CCCma model data (Figure 5.18c) though the reduction in wind speed with the onset of the monsoon is overestimated. Following downscaling the absolute values are closer to observations. The maximum wind speeds are not as prolonged as in the observations, though the seasonality and monsoon wind speeds are improved compared to the raw CORDEX data.

Modelled radiation components are subject to biases from parameterisations of cloud feedbacks and land-atmosphere interactions within RCMs. The SW_{in} temporal patterns in the raw IPSL data

are able to simulate the seasonality and the high variability seen in the observational record. The reduction in SW_{in} with the onset of the monsoon (Figure 5.18a) is not resolved by the three CORDEX RCMs. This reduction in SW_{in} is mirrored by an increase in observed LW_{in} which has a much clearer seasonal signal than SW_{in}. This increase with the monsoon onset is apparent and slightly overestimated in the raw CORDEX data (Figure 5.18b). The seasonality and absolute values are much improved following QM using a beta distribution. The sub-daily patterns of these components are also critical for energy balance modelling, particularly for SW_{in} which has a strong diurnal signal that varies by season, and these are well resolved (Figures 5.6 and 5.7).

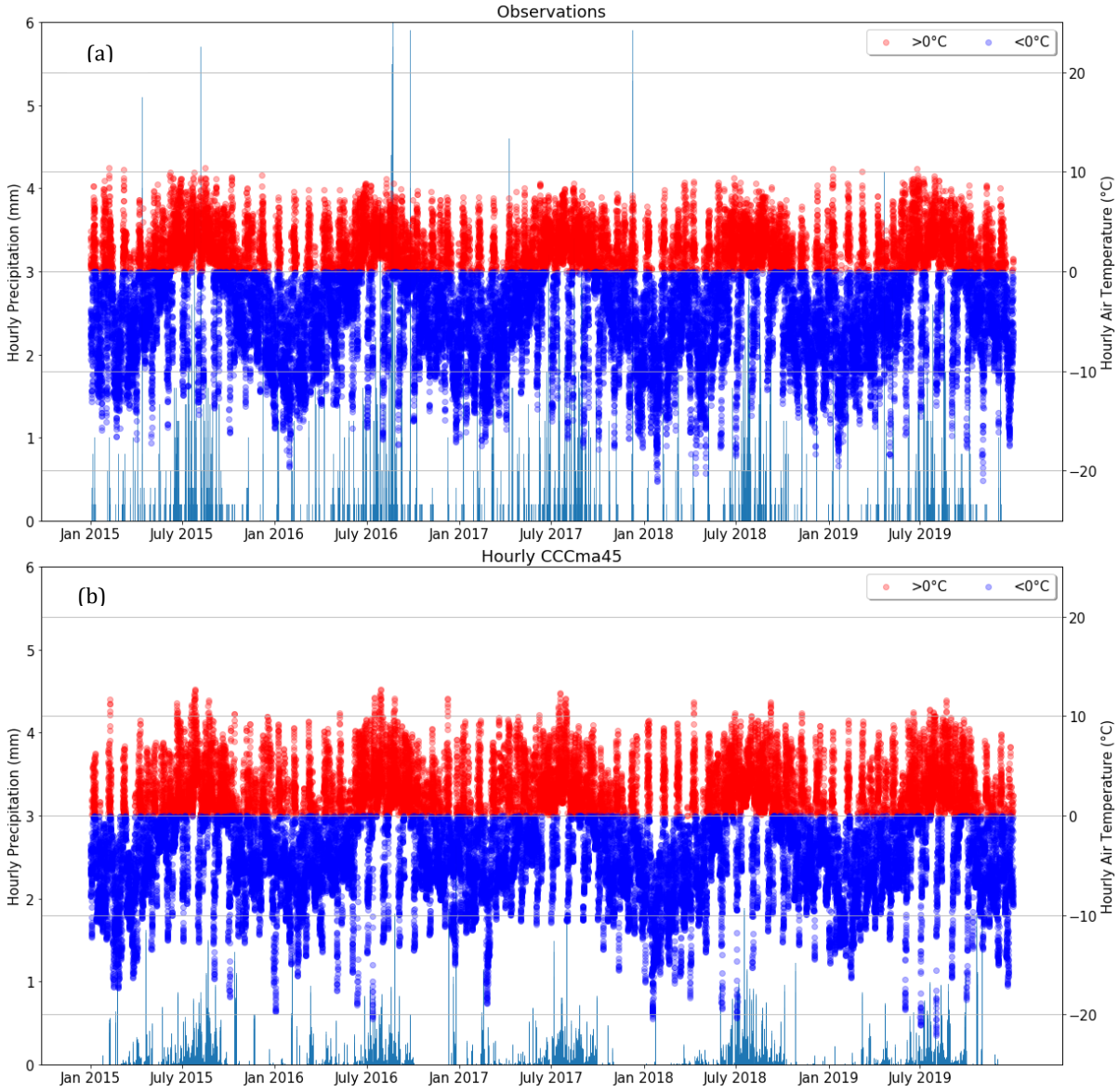

Figure 5.17 Hourly observations (a) and disaggregated hourly data for CCCma (b) as an example of disaggregated data.

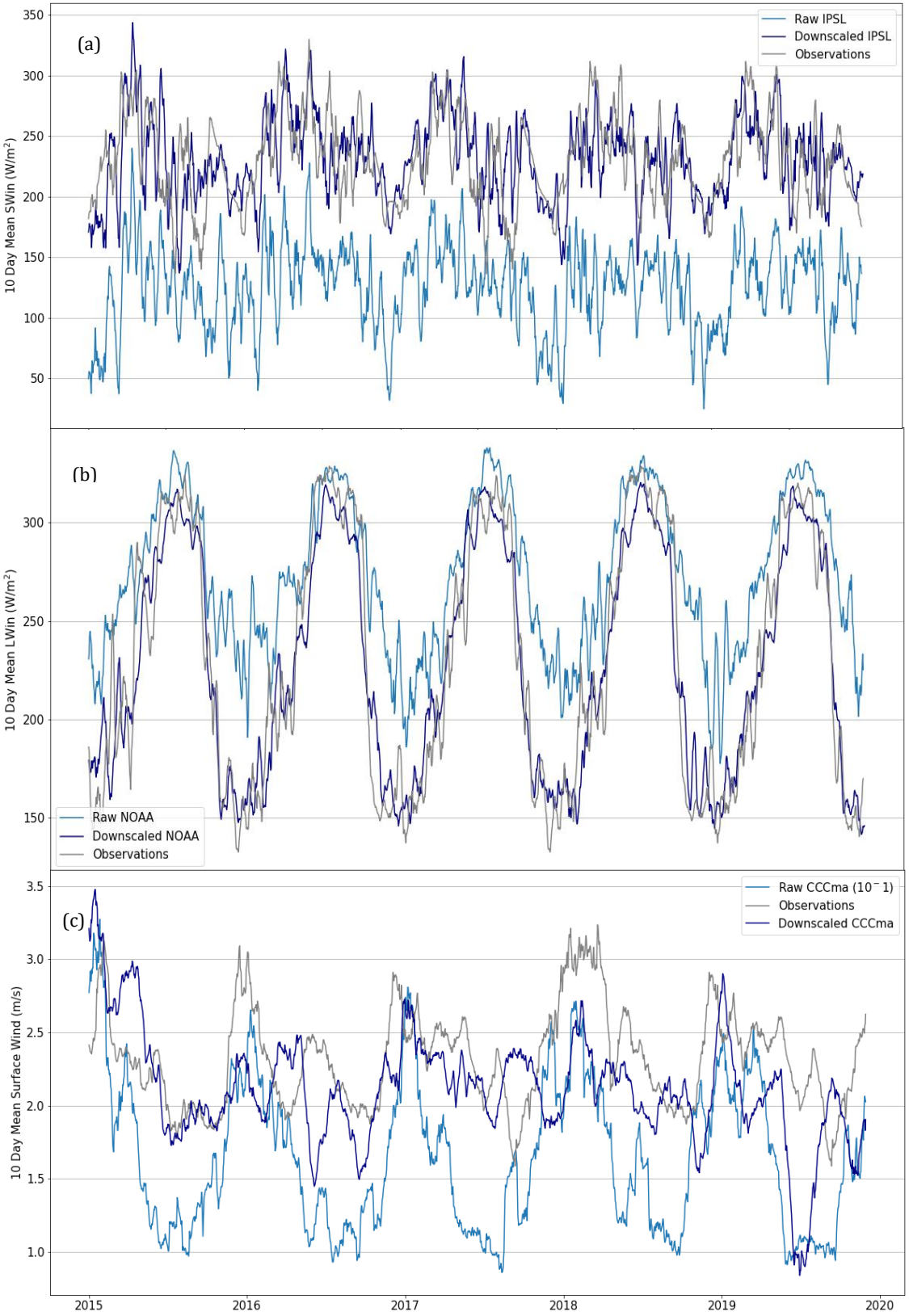

Figure 5.18 Raw CORDEX, observed and downscaled SWin (a), LWin (b) and wind speed (c). Each of the three CORDEX RCMs are used as example. Note that the raw wind speeds are 10-1 so as to fit on the same scale as observations, as were at times an order of magnitude higher.

5.3.2 Future downscaled climate scenarios for Khumbu Glacier

Both prior to and following downscaling, under all RCPs and across all seasons, temperatures are higher in the future time slice than for the present day. Disparities in T_{mean} between RCMs in the increase into the future. Under RCP4.5, for IPSL annual temperatures are -0.56°C for IPSL, -0.03°C for CCCma and -0.73°C for NOAA. Under RCP8.5, these were 1.63°C for IPSL, 1.96°C for CCCma and 1.62°C for NOAA. Annual temperature rise is most significant in the downscaled CCCma dataset, with increases of as much as 2.2°C and 4.1°C for RCP4.5 and 8.5 in the 80 years between time-slices.

There is higher disagreement between models for T_{max} and T_{min} than for T_{mean}, and this is particularly true under RCP8.5. At points in the year the difference between T_{min} and T_{max} is significantly larger under RCP8.5 than under 4.5. This is particularly true during the pre-monsoon. For example, in April the difference between T_{min} and T_{max} under RCP4.5 is the same as the difference between T_{min} and T_{mean} under RCP8.5. There is better agreement between models under the present day than for either of the future RCP downscaled monthly temperatures (Figure 5.16).

Monthly T_{mean} exceeds 0°C one month earlier (May) in the future time-slice under RCP4.5 (5.19a) compared to the downscaled PD time-slice (Figure 5.16). This occurs in April under RCP8.5 for IPSL and CCCma. This timing is likely to be similar for much of the ablation area of Khumbu Glacier given the low angle of the tongue, though will be delayed for the steeper upper ablation area and accumulation area. There is reduced seasonality in T_{max} for the CCCma dataset under RCP4.5 compared to RCP8.5. Interestingly, the monsoon period is the only time of year where monthly CCCma T_{max} is significantly warmer (approximately 2.5°C) under RCP8.5 compared to RCP4.5.

Discrepancies in future annual and seasonal precipitation totals between RCMs remain, though are reduced following downscaling (Figure 5.20). There is no evidence of a strengthening in the monsoon before or following downscaling, seen by the proportion of monsoon precipitation compared to present day (cf. Figure 5.14 c and d vs Figure 5.20 c and d). However total annual precipitation increases for all RCMs in the future time-slice, by on average 14.8% with little difference between the two RCPs. The mean annual precipitation difference between the present and future time-slices in the raw RCM data is 6%. Future annual precipitation for 4 out of 6 of the downscaled RCMs exceeds 600 mm, whereas none of the present-day RCMs or observations exceed this. An increased frequency of days with high precipitation (defined here as > 15 mm daily precipitation) mostly in the pre and post monsoon is mostly responsible for this. Monsoon precipitations remains predominantly drizzle into the future. The number of high precipitation days increases by a factor of 5 and 7 under RCP4.5 and 8.5 in the IPSL data, respectively. For the NOAA

data, the number of high precipitation days doubles relative to observations (where there are 22 days) for both RCPs, though is higher under RCP4.5.

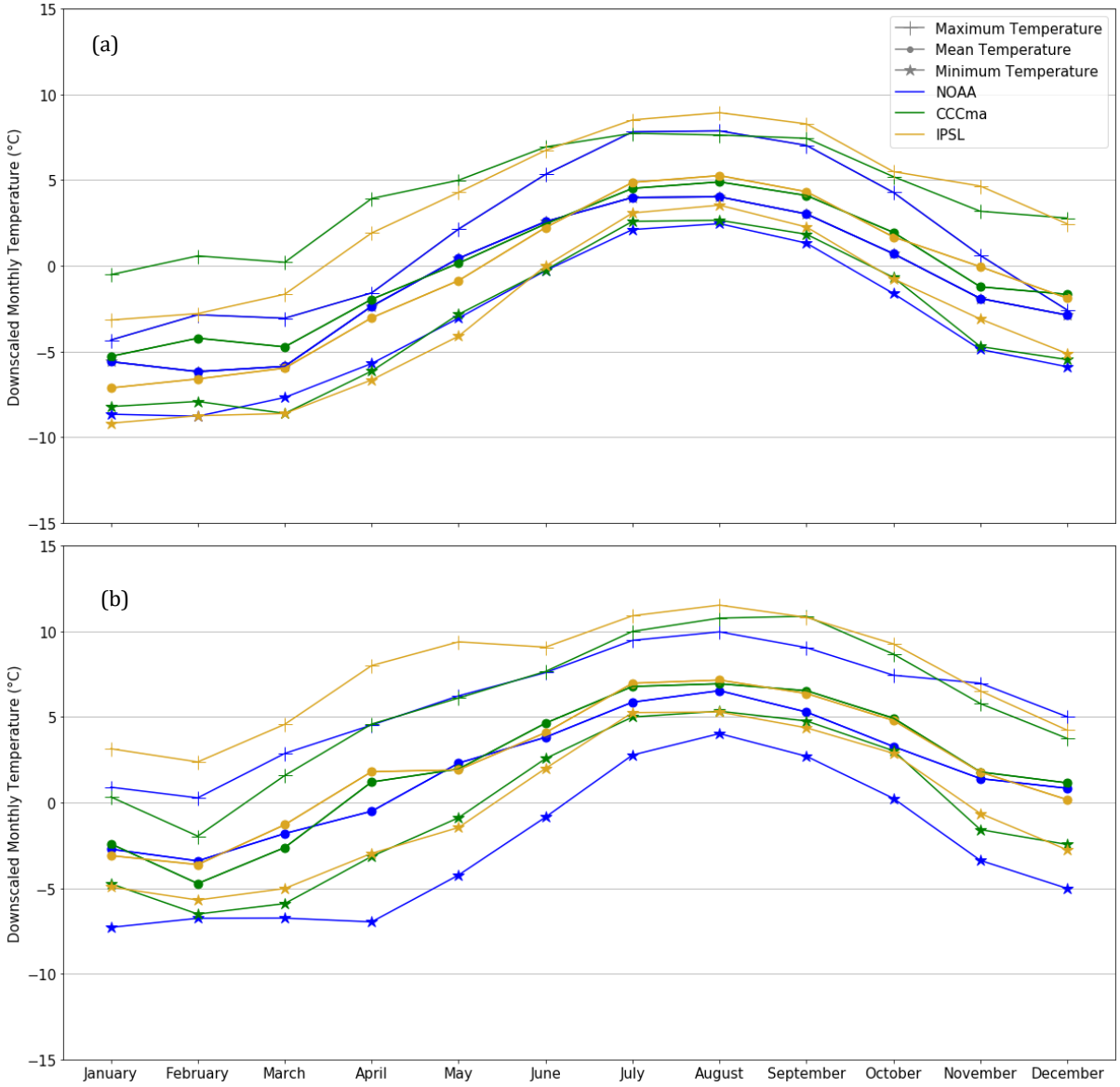

Figure 5.19 Downscaled monthly mean, maximum and minimum temperature calculated for the future time-slice under (a) RCP4.5 and (b) RCP8.5.

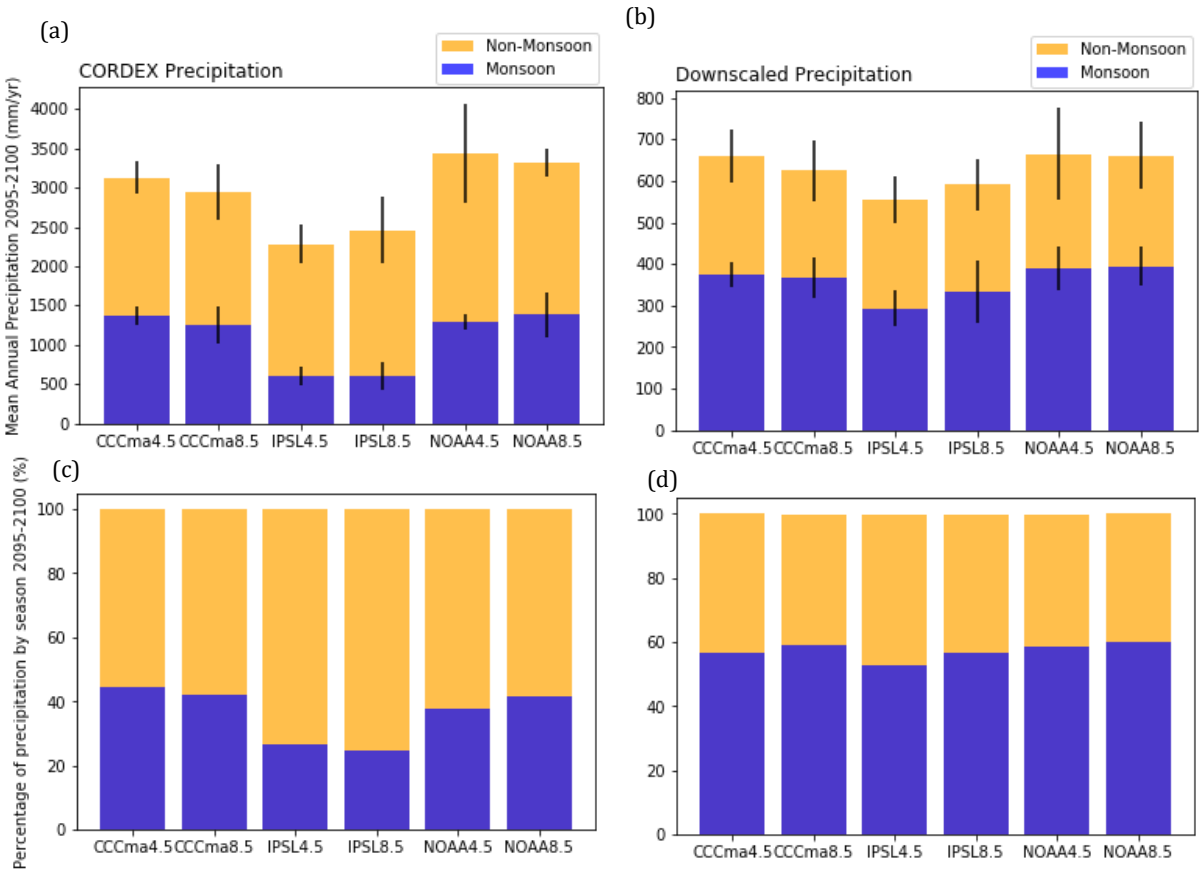

Figure 5.20 (a and b) Future time-slice annual precipitation totals for non-monsoon and monsoon months pre and post downscaling with standard deviation between selected years shown by black bars and (c and d) split as seasonal percentages. Note different scales on the y axis between the raw and downscaled precipitation.

5.4 Discussion

5.4.1 Implications for glacier modelling

Quantile mapping improves the representation of the monsoon in the seasonal precipitation cycle compared to the raw RCM data. However, high magnitude events outside of the monsoon, such as those recorded over several days in December 2015 and January 2016 in the observations, are less frequent or of lower magnitude in the downscaled PD precipitation data. NOAA precipitation has the closest match to observations, with 49 days with precipitation totals >15 mm compared to 84 for observations, and IPSL only has 23 days. These events are often triggered by winter westerly disturbances (Ueno et al., 2008) and can substantially alter annual glacier mass balance.

The disaggregation methods used here for all variables excluding precipitation match the mean diurnal cycles, whilst allowing some stochasticity through the varied amplitudes that force the

disaggregation, particularly for temperature. The proportion of temperatures above and below 0°C is generally the same following disaggregation, with any differences stemming from daily t_{max} and t_{min} which determine the amplitude (Figure 5.21). A temperature-index approach would produce highest mass loss in the present under IPSL and in the future under a CCCma RCP8.5 climate (Figure 5.21). At the time of writing, there appears to be only one study that has explicitly used or required temporal disaggregation for glacier modelling in the literature. Hanzer et al. (2017) used a variety of disaggregation procedures with EURO-CORDEX daily data to hourly for modelling glaciers of the Ötztal Alps, Austria.

Quantile mapping improves the representation of the monsoon in the seasonal precipitation cycle compared to the raw RCM data. However, high magnitude events outside of the monsoon, such as those recorded over several days in December 2015 and January 2016 in the observations, are less frequent or of lower magnitude in the downscaled present day precipitation data. The present day NOAA precipitation has the closest match to observations, with 49 days with precipitation totals >15 mm compared to 84 for observations, and IPSL with only 23 days. These events are often triggered by winter westerly disturbances (Ueno et al., 2008) and can substantially alter annual glacier mass balance. The mass balance modelling results from these three downscaled climates and comparison with observations will help determine the most realistic present day climate.

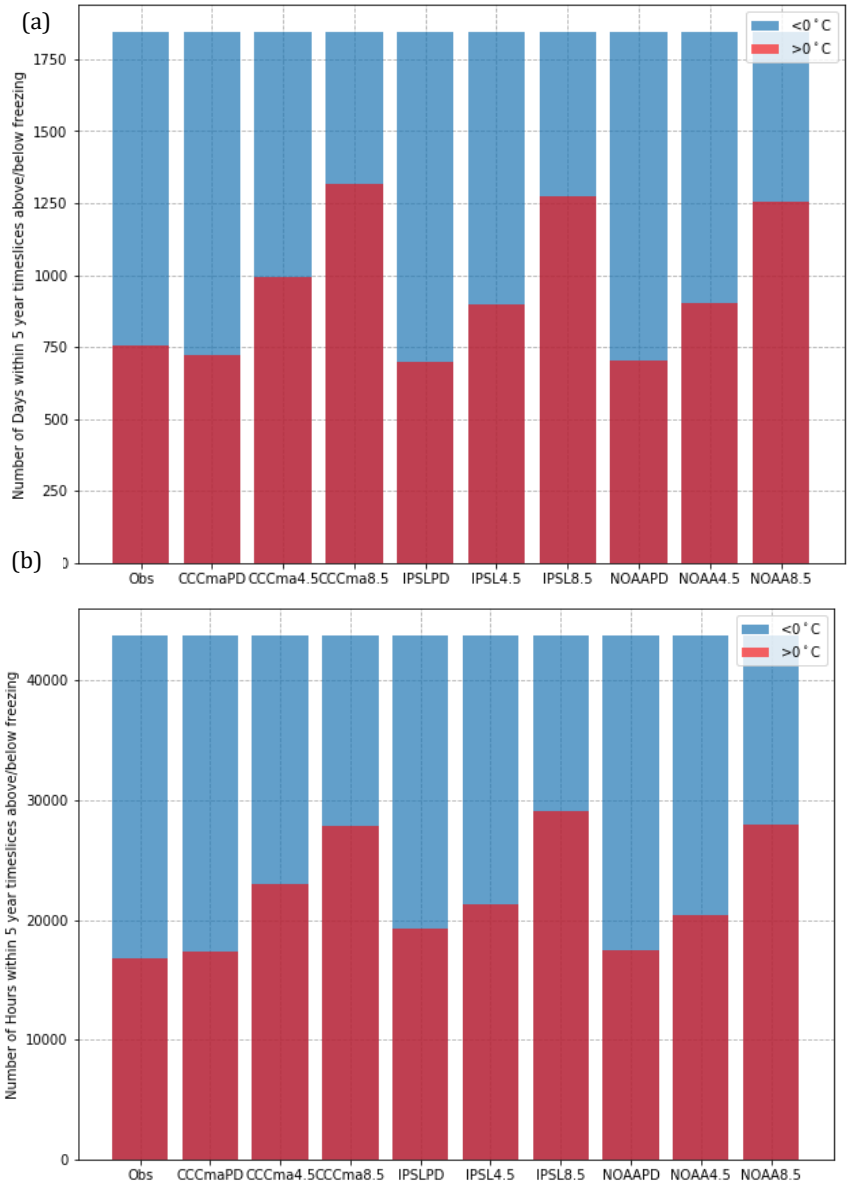

Figure 5.21 Proportion of temperatures occurring above and below freezing for the PD time-slice and future time-slice (for each RCP) for the (a) downscaled daily data and (b) following disaggregation. NB (a) only includes the daily T_{mean} and a change in the temperature split above/below freezing following disaggregation may stem from the amplitude defined by T_{min} and T_{max}.

The precipitation diurnal cycle is prominent in this region, and in the absence of other appropriate methods for the local climate, the mean diurnal trend was applied to the daily data. Given the more extreme diurnal cycle during the monsoon, with the "nocturnal peak" that is so distinct for the south facing slopes of the Central Himalaya (Ueno et al., 2001), it is important to differentiate this pattern from the annual trend for disaggregation. Given that ≥60% of annual precipitation falls during the monsoon and that the 0°C isotherm, and thereby the rain/snow threshold, can reach elevations of at least 6,250 m.a.s.l. (as shown in Figure 4.16, Chapter 4), it is critical that this

nocturnal peak is somehow integrated into the disaggregation process, even if in a simple manner as done so here.

The reason behind this peak is disputed, but it has been hypothesised as resulting from interactions between gravity waves and atmospheric instability over the region's high peaks (Barros et al., 2004). It could also be due to meridional circulation bringing depressions from the Bay of Bengal to interact with orographic vertical shear winds from the east, triggering return flows and formation of localised but persistent night-time depressions (Bhatt and Nakamura, 2005). The disaggregation method used in this chapter relies on the assumption that this nocturnal peak will be similar in the future. In the Central Himalaya, strengthened downslope nocturnal winds across seasons since 1987 are associated with significant nocturnal drying at higher elevations (Norris et al., 2020), indicating that this nocturnal peak may become less prominent into the future. This is contrasted by anabatic winds that have acted to prevent diurnal drying in higher elevation regions. The likelihood of precipitation falling as snow rather than rain is much higher during the night-time, particularly during the monsoon, so a reduction in this nocturnal precipitation peak could bring an associated reduction in this accumulation input for the region's glaciers.

Wind speed absolute values are at times an order of magnitude too high amongst all three CORDEX RCMs relative to observations of the same period (Figure 5.18a). The significant discrepancy in the raw RCM wind data is likely in part due to winds from CORDEX being modelled 10 m from the surface, whereas the AWS anemometer height is 5 m. This height correction would decrease RCM winds by ~30% (see Chapter 3, section 4.3). There are several >7000 m peaks within the CORDEX grid box and these features may produce higher modelled wind speeds (gusts of up to 50 m/s have been recorded by the South Col AWS; Matthews et al., 2020). Overestimation of wind speeds within CORDEX RCMs have also been highlighted in other regions with less complex terrain (Li et al., 2019), and was also found in grid boxes in the lowlands south of the Khumbu as a sense check for this study. An increase (decrease) in wind speed of 0.75 m/s decreased (increased) spatially averaged glacier MB by 1 m w.e. a^{-1} (0.87 m w.e. a^{-1}). Though this sensitivity is not additive (Figure 4.14, in Chapter 4), calculating glacier MB with raw RCM wind data could produce highly erroneous results. Following downscaling, this systematic bias in annual mean absolute wind and seasonality of wind speeds was substantially lessened.

5.4.2 Comparison of future climate with other studies

Under RCP4.5 (8.5) mean annual temperatures are -0.56°C (1.63°C) for IPSL, -0.03°C (1.96°C) for CCCma and -0.73°C (1.62°C) for NOAA. Annual temperature rise is most significant in the downscaled CCCma dataset, with increases of as much as 2.2°C and 4.1°C for RCP4.5 and 8.5, respectively in the 80 years between time-slices. Temperature change is most substantial in the winter, mirroring findings for the Central Himalaya and the Koshi river (Table 5.3).

On average, T_{max} increases by 0.2°C more than T_{min} under the two future emission scenarios. This contrasts with observed historical trends, where DTR reduced due to a disproportionate increase in T_{min} at Pyramid and the wider HKKH (Salerno et al., 2015; Ren et al., 2017; Sun et al., 2017, Table 2.1). However this trend in increased T_{max} relative to T_{min} has been observed in Nepal up to 2,566 m.a.s.l (Thakuri et al., 2019, Table 2.1). This indicates that this trend is an artefact from the raw RCM data and reaffirms the earlier point based on the annual total precipitation, that this gridpoint is representative of the Dudh Koshi at ~2,000 m.a.s.l..

Annual precipitation increases amongst all downscaled RCMs relative to present day by up to 100 mm for CCCma under RCP4.5. Despite this, there is no evidence of future weakening or strengthening of the monsoon with the seasonal split remaining the same both prior to and following downscaling (Figures 5.14 and 5.20). Sanjay et al. (2017b) found poor consensus between CORDEX RCMs for future changes in monsoon and winter precipitation particularly in the Central Himalaya. Future intensification of the monsoon in the Koshi river of up to 44% (Table 5.3, Kaini et al., 2019) contrasts strongly with the findings here. There is an absence of downscaled climate scenarios for this region to compare with the results here. It should be noted that QM depends on the assumption that the bias between the RCM gridpoint and the observations will be the same into the future as it is in the present day (Cannon et al., 2018). Future work to improve regional atmosphere/land feedbacks in RCMs, but also effective future climate downscaling methods, could bring a higher degree of certainty in the direction and magnitude of precipitation seasonality over the coming centuries.

The climate scenarios produced in this study show increased high magnitude precipitation events into the future. This increase is most stark in the NOAA data for both RCPs and in the CCCma data under RCP4.5, where the number of days with >15 mm precipitation is 1.2-1.7 times higher than the present-day equivalents. The future IPSL climate shows an increased frequency of higher magnitude events than the present day, particularly under RCP8.5. Winter precipitation strengthens in line with annual trends, contrasting with projections of decreased winter precipitation for the Central Himalaya (Sanjay et al., 2017b) and under RCP4.5 for the Koshi river (Table 5.3, Kaini

et al., 2019). The low winter precipitation seen at Khumbu Glacier means that just a 15 mm increase in precipitation is a 20% increase into the future, and this is largely due to the increased frequency of high magnitude precipitation days.

The changes in the other downscaled climate parameters are significant compared to the present day, though an increase in incoming longwave radiation is observed, particularly under RCP8.5 (by up to 5% before and following downscaling).

Region	**Emission scenario**	**Temperature change (°C)**	**Precipitation change (%)**	**Year**	**Data source**	**Reference**
Khumbu Glacier	RCP4.5	1.81±0.38 (annual) 1.45±0.44 (summer) 1.77±0.88 (winter)	14.8±4.64 (annual) 5.43±9.47 (summer) 14.1±7.17 (winter)	2015-2020 to 2095-2100	QM of CORDEX South Asia	This study
	RCP8.5	3.91±0.19 (annual) 3.74±0.58 (summer) 4.44±0.23 (winter)	14.87±2.32 (annual) 9.75±4.1 (summer) 19.43±9.69 (winter)			
Central Himalaya	RCP4.5	2.2 (summer) 3.3 (winter) *2.7 (summer)* *3.6 (winter)*	10.5 (summer) 1.5 (winter) *11.8 (summer)* *-0.7 (winter)*	1976-2005 to 2066-2095 *1976-2005 to 2066-2095*	CORDEX South Asia *CMIP5 AOGCMs*	Sanjay et al. (2017b)
	RCP8.5	4.3 (summer) 6.0 (winter) *4.7 (summer)* *5.8 (winter)*	19.1 (summer) -8.8 (winter) *19.1 (summer)* *-8.1 (winter)*			
Koshi river Basin (Nepal/Tibet)	RCP4.5	2.0 (annual) 2.1 (summer) 2.3 (winter)	16 (annual) 20 (summer) -9 (winter)	1981–2010 to 2071-2100	CMIP5 AOGCMs	Kaini et al. (2019)
	RCP8.5	4.1(annual) 3.6 (summer) 4.7 (winter)	39 (annual) 44 (summer) 13 (winter)			

Table 5.3 Summary of temperature and precipitation projections found here and compared to two other studies. Summer/winter are categorised as the summer monsoon (June-September) and winter (December-February) as in Sanjay et al. (2017b). Note the difference between the median of the reference and end-of-century periods is 90 years for the Sanjay et al. (2017b), Kaini et al. (2019) and this study and making temperature/precipitation change more comparable.

5.5 Conclusion

Based on the above analysis the following concluding remarks are made:

- Downscaling with quantile mapping greatly improves the representation of seasonality of climate relative to observations. This is particularly true for monsoon precipitation that was previously poorly resolved in the raw CORDEX RCMs. However, there is less noise following quantile mapping, and less day-on-day variability relative to observations.
- Following disaggregation, the variability is improved, particularly for temperature using T_{min} and T_{max}. The seasonality of the diurnal cycle for temperature and the radiation components is reproduced. Forcing the EBM with this disaggregated climate will determine the efficacy of the present day climate scenarios.
- Annual and seasonal temperature increases are in line with findings from other studies for the region, and are strongly linked to RCP.
- Mean annual precipitation is projected to increase by 14.8% over the next 80 years, but shows no dependency on RCP. Precipitation trends are more linked to the selected RCM demonstrating the poor agreement on strength of future precipitation trends. There is little evidence of monsoon intensification, contrasting with findings from other studies.

Chapter 6 Present-day and future evolution of Khumbu Glacier

6.1 Introduction

Calculations and measurements of glacier mass balance are critical for determining the footprint of anthropogenic warming on glaciers and how this will change into the future. However, the relationship between mass balance and glacier dynamics has been much less explored, particularly for the HKKH (Shea et al., 2015a; Rowan et al., 2015; Wijngaard et al., 2019). Debris-covered glaciers manifest negative mass balances through ice thinning (Benn and Lehmkuhl, 2000; Figure 6.1) and associated deceleration (Dehecq et al., 2019). Surface lowering on both clean and debris-covered ice is strongly related to mass balance change as well as ice flux change (Pellicciotti et al. 2015; Banerjee, 2017). Historical and future projections of glacier change would therefore be incomplete without the consideration of ice dynamics, though mass balance and ice flow modelling are often considered separately. This chapter aims to address this shortcoming in a novel way by integrating a distributed mass balance model with an ice flow model.

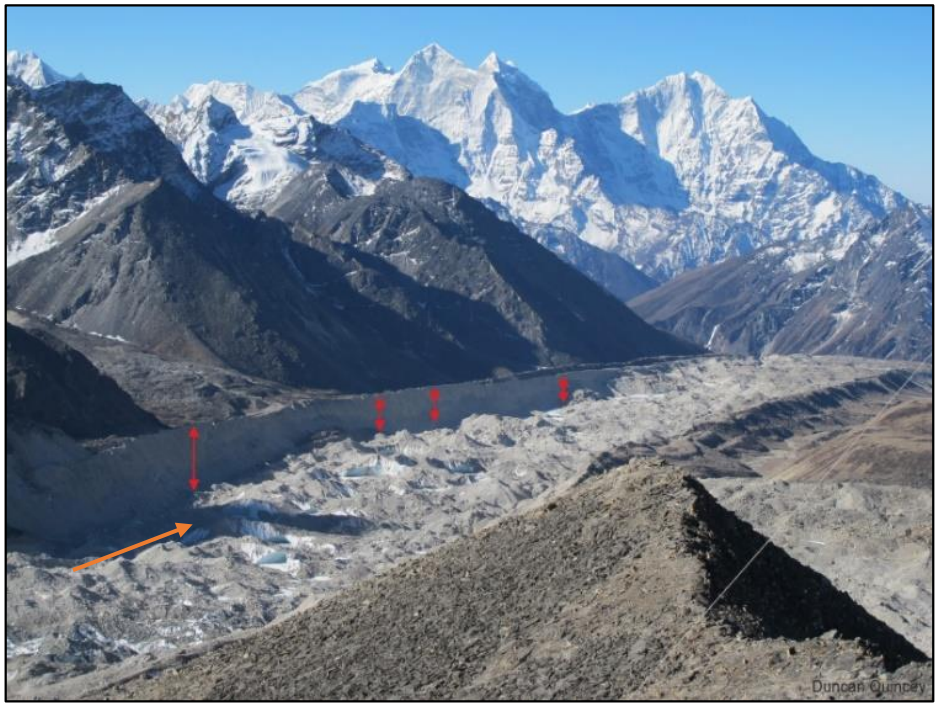

Figure 6.1 Looking down-glacier towards the terminus of Khumbu Glacier where surface lowering from the Little Ice Age lateral moraine crests is clearly visible (surface lowering shown by red arrows and direction of glacier flow by orange arrow). The glacier surface is pitted with supraglacial ponds and exposed ice cliffs.

Mass balance studies usually provide a snapshot of the influence of a climate change signal on glacier ablation/accumulation rates. However, the present-day climate is not immediately exhibited in glacier volumes and ice flow. Glacier response time is the length of time taken for glacier volume to adjust to a new geometry and reach a new equilibrium, or hypothetical steady-state, following a mass balance perturbation (Jóhannesson et al., 1989). This period is typically between 50-100 years for valley glaciers, though is less well constrained for glaciers of the HKKH, particularly DCGs (Rowan et al., 2015; Anderson and Anderson, 2016). The response time is controlled by a multitude of factors that are not restricted to atmospheric forcing. For clean-ice glaciers the response time of a given mass balance change is dependent on glacier length, thickness and velocity at the (active) terminus (Pelto and Hedlund, 2001; Raper et al., 2009; Kirkbride et al., 2012) and ELA (Pelto, 2010). This is much more complex for debris-covered ice surfaces given their well-evidenced non-linear responses to external forcings (Benn et al., 2012).

The presence of thick supraglacial debris complicates the response of glaciers over space and time (Rowan et al., 2015, 2021; Pellicciotti et al., 2015; Anderson and Anderson, 2016). Preferential melt on clean-ice areas will trigger melt-out of englacial debris and ultimately increase debris coverage. Mass loss through surface lowering on debris-covered areas will also enable supraglacial layers to thicken. In theory, this should allow DCGs to be sustained for longer into a warmer future than their clean-ice equivalents, given the insulating effect of debris on ablation rates (Østrem, 1959, and see Figure 4.4). However, observations indicate that mass loss of debris-covered glaciers is close to that of glaciers without debris (e.g. Banerjee, 2017). A contributing mechanism to this debris-cover anomaly (Pellicciotti et al., 2015; Kraaijenbrink et al., 2017; Brun et al., 2019; Rowan et al., 2021) may be the accelerating development of supraglacial ponds and ice cliffs in response to historical warming which act as hotspots of melt and inflate glacier-wide calculations of mass loss. Understanding how debris-covered glaciers respond to changes in climate relies on effective ice flow models designed for DCGs with heterogenous surfaces, that are also able to effectively model the dynamics of ice flux change over time (Banerjee, 2017).

Modelling glacier flow in steep terrain is particularly challenging. Existing ice flow models vary hugely in complexity, from simple flowline models (Oerlemans et al., 1998; Huss et al., 2007; Banerjee and Shankar, 2013) to higher-order three dimensional models (Egholm et a., 2011; Scherler and Egholm, 2020; Rowan et al., 2015, 2021) or Full Stokes models that resolve all flow equations (Zwinger et al., 2007; Pattyn et al., 2008). The Shallow Ice Approximation (SIA) (Hutter, 1983) is the simplest representation of the Full Stokes model, that assumes basal drag perfectly counters the gravitational driving stress and neglects all transverse and most longitudinal stress gradients (Figure 6.2). The SIA is particularly effective for ice masses with small aspect ratios (i.e. “shallow” relative to their horizontal extension; Pattyn, 2002; Le Meur, et al., 2004)

such as ice sheets. The SIA is unsuitable for areas where basal sliding contributes significantly to glacier velocity, such as ice streams and ice divides (Pattyn, 2003) and glaciers in steep terrain (Egholm et al., 2011).

The flow of glaciers in high mountains is restricted by steep, confined valley sides that act to impose more complex stresses on flow. This is especially true for the Khumbu icefall, where the narrow valleys and steep slopes lead to convergence and high velocities, which is evidenced by the fractured surface of evolving crevasses (Altena and Kaab, 2020). To resolve these more complex stresses on flow, higher-order or second-order models include longitudinal and transverse stress. The integrated second-order shallow-ice approximation (iSOSIA, a coupled ice flow and landscape evolution model; Egholm et al., 2011) accounts for these two stresses that govern mountain glacier flow (Figure 6.1). Ice thicknesses simulated using iSOSIA have been shown to compare well with those from a full Stokes model (underestimation of 4%), representing a vast improvement on simple SIA modelling approaches (underestimation of 25%). Ice extents derived from iSOSIA have also been shown to agree well with the full Stokes approach (Egholm et al., 2011).

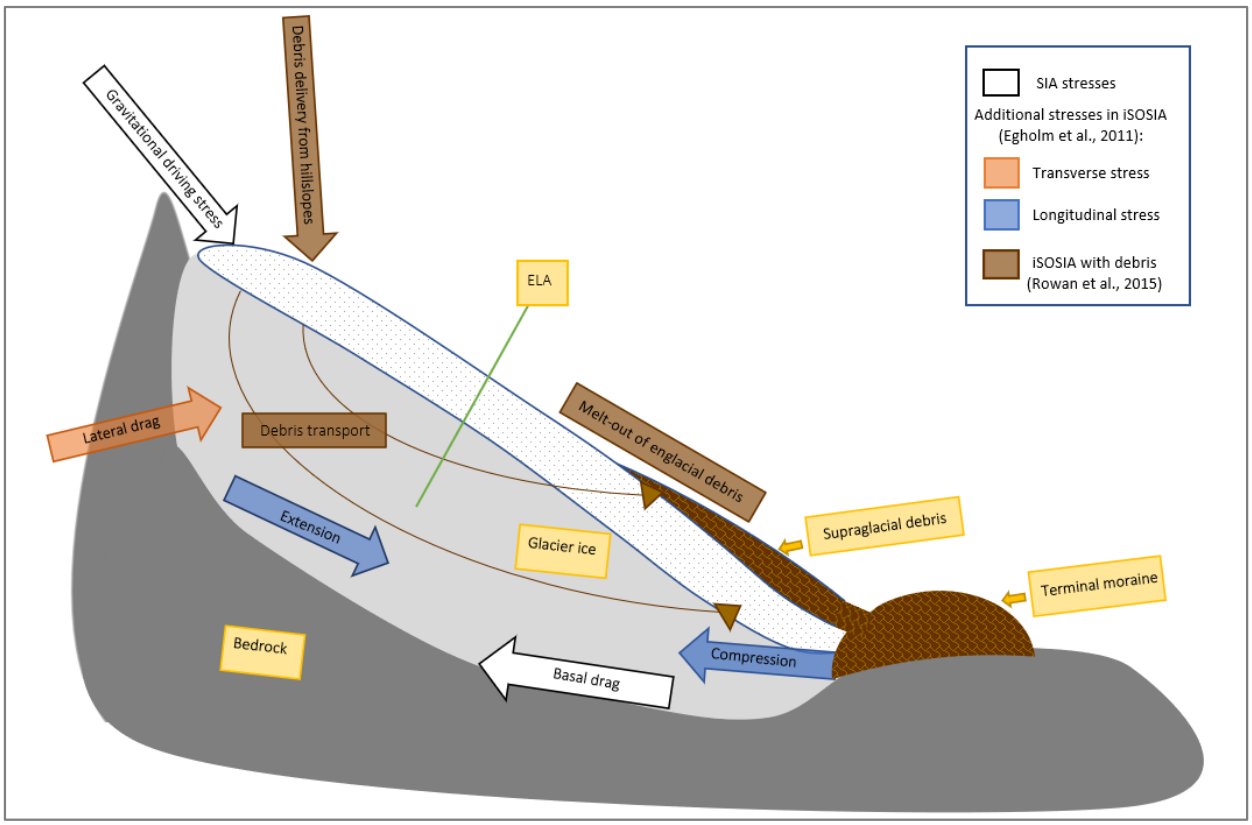

Figure 6.2 Schematic of stresses that are resolved in basic SIA models, and the additional stresses resolved by iSOSIA that are critical for simulating mountain glacier flow. The debris model component is a novel approach to coupling ice flow with debris transport and accumulation, and feedbacks with glacier mass balance (Rowan et al., 2015). This is used in simulations throughout this chapter.

Varying approaches to modelling ice flow in the Himalaya have produced projections of future glacier evolution in the region that differ markedly. At the most extreme end, work using an ice redistribution model intended for clean-ice glaciers predicted that 70 to 99% of glaciers in the Everest region will be lost under RCP4.5 and 8.5, respectively (Shea et al., 2015). Reductions in ice volume of up to 50% in the Dudh Koshi catchment were predicted by Soncini et al. (2016) using a glacio-hydrological model, where glacier flow was driven by a simplified force balance (Wallinga and van de Wal, 1998). This model corrected for the suppression of ablation under a homogenous supraglacial debris cover, albeit in a relatively crude and spatially invariant manner. In this study, glacier mass loss was found to be most significant for elevations ≤6,500 m.a.s.l.. Volume loss of 8-10% was predicted under RCP4.5 by Rowan et al. (2015) using the iSOSIA model. The addition of englacial debris transport, an evolving supraglacial debris layer (Figure 6.2) and the associated feedbacks on glacier mass balance resulted in a much more realistic representation of the complex dynamics that govern Khumbu Glacier evolution, although simulated mass loss was underestimated relative to observations. For this reason, a stronger sub-debris ablation parameterisation developed in Rowan et al. (2021) is used in for the simulations in this study and is discussed in more detail later.

Shea et al. (2015a) and Soncini et al. (2016) parameterised mass balance using a degree-day approach that (a) accounts for aspect (Shea et al., 2015a) or (b) includes the short-wave radiation balance (Soncini et al., 2016). Rowan et al. (2015) parameterised MB as a function of elevation, where ablation/accumulation rates scaled linearly with temperature. In their study, future climate change was represented using the delta method and the ELA was adjusted in line with the temperature scenarios; other climate parameters were not considered.

In Chapter 4, the degree-day approach was considered unsuitable for Khumbu Glacier, in part due to it being a summer-accumulation type glacier. Large parts of the tongue lie along the 0°C isotherm between June and September meaning sub-daily temperature and precipitation cycles are vital for simulating accurate ablation/accumulation rates. A high sensitivity of glacier MB to the radiation components SW_{in} and LW_{in} was also noted, and the contribution of these fluxes to the mass budget was found to vary significantly both spatially and seasonally. The non-linearity of the mass balance of DCGs with elevation, including Khumbu Glacier, with the highest ablation rates in the upper ablation area causing a reversal of the MB gradient and glacier slowdown (Quincey et al., 2009; Benn et al., 2009), suggests that the methods used by Shea et al. (2015), Soncini et al. (2016) and Rowan et al. (2015, 2021) are not adequate representations of mass balance. This reinforces that a distributed MB approach is preferable.

In this chapter, a distributed glacier mass balance that accounts for many of these factors which complicate the mass balance of Khumbu Glacier is used to force the higher-order ice flow model

iSOSIA. At the time of writing, a higher-order ice flow model has not been forced with a distributed mass balance to model present-day and future evolution of a glacier. This work builds on the study by Rowan et al. (2015) with the novel contribution being the distributed mass balance forcing, and improved representation of climate (including the seven parameters that are used to force COSIPY, rather than just temperature) and future climate scenarios. An ensemble of mass balance forcings from the three downscaled RCMs (Chapter 5) are used to explore how present day and future climate uncertainty impact on glacier evolution. Improved parameterisations of sub-debris ablation, developed and evaluated against three decades of mass loss in Rowan et al. (2021), is used alongside this novel distributed glacier-wide mass balance forcing to produce more robust projections of glacier change. The interplay of glacier-wide mass balance with three sub-debris ablation parameterisations is first investigated in the historical simulations. This study then builds further on the work by Rowan et al. (2021) by simulating future glacier evolution.

6.2 Model description

iSOSIA is a depth-integrated, higher-order model that resolves the longitudinal and transverse stress gradients that are imposed by the topography. It was originally used to study landscape evolution, including erosion and moraine building (Egholm et al., 2011; Brædstrup et al., 2016), but it has since been applied to model glacier response to climate change (Rowan et al., 2015).

Ice flow in iSOSIA is driven by internal ice deformation and basal sliding with

$$\bar{u} = \bar{u}_d + u_b \tag{6.1}$$

where the contribution of ice deformation ($\bar{u}_d$) to velocity ($\bar{u}$) depends on a polynomial function of ice thickness, coefficients that account for the angle of the ice surface and bed, as well as longitudinal stress gradients (Figure 6.2, Egholm et al., 2011; Rowan et al., 2015). u_b refers to velocity from basal sliding.

Basal sliding is regulated by basal shear stress, which is controlled by ice thickness, velocity and surface and basal slope. There is a maximum bound on basal sliding that comes from drag from basal protuberances (Schoof, 2005). The relationship between basal shear stress and sliding velocity is parameterised as follows

$$\tau_s/N = C_c \left(\frac{u_b/N^n}{u_b/N^n + \lambda_0}\right)^{1/n} \tag{6.2}$$

where τ_s is basal shear stress C_w, C_e, and C_c are sliding coefficients (defined in Table 1 of Brædstrup et al., 2016), u_b is the velocity from basal sliding and λ_0 is a constant that defines the bed geometry

(Schoof, 2005; Gagliardini et al., 2007). The inaccessibility of the ice-bed interface means the various sliding laws that are used in glacier models cannot be tested (Zoet and Iverson, 2017). However, resolving the impact of these obstacles on basal drag, including separation of the basal ice from their leeward side, is an improvement to the standard empirical, power-law approach that assumes infinite levels of basal drag from the bed with increased basal sliding (Nye, 1970, Kamb, 1970; Budd et al., 1979).

Few mass balance models resolve avalanching, including COSIPY. In Chapter 4 this was discussed as a major limitation, as avalanching from the steep hillslopes of the Western Cwm is thought to comprise 66-75% of the total accumulation of Khumbu Glacier (Inoue, 1977; Benn and Lehmkuhl, 2000). In these iSOSIA experiments snow and ice are removed from hillslopes with a critical slope angle greater than 28° and are then distributed uniformly across the ice surface, with mass conserved. This threshold was previously applied in the simulations by Rowan et al. (2015) and was found to be low enough to prevent snow/ice accumulation on slopes that are observed to be bare, whilst allowing accumulation on steep sections of the glacier.

6.2.1 Debris transport

Debris is fed to the glacier surface from upper hillslopes, and debris concentrations were estimated from hillslopes that are without ice and assuming erosion rates of 1 mm a^{-1} (Rowan et al., 2015, 2021). Avalanching is likely responsible for much of the debris accumulation on the surface, but there is little information regarding the magnitude and frequency of these avalanches, Therefore for the purposes of these simulations this eroded debris from the headwalls, which is then transport via avalanching onto the glacier, is assumed to be uniformly spatially distributed across the accumulation area.

Debris is diffused englacially via a Eulerian advection scheme:

$$\frac{\partial c}{\partial t} = -\nabla.\{cu\} \tag{6.3}$$

where debris concentration (c) within the ice updates over time (t). Though iSOSIA is two-dimensional and velocity (u) is depth-integrated, depth-dependent calculations with 20 vertical glacier layers were used for tracking of the englacial debris (Rowan et al., 2015; Scherler and Egholm, 2020). The vertical distribution of velocity assumes that horizontal velocity through ice deformation reduces with depth as a fourth-order polynomial:

$$u(z) = \frac{5}{4}\left[1 - \left(\frac{z}{h}\right)^4\right]\bar{u} + u_b \tag{6.4}$$

where z is the burial depth below the ice surface, h is ice thickness and ū is the horizontal velocity across the 20 vertical layers.

Vertical velocity is scaled linearly with surface ablation/accumulation and basal melting, the calculation for which is described in Rowan et al. (2015).

Debris is transported passively with ice flow, generally following a concave path with submergence in the accumulation zone and emergence in the ablation zone (Figure 6.2). Numerical diffusion of debris occurs between grid cells meaning the debris input mechanism from the headwalls of the accumulation area does not impact supraglacial debris distribution following melt-out at lower elevations. The distribution of debris in the ablation area is a function of mass conservation, thinner debris layers are found where ice flow lines diverge, as they often do in the ablation area. In one-dimensional glacier models (e.g. Anderson & Anderson, 2016, 2018) debris thickens with distance downglacier, which is less realistic. Simulated debris thicknesses were compared with observations and found to correlate well, albeit over-estimating slightly in some areas (Nakawo, 1986; Rounce et al., 2018; Figures C4, C5).

The sub-debris ablation schemes used in the simulations in this chapter are described in section 6.2.3.2.

6.2.2 Static surface data

A 30 m digital elevation model (DEM) was acquired from the Shuttle Radar Topography Mission (SRTM) (Farr et al., 2007). The DEM was resampled to a 100 m grid spacing to match the resolution of the energy balance and ice flow modelling experiments. Spatial resolutions finer than 100 m were tested but found to add minimal value to the energy balance modelling results (Chapter 4). This same 100 m grid spacing, was used in iSOSIA simulations by Rowan et al. (2015) allowing for direct comparisons with the future projections to be made, enabling the added value of an improved representation of glacier mass balance, climate and sub-debris ablation to be assessed.

Estimates of distributed ice thickness and volume provided by Farinotti et al. (2019) were removed from the DEM to produce the subglacial topography required to initialise experiments. This yielded an ice-free domain that incorporated the full hydrological catchment and included the steep hillslopes of the Western Cwm that provide avalanche material into the glacier accumulation zone. The domain comprised 19,164 glacier points, in a square grid, and provided the basis for both the mass balance and ice flow simulations.

6.2.3 Experimental design

Khumbu Glacier is surrounded by a terminal moraine complex and roughly two sets of lateral moraines (Figure 6.1) denoting the late Holocene advance and the Little Ice Age (LIA) advance, and thereby the glacier extent and thickness which also aid evaluation of historical simulations (Hambrey et al., 2008; Owen et al., 2009; Rowan et al., 2017). The delay in glacier response to

climate also necessitates the ice flow modelling experiments to spin up from a stable period when the glacier was in equilibrium with climate.

The Late Holocene Khumbu Glacier was reconstructed with a 5000-year steady-state simulation starting from an ice-free domain and with the same elevation dependent mass balance forcing used in Rowan et al. (2015, 2021). For this, the LIA maximum was simulated by forcing the Late Holocene ice mass with a mean sea level temperature of 21.3°C, assuming a temperature lapse rate of 0.004°C/m, to produce an ELA of ~5,325 m.a.s.l.. The supraglacial debris layer at this time was negligible, as debris was being exported to the margins to build the moraines seen today (Owen et al., 2009; Rowan et al., 2015). Glacier slowdown allowed supraglacial debris export which, aided by the enclosing moraines, enabled the glacier to thicken (Rowan et al., 2015).

A variety of dating techniques indicated that the LIA advance occurred approximately 500 years before present (Owen et al., 2009; Rowan et al., 2017). The present day in the iSOSIA simulations starting from the LIA maximum was placed at 200 years. The glacier would likely have had a delayed response to retreat from the LIA moraines due to the presence of supraglacial debris. The inner moraines show no vegetation, suggesting they are relatively young (towards the very end of the LIA, around 1900 CE).

From this point in time onwards the simulations were forced by present-day distributed mass balance, and a variety of sub-debris ablation schemes were used.

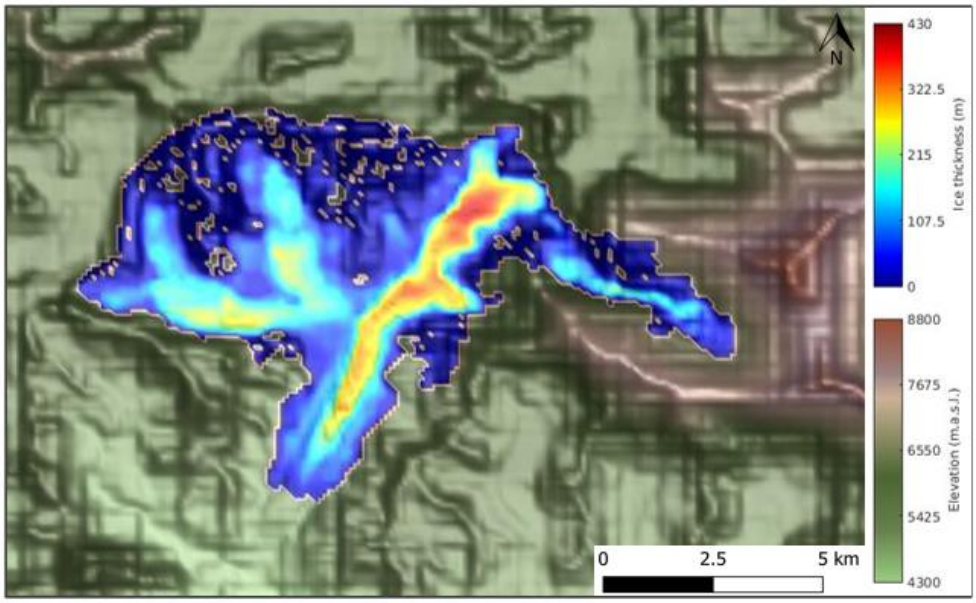

Figure 6.3 Simulated Khumbu ice thickness at the LIA maximum that matches well with moraines seen in valley today.

6.2.3.1 Mass balance forcing

Each iSOSIA experiment was forced by a 100 m grid of annual glacier mass balance. This grid was generated using COSIPY, with each five year time-slice experiment forced by one of the three downscaled CMIP5 model datasets outlined in Chapter 5. The mean of the 5 annual clean-ice mass balance grids was calculated, and then used to force the ice flow simulations. COSIPY calculates the clean-ice mass balance, meaning the impact of supraglacial debris on ablation rates was not double counted following integration with iSOSIA. The debris component of iSOSIA is more sophisticated than the relatively simple ablation correction implemented in Chapter 4, and includes debris transport which no existing glacier mass balance models do.

Present day MB simulations were forced with the three downscaled RCM datasets described in Chapter 5 for 2015-2019, and these resultant grids were used to generate present day glaciers in iSOSIA. These present-day glaciers were forced with end-of-century MB grids (2095-2100) from the downscaled RCM datasets for both RCP4.5 and 8.5. A mid-century MB grid (2059-2064) was selected for two of the RCMs (CCCma under RCP4.5 and NOAA under RCP8.5) and these were used to assess the response of the ice-flow model to this mid-way MB forcing.

The eleven MB forcings produced by the above downscaled datasets are shown in Figure 6.4, as their cumulative MB calculated from the glacier-wide MB simulations. Simulated glacier-wide mass balance became more negative into the future, particularly under RCP8.5. Mass balance forced by the downscaled NOAA climate remained the lowest relative to the CCCma and IPSL RCMs.

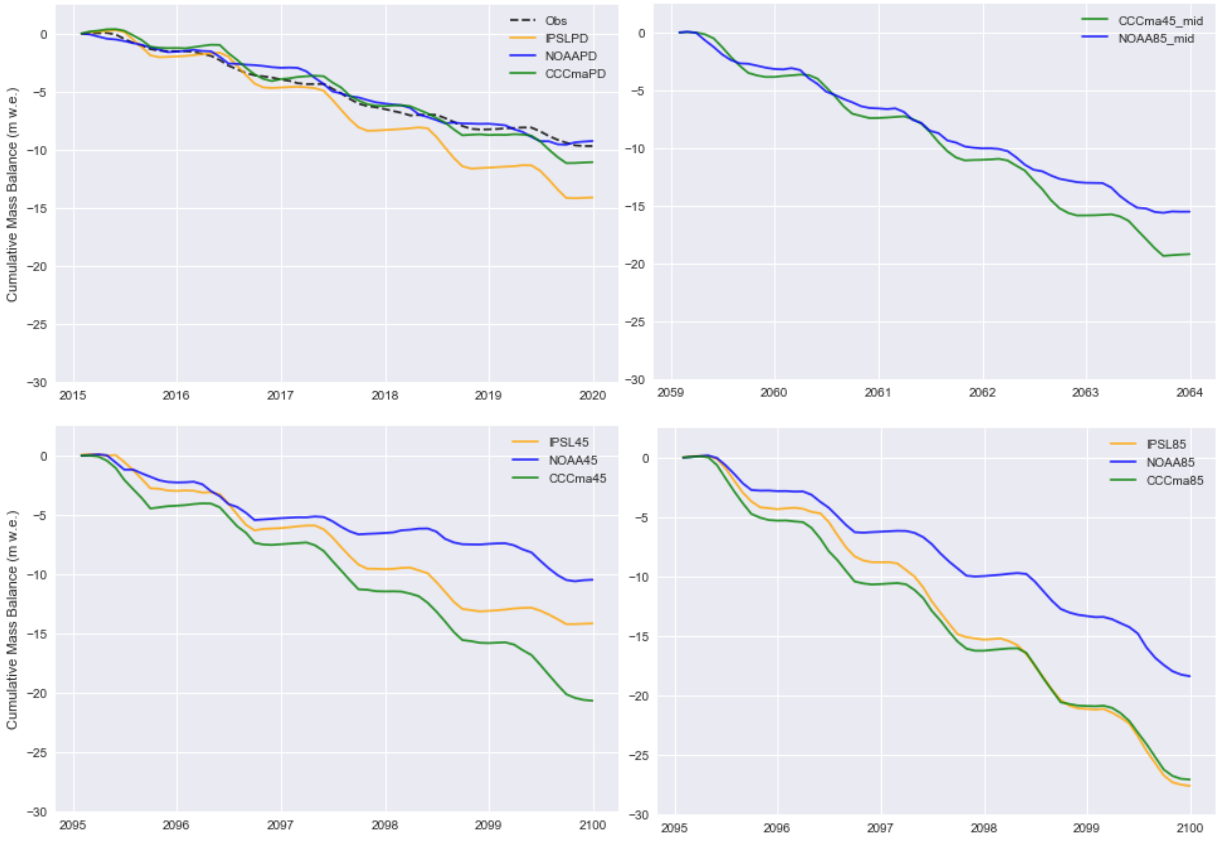

Figure 6.4 Spatially averaged cumulative mass balance with clear seasonality for (a) the present day time-slice (including the MB forced by the observations used in downscaling) (b) the mid-century time-slice (c) the future time-slice under RCP4.5 (d) the same, but under RCP8.5.

The downscaled future time-slice of the NOAA climate under RCP4.5 was 1.4°C higher than present day (mean annual temperatures of -0.75°C and -2.15°C, respectively). However the spatially averaged cumulative mass balance was only slightly lower in the future time-slice (0.7 m w.e. lower, equating to a 0.14 m w.e. clean-ice annual MB). The impact of warming on mass balance was likely offset by the projected increased in precipitation (annual precipitation totals were 581.4 mm in the present day, against 664.8 mm per year in the future under RCP4.5; Figures 5.14 and 5.20).

It should be noted that the cumulative mass balances shown here are not directly comparable to the simulations in Chapter 4 (Figure 4.9) as the larger glacier square grid used for these simulations with iSOSIA includes a higher proportion of lower elevations than those of the existing glacier, thereby reducing simulated MB. Equally, for present day and future simulations the initial snow depth was 0.2 m, chosen as there were measurements of up to 0.25 m from the Pyramid ultrasonic depth in November 2014 (Figure A2).

At the time of writing, there was an absence of regional temperature projections beyond 2100, with downscaling experiments such as CORDEX only running until 2100. There are also no global

projections of post-2100 precipitation change, or of other climate parameters used to force the EBM. For these post-2100 experiments only, the delta change method (described in Chapter 5, page 122) was therefore used to apply the following global temperature change projections to the end-of-century climate for RCP4.5 and 8.5. Given the lack of post-2100 projections for the other climate parameters, and the significant uncertainty and error associated with precipitation even in the present day within RCMs, the precipitation and other climate variables from the downscaled 2100 climate were used. The simulations forced with 2095-2100 MB were also left to run with no further warming until they reached steady state. This was to ascertain when in the future the glacier is likely to reach equilibrium following present day warming and as, under RCP2.6, some GCMs project stabilising or even minor cooling (<0.5°C) of global temperatures after 2100.

Temperature changes for the post-2100 transient simulations, as described below, were all taken from Collins et al. (2013).

Transient simulations 2100-2200:

1. For RCP4.5, warming of 0.5°C was applied to MB mean of 3 RCMs for 2100 RCP4.5 climate.
2. For RCP8.5, warming of 2.8°C was applied to MB mean of 3 RCMs for 2100 RCP8.5 climate.

Transient simulations 2200-2300:

1. For RCP4.5, warming of 0.2°C was applied to MB mean of 3 RCMs for 2200 RCP4.5 climate.
2. For RCP8.5, warming of 1.3°C was applied to MB mean of 3 RCMs for 2200 RCP8.5 climate.

6.2.3.2 Sub-debris melt parameterisation

In these simulations, several approaches to parameterising the role of supraglacial debris on ablation rates were used.

The first approach was to emulate the exponential method used in Rowan et al. (2015) where suppression of ablation was scaled from the clean-ice rate (b_{clean}) via an exponential function to generate the reduction of ablation from debris (b_{debris})

$$b_{debris} = b_{clean} \times \exp\left(\frac{-h}{0.72}\right) \quad (6.5)$$

where ablation was suppressed by 50% under a debris thickness (h) of 50 cm to give a value of 0.72 (as was calculated for neighbouring Ngozumpa Glacier; Nicholson and Benn, 2013). This is referred to as 'exponential' hereafter (Table 6.1) and the resultant ablation reduction curve can be seen in Figure 6.5. This assumed a uniform debris layer, as in Chapter 4, though the melt reduction curve here differs from that created by the DADDI model (Figure 4.20). However as simulated debris thickness is higher than that found by Rounce et al. (2018), generally ≥1.5 m across Khumbu Glacier, the impact on glacier melt between these two curves would be minimal here.

The observed heterogeneity of the surface of Khumbu Glacier meant a parameterisation that represents differential ablation was considered preferable (Rowan et al., 2021), and this formed the basis for the remaining three approaches.

$$b_{debris} = b_{clean} \times \frac{h_0}{h + h_0} \quad (6.6)$$

Reciprocal functions were used to determine differential sub-debris ablation. Variability in debris thickness at the 1-m grid scale was estimated as the mean of 1000 thickness values. In comparison to the exponential method, the sub-grid randomised variation in h produced higher sub-debris ablation rates, as the thin or clean ice areas act to increase the spatially averaged ablation rates for each grid cell.

The parameterisations selected for this study represented varying levels of differential ablation: those that match the thickness distributions on Ngozumpa Glacier, which are highly positively skewed (h_0=1.1) (Nicholson and Mertes, 2017), positively skewed (h_0=0.8) and uniform (h_0=0.4) (Table 6.1 and Rowan et al., 2021). The uniform (h_0=0.4) sub-debris ablation correction with debris thickness matched most closely to the exponential method (Figure 6.5). The presence of clean-ice surfaces e.g. ice cliffs meant for the reciprocal functions the lower limit of h was 0 m. In the positively skewed distribution, 6% of h values were 0 m to 0.05 m, denoting the proportion of the debris-covered tongue on Khumbu Glacier that comprises ice cliffs (Watson et al., 2017).

Debris forcing / **MB Forcing**	**Exponential**	**h_0= 0.4 m**	**h_0= 0.8 m**	**h_0= 1.1 m**
IPSL PD	1	2	3	4
CCCma PD	5	6	7	8
NOAA PD	9	10	11	9

Table 6.1 Experiments for LIA maximum to PD using the three different MB grids and four sub-debris ablation parameterisations. h0 = 0.4, 0.8 and 1.1 m refer to the reciprocal schemes used in Rowan et al. (2020) and Exponential to the exponential scheme in Rowan et al. (2020) and Exponential to the exponential scheme in Rowan et al. (2015).

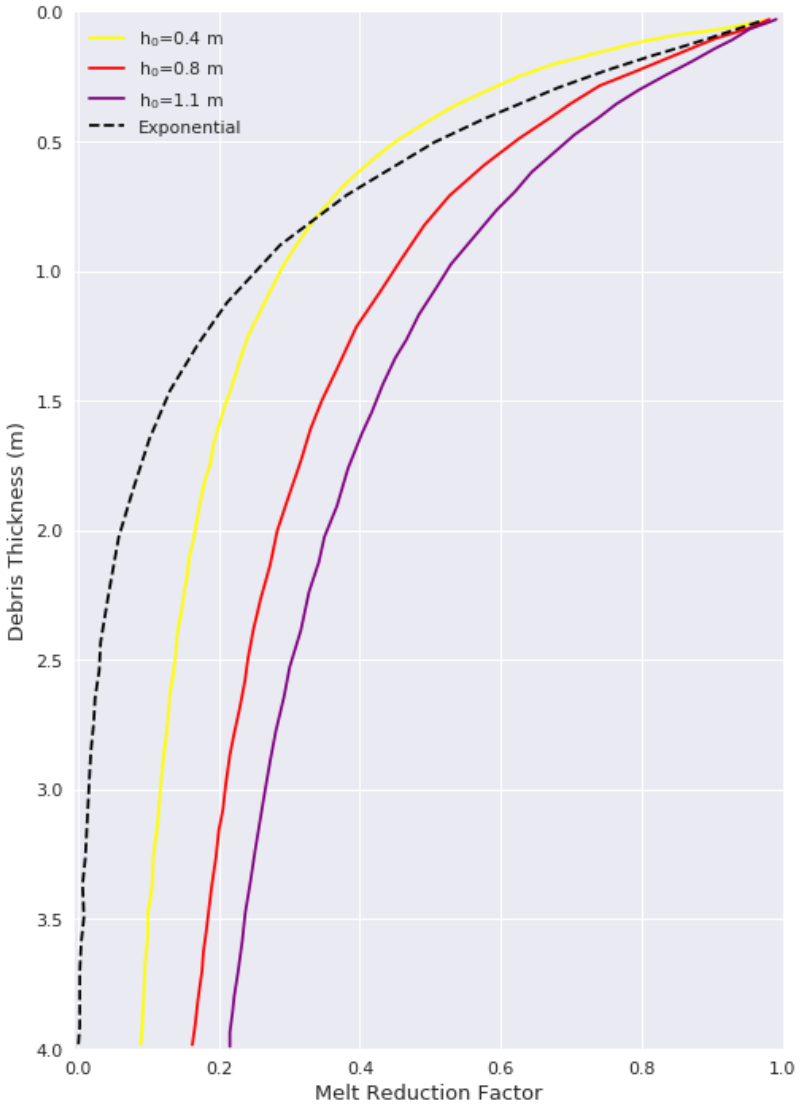

Figure 6.5 Melt reduction factors for the sub-debris ablation parameterisations as a function of debris thickness, modified from Rowan et al. (2021).

The four sub-debris ablation parameterisations (exponential, h_0=0.4, h_0=0.8, h_0=1.1) were used in the LIA maximum until present day simulations to investigate the role of differential ablation on glacier mass balance in observed mass loss. The present day simulated glacier produced by the combination of mass balance and debris forcing (Table 6.1) that best matched the historical and present-day dynamics of Khumbu Glacier was used as the starting point for the future simulations.

6.3 Results

6.3.1 Integration of gridded mass balance with iSOSIA

The spatial mass balance following integration with iSOSIA is a much closer match to reality for all simulations than the clean-ice mass balance forcing (Figure 6.6). The location of the ELA is broadly similar between the two, but the debris cover element of iSOSIA produces the inverse MB gradient that is matched by observations. In all experiments iSOSIA effectively simulates the highest ablation rates observed just below the ELA. At this location, the ablation rates closest to observations are from experiments with parameterisations that resolve differential ablation.

Avalanching changes the distribution of accumulation in the upper reaches of the glacier, with increased accumulation occurring along the glacier centreline. The contribution of avalanching to accumulation was tested by forcing the ice flow model with a gridded MB from a very weak precipitation gradient (used to aid model evaluation in Chapter 4) and no precipitation gradient. Historical glacier evolution was remarkably similar in both, with maximum ice thickness 10 lower with the latter MB forcing used in these simulations.

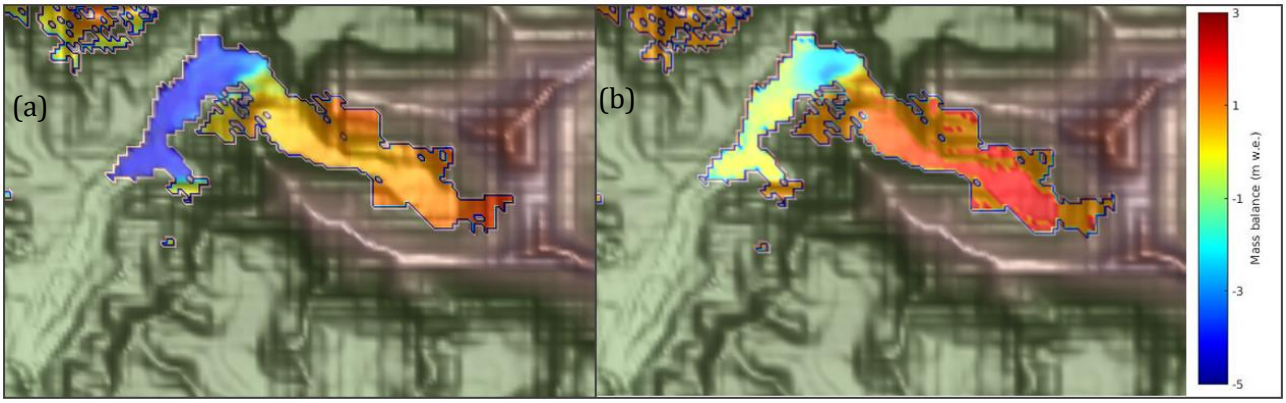

Figure 6.6 (a) Clean-ice mass balance from the NOAA present day time-slice prior to integration with iSOSIA and (b) mass balance from the same climate forcing, but following integration with iSOSIA at the timestep considered to be present day (experiment 11).

The Changri Nup and Changri Shar glaciers thinned much more rapidly than Khumbu Glacier, with volume loss of up to 50% in the 80 years since the LIA maximum starting point and are mostly absent in the simulated present-day. These glacier systems are very distinct from Khumbu Glacier, with low observed and simulated accumulation rates that are at times close to zero due to their low maximum elevations (Figure A4). Simulated detachment of these tributary glaciers from Khumbu Glacier occurs 110±30 years before present; the end of the LIA.

6.3.2 Historical glacier evolution until present day

The simulations forced with the three present-day (2015-2019) MB grids from the LIA maximum until present all show varying but marked mass loss (Figure 6.7). Glacier evolution is highly sensitive to the parameterisation of sub-debris ablation. Experiment 9 (Table 6.1) exhibits the lowest volume loss from LIA maximum to PD and experiment 4 the highest (Figure 6.8). These two experiments also represent the upper and lower bounds of the simulated ELAs of 5,650 and 6,050 m.a.s.l.. Similar simulated PD ice thickness and extent to experiment 9 were produced in Rowan et al. (2015). Supraglacial debris thickness increases with decreasing elevation, as is seen in observations (Nakawo et al., 1986) though is slightly higher than has been estimated elsewhere, particularly within 5 km of the terminus (Rounce et al., 2018; Figure C5). It does however appear reasonable when compared with field measurements collected by Nakawo et al. (1986; Figure C5).

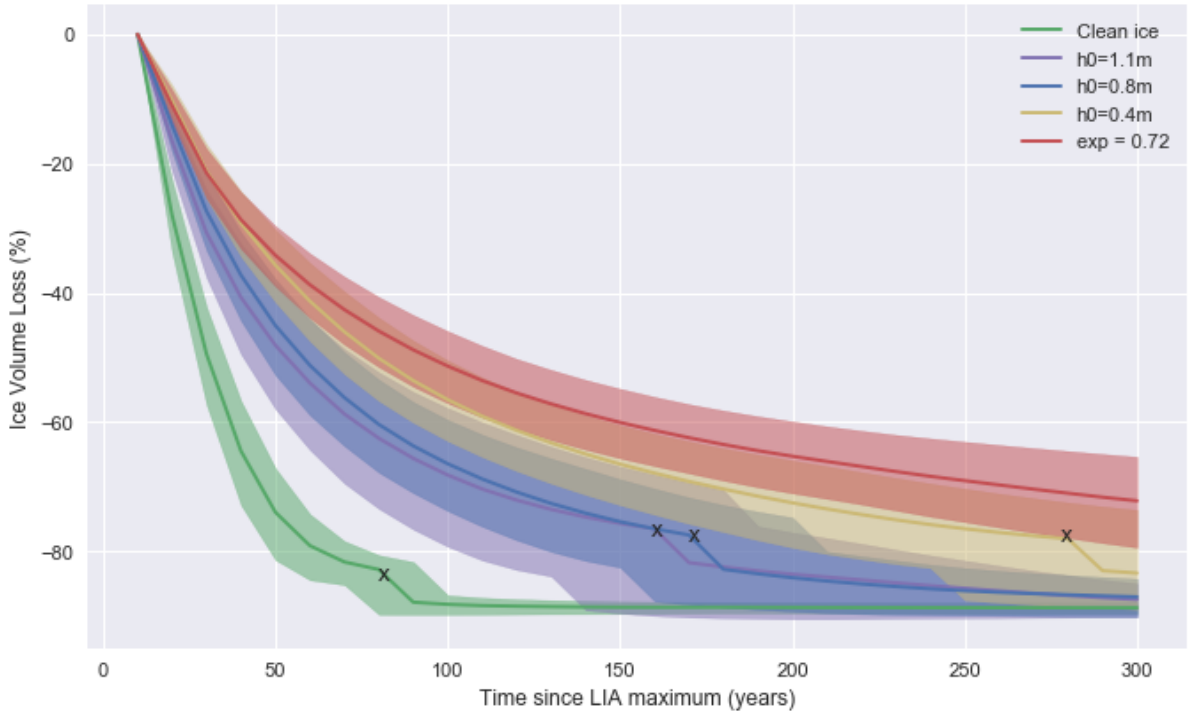

Figure 6.7 Historical volume loss of Khumbu Glacier since LIA maximum, grouped by parameterisation of sub-debris ablation with bold line showing the mean of the three RCM MB forcings and shading the range. Note that the tributary Changri Nup and Changri Shar Glaciers are present at the start of the simulations as they are attached to Khumbu Glacier during the LIA maximum. Volume loss is therefore inclusive of the simulated historical detachment and rapid decay of these glaciers. The crosses denote simulated detachment of the stagnant Khumbu Glacier tongue from the active glacier (explained in more detail later).

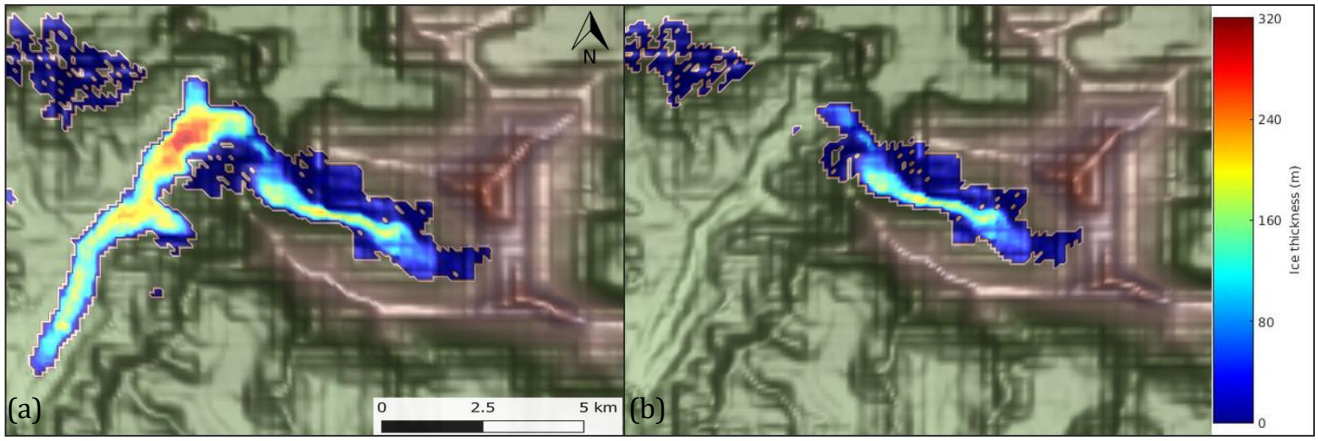

Figure 6.8 Present-day simulated ice thickness for (a) experiment 9 (b) experiment 4.

6.3.2.1 Validation of the 'best fit' present-day simulated glacier

The present-day simulated Khumbu Glacier from experiment 11 shows a good fit with the observed active glacier extent (Nakawo et al., 1986, Rowan et al., 2015, 2021; King et al., 2020). The associated sub-debris ablation parameterisation (h_0 = 0.8m) that resolves differential ablation is known to better simulate observed mass loss than the uniform exponential approach (Rowan et al., 2021). Equally, the downscaled NOAA climate is most similar to observations and produces spatial (not shown) and cumulative mass balances that are closest to those driven by observations (Figure 6.4a). Ablation rates are overly suppressed using the exponential parameterisation with the NOAA MB forcing (Figure C3b), this may partly stem from the slight overestimation of supraglacial debris relative to observations (Figure C4, C5) but is thought to mostly demonstrate the importance of differential ablation for observed mass loss. The median height of the ELA is 5,850 m.a.s.l..

The added value of forcing iSOSIA with a gridded MB is seen in the simulated present-day velocities that are a much better fit to remote sensing observations than previous simulations using an elevation-dependent mass balance forcing (Rowan et al., 2015, 2021) where the maximum simulated velocities were 117.9 m a^{-1}. Here, the surface velocity in the Khumbu icefall is up to 320 m a^{-1} (Figure 6.9a). Altena and Kääb (2020) used a novel approach to estimate icefall velocities through satellite image matching, with validation from Everest mountaineers' navigation devices from May 2018. They calculated surface velocities of just over 1 m d^{-1} but for a limited period. The icefall likely exhibits faster (slower) flow in the monsoon (winter), but both periods are excluded in their surface velocity estimates. Feature-tracking estimates of the upper ablation area

on Khumbu Glacier indicate velocities of up to 20 m a^{-1} (Quincey et al., 2009 and Figure 6.10a), which agree well with simulated velocities in this section (Figure 6.9b).

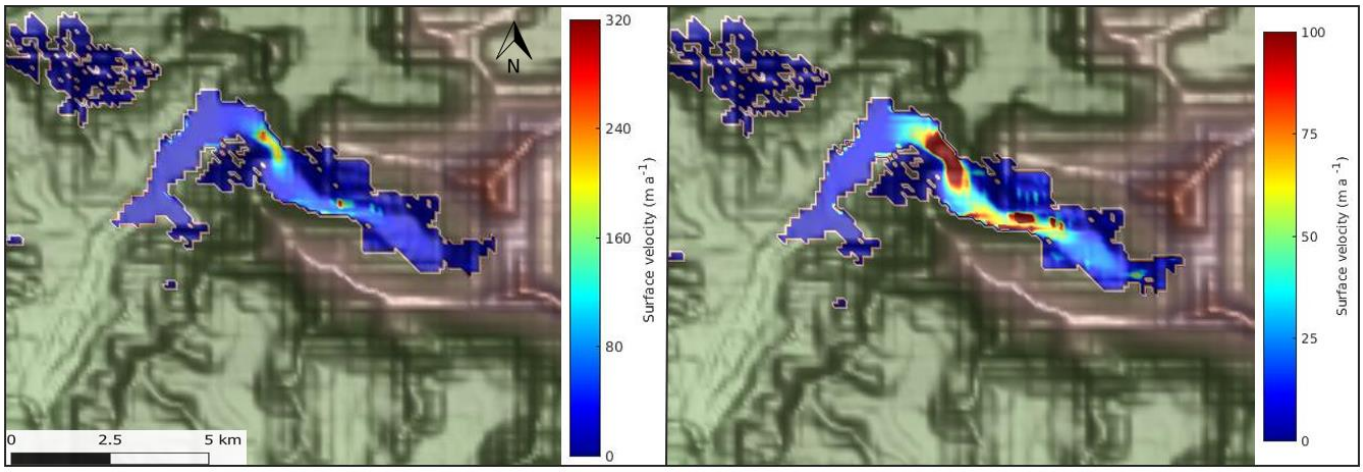

(a) (b)

Figure 6.9 (a) Present day simulated surface velocity supraglacial debris thickness and (b) capped at 100 m a^{-1} for experiment 11 (NOAA climate MB forcing and h_0 = 0.8 m).

The inability to simulate both the stagnant tongue and these higher, more realistic velocities in the active glacier indicates that the debris-covered tongue has dynamically detached from the active part of Khumbu Glacier (i.e. the upper ablation area and accumulation area). This implies that the active glacier and the largely stagnant tongue are already acting as two separate systems, with the debris-covered tongue in an advanced state of decay and absent in these simulations. They should therefore be modelled as such. Indeed, treating these two glacier sections separately, that are exhibiting such different behaviour, improves the active glacier dynamics relative to observations. For this reason, the focus of the subsequent historical and future simulations shifted to resolving the active glacier, approximately 6 km upglacier of the terminal moraine, rather than the 'dead' ice.

An additional suite of observations, that also lend support to the idea of active and stagnant ice co-existing in the glacier tongue, comes from englacial optical televiewing (OPTV) records of Khumbu Glacier, which indicate that thrusting occurs at several sites, as denoted by skewed internal debris layers (Miles et al., 2021b). It is plausible that these arise from variations in velocity at the base of the icefall as fast-flowing ice is shunted above the stagnant tongue. There are also observations of basal ice that has been thrusted to the surface near to the relict Changri Nup confluence but from the direction of Khumbu icefall (Figure C1).

In order to resolve this thrusting in the modelling experiments, the stagnant tongue was integrated into the subglacial topography with the following steps using a similar method to Rowan et al. (2021):

1) Tongue at close to fullest extent (ice mass 1).
2) Active glacier prior to what simulated PD (ice mass 2).
3) Subtraction of ice mass 1 from ice mass 2 (ice mass 3).
4) Integrate ice mass 3 into the subglacial topography, so the stagnant tongue is represented in the LIA maximum until present day simulation.

This results in an active glacier that evolves with a stagnant dynamically detached tongue downvalley, as is observed in the valley today (Figure 6.10b).

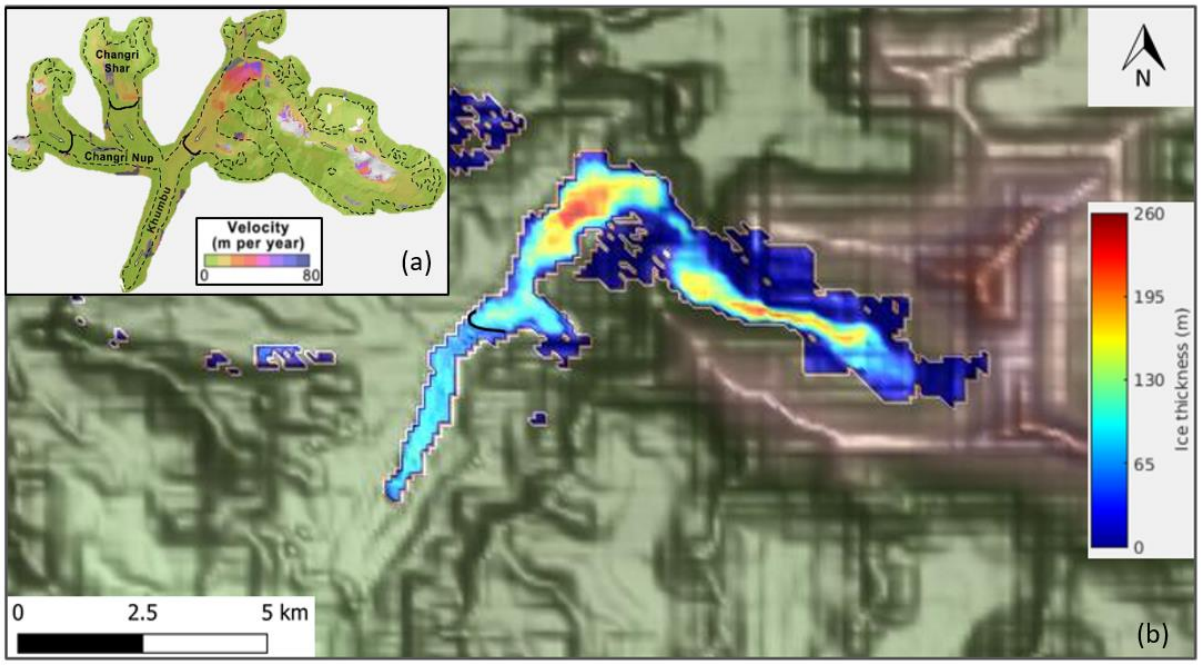

Figure 6.10 (a) Velocity and active glacier demarcation (black line) from feature tracking estimates between 4th May 2013 and 23rd May 2014 (taken from Rowan et al., 2015) (b) present day simulated active glacier ice thickness and the stagnant glacier tongue represented as ice rather than topography, with the active terminus marked by a black line.

Following integration of the stagnant tongue into the basal topography, after the LIA maximum, the simulated glacier tongue is forced to melt more quickly over the stagnant tongue in the topography, however the resultant active glacier extent remains the same. This was also found by Rowan et al. (2021) where this incorporation of the stagnant tongue was used to generate the active glacier (rather than the climate/mass balance forcing as in this work). In this simulation, the rate of tongue retreat is not faster than the simulation with normal subglacial topography. Once the

ice tongue has retreated to above this point, simulated active glacier extent from 40 years before present day matches the position estimated by Nakawo et al. (1986) from fieldwork during the 1979 monsoon season. The simulated active terminus thickness was approximately 175 m at that time, which agrees well with observations of thinning of up to 55 m at this location between 1984 and 2018 (King et al., 2020).

In the simulated present day, the active glacier terminus is 130 m thick, 40 m thicker than prior to tongue integration, and a closer match to observations. Radio-echo sounding from 1999 (Gades, et al., 2000) obtained thickness estimates close to the active terminus (just above Gorak Shep) of ~160 m. The simulated active glacier terminus thickness implies that this section of Khumbu Glacier has thinned by 30 m in 20 years, which is reasonable given downwasting estimates of 40 m for 1984-2015 for this section from King et al. (2020).

6.3.3 Future active glacier evolution

For the future experiments of the active glacier, the sub-debris ablation parameterisation of h_0 = 0.8 m is used. For clean-ice and other parameterisations produced no significant difference in results, as for many simulations the active glacier had retreated above the zone of supraglacial debris.

The mean simulated volume loss by 2100 for the three RCM MB forcings under RCP4.5 is 0.399 × 10^9 km^3 (46%) and 0.506 × 10^9 km^3 (58%) under RCP8.5. There is only a 1% difference in volume loss between the two climate scenarios for the CCCma forced simulations, despite a 1.9°C difference in downscaled mean temperature change between the two scenarios in the 80 years since present. The rate of volume loss is highest from the present day until 2070, as the simulated glaciers slowly start to reach a new hypothetical steady-state by the end of the century following the present-day mass balance forcing (Figure 6.11).

In 2100, the maximum ice thickness in the icefall is 214 ±17 m under RCP4.5 and 197±12 m under RCP8.5 and the ELA height is 6,050±150 m.a.s.l. and 6,310±96, respectively. This represents an average increase in ELA elevation of 200 and 460 m for RCP4.5 and 8.5. Under the most extreme scenarios, there is thinning of up to 73 m in the icefall over the next 80 years.

The committed mass loss demonstrates the loss that would occur even if warming ceases in the present day and the impact of historical glacier-climate imbalance on future mass loss (Figure 6.11). For the active glacier this ranges from 10 to 22% by 2100 and 13 to 34% by 2300.

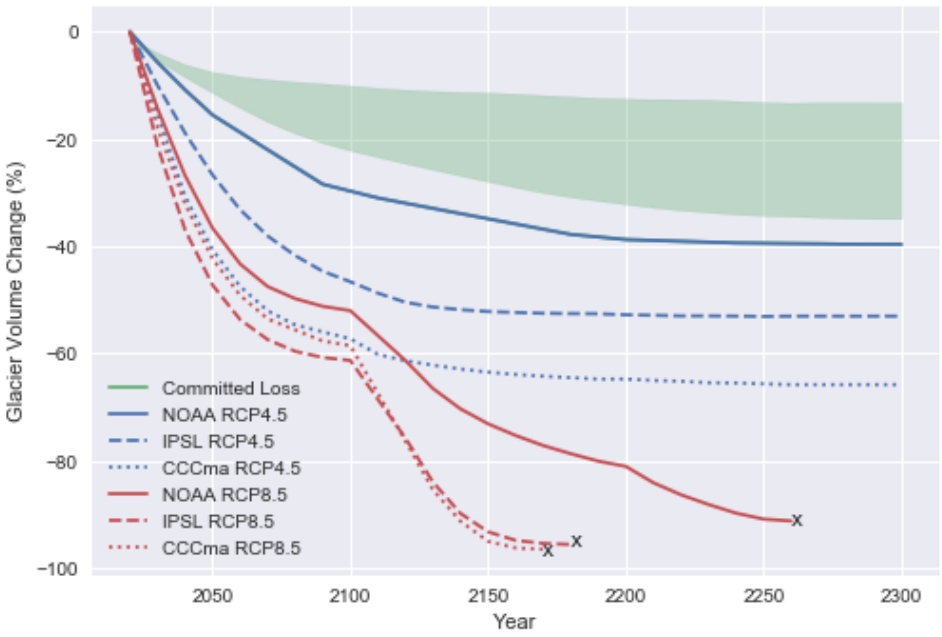

Figure 6.11 Glacier volume change from present (2015-2020) into the future under two RCPs for the three RCMs. The accelerated mass loss following the start-of-century MB perturbations is particularly clear for the RCP8.5 simulations.

The NOAA MB simulations under RCP4.5 show a similar glacier wide cumulative mass balance to the present day (Figure 6.4a), owing to the additional 83 mm (15% increase) in annual precipitation in the future that acts to offset the 1.4°C of warming. Despite this, over the next 80 years, Khumbu Glacier retreats 2.1 km up-valley and the maximum thickness decreases by 40 m (Figure 6.12a). This simulated glacier is likely in a hypothetical steady-state given the minimal 2100 MB perturbation relative to present day. In fact, a steady-state simulation, starting with an ice-free domain and using the same present-day MB forcing and sub-debris ablation parameterisation, produced an almost identical glacier in terms of ice thickness, extent (Figure 6.12b), mass balance and velocity (not shown).

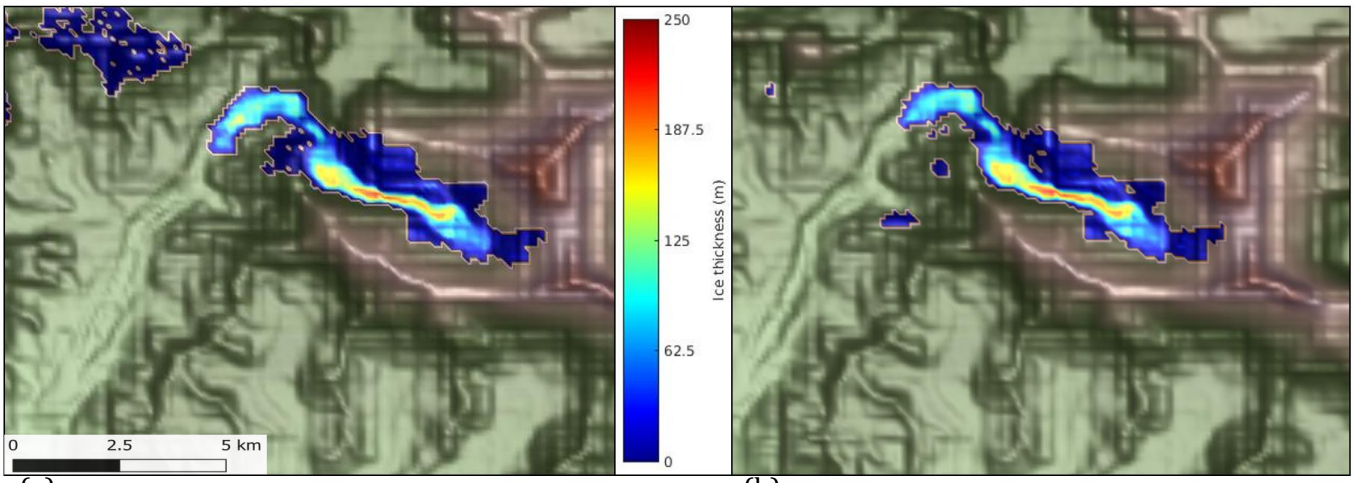

Figure 6.12 : (a) Khumbu Glacier in the year 2100 under RCP4.5 and NOAA RCM MB forcing and (b) Khumbu Glacier in equilibrium with present day climate (same climate forcing) produced from a steady-state simulation (ice-free domain spin-up).

The present day until 2100 simulations were left to run until the glacier reached steady state. The CCCma and IPSL forced simulations under RCP4.5 led to significant volume loss, with the latter leading to a glacier that has retreated 5 km above the present-day active terminus.

Once the glacier recedes into the Western Cwm, the temperature forcing from RCP4.5 is not sufficient to produce significant change, indicating that the glacier has reached a new equilibrium that can sustain a moderate warming scenario. For example, between 2200 and 2300, thinning of only 8 m occurs for the experiments forced by CCCma RCM and there is no change in length. The simulated 2300 glacier for the NOAA RCP4.5 forced MB experiment shows little change from the 2200 glacier. The large accumulation area relative to ablation area and annual precipitation rates of 665 mm (used from the 2100 downscaled climate forcing), allows the glacier to endure the moderate warming.

Khumbu Glacier is no longer considered a viable glacier system when there is no distinct ice mass present in the Western Cwm, and ice velocity is negligible. This occurs in 2160 (2170) under RCP8.5 and a climate forcing from the CCCma (IPSL) RCM (Figure 6.11). Though there is more ice present in the Western Cwm under the NOAA RCM, maximum surface velocity is reduced to 35 m a^{-1} in 2260 and the glacier is no longer considered viable (Figure C7).

Detachment occurs in several future simulations of the active glacier. For example, in 2100 under RCP4.5 with the IPSL MB forcing, the icefall disconnects from the upper ablation area as the clean ice upper ablation area below the present-day ELA has thinned so significantly that it is no longer present (Figure C7). This also occurs in 2070 under a NOAA RCP8.5 forcing. In 2140 the CCCma RCP8.5 MB forcing experiment shows detachment of the small ablation area that occupies the

Western Cwm from the accumulation area (Figure C7), ultimately leading to cessation of the glacier.

6.3.4 Glacier response time to mass balance forcing

In this section, the response time of Khumbu Glacier for the historical and present day to 2100 simulations is investigated. This response time can be expressed via an e-folding scale, which is defined as the time taken to complete $1\text{-}e^{-1}$ (or 63.2%) of the overall volume change (Leysinger Vieli and Gudmundsson, 2004, Oerlemans, 2018 and Zekollari et al., 2019). This is preferable to calculating response time from the time it takes for volume change to stabilise, as minor volume change can often continue for centuries. E-fold response time is hereon referred to as response time.

For the historical experiments, the glacier response times with a present-day MB forcing range from 28 to 199 years (Figure 6.13). This range stems from the differing sub-debris ablation parameterisations, which roughly cluster the three present day downscaled RCMs driving the experiments. Response times reduce under more negative present-day MB forcings. The experiments with the selected sub-debris ablation parameterisation of h_0 = 0.8m produce glacier response times of 75 ± 10 years.

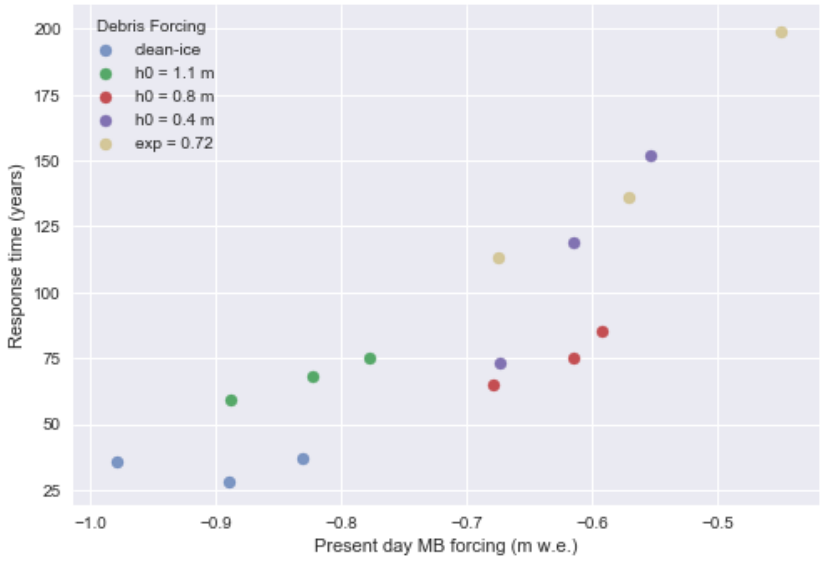

Figure 6.13 E-fold response time as a function of present-day MB forcing (following integration with iSOSIA) from LIA maximum to present day.

Evolving glacier-wide mass balance is a function of the clean-ice MB calculated from COSIPY; the correction of this with the sub-debris ablation parameterisation and avalanching following integration with COSIPY, and also changing glacier volume, geometry and accumulation area ratio.

The response time of the present day to 2100 simulations is 26-44 years (Figure 6.14) and is strongly positively correlated with the MB forcing (not shown). Interestingly, unlike the change in MB forcing, the change in glacier-wide mass balance becomes slightly more positive over time particularly under the more extreme climate scenarios (Figure 6.14), as the accumulation area ratio increases into the future. Glacier-wide mass balance becomes more positive over time, particularly under RCP4.5 but remains negative overall despite the larger (relative) accumulation area and retreat to higher elevations. The ablation zone retreats to higher elevations over time, where ablation rates are up to twice that of accumulation rates, particularly under RCP8.5.

The mass balance and volumes of the end-of-century IPSL and CCCma glaciers are similar. A very small area of debris-covered ice below the present-day ELA persists throughout the CCCma RCP8.5 simulation, reducing glacier-wide MB and thereby change in MB since present day (Figure 6.14).

This relationship between response time and MB is not included for the post-2100 experiments as the starting ice volumes differ hugely, and glacier masses become so insignificant that the analysis is not considered valuable. Post-2100 glacier mass balance remains negative amongst all future scenarios, but is close to 0 m w.e. for the RCP4.5 simulations, particularly after 2200. This likely explains the resulting insignificant volume change (Figure 6.11).

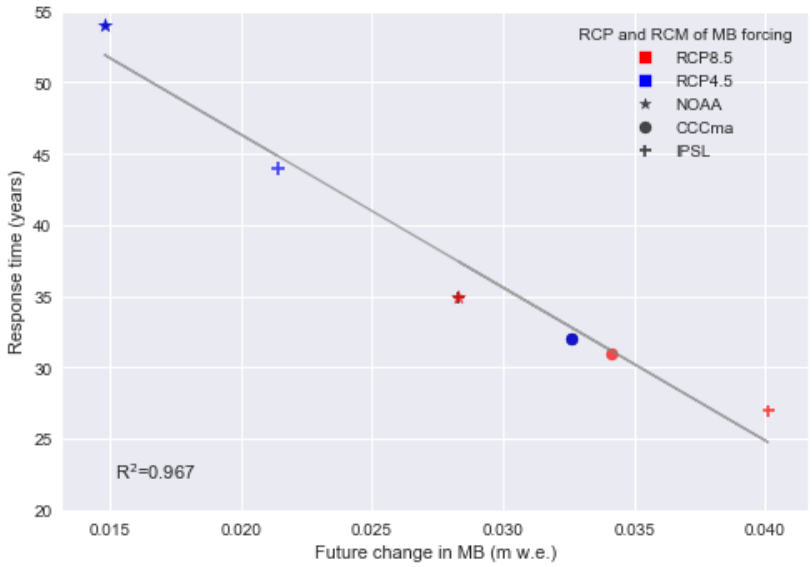

Figure 6.14 E-fold response time as a function of change in MB (following integration with iSOSIA) between present day until 2100. The low MB change stems from the higher accumulation area ratios into the future with the retreat of the remaining ablation area.

Under RCP4.5, mean annual air temperature increases by 2.1°C between the NOAA present-day climate, that is used to force historical simulations to produce the present-day glacier, and the CCCma 2100 climate. Interestingly, the response time for this experiment is much lower than for the two other RCP4.5 experiments (Figure 6.15). The 2100 mean annual air temperature at 5,050 m.a.s.l. under this scenario is -0.03°C (compared to -0.75°C and -0.56°C for the NOAA and IPSL climates under RCP4.5). Winter temperature is particularly high in the downscaled CCCma climate compared to the two other RCMs under RCP4.5 (Figure B2.1c).

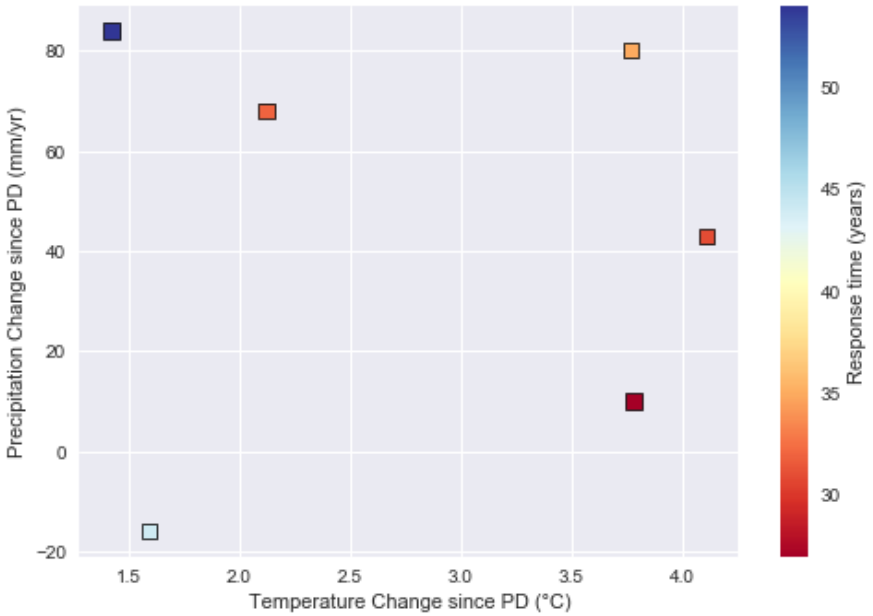

Figure 6.15 Annual temperature and precipitation change between simulated present day Khumbu Glacier (experiment 11) and 2100. The colour scale denotes the (e-fold) response time.

6.4 Discussion

6.4.1 Validation and comparison with previous work

6.4.1.1 Historical glacier change

The preceding modelling setup and set of results represents an advance on previous efforts through its robust representation of mass balance, sub-debris ablation, debris transport and glacier dynamics. This simulates a present-day glacier extent that is considerably smaller than the generally accepted glacier outline, but simulates a more realistic extent of active glacier ice than previous studies have achieved (Shea et al., 2015a; Rowan et al., 2015). Indeed, the simulated active glacier matches estimates from other studies derived from approximations based on the spatial distribution of surface debris (Nakawo et al., 1986) and more detailed feature-tracking and remote-sensing approaches (Quincey et al., 2009; Rowan et al., 2015; King et al., 2020).

The representation of an inverse mass balance, particularly the high ablation rates in the upper ablation area, produces simulated velocities in the upper ablation area and the icefall that are much closer to observations than previous estimates using a linear MB function with elevation (Rowan et al., 2015, 2021). The recent study by Rowan et al. (2021) found that mass loss and velocity are improved relative to observations if dynamic detachment is assumed to have already occurred.

Active glacier velocities in the simulations here match more closely with remote sensing studies, particularly in the icefall. The present-day mass balance simulated using an approach designed for a clean-ice glacier, and calibrated using mass balance gradients from Mera Glacier, found highest rates of mass loss on the lower tongue of Khumbu Glacier, which reduced with distance upglacier (Shea et al., 2015a). The spatial distribution of mass loss presented here therefore demonstrates the added value of the distributed mass balance forcing.

Volume loss in the historical experiments here and in those by Rowan et al. (2021) is manifested first through thinning, and then is followed by recession. In this study, using the exponential and negatively-skewed reciprocal sub-debris ablation parameterisations, recession is significantly reduced and thinning dominated, mirroring the historical simulations of Khumbu Glacier from Rowan et al. (2015). Simulated debris thickness patterns and true values from the exponential experiment (experiment 9) compare well with observations, though are over-estimated slightly in some areas (Figure C5). For the positively skewed simulations, the debris thickness of the remaining active glacier is comparable with the equivalent debris-covered sections from experiment 9.

6.4.1.2 Future glacier change

The current simulations commit a loss of the active glacier of 15±5% by 2100 under no further warming. This value is similar to committed loss estimates for the HKKH region, that range from 14% (Kraaijenbrink et al., 2017), 21% (Miles et al., 2021a) to 27% (Zemp et al., 2015). These approaches depend on ELA or AAR scaling approaches, which are known to be skewed for avalanche-fed DCGs, and rely on simplistic parameterisation of the influence of supraglacial debris and an absence of parameterisation of avalanching. The estimates from these studies are also calculated from present day warming (from 1996) and as such will not account for warming that predates this.

Previous mass loss estimates for Khumbu Glacier are 53% by 2100 and 32% by 2050 (Soncini et al., 2016) under no further warming, though model structure and approach also differ significantly to this study. For simulations using iSOSIA by Rowan et al. (2015), committed mass loss is 18% with Khumbu Glacier projected to continue to lose mass from post-LIA warming until 2500. In this thesis, the historical simulations using the exponential sub-debris parameterisations (as in Rowan et al., 2015) show a stagnant tongue which is sustained into the future with no further warming, and committed mass loss from present until 2100 is 15%. Though mass loss is minimal, Khumbu Glacier continues to respond to post-LIA warming until approximately 2440 (still assuming present day occurs 200 years since the LIA maximum), close to findings from Rowan et al. (2015).

Under RCP4.5 and 8.5 glacier mass loss estimates between present and 2100 is 54% and 59% (Soncini et al., 2016) and 84% and 95% (Shea et al., 2015a), respectively. Rowan et al. (2015) simulated historical and future Khumbu Glacier evolution by shifting the height of the ELA to represent future MB change. The results from this study are not directly comparable with those of Rowan et al. (2015) as the future experiments here focus on the active glacier. Rowan et al. (2015) found that warming of 1.6°C results in volume loss of 0.21 x 10^9 km^3 or 10% over 100 years. Here, the two RCP4.5 experiments with an equivalent warming since present day found active glacier volume loss of 0.294 x 10^9 to 0.394 x 10^9 km^3 over 80 years, with this range mostly stemming from varying projections of future precipitation (Figure 6.15). This represents 35-46% volume loss given the smaller present-day active glacier volume compared to that used in Rowan et al. (2015). The active glacier therefore experiences more volume loss compared to the experiments using the linear MB forcing in Rowan et al. (2015), despite it having receded to a higher elevation.

The presence of the supraglacial debris on the glacier tongue that thickens over time in the simulations by Rowan et al. (2015) allows the glacier to be sustained into the future, thereby reducing total volume loss. For these active glacier simulations conducted here, much of the glacier comprises clean-ice, and so suppression of ablation by debris is limited and mass is lost through retreat and thinning. It is also possible the higher rate of mass loss between present day and 2100 in the simulations with comparable warming is due to the representation of the high ablation rates below the ELA that have not previously been represented.

Glacier mass balance signifies the interaction between mass balance, glacier volume and geometry. As Khumbu Glacier retreats to higher elevations under both future climate scenarios, the ablation area is reduced, which may have a stabilising feedback on mass balance and lead to a new hypothetical steady-state. This is seen under RCP4.5 yet does not occur under RCP8.5, as the ablation zone is able to rapidly propagate far up the Western Cwm following the MB perturbation. Under this scenario, the temperature increase is significant enough to still decrease glacier mass balance despite the high elevation and exacerbate the glacier-climate imbalance (Rottler et al., 2019).

Prior to this work, the relationship between mass balance and response time had only been explored in a single study (Zekollari and Huybrechts, 2017), where hypothetical MB perturbations (–2.0 to +1.25 m w.e with intervals of 0.25m w.e.) were applied to a steady-state Morteratsch Glacier in the Austrian Alps. The response time ranged from 22 to 43 years, which increased with a more positive MB forcing, as was found here. Although Morteratsch Glacier is smaller than Khumbu Glacier (16 and 26 km^2, respectively) similar response times of 30 and 33 years, respectively, with ~1.0 m w.e. annual MB forcing are seen (Figure 6.13). This relation between MB and response time is likely because more extreme warming scenarios (negative MBs) cause

accelerated glacier shrinkage causing response times to decrease into the future with glacier steepening. Zekollari and Huybrechts (2017) also suggested that warming may enhance glacier flow, and thereby increase basal sliding, further decreasing response time. There is some evidence of this amongst the historical Khumbu Glacier experiments, however the interplay with the impact of differing accumulation rates from the varied RCM precipitation scenarios, which also act to influence ice flux and velocities, complicates this potential coupling.

The mean annual temperature in 2100 under the downscaled IPSL and NOAA climates is 0.49°C and 0.72°C cooler than that of the CCCma 2100 climate. This partly stems from the winter maximum temperature that is 1.7°C higher in the downscaled CCCma RCM than for the two other RCP4.5 scenarios. Under this CCCma RCP4.5 scenario, there will be significantly increased ablation and proportion of liquid precipitation. This represents a warming threshold beyond which glacier mass balance does not become significantly more negative (unless offset by a significant increase in precipitation, which may fall as snow particularly at higher elevations). This is reflected in the similar clean-ice mass balance between the two CCCma emission scenario experiments (Figure 6.4), and resultant volume loss from the two future iSOSIA experiments (Figure 6.11).

6.4.2 The modelling approach

Simulating change in a glacier in an advanced state of decay is challenging. Though the active and stagnant sections of the glacier are effectively behaving as two separate systems, the stagnant tongue situated at the active glacier terminus can still influence active glacier evolution. Here and in Rowan et al. (2021), it is postulated that the thrusting, that is evidenced from OPTV records showing tilted englacial debris layers (Miles et al., 2021b) and observed basal ice at the surface (Figure C1a), is the result of fast-flowing ice from the icefall being pushed up over the stagnant tongue. This theory has also been suggested by Benn et al. (2009) as a contributing mechanism to hydrofracturing of supraglacial ponds on the debris-covered tongue, with compressive stresses forming in the down-glacier direction as the active glacier meets the stagnant tongue. The active glacier terminus may also be the transition from cold/warm ice, and so a change in glacier thermal regime may also contribute to the observed thrusting, as observed by internal ice temperatures in this glacier section (Miles et al., 2018a and 2021b; Figure C2). In the simulations here, the integration of the stagnant tongue in the domain leads to a higher active glacier terminus thickness that matches better with observations; supporting this thrusting theory.

For glaciers in an advanced state of decay such as Khumbu Glacier, it was found to not be possible to resolve the dynamics of the debris-covered tongue using a higher-order ice flow with a robust

representation of mass balance, differential ablation and debris transport. This was also found by Rowan et al. (2021) using the same differential ablation parameterisations though a linear mass balance function. In this Chapter this modelling approach goes further by then focussing on how this larger, active section of the glacier evolves into the future, with this active glacier being of greater importance for future glacier viability relative to the 'dead' (i.e. stagnant) debris-covered ice. If the dynamics of the stagnant tongue were able to be well resolved along with the active ice in the future simulations, the volume loss found here would be higher. Treating the debris-covered tongue in isolation within future glacier modelling efforts would be valuable so as to explore the rate of decay following detachment from the accumulation area.

The committed mass loss demonstrates the spread of disequilibrium of Khumbu Glacier from the present-day climate (Figure 6.11). The historical simulation from the LIA maximum allowed this present-day glacier-climate imbalance to be accurately represented, and as such is a preferable modelling approach for a glacier of this size that has long steady-state response times.

Glacier mass loss slows as it approaches end-of-century, particularly under the more extreme MB forcing scenarios (RCP8.5 and RCP4.5 from the CCCma RCM, Figure 6.11) as these simulated glaciers shrink and adapt to a new geometry, or equilibrium. To address this, mid-century mass balance forcings were used for the CCCma run under RCP4.5 and NOAA under RCP8.5, as the end-of-century MB for CCCma was considerably more negative compared to the MB forced by the two other RCMs under RCP4.5 (Figure 6.4) and resulted in volume loss that was higher than that of the NOAA forced MB simulation under RCP8.5 (Figure 6.11). However, the 2100 volume loss was similar for experiments with and without a mid-century MB forcing, likely as the response time of the simulated glaciers at this moment in their lifecycle was longer than the 40 year time period between the PD and future time-slices.

6.4.3 Sources of uncertainty

The use of several RCMs to force present day and future MB has allowed the implications of climate uncertainty on glacier evolution to be illustrated. The differences that stem from RCM forcing are at times greater than those from the future RCP, due to varied predictions of future precipitation and the impact of this on glacier volume change and response time. As the CORDEX project only produces dynamically downscaled RCMs of RCP4.5 and 8.5, the implications of alternative future climate scenarios for future glacier evolution have not been assessed.

The time-slice based MB forcing approach means that it was important to ensure that the time-slices were representative of conditions for that time period and did not reflect an extreme phase of natural climate oscillation. The quantile mapping approach meant that the time-slices were the product of the 14 years of the calibration period. Analysis of the temperature and precipitation trends between the PD and future time-slices and 1 km mass balance simulations of the 12 years preceding both time-slices were conducted. However, information on signal and variability between the PD time-slice (2015-2020) and future (2095-2100) is not included. It is possible that this would alter the glacier-climate imbalance into the future.

The projected temperature changes used for the post-2100 simulations are global averages. Warming is likely to be higher for the Khumbu region given that warming over land is generally at least ~0.2°C higher than the global mean applied here (Collins et al., 2013). Historically, higher elevations have also warmed at a faster rate than lowland regions, with warming rates up to twice that of the global mean (Hock et al., 2019). Uncertainty increases with time from 2100, particularly under the most extreme radiative forcing scenario (RCP8.5). For example, forecasts of warming for 2281-2300 relative to 1986-2005 under RCP8.5 range from 3°C to 12.6°C (Table 12.2, Collins et al., 2013). In the absence of post-2100 precipitation data, the 2100 precipitation was maintained for the post-2100 mass balance and ice flow experiments. This is unlikely to be reflective of these climates and more realistic precipitation projections may allow the active glacier to be sustained for longer into the future or lose mass more quickly. However, it is highly unlikely that there will be a precipitation increase significant enough to compensate for the post-2100 projected warming under RCP8.5.

Snow depth and other glaciological constants will change into the future, such as the albedo of fresh snow and the rate of albedo decay. These are kept constant in the future COSIPY simulations, as there is high uncertainty regarding future industrial activity in the region, and the associated influx of particulate matter onto glacier surfaces. This also allows the mass balance signal and resultant glacier evolution from changing future atmospheric forcing to be more robustly established.

The distribution and rates of accumulation were greatly improved following integration with iSOSIA. The parameterisation of avalanching as regular snow fall from hillslopes onto the glacier surface is an improvement on previous studies and improves agreement of simulated accumulation rates relative to the few observations that are available. Future work to resolve the low frequency, high magnitude events that may contribute significantly to accumulation rates would be of real value. Representation of these events may also allow Changri Nup Glacier to persist in these simulations, with large serac avalanches from the steep southern slopes reported to contribute significantly to accumulation (Vincent et al., 2016). However, parameterisation and

evaluation of the contribution of these events to accumulation rates is highly challenging, particularly from a field perspective, owing to the dangerous and remote upper reaches of Khumbu Glacier.

6.4.4 Wider implications

As with other debris-covered glaciers, it is expected that the tongue of Khumbu Glacier will continue to thin and stagnate. The smaller accumulation area ratios associated with debris-covered glaciers relative to clean-ice glaciers was less important under historically cooler climates (Anderson and Anderson, 2016). However, the long ablation zones relative to the small accumulation areas means it is perhaps unsurprising that the debris-covered tongue of Khumbu Glacier is unable to persist under the present-day highly negative mass balance perturbation.

The rate of decay is also dependent on dynamic detachment from the accumulation area, which the modelling results in this study suggest has already occurred. The debris-covered tongue will continue to thin *in situ,* though sensitivity to atmospheric warming may decrease with thickening of surface debris with englacial melt-out. The proportion of the glacier surface covered by supraglacial ponds and ice cliffs has increased by 20% between 1984 and 2016 (King et al., 2020), and if this continues it is likely that supraglacial ponds and ice cliffs will continue to develop, counteracting the effect of debris thickening on ablation rates and encouraging the disintegration of the glacier tongue. The high climate sensitivity of these flat, low elevation tongues makes these glaciers more prone to developing proglacial lakes (Benn et al., 2012). The true-left flank of the Khumbu Glacier tongue, where a long line of connected ponds exists, does already show signs of break-up, mirroring the development of the proglacial lake at neighbouring Ngozumpa Glacier.

Glaciers with steep accumulation and flat ablation areas are possibly more prone to glacier detachment presently, and in future decades. Rapid surface lowering in the upper ablation area combined with reduced ice flux from the accumulation area have likely contributed to observed and simulated dynamic detachment. A progressive decrease in velocities has been observed in the upper ablation area since 1956-1978 ($\sim$56 m a^{-1}) until 1995-2004 ($\sim$20 m a^{-1}) (Seko et al., 1998 and Nuimura et al., 2011). This slowdown is likely driven by ice thinning and a lowered surface gradient in response to climate change.

Dynamic detachment is a precursor to physical detachment (Rowan et al., 2021). Ultimately, either dynamic or physical detachment of the ablation zone from the accumulation zone will accelerate glacier decay exponentially as replenishment of ablation of ice by upglacier flow is lost. This is critical for the viability of glaciers and as such is an area that requires further research. For other debris-covered glaciers that exhibit this inverse mass balance, and specifically the

significant rates of mass loss just below the ELA as well as sustained slowdown, detachment is also likely to occur. Delineation of the active terminus is challenging for debris-covered glaciers, though advances in feature-tracking and remote-sensing of glacier velocities can aid these efforts. This phenomenon could be a contributing non-linear mechanism to the debris cover anomaly that will likely increase in prevalence in the coming decades.

At the time of writing there had only been one previous study attempting to model glaciers during periods of dynamic or physical detachment (Rowan et al., 2021), where the stagnant tongue was also incorporated into the model domain. This forced the tongue to melt rapidly to generate the present day active glacier. The simulated active glacier in this Chapter using the improved mass balance forcing is a step forward, as this simulated active glacier is the combined result of the distributed mass balance and sub-debris ablation parameterisation. Nevertheless, results were improved with the incorporated stagnant tongue by being more representative of likely dynamics, and improving active glacier terminus thickness relative to observations, A growing number of observations of detachment occurring across the Nepal Himalaya indicate that further work in this area is required. Physical detachment is already apparent at the adjacent Lobuche Glacier, which spans a much lower elevation range than Khumbu Glacier (Watson et al., 2018). Basal ice is visible between the active glacier and the debris-covered tongue on the Shalbachum Glacier in the Langtang valley, which is indicative of detachment (Pellicciotti et al., 2015).

Although the remaining ice is small, the detachment that occurs in 2100 under RCP4.5 and the IPSL RCM demonstrates that detachment can continue even after the main tongue of the ablation zone is disconnected from the active glacier. Glacier dynamics models that are able to represent this mechanism are required to accurately predict the timing of glacier termination, and these findings reaffirm the value of catchment-scale studies.

Future simulated mass balance indicates that mass loss will significantly increase in the summer months particularly under RCP8.5 (Figure 6.4d), as the proportion of liquid precipitation increases with atmospheric warming. The implications for this active glacier are also significant, seen by the mean monthly temperature that is projected to be ~0°C at the end of the century during the monsoon as high as 6,480 m.a.s.l. (Figure C8). Downscaled future precipitation suggested that winter precipitation, when precipitation will most likely fall as snow, will increase by 19.4±9.7% under RCP8.5, partly through increased frequency of high magnitude events from winter westerly disturbances (Chapter 5). Under this high-end warming scenario, Khumbu Glacier's mass balance regime may shift from being summer-accumulation type only at the highest limit of Khumbu Glacier. Lower elevations will depend on avalanches from higher elevations and will otherwise become predominantly winter-accumulation type. However, the future evolution results here suggest that this projected increase in winter precipitation will not be able to slow mass loss.

Recent analysis indicates that global emissions are following the trajectory of the middle range scenarios, and that RCP8.5 should be described as "low-possibility, high-impact" (Pedersen et al., 2020). However, elevation dependent warming (EDW) could mean that higher elevations are more prone to the climate impacts of the high emission scenarios. Downscaled future climate scenarios used here for Khumbu Glacier are in line with projections from other studies where EDW is found, though the pointwise downscaling approach means the presence of an EDW signal cannot be fully explored (Chapter 5). Therefore, it is possible that future glacier evolution may follow a more extreme trajectory than that found under RCP4.5, that may be closer to RCP8.5. Under the downscaled RCP8.5 climates used here, there was no evidence of future precipitation increase being able to offset the greater than 3.5°C of projected warming over the next 80 years.

6.5 Conclusions

The following concluding remarks can be made regarding the added-value of this modelling approach for simulating the historical evolution of Khumbu Glacier:

- The integration of the distributed mass balance and ice flow models posed some interesting challenges (including evaluation of the clean-ice mass balance forcing, and resolving sub-debris ablation and avalanching in iSOSIA). The value of using distributed mass balance forcing is seen in the simulated present-day velocities in the Khumbu icefall, which give a better fit to remote-sensing observations than previous simulations using a linear elevation-dependent mass balance forcing (Rowan et al., 2015, 2021).
- The debris-covered tongue, known to be losing mass at an accelerating rate, is virtually absent from these results, and is indicative of a stagnant tongue that is now or very soon to be physically disconnected from the active upper reaches of Khumbu Glacier.

Considering the above, focus on resolving the active glacier was considered most pragmatic from a modelling perspective. The findings from this analysis of the future evolution of the active Khumbu Glacier can be summarised as follows:

- The high variability between RCMs, and implications for glacier mass loss, demonstrates the high degree of uncertainty that mostly stems from future precipitation trends.
- Future precipitation increase can act to compensate the impact of atmospheric warming on glacier mass balance, as seen by the NOAA RCM driven MB under RCP4.5. However, historical climate change means committed mass loss still remains considerable, and this

is exhibited with a 2.1 km retreat of Khumbu Glacier and thinning of maximum thickness by 40 m.

- Glacier response time is strongly correlated to historical and future glacier mass balance for simulations with the same initial glacier volumes.
- The committed mass loss of the active section of Khumbu Glacier ranges from 10 to 22% by 2100 and 13 to 34% by 2300. Delayed mitigation efforts to limit atmospheric warming will increase this committed mass loss and the climate-glacier imbalance.
- After 2100 under RCP8.5 Khumbu Glacier experiences substantial ablation in the Western Cwm. Following this trajectory would mean that it will likely cease to exist as a glacier in the next 140 years (i.e. by 2160).

Chapter 7 Conclusions

Glaciers of the Hindu-Kush Karakoram Himalaya act as vital seasonal buffers against drought for mountain and downstream communities; 25% of the world's population are estimated to rely on the five major rivers that are partially sustained by glacier meltwater (Immerzeel et al., 2010; Pritchard, 2019). In Nepal, 80% of the population practise agriculture and 90% of electricity is generated by hydropower. Glacier meltwater provides 65% of the water supply for the communities of the Khumbu region during the pre-monsoon (Shrestha and Aryal, 2010, Zarfl et al., 2014; Wood et al., 2020). As such, thorough catchment-scale projections of atmospheric and glacier change are required. This thesis addresses a gap in future projections to date, which are often regional scale estimates that rely on simplistic representations of climate, using the delta change approach applied solely to temperature. Glacier change is frequently based on projections that use linear scaling or simplified ice redistribution modelling approaches, which are not appropriate for debris-covered or avalanche-fed glaciers. These studies are not able to include representation of the finer spatial and temporal climatic details, and how this is exhibited through glacier mass balance and mediated through glacier dynamics over time.

The work presented in this thesis has sought to understand the implications of atmospheric change for glacier mass balance and evolution at the catchment-scale. Despite the challenges that modelling Khumbu Glacier provides, it has been an ideal study site thanks to the presence of meteorological and glaciological observations that have been used extensively for calibration and evaluation of this novel modelling approach. The structure of this thesis relates to the overarching modelling chain. It highlights the importance of resolving detailed present-day and future climate for glacier mass balance and uncertainty estimates. This thesis advances the representation of the mass balance and evolution of Khumbu Glacier, through the parameterisations of the influence of supraglacial debris and transport on ablation and avalanching on accumulation used in the integrated modelling approach.

7.1 Evaluation of thesis aims

Aim 1: To investigate the complexities of catchment-scale meteorology using a network of weather stations, and the implications for glacier modelling.

High elevation meteorology is the dominant control over glacier viability, yet *in situ* observations of basic parameters such as temperature, precipitation and incoming and outgoing radiation are lacking, particularly for the HKKH region. In Chapter 3, analysis of meteorological data from six weather stations in the Ev-K2-CNR network, mounted at elevations from 2,680 to 5,700 metres, in the glacierised Dudh Koshi catchment for the 2009-2012, period was conducted.

The monsoon was characterised by higher and more stable temperatures, and low magnitude, high frequency precipitation. Measured temperature lapse rates were always lower than the Environmental Lapse Rate, varying significantly seasonally and diurnally, and were lowest overnight during the monsoon period. Precipitation gradients were weak and slightly negative, which may represent undercatch of solid precipitation at the higher elevations. Clear gradients for the entire catchment could not be derived. Though temporal patterns were captured, observed wind speeds were appreciably higher than ERA-5 modelled (reanalysis) winds, a difference that increased following correction of the modelled data to sensor height. Valley orientation dictated the dominant wind direction, aiding the southerly passage of the monsoon, and with upslope flow during the day and lighter downslope flow at night. Comparison with upper level (250 hPa) wind from ERA-5 indicated that valley winds are driven by temperature-induced density perturbations and controlled by topography.

Aim 2: To explore the sensitivity of Khumbu Glacier mass balance to atmospheric and glaciological forcing in the present day.

The energy balance modelling approach allowed the meteorological drivers of ablation to be defined, and these were found to vary significantly over time and space in the present day. The seasonality of these meteorological drivers was increasingly pronounced with decreasing elevation. For a hypothetical, clean-ice Khumbu Glacier tongue in this climatic setting, net shortwave radiation was the dominant energy input, though net longwave also contributed substantially to ablation during the monsoon. At higher elevations (> 6,500 m.a.s.l.), ablation was mostly driven by the sensible heat flux. The low net shortwave radiation stems from the high albedo with the

persistence of snow, and COSIPY is able to simulate the extremely high incoming shortwave radiation (>1,250 W/m^2 at times). Distributing temperature using different lapse rate schemes altered mass balance by up to 24% around the ELA (within the range of the 0°C isotherm), though did not significantly influence glacier-wide mass balance.

Unlike with clean-ice glaciers, the highly non-linear mass balance gradient observed on debris-covered glaciers such as Khumbu Glacier provides challenges for modelling. The calculation of a Khumbu Glacier specific ablation reduction curve and the addition of this sub-debris ablation correction to the simulated mass balance, substantially reduces ablation rates, producing glacier-wide and altitudinal mass balance rates that matched geodetic and *in situ* estimates. This is a computationally inexpensive approach to resolving the impact of supraglacial debris on ablation and could be used by future COSIPY users studying debris-covered glaciers as the meteorological data requirements are the same as for COSIPY. This debris component also allows evaluation of the simulated clean-ice mass balance, which is essential for integration with iSOSIA later.

Aim 3: To produce an ensemble of downscaled, hourly resolution present day and future climate scenarios for Khumbu Glacier from a selection of Regional Climate Models.

The third aim in this thesis is investigated in Chapter 5, where quantile mapping (and generalized analog regression for wind) is used to downscale daily climate from three RCMs. The systematic biases within the raw RCMs are substantial and the monsoon signal almost absent. The seasonality of climate variables is much improved following downscaling, though is perhaps overcorrected as seen by the removal of noise relative to observations and raw RCMs. The disaggregation to produce the hourly climate data is rarely performed in future climate impact studies but was a necessary step for the energy balance modelling. The approaches used allowed the observed seasonality of diurnal trends to be replicated, whilst maintaining some stochasticity, thereby improving this overcorrection of the daily climate data.

Under RCP4.5, temperature is projected to increase by 1.81°C by the end of the century, with high rates of warming in the winter and pre-monsoon. Atmospheric warming of 3.91°C is estimated over the next 80 years for Khumbu Glacier under RCP8.5, with 4.44°C in winter months. These findings are in line with those reported in other studies for this region (Sanjay et al., 2017b; Kaini et al., 2019).

Mean annual precipitation increases amongst all RCMs with a multi-model mean increase of 14.8%. There is little evidence of monsoon intensification or dependency on RCP, with the trend

more constrained by the RCM. High magnitude precipitation events become more frequent, by up to a factor of 7 relative to present day. The discrepancy between RCMs reaffirms the high uncertainty regarding future precipitation trends that is mirrored in other studies (Immerzeel et al., 2013 and Sanjay et al., 2017b).

Aim 4: To improve accuracy of simulated historical and future evolution of Khumbu Glacier through integrating a more robust representation of glacier mass balance into ice flow modelling.

The novel integration of the distributed mass balance and ice flow models produces simulated present-day velocities in the Khumbu icefall and upper ablation area that match closely with observations. This is a substantial improvement from previous simulations that use an elevation-dependent mass balance forcing (Rowan et al., 2015, 2021). This is particularly true for the experiment using the sub-debris ablation parameterisation that represents differential ablation, and the downscaled RCM that matches most closely with observations for the present day. Under this mass balance forcing, the debris-covered tongue is absent and the active glacier terminus matches estimates from other studies. This indicates that the stagnant tongue has dynamically, and perhaps physically, detached from the active Khumbu Glacier. This has occurred already for nearby glaciers, such as Lobuche and North Changri Nup Glaciers (Watson et al., 2018; Vincent et al., 2016, respectively) though delineating the transition zones between the active and stagnant sections of debris-covered glaciers is challenging (Neckel et al., 2017).

The evolution of the active glacier, with the simulated stagnant tongue downglacier, is a realistic representation of present-day dynamics (Rowan et al., 2021). The modelling approach here allows the committed mass loss of the active section of Khumbu Glacier to be assessed, which is up to 22% by 2100 and 34% by 2300. After 2100 under RCP8.5 Khumbu Glacier experiences substantial ablation in the Western Cwm. Following this trajectory would mean that it will likely cease to exist as a glacier in the next 140 years (i.e. by 2160).

Glaciers are key indicators of atmospheric change, yet the climate signal is not immediately or clearly exhibited by large mountain debris-covered glaciers. The modelling approach used in this chapter allowed the relationship between glacier response time and mass balance, controlled by the clean-ice distributed mass balance forcing, the sub-debris ablation parameterisation and the changing glacier extent, to be explored. This relationship has only been discussed in a theoretical manner previously or using hypothetical mass balance perturbations to steady-state glacier simulations (Zekollari and Huybrechts, 2017). The transient simulations here show that, as the active Khumbu Glacier shrinks and recedes under more extreme future glacier mass balance forcings,

glacier-wide mass balance becomes less negative as the relative accumulation area grows. However, glacier-wide mass balance never becomes positive, and simulated ablation rates in the Western Cwm are sometimes twice that of the accumulation rates, particularly under RCP8.5. The relationship between temperature or precipitation change and response time was less clear than with mass balance forcing, though clearly demonstrated the possible compensatory effect of increased future precipitation for glacier viability under moderate atmospheric warming only, though the substantial committed mass loss from historical warming may hinder this.

7.2 Cross-chapter conclusions

Using an ensemble of RCMs demonstrated the high uncertainty regarding future climate (mostly of precipitation) and the significant impact of this on glacier mass balance. The proportions of both days and hours above/below 0°C are similar, particularly in the present day (Figure 5.21). Despite this, simulated mass balance and glacier evolution for the climate from the three RCMs in the present day and future differ substantially. These differences stem from the intricate sub-daily timings of precipitation and temperature for estimates of ablation and accumulation that are particularly important for summer-accumulation type glaciers. The energy balance modelling approach used here to calculate glacier mass balance is also able to represent the radiative fluxes and thereby meteorological drivers of Khumbu Glacier ablation that vary over space and time.

Analysis of *in situ* meteorology and present-day simulated mass balance indicate that previous estimates of monsoon contribution to annual precipitation (of up to 80% e.g. Burbank and Bookhagen, 2002; Salerno et al., 2015 compared with 60% in this analysis) have been overestimated, likely due to an undercatch of winter snowfall by the tipping bucket gauges of the Ev-K2-CNR network (Sherpa et al., 2017). In this thesis, these winter precipitation events are found to be significant for glacier-wide simulated mass balance. The persistent mass loss seen in the monsoon months demonstrates how ablation and accumulation overlaps across short timescales for Khumbu Glacier. Though Khumbu Glacier is a summer-accumulation type glacier, and monsoon precipitation plays a significant role in reducing rates of mass loss, monsoon precipitation was never significant enough to offset glacier-wide mass loss. The contribution of winter precipitation to accumulation rates has been previously underestimated and is characterised here by infrequent but higher magnitude events relative to monsoon precipitation.

The contribution of monsoon precipitation to accumulation reduces towards the end-of-the-century as the proportion of liquid precipitation increases with atmospheric warming. This is particularly true under RCP8.5, with significantly enhanced summer mass loss (Figure 6.4) relative to the present day. It is likely that the sole source of accumulation for the debris-covered tongue will

be winter precipitation under this scenario. Much of the active Khumbu Glacier will rely on winter precipitation, with only the highest limit remaining as a summer accumulation dominant regime under RCP8.5.

The impact on ablation between the sub-debris ablation correction used in Chapter 4 (generated with the DADDI model) and the exponential correction in Chapter 6 differed substantially for debris thicknesses <0.5 m. In Chapter 4, following correction of the simulated clean-ice mass balance using the exponential correction (Nicholson and Benn, 2013; Rowan et al., 2015), glacier-wide mass balance was higher than observations, though point-based ablation rates below the ELA were close to observations. This may partially be a product of the data produced by Rounce et al. (2018) which, though an improvement from previous efforts, underestimates debris thickness slightly relative to measurements by Nakawo et al. (1986), meaning the impact on ablation is increased. Nevertheless, these two curves, one produced using the DADDI model that matches well with those found elsewhere (Figure 4.20), and one that is based on measurements from nearby Ngozumpa glacier (Nicholson and Benn, 2013) demonstrates the inherent difficulties and uncertainties associated with producing accurate simulations of debris-covered glacier mass balance.

The spatial distribution of simulated debris thickness by iSOSIA matches well with observations, though absolute values are slightly higher than observations (Nakawo et al., 1986) or estimates used in Chapter 4 (Rounce et al., 2018). For this reason, the contrasting exponential sub-debris ablation correction curve used in three experiments here, and that generated by the DADDI model would not significantly alter mass balance and ice flow modelling results, as debris thickness simulated by iSOSIA is often ≥ 1.5 m. This demonstrates the challenges associated with model evaluation of debris-covered glaciers, with the bulk of glacier models being designed for clean-ice glaciers. To date the contribution of avalanches to accumulation rates have been largely neglected in modelled representations of Himalayan glacier mass balance. The importance of avalanching and supraglacial debris for Khumbu Glacier mass balance, that applies to many glaciers of the HKKH, highlights the need for a coupled mass balance/ice flow model, where key mass balance elements are treated within one streamlined approach.

Future precipitation increase can act to offset the impact of increased temperatures for glacier mass balance, exhibited by the similar NOAA forced mass balance under RCP4.5 at the end of the century to that of the present day. This 14.5% precipitation increase can mostly offset the impact of the 1.4°C temperature rise on glacier mass balance. Similar results were seen in the coupled parameter testing in Chapter 4, where 1.5°C of warming was offset by a 10% increase in precipitation. Despite this minimal change, the integration of the NOAA forced mass balance with the ice flow model meant that the impact of historical warming was exhibited by a 2.1 km retreat of Khumbu Glacier and thinning of 40 m in the icefall.

7.3 Future work

The focus on studying glacier change in the HKKH region has grown considerably during this project in several ways. Remote-sensing analyses have allowed estimates of glacier change to span 60 years (e.g. Maurer et al., 2019), and to cover the entire HKKH range in a single analysis (e.g. Brun et al., 2017). Further studies assessing surface lowering and velocities to identify additional glaciers that may be prone to or close to detachment from the active glacier would be beneficial and would aid future modelling efforts to represent this process. To date this phenomenon has been understudied, and at the time of writing the work in this thesis is the first to simulate this, despite the considerable implications for future glacier viability. Open-access glacier models are growing in number, enabling research communities worldwide to contribute to model development and undertake climate impact studies on Himalayan glaciers. The energy balance modelling approach used in this thesis has been made possible as COSIPY is open-source, but also due to the high elevation meteorological observations that have been used for glacier model forcing and evaluation, and downscaling calibration and validation. These has been particularly important for precipitation, given the poor representation of the monsoon signal in climate products. Many glacierised regions of the HKKH remain unrepresented in modelling efforts due to a paucity of glaciological and meteorological data.

The simulated mass balance revealed that ablation can occur high above the ELA, where temperatures are well below freezing. Future, finer detail simulations focusing on the mass balance in the upper reaches of high elevation glaciers, such as Khumbu Glacier, to build on the work here and the preliminary results from Matthews et al. (2020), would be beneficial. Installation and maintenance of precipitation and/or snow-depth sensors in high elevation accumulation areas is highly challenging, but would be particularly pertinent for helping to constrain the contribution of avalanches to accumulation rates. There would be real value in exploring the energy balance dynamics that could allow ablation in the upper reaches, which is now possible with the release of meteorological observations above 6,500 m.a.s.l.. For example, the strong correlation between net shortwave radiation and albedo found in this thesis, and the persistence of snow throughout much of the year, makes these upper reaches particularly susceptible to darkening of snow from industrial pollutants. Melting near to the summit of Everest, considered one of the most remote and extreme locations, would be an extraordinary phenomenon that would highlight the far-reaching influence of human activity on the cryosphere.

The integrated modelling approach used in this thesis would improve accuracy of projections of glacier change elsewhere, such as in other regions of steep terrain where debris-covered glaciers exist e.g. the Andes, Southern Alps of New Zealand or the European Alps. Glaciers in these regions

are also often avalanche-fed. Forcing glacier dynamics models (that resolve avalanching) with distributed mass balance is preferable for such glaciers, and is a vast improvement from scaling of ELAs or accumulation area ratios, which often neglect avalanching and currently dominate glacier change studies. This modelling approach is also able to resolve dynamic and physical detachment, and as such could be applied to other regions. Detachment has been observed at Chorabari Glacier in the Garhwal Himalaya (Dobhal et al., 2013), and at Lirung Glacier in the Langtang Valley (Immerzeel et al., 2014a). More widely, there is evidence of this occurring in the Canadian Rockies (Rippin et al., 2019) and the Alaskan icefields (Davies, et al., 2021).

Forcing a higher-order ice flow model with distributed glacier mass balance derived from energy balance modelling, is a major advance in the representation of the complex mechanisms of glacier change. Clean-ice mass balance was used to force iSOSIA, as iSOSIA treated englacial debris transport and sub-debris ablation in a more sophisticated manner than COSIPY. Following integration with iSOSIA, glacier mass balance for the chosen sub-debris parameterisation was found to match well with observations despite the overestimated simulated debris thickness. However, the clean-ice mass balance forcing is a more time consuming and indirect approach both for computational expense but also for model calibration and validation. This is also made more complex given the substantial contribution of avalanching to accumulation rates for Khumbu Glacier.

A coupled version of the modelling approach developed in this thesis would be a valuable next step for resolving the feedbacks between debris-covered glacier mass balance, debris transport and ice flow. Further improvements could include representation of ice-climate interactions and how these may change over time which would be of immense value for future glacier projections. These are currently lacking, particularly for debris-covered glaciers, and are somewhat hindered by the computational expense of running atmosphere-ice models at the required spatial resolution.

Analysis of the Ev-K2-CNR meteorological observations indicated that precipitation LRs were slightly negative but very weak in this catchment. Given the high incidence of missing precipitation data from these stations, the known undercatch of solid winter precipitation associated with these rain gauges and the absence of precipitation data above 5,600 m.a.s.l., no precipitation lapse rate was used for the present day and future integrated mass balance modelling. The high spatial variability of the local meteorology, particularly precipitation, supports the need for the complex terrain to be well-resolved using higher resolution climate models rather than through distribution of meteorology via elevation-based lapse rates.

The representation of debris-covered glaciers in regional climate model simulations of the Everest region allowed the thermal up-valley winds to propagate further than if they were clean-ice (Potter et al., 2021). Removal of these ice masses to represent future glacier shrinkage enhanced

this propagation further (Potter et al., 2018). This may contribute to orographic enhancement of precipitation. Despite these recent advances, the representation of these processes in modelling remains one-way. High resolution atmospheric modelling that captures local (valley) winds, and quantifies how these impact glacier surface temperature, energy balance, and thereby mass balance, would be of immense value.

More widely, this coupled modelling approach presents a broader need for interdisciplinary research to ensure robust projections of glacier change. This thesis has used detailed climatology to force and evaluate glacier models, and has relied on geomorphology, *in situ* and satellite imagery derived glaciological data for model evaluation. There are currently no co-ordinated efforts, such as model intercomparison projects, that focus on high mountain climates and the atmospheric feedbacks associated with cryospheric change. Higher spatial and temporal resolutions of atmospheric modelling will reveal how sub-daily meteorology may change into the future, including the nocturnal precipitation peak and the diurnal temperature range. Given the huge implications of elevation dependent warming for mountain environments, and the high uncertainty regarding future precipitation trends for the HKKH, a focussed effort on high mountain climate projections would be hugely beneficial for a multitude of disciplines.

7.4 Final remarks

The work presented in this thesis represents a great advance in the representation of the mass balance of this complex, debris-covered Himalayan glacier. Specifically, the integration of the clean-ice mass balance model with the higher-order ice flow model is able to resolve three key elements of Khumbu Glacier mass balance that have not previously been sufficiently resolved in modelling approaches: the inverse ablation rates gradient, particularly the high ablation rates below the ELA, supraglacial debris and avalanching. The detail associated with each stage of the modelling chain means that the projections of future change of Khumbu Glacier can be considered the best estimates to date. The sources of uncertainty have been addressed and quantified where possible, within the constraints of data availability.

The projections of future Khumbu Glacier evolution may be representative of other DCGs in the region. However, the high elevation and size of the avalanching contributing area likely allow the active part of Khumbu Glacier to be sustained further into the future than other glaciers. Detachment from the active glacier or accumulation area is an important non-linear response that here acts to bring forward the cessation of Khumbu Glacier. The significant committed mass loss demonstrates the high climate-glacier imbalance that exists due to historical warming, even for this high elevation active section of Khumbu Glacier and emphasises the urgency for substantial and sustained efforts to curtail anthropogenic warming.

Appendix A: Investigating the sensitivity of Khumbu Glacier mass balance in the present day

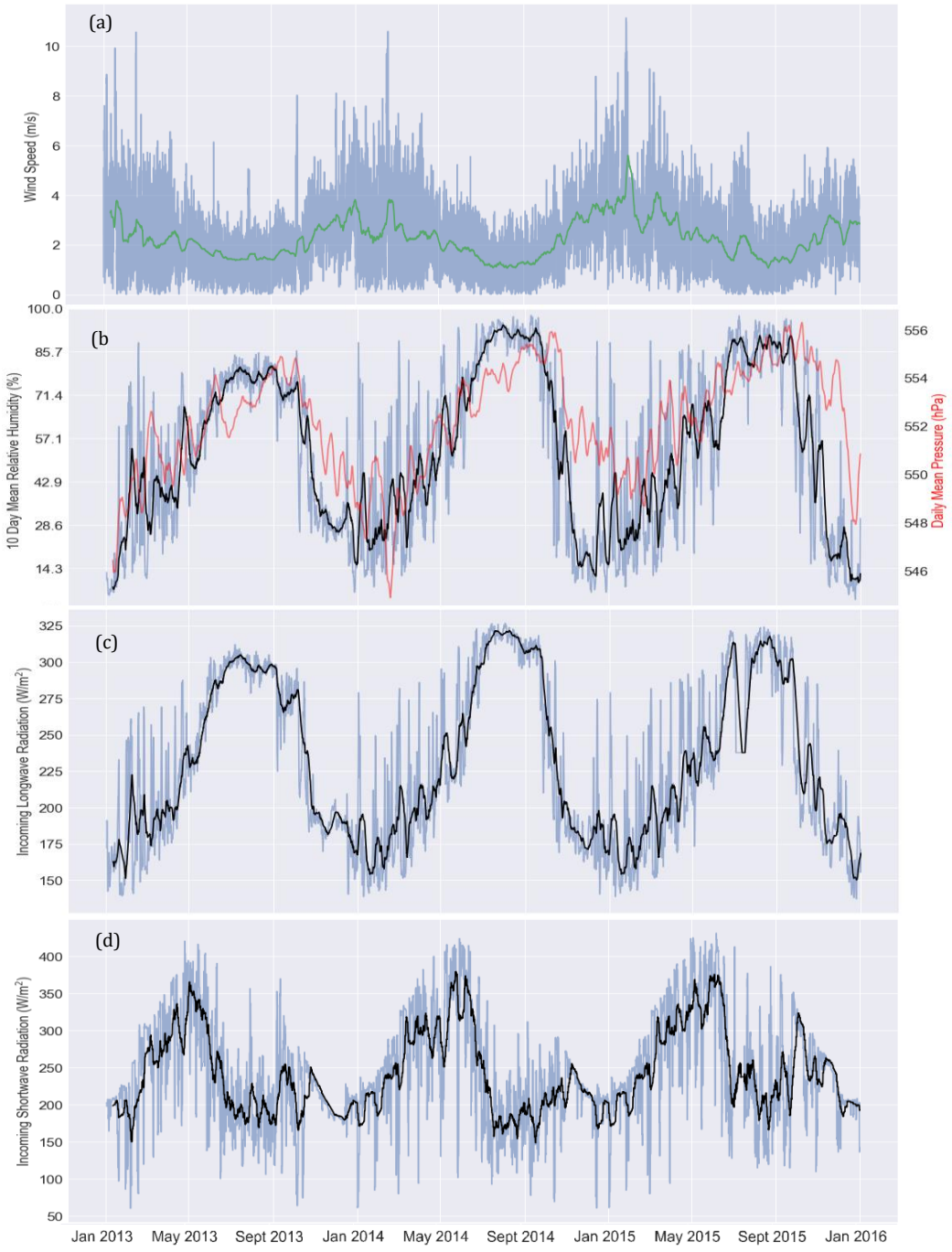

Figure A1: (a) 10 day (green) and daily (shaded blue) wind speed, (b) 10 day (black) and daily (shaded blue) relative humidity and daily air pressure (red) (c) 10 day (black) and daily (shaded blue) incoming shortwave and (d) longwave radiation.

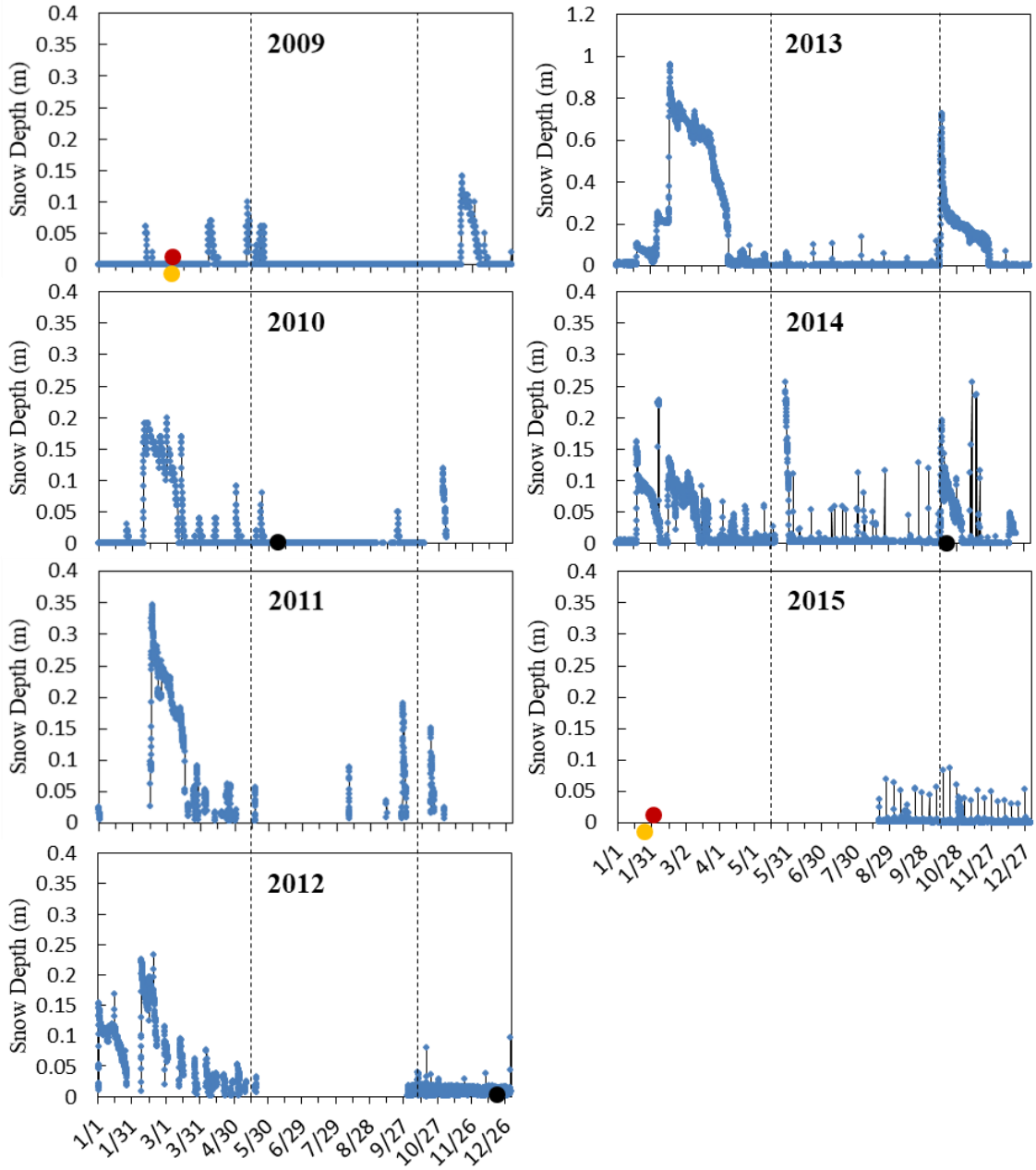

Figure A2: Snow depth measurements from Pyramid ultrasonic depth gauge from 2009 – 2015. Note the y-axis is scaled differently in 2013. Supplementary figure S2 from Rounce et al. (2018).

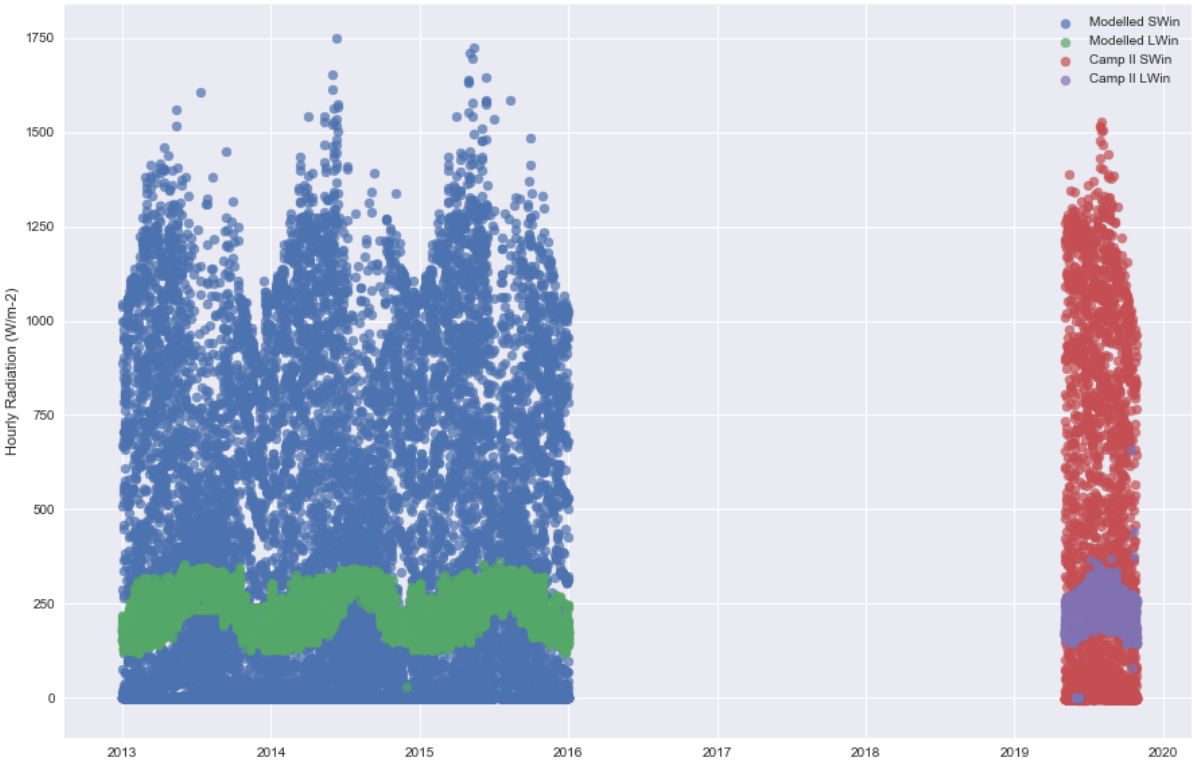

Figure A3: Modelled SWin and LWin for nearest gridpoint to Camp II AWS (6,864 m.a.sl.) and preliminary Camp II radiation.

The mass balance simulations were calibrated for the Khumbu, namely the precipitation gradient so as to match accumulation observations (Inoue, 1977 and Benn and Lehmkuhl, 2000). This results in high ablation rates for the West Changri Nup, that exceed those from observations (Figure A4; Sherpa et al., 2017). The simulated accumulation rates were low and were at times close to zero due to low maximum elevations. Accumulation area ratios of zero were observed at times on West Changri Nup during 2010-2015 (Sherpa et al., 2017). Low modelled accumulation rates will not be able to represent the significant serac avalanches from the steep south-facing slopes that are thought to act as critical inputs to the Changri Nup glacier (Vincent et al., 2016). Debris-covered portion of the glacier MB of −1.21 ± 0.2 m w.e. a−1 between 2011 and 2015 after correction of emergence velocity (Vincent et al., 2016).

Figure A4: Point measurements of cumulative mass balance for the clean-ice West Changri Nup with observations from Sherpa et al. (2017).

Appendix B: Downscaling of Regional Climate Model data

B1: Model Selection

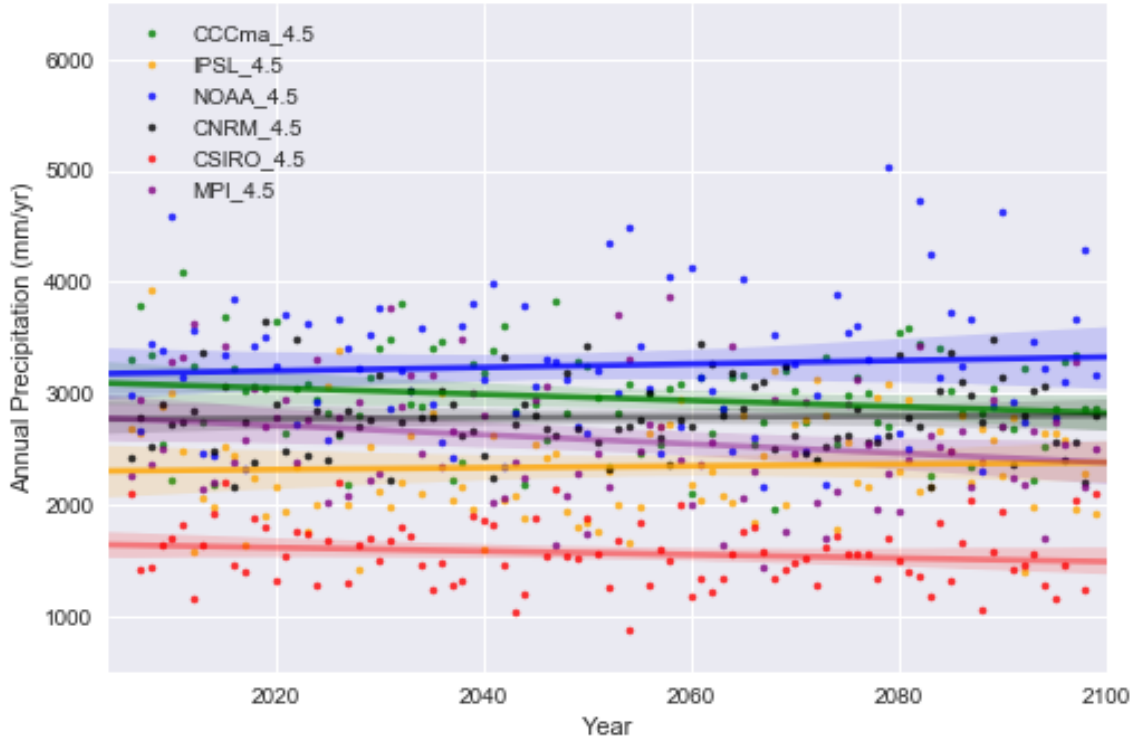

Figure B1.1: Annual precipitation sums (dots) with fitted trend line from the start of the RCP experiments (2006) until the end (2100) for each of the Indian Institute for Tropical Meteorology CORDEX models for RCP4.5.

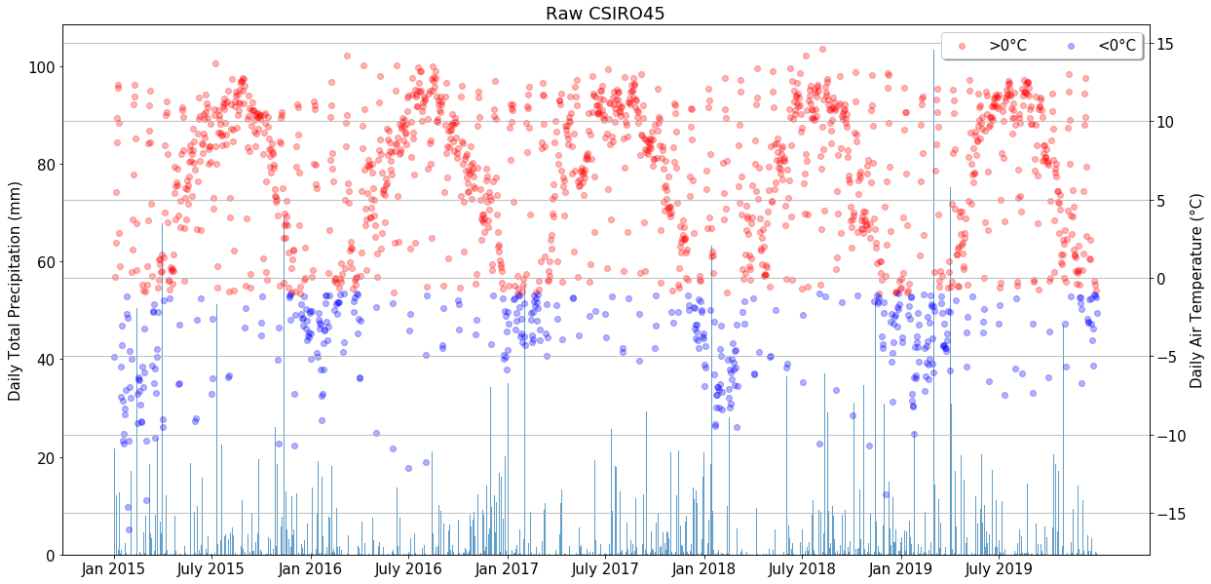

Figure B1.2: Daily mean temperature and daily total precipitation prior to downscaling for PD time-slice for CSIRO driven RCM. Despite CSIRO precipitation annual precipitation sums being closest to observations (B1.1), the seasonality and particularly monsoon signal is absent with a dominance of winter precipitation.

B2: Downscaled Climate

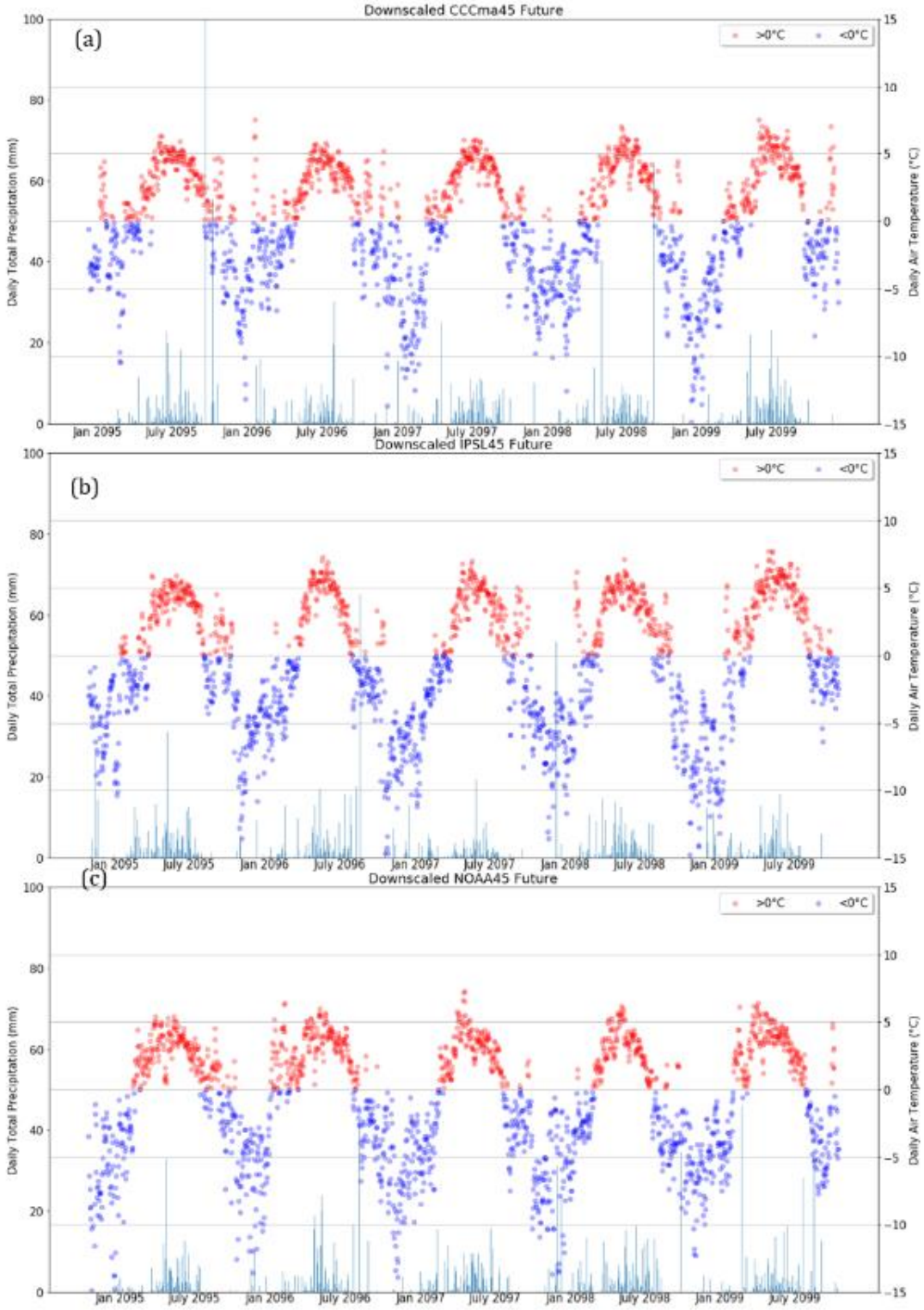

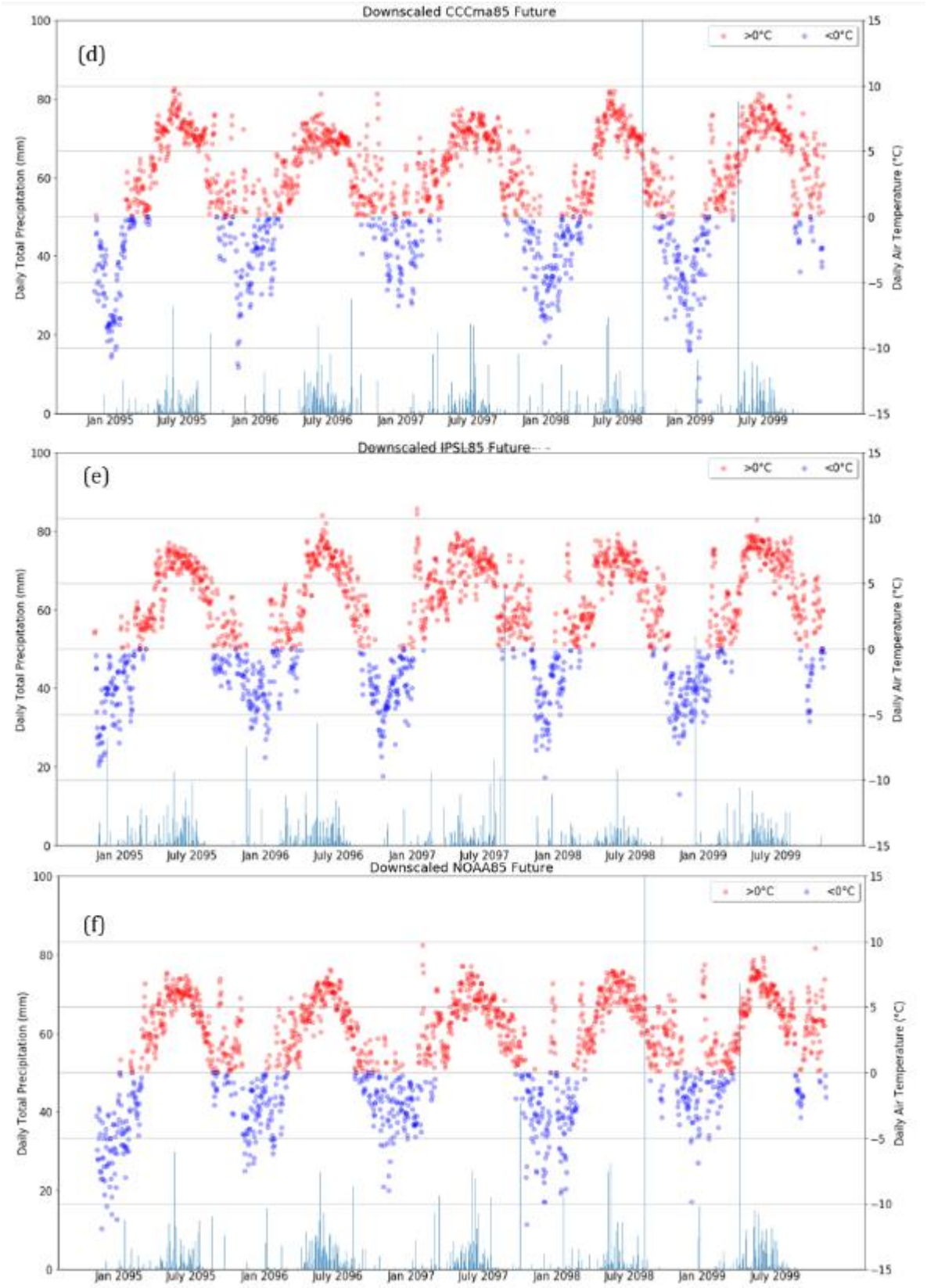

Figure B2.1: (a-c) End-of-century downscaled temperature and precipitation under RCP4.5 and (d-f) the same but under RCP8.5.

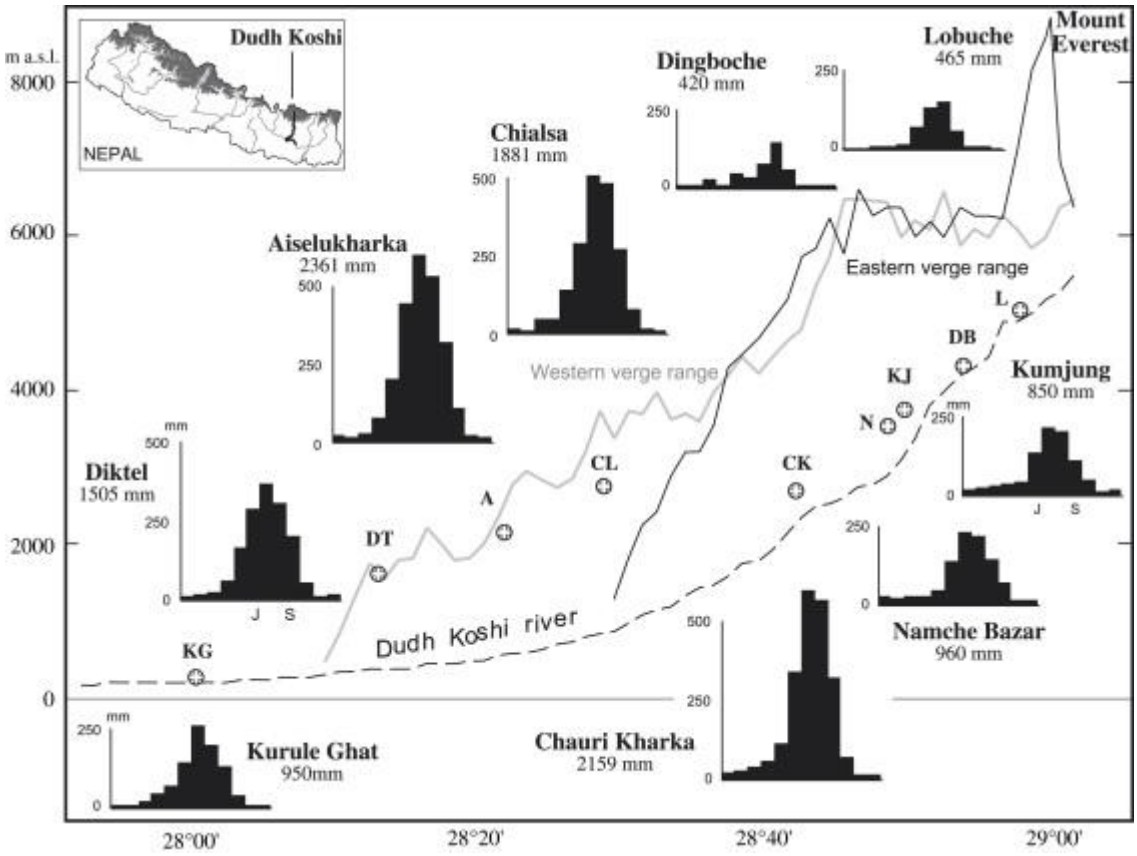

Figure B2.2: Latitudinal variations of precipitation along the Dudh Koshi valley in the southern flank of the Khumbu region. Histograms show mean monthly precipitation with mean annual precipitation displayed under station name. From Asahi et al., 2010.

B3: Implications of temperature disaggregation for glacier mass balance

Resolving the meteorological complexity of the sub-daily temporal scale, was critical for ensuring accurate glacier mass balance. Ensuring an accurate representation of disaggregated temperature was found to be important both for a statistically significant relationship with hourly observations, but also realistic modelled mass balance. Downscaled T_{max} and T_{mean} and hourly observations were critical for calibration to produce this data; reiterating the importance of *in situ* temperature observations for robust glacier melt simulations.

The output from the temperature disaggregation method (Debele et al., 2007) was compared against several other disaggregation functions from the open-source MEteoroLOgical observation time series DISaggregation Tool (MELODIST - gathered from the site: https://github.com/kristianfoerster/melodist). The results from the method from Debele et al. (2007) were found to produce strong correlations with hourly observations and day-on-day variability as a result of the

diurnal amplitude being forced by the daily downscaled T_{min} and T_{max} variables (rather than a fixed amplitude). The monsoon lowering of diurnal temperature range is also better resolved with this method. Diurnal temperature trends will not necessarily be the same as present day and this may be better represented in future T_{min} and T_{max} trends than a fixed amplitude. The impact of using the Debele et al. (2007) method (sineminmax) and the three MELODIST methods on glacier mass balance is shown in Figure B2.

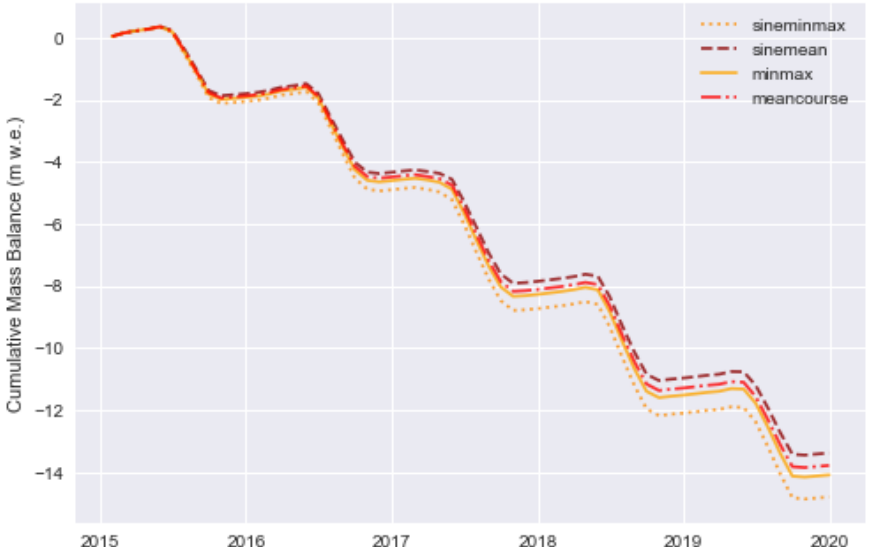

Figure B2: Cumulative mass balance driven by downscaled IPSL climate using four different disaggregation methods.

The slight warm bias observed in the disaggregated CCCma data relative to observations (mainly exhibited by a lower frequency of < -10°C temperatures than observations) does not translate into increased mass loss. The MB simulation forced by the downscaled NOAA climate data produced a MB change most similar to observations, both in terms of absolute values but also temporal patterns. It cannot be expected that the timings of ablation or accumulation will match with the simulation forced by observations, as the downscaled climate data is a product of the RCM and driving GCM as well as the 14 years of observations. However, the downscaled NOAA data shows more interannual variability in the timings of mass change, similar to that forced by observations. Winter accumulation in 2017/2018 was absent in the simulations forced by observations and NOAA, and mass loss continued unabated. The downscaled IPSL forcing produces extensive modelled clean-ice mass loss due mostly to the much lower precipitation that is apparent both prior to and following downscaling.

Appendix C: Present-day and future evolution of Khumbu Glacier

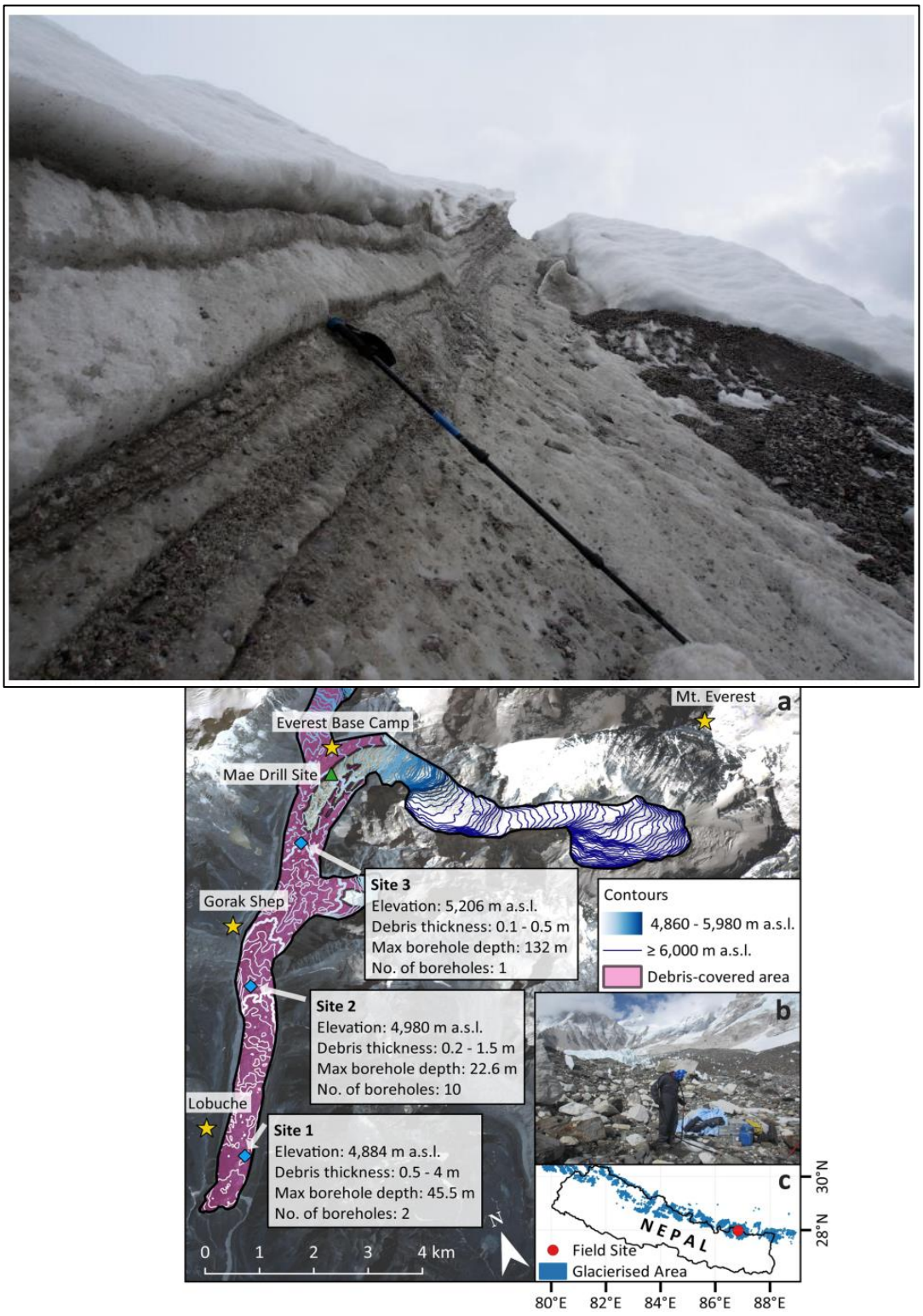

Figure C1: (a) Layers of basal ice observed at the glacier's surface, close to Site 2 (supplementary Figure 8 from Miles et al., 2021b) (b) Location map of Khumbu Glacier denoting drill sites referred to in (a) and Figure C1.2 (next figure)

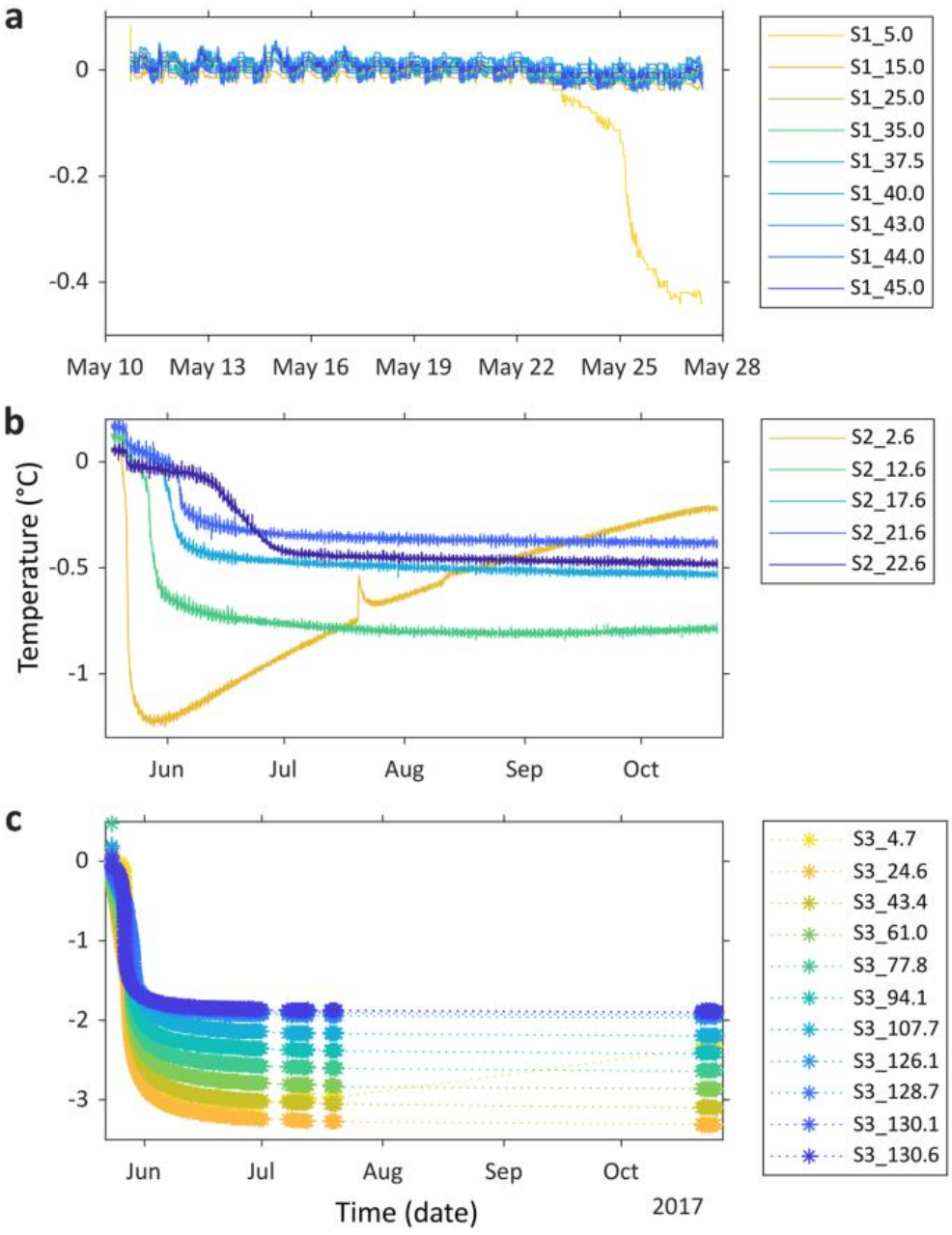

Figure C2 Figure Englacial temperature measured for each borehole thermistor string colour-coded by depth for: (a) Site 1; (b) Site 2; and (c) Site 3. Note different axes limits. Thermistors are colour coded by depth.

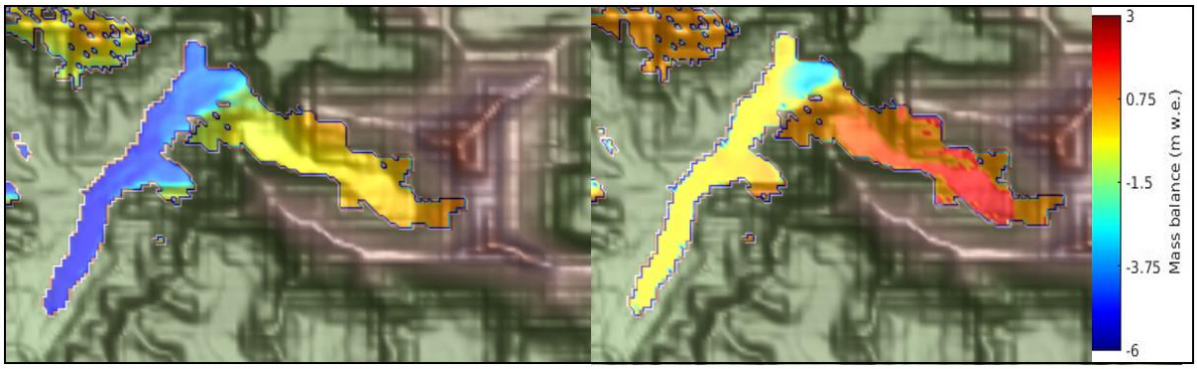

Figure C3 (a) Clean-ice glacier mass balance (b) present day glacier mass balance following integration with iSOSIA, from experiment 9 (NOAA MB forcing and exponential sub-debris ablation parameterisation).

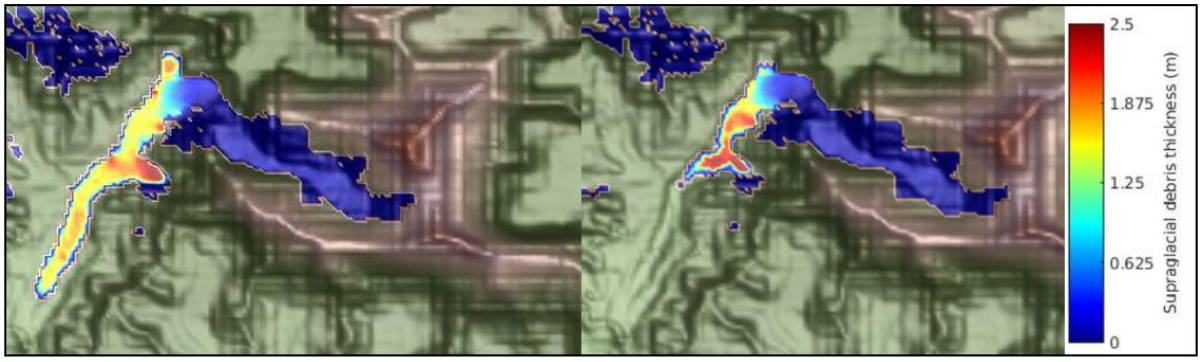

Figure C4 Present day simulated supraglacial debris thickness from NOAA MB forcing but (a) with the exponential sub-debris ablation parameterisation and (b) the reciprocal of h0 = 0.8 m.

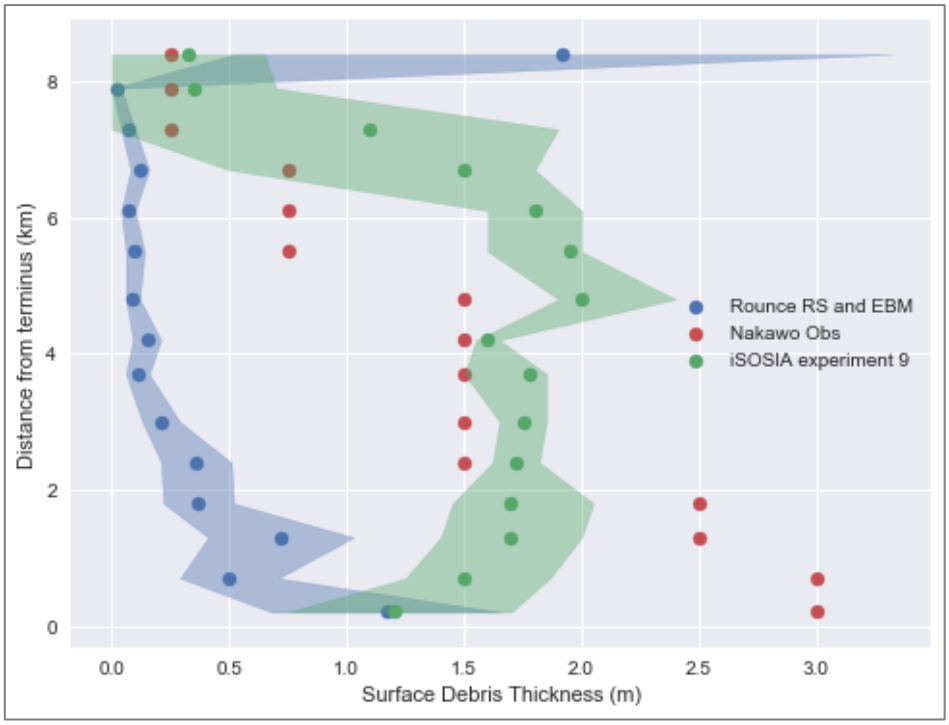

Figure C5 Surface debris thickness along the glacier tongue calculated via remote-sensing and EBM (Rounce RS and EBM; Rounce et al., 2018), *in situ* measurements (Nakawo Obs; Nakawo et al., 1986) and ice-flow modelling (iSOSIA experiment 9; Chapter 6). Points represent mean value and shading standard deviation.

Figure C6 Simulated velocities in 2250 under the MB forcing from the NOAA RCP8.5 climate scenario.

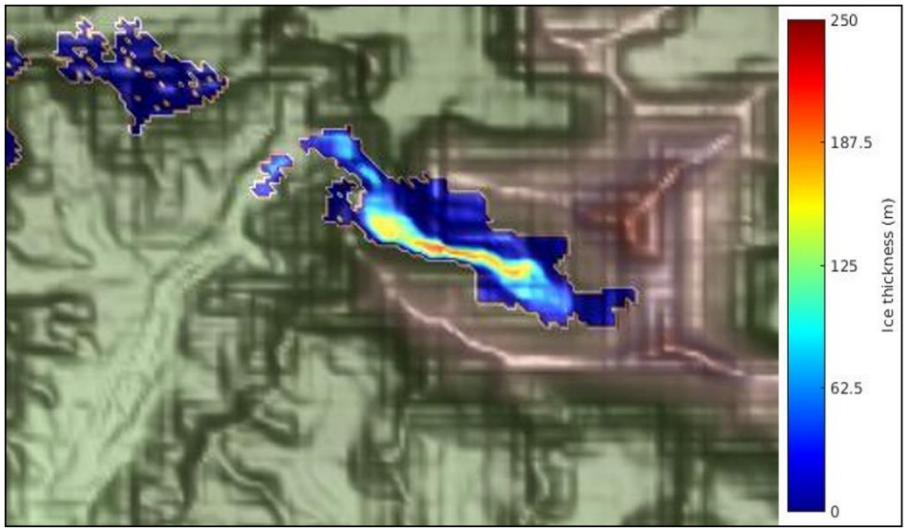

Figure C7 Simulated ice thickness in 2100 under the MB forcing from the IPSL RCP4.5 scenario. Note the small remaining patch of debris-covered ice following detachment from the accumulation area.

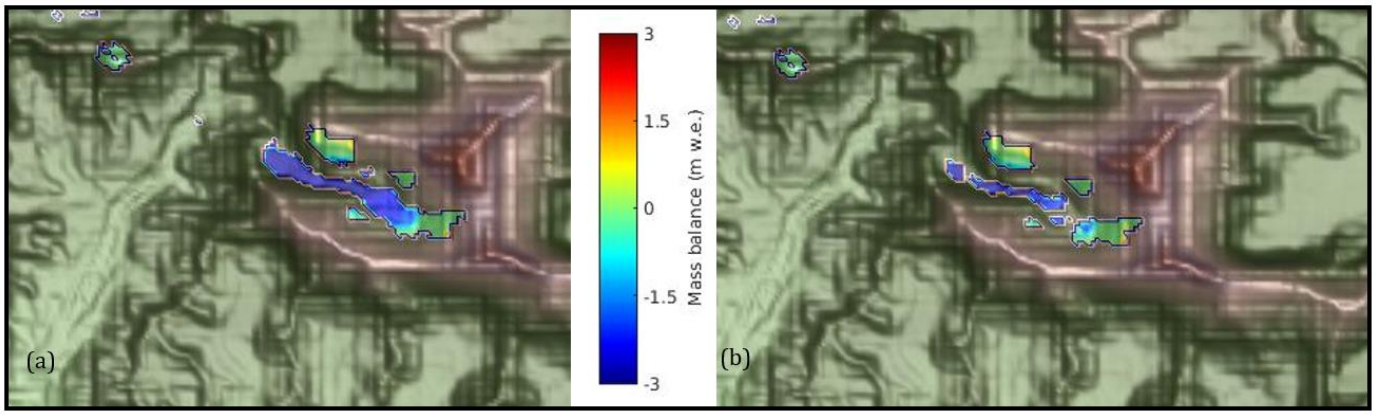

Figure C8 (a) Mass balance in 2120 and (b) in 2140 under the RCP8.5 CCCma MB forcing.

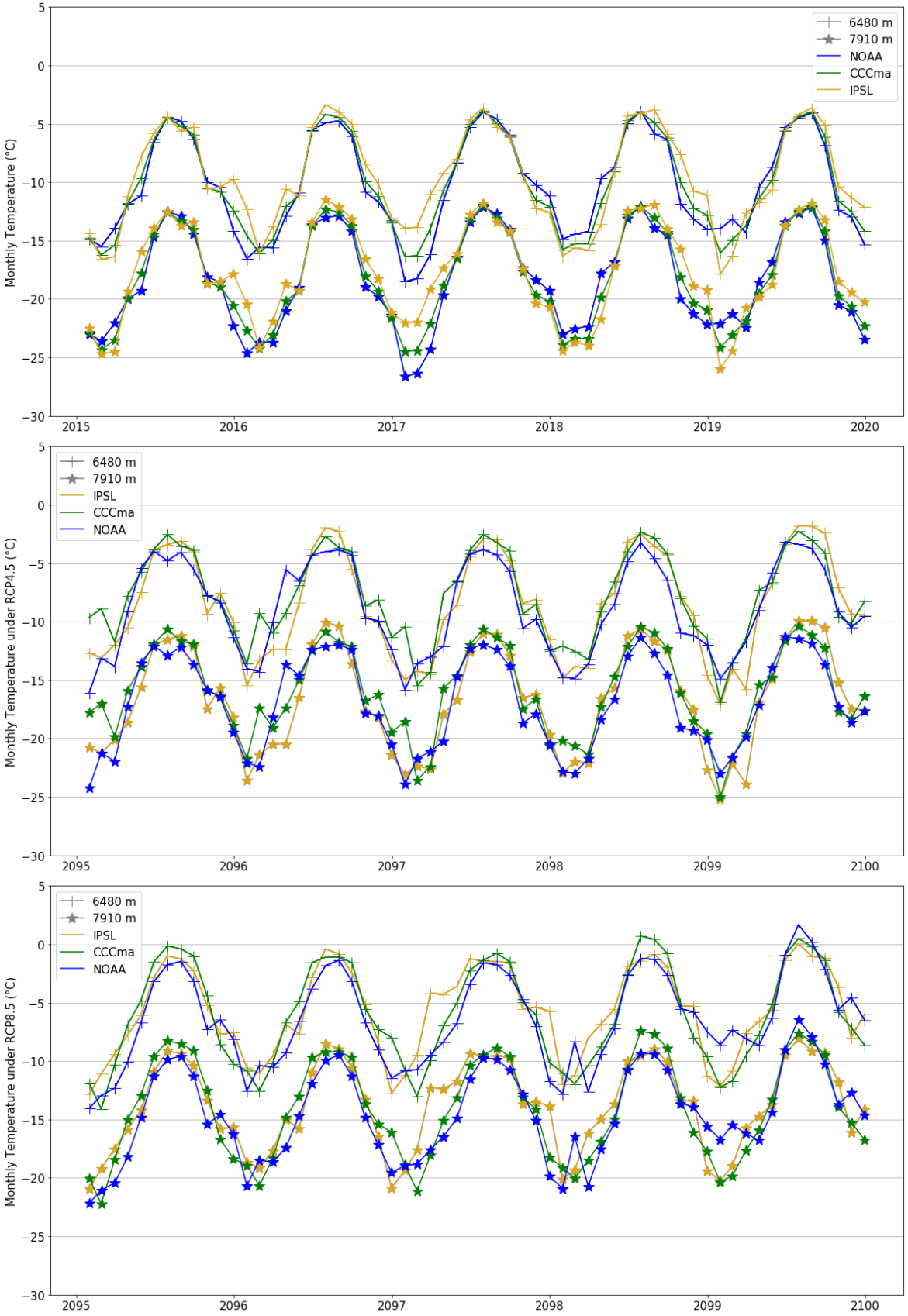

Figure C9 Monthly temperature at 6,480 m.a.sl. (Camp II, the Western Cwm) and 7,910 m.a.sl. (South Col, the highest limit of Khumbu Glacier) in (a) present day and at the end of the century under (b) RCP4.5 and (c) RCP8.5.

References

Ageta, Y. (1976). Characteristics of precipitation during monsoon season in Khumbu Himalaya. Seppyo. 38: 84–88. doi: 10.5331/seppyo.38.Special_84.

Ageta, Y. and Higuchi, K. (1984). Estimation of Mass Balance Components of a Summer-Accumulation Type Glacier in the Nepal Himalaya. *Geografiska Annaler. Series A, Physical Geography*. 66(3): 249-255.

Akhtar, M., Ahmad, N. and Booij, M. (2008) The impact of climate change on the water resources of Hindukush–Karakorum–Himalaya region under different glacier coverage scenarios, *Journal of Hydrology, 355*(1-4): 148-163. doi: 10.1016/j.jhydrol.2008.03.015.

Altena, B. and Kääb, A. (2020) Ensemble matching of repeat satellite images applied to measure fast-changing ice flow, verified with mountain climber trajectories on Khumbu icefall, Mount Everest. *Journal of Glaciology.* 66(260): 905-915. doi: 10.1017/jog.2020.66.

Anderson, R.S., (2000). A model of ablation-dominated medial moraines and the generation of debris-mantled glacier snouts. *Journal of Glaciology,* 46(154): 459-469.

Anderson, L.S. and Anderson, R.S., (2016). Modelling debris-covered glaciers: response to steady debris deposition. *The Cryosphere,* 10(3): 1105-1124.

Anderson, L.S. and Anderson, R.S., (2018). Debris thickness patterns on debris-covered glaciers. *Geomorphology,* 311: 1-12.

Archer, D. R. and Fowler, H. J. (2004). Spatial and temporal variations in precipitation in the Upper Indus Basin, global teleconnections and hydrological implications. *Hydrological Earth System Sciences*. 8, 47–61.

Arendt, A. et al. (2013). Randolph Glacier Inventory [v3.2]: a dataset of global glacier outlines. Global Land Ice Measurements from Space, Boulder, CO. Digital media: http://www.glims.o214odellinandolph.html

Arendt, A. et al. (2015). Randolph glacier inventory–a dataset of global glacier outlines: Version 5.0. Global Land Ice Measurements from Space, Boulder, CO. Digital media: http://www.glims.o214odellinandolph.html

Ayala, A., Pellicciotti, F. and Shea, J. (2015). Modeling 2 m air temperatures over mountain glaciers: Exploring the influence of katabatic cooling and external warming. *Journal of Geophysical Research: Atmospheres*. 120: 3139-3157. doi: 10.1002/2015JD023137.

Bajracharya, S. R., & Shrestha, B. (Eds.). (2011). The status of glaciers in the Hindu Kush Himalayan region. *Kathmandu: ICIMOD.*

Bajracharya, S.R., Maharjan, S.B., Shrestha, F., Guo, W., Liu, S., Immerzeel, W. and Shrestha, B. (2015). The glaciers of the Hindu Kush Himalayas: current status and observed changes from the 1980s to 2010. *International Journal of Water Resources Development*. 31: 161–173. doi:10.1080/07900627.2015.1005731

Bamzai, A. S., and Shukla, J. (1999). Relation between Eurasian snow cover, snow depth, and the Indian summer monsoon: An observational study. *J. Climatology.* 12: 3117 – 3132.

Banerjee, A. (2017), Brief communication: Thinning of debris-covered and debris-free glaciers in a warming climate, *The Cryosphere*, 11(1), 133–138, doi:10.5194/tc-11-133-2017.

Banerjee, A., Patil, D. and Jadhav, A. (2020). Possible biases in scaling-based estimates of glacier change: a case study in the Himalaya*. The Cryosphere,* 14: 3235–3247.

Barton, M. (2017). Twenty-Seven Years of Manual Fresh Snowfall Density Measurements on Whistler Mountain, British Columbia. *Atmosphere-Ocean*. 55: 144-154. doi: 10.1080/07055900.2017.1331157.

Bazai, N. A., Cui, P., Carling, P. A., Wang, H., Hassan, J., Liu, D., Zhang, G. and Jin, W. (2021) Increasing glacial lake outburst flood hazard in response to surge glaciers in the Karakoram. *Earth-Science Reviews*, 212: 103432. doi: 10.1016/j.earscirev.2020.103432

Benn, D. and Lehmkuhl, F. (2000). Mass balance and equilibrium-line altitudes of glaciers in high-mountain environments, *Quaternary International,* 65/66: 15-29. doi: 10.1016/S1040-6182(99)00034-8.

Benn, D., Bolch, T., Hands, K., Gulley, J., Luckman, A., Nicholson, L., Quincey, D., Thompson, S., Toumi, R. and Wiseman, S. (2012). Response of debris-covered glaciers in the Mount Everest region to recent warming, and implications for outburst flood hazards. *Earth-Science Reviews.* 114(1-2): 156-174. doi: 10.1016/j.earscirev.2012.03.008

Benn, D., Thompson, S., Gulley, J., Mertes, J., Luckman, A. and Nicholson, L. (2017). Structure and evolution of the drainage system of a Himalayan debris-covered glacier, and its relationship with patterns of mass loss. *The Cryosphere*. 11(5): 2247-2264. doi: 10.5194/tc-11-2247-2017.

Bolch, T., Kulkarni, A., Kaab, A., Huggel, C., Paul, F., Cogley, J. G., Frey, H., Kargel, J. S., Fujita, K., Scheel, M., Bajracharya, S. and Stoffel, M. (2012). The State and Fate of Himalayan Glaciers. *Science*. 336 (6079): 310-314. doi: 10.1126/science.1215828.

Bollasina, M., Bertolani, L. and Tartari, G. (2002). Meteorological observations at high altitude in the Khumbu Valley, Nepal Himalayas, 1994– 1999. *Bull. Glaciol. Res*., 19: 1 –11.

Bolton, D. (1980). The computation of equivalent potential temperature. *Monthly Weather Review.* 108: 1046–1053.

Bonasoni, P., Laj, P., Marinoni, A., Sprenger, M., Angelini, F., Arduini, J., Bonafè, U., Calzolari, F., Colombo, T., Decesari, S., Di Biagio, C., di Sarra, A. G., Evangelisti, F., Duchi, R., Facchini, M., Fuzzi, S., Gobbi, G. P., Maione, M., Panday, A., Roccato, F., Sellegri, K., Venzac, H., Verza, G., Villani, P., Vuillermoz, E. and Cristofanelli, P. (2010) Atmospheric Brown Clouds in the Himalayas: first two years of continuous observations at the Nepal Climate Observatory-Pyramid (5079 m). Atmospheric Chemistry and Physics, 10(15): 7515-7531. doi: 10.5194/acp-10-7515-2010.

Bookhagen, B., & Burbank, D. W. (2006). Topography, relief, and TRMM-derived rainfall variations along the Himalaya. *Geophysical Research Letters.* 33(8), 1 – 5. doi:10.1029/2006GL026037

Bookhagen, B. and Burbank, D. W. (2010). Toward a complete Himalayan hydrological budget: Spatiotemporal distribution of snowmelt and rainfall and their impact on river discharge. *Journal of Geophysical Research: Earth Surface*, 115(F3).

Bonekamp PNJ, de Kok RJ, Collier E and Immerzeel WW (2019). Contrasting Meteorological Drivers of the Glacier Mass Balance Between the Karakoram and Central Himalaya. Front. Earth Sci. 7:107. doi: 10.3389/feart.2019.00107.

Bosshard, T., S. Kotlarski, T. Ewen, and C. Schär (2011), Spectral representation of the annual cycle in the climate change signal, *Hydrology Earth System Science.,* 15: 2777–2788,

Brædstrup, C., Egholm, D., Ugelvig, S. and Pedersen, V., (2016). Basal shear stress under alpine glaciers: insights from experiments using the iSOSIA and Elmer/Ice models. *Earth Surface Dynamics*, 4(1): 159-174.

Bravo-Lechuga, C., Quincey, D., Ross, A., Rivera, A., Brock, B., Miles, E. and Silva, A. (2019). Air Temperature Characteristics, Distribution, and Impact on Modeled Ablation for the South Patagonia Icefield. *Journal of Geophysical Research: Atmospheres*. 124: 907-925. doi: 10.1029/2018JD028857

Brun, F., Dumont, M., Wagnon, P., Berthier, E., Azam, M., Shea, J., Sirguey, P., Rabatel, A. and Ramanathan, A. (2015). Seasonal changes in surface albedo of Himalayan glaciers from MODIS data and links with the annual mass balance. *The Cryosphere*. 9: 341-355. doi: 10.5194/tc-9-341-2015.

Brun, F., Berthier, E., Wagnon, P., Kääb, A., and Treichler, D. (2017). A spatially resolved estimate of High Mountain Asia glacier mass balances from 2000 to 2016. *Nature geoscience,* 10(9):668.

Brun, F., Wagnon, P., Berthier, E., Shea, J. M., Immerzeel, W. W., Kraaijenbrink, P. D. A., Vincent, C., Reverchon, C., Shrestha, D. and Arnaud, Y. (2018) Ice cliff contribution to the tongue-wide ablation of Changri Nup Glacier, Nepal, central Himalaya, *The Cryosphere*, 12(11): 3439-3457. doi: 10.5194/tc-12-3439-2018.

Brun, F., Wagnon, P., Berthier, E., Jomelli, V., Maharjan, S. B., Shrestha, F. and Kraaijenbrink, P. (2019) Heterogeneous Influence of Glacier Morphology on the Mass Balance Variability in High Mountain Asia, *Journal of Geophysical Research: Earth Surface*, 124(6): 1331-1345. doi: 10.1029/2018jf004838.

Budd, W, Keage, P. and Blundy, N. (1979). Empirical studies of ice sliding. *Journal of Glaciology*., 23(89), 157–170.

Buri, P., Miles, E. S., Steiner, J. F.,Immerzeel, W., Wagnon, P., and Pellicciotti, F. A physically-based 3-D model of ice cliff evolution on a debris-covered glacier. *J. Geophys. Res. Earth Surf.* 121: 2471-2493. doi:10.1002/2016JF004039.

Cannon, F., Carvalho, L. M. V., Jones, C. and Bookhagen, B. (2015a). Multi-annual variations in winter westerly disturbance activity affecting the Himalaya. *Climate Dynamics*. 44, 441–455.

Cannon, A., Sobie, S. and Murdock, T. (2015b) Bias Correction of GCM Precipitation by Quantile Mapping: How Well Do Methods Preserve Changes in Quantiles and Extremes? *Journal of Climate*, 28(17): 6938-6959. doi: 10.1175/jcli-d-14-00754.1.

Cannon, A. (2016) Multivariate Bias Correction of Climate Model Output: Matching Marginal Distributions and Intervariable Dependence Structure, Journal of Climate, 29(19): 7045-7064. doi: 10.1175/jcli-d-15-0679.1.

Cape, M., Vernet, M., Skvarca, P., Marinsek, S., Scambos, T. and Domack, E. (2015). Foehn winds link climate-driven warming to ice shelf evolution in Antarctica. *Journal of Geophysical Research: Atmospheres,* 120: 11,037-11,057.

Chambers J, R., Smith M, W., Quincey D, J., Carrivick J, L., Ross A, N., James M, R. (2019). Glacial aerodynamic roughness estimates: uncertainty, sensitivity and precision in field measurements. *Journal of Geophysical Research.* 125. doi: 10.1029/2019JF005167.

Che, Y., Zhang, M., Li, Z., Wei, Y., Nan, Z., Li, H., Wang, S. and Su, B. (2019.) Energy balance model of mass balance and its sensitivity to meteorological variability on Urumqi River Glacier No.1 in the Chinese Tien Shan. *Sci Rep.* 9: 13958. doi: 10.1038/s41598-019-50398-4.

Collier, E., Nicholson, L., Brock, B., Maussion, F., Essery, R., and Bush, A. (2014). Representing moisture fluxes and phase changes in glacier debris cover using a reservoir approach. *The Cryosphere*. 8(4):1429–1444.

Collier, E, Maussion, F., Nicholson, L., Mölg, T., Immerzeel, W.W and Bush, B. G. (2015). Impact of debris cover on glacier ablation and atmosphere–glacier feedbacks in the Karakoram. *The Cryosphere.* 9: 1617-1632. doi: 10.5194/tc-9-1617-2015.

Collier, E. and Immerzeel, W. (2015). High-resolution modelling of atmospheric dynamics in the Nepalese Himalaya. *Journal of Geophysical Research: Atmospheres*. 120(19): 9882-9896. doi: 10.1002/2015JD023266.

Collins, M., R. Knutti, and J. Arblaster (2013), Long-term Climate Change: Projections, Commitments and Irreversibility. *In: Climate Change 2013: The Physical Science Basis. Contribution of Working Group I to the Fifth Assessment Report of the Intergovernmental Panel on Climate Change* [Stocker, T.F., D. Qin, G.-K. Plattner, M. Tignor, S.K. Allen, J. Boschung, A. Nauels, Y. Xia, V. Bex and P.M. Midgley (eds.)]. Cambridge University Press, Cambridge, United Kingdom and New York, NY, USA,, 1–108.

Cook, B. I., Shukla, S. P., Puma, M. J. and Nazarenko, L. S. (2015). Irrigation as an historical climate forcing. *Climate Dynamics.* 44, 1715–1730.

Cuo, L. and Zhang, Y. (2017). Spatial patterns of wet season precipitation vertical gradients on the Tibetan Plateau and the surroundings. *Sci Rep.* 7: 5057. doi: 10.1038/s41598-017-05345-6.

Davies, B., Bendle, J., McNabb, R., Carrivick, J., McNeil, C., Campbell, S., and Pelto, M. (2021). Recent, rapid and profound changes to glacier morphology and dynamics, Juneau Icefield, Alaska, *EGU General Assembly 2021,* EGU21-1539. doi.org/10.5194/egusphere-egu21-1539.

Debele, B., Srinivasan, R. and Yves Parlange, J., 2007. Accuracy evaluation of weather data generation and disaggregation methods at finer timescales. *Advances in Water Resources*. 30(5): 1286-1300.

Dehecq, A., Gourmelen, N., Gardner, A., Brun,F. ,Goldberg, D. Nienow, P., Berthier, E., Vincent, C., Wagnon, P. and Trouve, E. (2019), Twenty-first century glacier slowdown driven by mass loss in High Mountain Asia, *Nature Geosciences*. 12(1): 1–8, doi:10.1038/s41561-018-0271-9.

Dimri, A., Niyogi, D., Barros, A., Ridley, J., Mohanty, U., Yasunari, T., and Sikka, D. (2015). Western disturbances: a review. *Reviews of Geophysics*, 53(2):225–246. doi: 10.1002/2014RG000460.

Duan, A., Wu, G., Zhang, Q., and Liu, Y. (2006). New proofs of the recent climate warming over the Tibetan Plateau as a result of the increasing greenhouse gases emissions. *Chinese Science Bulletin*, 51(11):1396–1400.

Edwards, T.L., Nowicki, S., Marzeion, B. et al. Projected land ice contributions to twenty-first-century sea level rise. *Nature.* 593: 74–82. doi: 10.1038/s41586-021-03302-y.

Egholm, D. L., Knudsen, M. F., Clark, C. D., and Lesemann, J. E. (2011). Modelling the flow of glaciers in steep terrains: The integrated second-order shallow ice approximation (iSOSIA*). Journal of Geophysical Research: Earth Surface*, 116: F02012, doi:10.1029/2010JF001900.

Eriksson, M., Jianchu, X., Shrestha, A. B., Vaidya, R. A., Nepal, S., Sandstrom, K. (2009). The changing Himalayas – Impact of climate change on water resources and livelihoods in the Greater Himalayas. *International Centre for Integrated Mountain Development (ICIMOD).*

Eyring, V., Bony, S., Meehl, G. A., Senior, C. A., Stevens, B., Stouffer, R. J., and Taylor, K. E. (2016). Overview of the Coupled Model Intercomparison Project Phase 6 (CMIP6) experimental design and organization. *Geoscientific Model Development.* 9: 1937-1958. doi:10.5194/gmd-9-1937-2016, 2016*.*

Farinotti, D. Huss, M., Fürst, J., Landmann, J., Machguth, H., Maussion, F. and Pandit, A. (2019). A consensus estimate for the ice thickness distribution of all glaciers on Earth. *Nature Geoscience*. 12: 168–173.

Farinotti, D., Immerzeel, W. W., de Kok, R. J., Quincey, D. J., & Dehecq, A. (2020). Manifestations and mechanisms of the Karakoram glacier Anomaly. *Nature Geoscience,* 13(1), 8-16. doi: 10.1038/s41561-019-0513-5.

Fowler, H. J. & Archer, D. R. (2006). Conflicting signals of climatic change in the upper Indus basin. *Journal of Climatology*. 19-: 4276–4293.

Fujita, K. and Sakai, A. (2014). Modelling runoff from a Himalayan debris-covered glacier. *Hydrol. Earth Syst. Sci..* 18: 2679-2694. doi: 10.5194/hess-18-2679-2014.

Fushimi, H. (1977). Structural studies of glaciers in the Khumbu Region. *Journal of the Japanese Society of Snow and Ice*. 39: 30–39. doi: 10.5331/seppyo.39.Special_30

Gades, A., Conway, H., Nereson, N., Naito, N. and Kadota, T. (2000). Radio echo-sounding through supraglacial debris on Lirung and Khumbu Glaciers, Nepal Himalayas. *IAHS-AISH Publication,* (264): 13-22.

Gaire, N.P., Koirala, M., Bhuju, D.R. and Borgaonkar, H.P. (2014). Treeline dynamics with climate change at the central Nepal Himalaya. *Climate of the Past*, 10(4): 1277–1290. doi: 10.5194/cp-10-1277-2014

Gaire, NP, Koirala, M, Bhuju, DR. (2017). Site- and species-specific treeline responses to climatic variability in eastern Nepal Himalaya. *Dendrochronologia* 41: 44–56. doi: 10.1016/j.dendro.2016.03.001.

Gagliardini, O., Cohen, D., Råback, P. and Zwinger, T. (2007). Finite-e220odellingodeling of subglacial cavities and related friction law. *Journal of Geophysical Research,* 112(F2). doi: 10.1029/2006jf000576.

Gardner, A., Sharp, M., Koerner, R., Labine, C., Boon, S., Marshall, S., Burgess, D. and Lewis, D. (2009). Near-Surface Temperature Lapse Rates over Arctic Glaciers and Their Implications for Temperature Downscaling. *Journal of Climate.* 22(16): 4281-4298. doi: 10.1175/2009JCLI2845.1

Gardelle, J., Berthier, E., Arnaud, Y., Kaab, A. (2011). Region-wide glacier mass balances over the Pamir Karakoram-Himalaya during 1999-2011. *The Cryosphere*, 7(6): 1885-1886.

Gibson, M., Glasser, N., Quincey, D., Mayer, C., Rowan, A. and Irvine-Fynn, T. (2017). Temporal variations in supraglacial debris distribution on Baltoro Glacier, Karakoram between 2001 and 2012. *Geomorphology,* 295: 572-585.

Gudmundsson, L., Bremnes, J., Haugen, J. and Engen-Skaugen, T. 2012. Technical note: Downscaling RCM precipitation to the station scale using statistical transformations - A comparison of methods. *Hydrology and Earth System Sciences.* 16: 3383–3390. doi:10.5194/hess-16-3383-2012.

Hambrey, M. J., Quincey, D. J., Glasser, N. F., Reynolds, J. M., Richardson, S. J. and Clemmens, S. (2008) Sedimentological, geomorphological and dynamic context of debris-mantled glaciers, Mount Everest (Sagarmatha) region, Nepal, *Quaternary Science Reviews*, 27(25-26): 2361-2389. doi: 10.1016/j.quascirev.2008.08.010.

Herreid, S., Pellicciotti, F. (2020). The state of rock debris covering Earth's glaciers. *Nature Geoscience*. 13, 621–627. doi: 10.1038/s41561-020-0615-0

Hewitt K. (2014) Glacier Mass Balance I: Snowfall and Glacier Nourishment. In: Glaciers of the Karakoram Himalaya. *Advances in Asian Human-Environmental Research.* Springer, Dordrecht. https://doi.org/10.1007/978-94-007-6311-1_4

Heynen, M, Miles, E., Ragettli, S., Buri, P., Immerzeel, W. and Pellicciotti, F. (2016). Air temperature variability in a high-elevation Himalayan catchment. *Annals of Glaciology*. 57: 212-222. doi: 10.3189/2016AoG71A076.

Hock, R., & Holmgren, B. (2005). A distributed surface energy-balance model for complex topography and its application to Storglaciären, Sweden. *Journal of Glaciology, 51*(172): 25-36. doi:10.3189/172756505781829566

Hock R., Jansson P., Braun L.N. (2005) Modelling the Response of Mountain Glacier Discharge to Climate Warming in Global Change and Mountain Regions. *Advances in Global Change Research. ed.* Huber U.M., Bugmann H.K.M., Reasoner M.A. 23: 243-252. (Springer International Publishing, Cham,).

Hock, R., G. Rasul, C. Adler, B. Cáceres, S. Gruber, Y. Hirabayashi, M. Jackson, A. Kääb, S. Kang, S. Kutuzov, Al. Milner, U. Molau, S. Morin, B. Orlove, and H. Steltzer, 2019: High Mountain Areas. In: IPCC Special Report on the Ocean and Cryosphere in a Changing Climate [H.-O. Pörtner, D.C. Roberts, V. Masson-Delmotte, P. Zhai, M. Tignor, E. Poloczanska, K. Mintenbeck, A. Alegría, M. Nicolai, A. Okem, J. Petzold, B. Rama, N.M. Weyer (eds.)].

Huss, M. and Farinotti, D. (2012). Distributed ice thickness and volume of all glaciers around the globe, *Journal of Geophysical Research: Earth Surface,* 117(F4). doi: 10.1029/2012jf002523.

Huss, M. and Hock, R. (2018). Global-scale hydrological response to future glacier mass loss. *Nature Climate Change.* 8: 135–140. doi: 10.1038/s41558-017-0049-x.

Immerzeel, V., Van Beek, L., Bierkens, M. (2010). Climate change will affect the Asian water towers. *Science*. 328: 1382-1385. doi: 10.1126/science.1183188.

Immerzeel, W., Pellicciotti, F., and Bierkens, M. (2013). Rising river flows throughout the twenty-first century in two Himalayan glacierized watersheds. *Nature Geoscience,* 6(9):742.

Immerzeel, W., Kraaijenbrink, P., Shea, J., Shrestha, A., Pellicciotti, F., Bierkens, M. and de Jong, S. (2014a). High-resolution monitoring of Himalayan glacier dynamics using unmanned aerial vehicles, *Remote Sensing of Environment*, 150: 93-103. doi: 10.1016/j.rse.2014.04.025.

Immerzeel, W., Petersen, L., Ragettli, S. and Pellicciotti, F. (2014b). The importance of observed gradients of air temperature and precipitation for modelling runoff from a glacierized watershed in the Nepalese Himalayas. *Water Resources Research*. 50: 2212-2226. doi: 10.1002/2013WR014506.

Jóhannesson, T., Raymond, C. F., and Waddington, E. D. (1989). Time-scale for adjustments of glaciers to changes in mass balance. *Journal of Glaciology*., 35(121), 355–369.

Jemmett-Smith, B., Ross, A.N. and Sheridan, P. (2018). A short climatological study of cold air pools and drainage flows in small valleys. *Weather*. 73(8): 256–262. doi: 10.1002/wea.3281.

Kääb, A., Berthier, E., Nuth, C., Gardelle, J. and Arnaud, Y. (2012). Contrasting patterns of early twenty-first-century glacier mass change in the Himalayas. *Nature.* 488, 495–498. doi: 10.1038/nature11324.

Kääb, A., Treichler, D., Nuth, C. & Berthier, E. (2015). Contending estimates of 2003–2008 glacier mass balance over the Pamir-Karakoram-Himalaya. *Cryosphere* 9: 557–564.

Kadota, T., Seko, K., Aoki, T. , Iwata, S. and Yamaguchi, S. Shrinkage of Khumbu Glacier, east Nepal from 1978 to 1995. M. Nakawo, C.F. Raymond, A. Fountain (Eds.), *Debris-Covered Glaciers,* Proceedings of the Seattle Workshop, USA, September 2000, IAHS Publication 264 (2000), pp. 235-243.

Kaini, S., Nepal, S., Pradhananga, S., Gardner, T. and Sharma, A. K. (2019) Representative general circulation models selection and downscaling of climate data for the transboundary Koshi river basin in China and Nepal. *International Journal of Climatology,* 40(9): 4131-4149. doi: 10.1002/joc.6447.

Kamb, B (1970) Sliding motion of glaciers: theory and observation. *Reviews of Geophysics and Space Physics*. 8(4), 673–728 (doi: 10.1029/RG008i004p00673)

Kapnick, S. B., Delworth, T. L., Ashfaq, M., Malyshev, S. and Milly, P. (2014). Snowfall less sensitive to warming in Karakoram than in Himalayas due to a unique seasonal cycle. *Nature Geosciences*. 7 : 834–840.

Kattel, D.B., Yao, T., Yang, K. et al. (2012). Temperature lapse rate in complex mountain terrain on the southern slope of the central Himalayas. *Theoretical and Applied Climatology.* 113: 671–682. doi.org/10.1007/s00704-012-0816-6.

Kayastha, R. B., Takeuchi, Y., Nakawo, M., and Ageta, Y. (2000). Practical prediction of ice melting beneath various thickness of debris cover on Khumbu Glacier, Nepal, using a positive degree-day factor. *IAHS PUBLICATION, 7182.*

Khadka, M., Kayastha, R. and Kayastha, R. (2020) Future projection of cryospheric and hydrologic regimes in Koshi River basin, Central Himalaya, using coupled glacier dynamics and glacio-hydrological models, *Journal of Glaciology*, 66(259): 831-845. doi: 10.1017/jog.2020.51.

King, O., Quincey, D., Carrivick, J. and Rowan, A. (2017). Spatial variability in mass loss of glaciers in the Everest region, central Himalayas, between 2000 and 2015. *The Cryosphere.* 11(1): 407-426. doi: 10.5194/tc-11-407-2017.

King, O., Bhattacharya, A., Ghuffar, S., Tait, A., Guilford, S., Elmore, A. and Bolch, T., 2020. Six Decades of Glacier Mass Changes around Mt. Everest Are Revealed by Historical and Contemporary Images. *One Earth,* 3(5): 608-620.

Klok, E. J., and Oerlemans, K. (2002). Model study of the spatial distribution of the energy and mass balance of Morteratschgletscher, Switzerland. *Journal of Glaciology.* 48: 505–518. doi: 10.3189/172756502781831133.

Kotlyakov, V.M. 1996. Variations of Snow and Ice in the past and at present on a Global and Regional Scale. UNESCO.

Kraaijenbrink, P., Bierkens, M., Lutz, A., and Immerzeel, W. (2017). Impact of a global temperature rise of 1.5 degrees Celsius on Asia's glaciers. *Nature*, 549(7671):257.

Krishna, K., Rajagapalan, B., Hoerling, M., Bates, G., & Cane, M. (2006). Unraveling the mystery of Indian monsoon failure during El Nino. *Science*, 314(5796), 115–119.

Krishnan, R., Shrestha, A. B., Ren, G., Rajbhandari, R., Saeed, S., Sanjay, J., Syed, M. A., Vellore, R., Xu, Y., You, Q. and Ren, Y. (2019) Unravelling Climate Change in the Hindu Kush Himalaya: Rapid Warming in the Mountains and Increasing Extremes. *The Hindu Kush Himalaya Assessment*, pp. 57-97. doi: 10.1007/978-3-319-92288-1_3.

Lala, J.M., Rounce, D.R., and McKinney, D.C. (2018). Modeling the glacial lake outburst flood process chain in the Nepal Himalaya: reassessing Imja Tsho's hazard. *Hydrology and Earth System Sciences*. 22: 3721–3737. 61.

Lejeune, Y., Bertrand, J.-M., Wagnon, P., and Morin, S. (2013). A physically based model of the year-round surface energy and mass balance of debris-covered glaciers. *Journal of Glaciology,* 59(214):327–344.

Li, Y., Tian, L., Yi, Y., Moore, J. C., Sun, S., & Zhao, L. (2017). Simulating the evolution of Qiangtang No. 1 Glacier in the central Tibetan Plateau to 2050. *Arctic Antarctic and Alpine Research*, 49(1): 1–12.

Litt, M., Shea, J., Wagnon, P., Steiner, J., Koch, I., Stigter, E. and Immerzeel, W. (2019). Glacier ablation and temperature indexed melt models in the Nepalese Himalaya. *Scientific Reports*. 9(1). doi: 10.1038/s41598-019-41657-5.

Locci, F., Melis, M., Dessì, F., Stocchi, P., Akinde, M., Bønes, V., Bonasoni, P. and Vuillermoz, E. (2014). Implementation of a webGIS service platform for high mountain climate research: the SHARE GeoNetwork project. *Geoscience Data Journal*, 1(2): 140-157. doi: 10.13116/C6B6060E-0648-4F88-B108-95EA00928171.

Lovell, A. M., Carr, J. R. and Stokes, C. R.. (2018). Topographic controls on the surging behaviour of Sabche Glacier, Nepal (1967 to 2017). *Remote Sensing of Environment,* 210: 434-443. doi: 10.1016/j.rse.2018.03.036.

Luckman A., Quincey D., and Bevan S. (2007). The potential of satellite radar interferometry and feature tracking for monitoring flow rates of Himalayan glaciers. *Remote Sensing of Environment.* 111(2): 172-181. doi.org/10.1016/j.rse.2007.05.019.

Maurer, J. M., Schaefer, J. M., Rupper, S. and Corley, A. (2019) Acceleration of ice loss across the Himalayas over the past 40 years, *Science Advances,* 5(6), doi: 10.1126/sciadv.aav7266.

Maussion, F., Scherer, D., Molg, T., Collier, E., Curio, J. and Finkelnburg, R. (2014). Precipitation Seasonality and Variability over the Tibetan Plateau as Resolved by the High Asia Reanalysis. *Journal of Climate.* 27: 1910-27. doi: 10.1175/JCLI-D-13-00282.1.

Mountain Research Initiative EDW Working Group. (2015). Elevation-dependent warming in mountain regions of the world. *Nature Climate Change*, 5(5), 424–430.

Mukherji A, Molden D, Nepal S, Rasul G, Wagnon P (2015) Himalayan waters at the crossroads: issues and challenges. *International Journal of Water Resources Development*. 31(2):151–160. doi: 10.1080/07900627.2015.1040871.

Miles, E. S., Steiner, J. F., & Brun, F. (2017). Highly variable aerodynamic roughness length (z_0) for a hummocky debris-covered glacier. *Journal of Geophysical Research: Atmospheres*. 122: 8447–8466. doi: 10.1002/2017JD026510.

Miles, K., Hubbard, B., Quincey, D., Miles, E., Sherpa, T., Rowan, A. and Doyle, S., (2018a). Polythermal structure of a Himalayan debris-covered glacier revealed by borehole thermometry. Scientific Reports, 8(1).

Miles, E. S., Watson, C. S., Brun, F., Berthier, E., Esteves, M., Quincey, D. J., Miles, K. E., Hubbard, B., and Wagnon, P. (2018b). Glacial and geomorphic effects of a supraglacial lake drainage and outburst event, Everest region, Nepal Himalaya, The Cryosphere, 12, 3891–3905, https://doi.org/10.5194/tc-12-3891-2018.

Miles, E., McCarthy, M., Dehecq, A., Kneib, M., Fugger, S. and Pellicciotti, F. Health and sustainability of glaciers in High Mountain Asia. *Nature Communications*. 12, 2868 (2021a). doi: 10.1038/s41467-021-23073-4

Miles, K., Hubbard, B., Miles, E., Quincey, D., Rowan, A., Kirkbride, M. and Hornsey, J., (2021b). Continuous borehole optical televiewing reveals variable englacial debris concentrations at Khumbu Glacier, Nepal. Communications Earth & Environment, 2(1).

Minder, J., Mote, P. and Lundquist, J. (2010). Surface temperature lapse rates over complex terrain: Lessons from the Cascade Mountains. *Journal of Geophysical Research.* 115(D14). doi: 10.1029/2009JD013493.

Nakawo, M., Iwata, S., Watanabe, O., and Yoshida, M. (1986). Processes which distribute supraglacial debris on the Khumbu Glacier, Nepal Himalaya. *Annals of Glaciology,* 8: 129-131. doi: 10.1017/S0260305500001294.

Nakawo, M., Yabuki,H. and Sakai, A. (1999). Characteristics of Khumbu Glacier, Nepal Himalayas: recent changes in the debris-covered area. *Annals of Glaciology,* 28: 118-122.

Nan, S., Zhao, P., Yang, S., & Chen, J. (2009). Springtime tropospheric temperature over the Tibetan Plateau and evolution of the tropical Pacific SST. Journal of Geophysical Research: Atmospheres, 114(10). doi: 10.1029/2008jd011559.

Nicholson, L., and Benn, D. (2006). Calculating ice melt beneath a debris layer using meteorological data. *Journal of Glaciology. 52*: 463-470. doi:10.3189/172756506781828584.

Nicholson, L., and D. I. Benn (2013). Properties of natural supraglacial debris in relation to modelling sub-debris ice ablation, *Earth Surf. Process. Landforms.* 38(5), 490–501. doi:10.1002/esp.3299.

Nicholson, L. I., McCarthy, M., Pritchard, H. D., and Willis, I. (2018). Supraglacial debris thickness variability: impact on ablation and relation to terrain properties, *The Cryosphere,* 12, 3719–3734, doi.org/10.5194/tc-12-3719-2018.

Norris, J. et al. (2017). The spatiotemporal variability of precipitation over the Himalaya: evaluation of one-year WRF model simulation. *Climate Dynamics.* 49: 2179–2204.

Norris, J., Carvalho, L., Jones, C. and Cannon, F. 2020. Warming and drying over the central Himalaya caused by an amplification of local mountain circulation. *Nature Partner Journals Climate and Atmospheric Science*, 3(1). doi: 10.1038/s41612-019-0105-5.

Nuimura, T. Fujita, K. Yamaguchi, S. and Sharma, R.R. (2012). Elevation changes of glaciers revealed by multitemporal digital elevation models calibrated by GPS survey in the Khumbu region, Nepal Himalaya, 1992-2008. *Journal of Glaciology.* 58(210), 648-656. doi: 10.3189/2012JoG11J061.

Nuimura, T., Sakai, A., Taniguchi, K., Nagai, H., Lamsal, D., Tsutaki, S., Kozawa, A., Hoshina, Y., Takenaka, S., Omiya, S., Tsunematsu, K. and Fuita, K. (2015). The GAMDAM glacier inventory: A quality-controlled inventory of Asian glaciers. *The Cryosphere,* 9(3): 849–864.

Nye, J. (1970) Glacier sliding without cavitation in a linear viscous approximation. *Proceedings of the Royal Society A*, 315(1522): 381–403. doi: 10.1098/rspa.1970.0050.

Ostrem, G. (1959). Ice Melting under a Thin Layer of Moraine, and the Existence of Ice Cores in Moraine Ridges. *Geografiska Annaler*, 41: 228–230.

Owen, L., Robinson, R. and Benn, D. (2009) Quaternary glaciation of Mount Everest. *Quaternary Science Reviews.* 28(15–16): 1412–1433.

Panday, P., Thibeault, J. and Frey, K. (2015) Changing temperature and precipitation extremes in the Hindu Kush-Himalayan region: an analysis of CMIP3 and CMIP5 simulations and projections. *International Journal of Climatology*, 35(10): 3058-3077. doi: 10.1002/joc.4192.

Pellicciotti, F., Brock, B., Strasser, U., Burlando, P., Funk, M., & Corripio, J. (2005). An enhanced temperature-index glacier melt model including the shortwave radiation balance: Development and testing for Haut Glacier d'Arolla, Switzerland. *Journal of Glaciology*, 51(175),:573-587. doi:10.3189/172756505781829124

Pellicciotti, F., Ragettli, S., Carenzo, M., and McPhee, J. (2014). Changes of glaciers in the Andes of Chile and priorities for future work. *Science of the Total Environment.* 493C: 1197–1210. doi: 10.1016/j.scitotenv.2013.10.055.

Pellicciotti, F., Stephan, C., Miles, E., Herreid, S., Immerzeel, W. W. and Bolch, T. (2015). Mass-balance changes of the debris-covered glaciers in the Langtang Himal, Nepal, from 1974 to 1999, *Journal of Glaciology*, 61(226): 373-386. doi: 10.3189/2015jog13j237.

Pepin, N. and Lundquist, J. (2008) Temperature trends at high elevations: Patterns across the globe. *Geophysical Research Letters*, 35(14). doi: 10.1029/2008gl034026.

Pepin, N. C., Bradley, S., Diaz, H. F., Baraer, M., Caceres, E. B., Forsythe, N., et al. (2015). Elevation-dependent warming in mountain regions of the world. *Nature Climate Change*, 5(5), 424–430.

Petersen, L. and Pellicciotti, F. (2011). Spatial and temporal variability of air temperature on a melting glacier: Atmospheric controls, extrapolation methods and their effect on melt modelling, Juncal Norte Glacier, Chile. *Journal of Geophysical Research: Atmospheres*. 116(D23). doi: 10.1029/2011JD015842.

Petersen, L., Pellicciotti, F., Juszak, I., Carenzo, M. and Brock, B. (2013). Suitability of a constant air temperature lapse rate over an Alpine glacier: testing the Greuell and Böhm model as an alternative. *Annals of Glaciology*. 54: 120–130. doi: 10.3189/2013AoG63A477.

Pokharel, B., Wang, S., Meyer, J., Marahatta, S., Nepal, B., Chikamoto, Y. and Gillies, R., (2019). The east–west division of changing precipitation in Nepal. *International Journal of Climatology,* 40(7): 3348-3359.

Potter, E., Orr, A., Willis, I., Bannister, D. and Salerno, F. (2018). Dynamical Drivers of the Local Wind Regime in a Himalayan Valley. *Journal of Geophysical Research: Atmospheres*. 123: 186-202. doi: 10.1029/2018JD029427.

Pritchard, H.D. (2019). Asia's shrinking glaciers protect large populations from drought stress. *Nature*. 569: 649–654. doi: 10.1038/s41586-019-1240-1.

Quincey D., Luckman A. and Benn D. (2009). Quantification of Everest region glacier velocities between 1992 and 2002, using satellite radar interferometry and feature tracking. *Journal of Glaciology*. 55(192): 596-606.

Quincey D., Braun M., Glasser N., Bishop M., Hewitt K. and Luckman A. (2011). Karakoram glacier surge dynamics. *Geophysical Research Letters.* 38(18).

Quincey, D., Glasser, N., Cook, S. and Luckman, A. (2015). Heterogeneity in Karakoram glacier surges. *Journal of Geophysical Research: Earth Surfaces.* 120: 1288–1300.

Quincey D., Klaar, M., Haines, D., Lovett, J., Pariyar, B., Gurung, G., Brown, L., Watson, C., England M. and Evans, B. (2017a). The changing water cycle: the need for an integrated assessment of the resilience to changes in water supply in High-Mountain Asia., *Wiley Interdisciplinary Reviews: Water,* 5(1), p. e1258. doi: 10.1002/wat2.1258.

Quincey D., Smith M., Rounce D., Ross A., King O., Watson C. (2017b). Evaluating morphological estimates of the aerodynamic roughness of debris-covered glacier ice. *Earth Surface Processes and Landforms*. 42: 2541-2553. doi: 10.1002/esp.4198

Ragettli, S., Immerzeel, W.W. and Pellicciotti, F. (2016). Contrasting climate change impact on river flows from high-altitude catchments in the Himalayan and Andes Mountains. *Proceedings of the National Academy of Sciences.* 113: 9222–9227. doi: 10.1073/pnas.1606526113.

Rajbhandari, R., Shrestha, A., Nepal, S. and Wahid, S. (2016) Projection of Future Climate over the Koshi River Basin Based on CMIP5 GCMs. *Atmospheric and Climate Sciences*, 6, 190-204. doi: 10.4236/acs.2016.62017.

Ramesh, K. V. and Goswami, P. (2007). Reduction in temporal and spatial extent of the Indian summer monsoon. *Geophysical Research Letters (Climate*). 34(25). doi: 10.1029/2007GL031613.

Reid, T. D., Carenzo, M., Pellicciotti, F., and Brock, B. W. (2012). Including debris cover effects in a distributed model of glacier ablation. *Journal of Geophysical Research.* 117: D18105. doi:10.1029/2012JD017795.

Ren, G., Sun, X., Shrestha, A., You, Q., Zhan,Y., et al. (2017). Observed changes in surface air temperature and precipitation in the Hindu Kush Himalayan region during 1901–2014. *Advance in Climate Change Research*, 8(3). doi: 10.1016/j.accre.2017.08.001.

Rippin, D. M., Sharp, M., Van Wychen, W. and Zubot, D. (2019). Detachment of icefield outlet glaciers: catastrophic thinning and retreat of the Columbia Glacier (Canada). *Earth Surface Processes and Landforms,* 45(2): 459-472. doi: 10.1002/esp.4746.

Rounce, D. and McKinney, D. (2014). Debris thickness of glaciers in the Everest area (Nepal Himalaya) derived from satellite imagery using a nonlinear energy balance model. *The Cryosphere*, 8(4): 1317-1329. doi: 10.5194/tc-8-1317-2014.

Rounce, D., Quincey, D. and McKinney, D. (2015). Debris-covered glacier energy balance model for Imja–Lhotse Shar Glacier in the Everest region of Nepal. *The Cryosphere*. 9: 2295-2310. doi: 10.5194/tc-9-2295-2015.

Rounce, D. R., Hock, R. and Shean, D. (2020) Glacier Mass Change in High Mountain Asia Through 2100 Using the Open-Source Python Glacier Evolution Model (PyGEM), *Frontiers in Earth Science,* 7. doi: 10.3389/feart.2019.00331.

Rounce, D. R., Hock, R., McNabb, R. W., Millan, R., Sommer, C., Braun, M. H., Malz, P., Maussion, F., Mouginot, J., Seehaus, T. C. and Shean, D. E. (2021) Distributed Global Debris Thickness Estimates Reveal Debris Significantly Impacts Glacier Mass Balance. *Geophysical Research Letters,* 48(8). doi: 10.1029/2020gl091311.

Rowan, A., Egholm, D., Quincey, D. and Glasser, N. (2015). Modelling the feedbacks between mass balance, ice flow and debris transport to predict the response to climate change of debris-covered glaciers in the Himalaya. *Earth and Planetary Science Letters.* 430: 427-438. doi: 10.1016/j.epsl.2015.09.004

Rowan, A. (2017). The 'Little Ice Age' in the Himalaya: A Review of Glacier Advance Driven by Northern Hemisphere Temperature Change. *The Holocene.*

Rowan, A., Egholm, D., Quincey, D., Hubbard, B., King, O., Miles, E., Miles, K. and Hornsey, J., (2021). The Role of Differential Ablation and Dynamic Detachment in Driving Accelerating Mass Loss From a Debris-Covered Himalayan Glacier. *Journal of Geophysical Research: Earth Surface*. 126(9). doi: 10.1029/2020JF005761.

Sabin T.P., Krishnan, R., Vellore, R.,Priya, P., Borgaonkar, H., Singh, B. and Aswin, S. (2020) Climate Change Over the Himalayas. In: Krishnan R., Sanjay J., Gnanaseelan C., Mujumdar M., Kulkarni A., Chakraborty S. (eds) Assessment of Climate Change over the Indian Region. Springer, Singapore. doi: 10.1007/978-981-15-4327-2_11.

Salerno, F., Guyennon, N., Thakuri, S., Viviano, G., Romano, E., Vuillermoz, E., Cristofanelli, P., Stocchi, P., Agrillo, G., Ma, Y., and Tartari, G. (2015). Weak precipitation, warm winters and springs impact glaciers of south slopes of Mt. Everest (central Himalaya) in the last 2 decades (1994–2013), *The Cryosphere*. 9: 1229-1247. doi: 10.5194/tc-9-1229-2015.

Salerno, F., Thakuri, S., Tartari, G., Nuimura, T., Sunako, S., Sakai, A., and Fujita, K. (2017). Debris-covered glacier anomaly? Morphological factors controlling changes in the mass balance, surface area, terminus position, and snow line altitude of Himalayan glaciers. *Earth and Planetary Science Letters,* 471:19–31. doi: 10.1016/j.epsl.2017.04.039.

Sanjay, J., Ramarao, M. V. S., Mujumdar, M. & Krishnan, R. (2017a). In: M. Rajeevan & S. Nayak (Eds.), Regional climate change scenarios. Chapter 16 in the book: Observed climate variability and change over the Indian region (pp. 285–304). Springer Geology. doi: 10.1007/978-981-10-2531-0.

Sanjay, J., Krishnan, R., Shrestha, A. B., Rajbhandari, R., and Ren, G.-Y. (2017b). Downscaled climate change projections for the Hindu Kush Himalayan region using CORDEX South Asia regional climate models. *Advances in Climate Change Research,* 8(3):185–198.

Sauter, T., Arndt, A. and Schneider, C., 2020. COSIPY v1.3 – an open-source coupled snowpack and ice surface energy and mass balance model. *Geoscientific Model Development*, 13(11): 5645-5662.

Schmidt, L., Aðalgeirsdóttir, G., Guðmundsson, S., Langen, P., Pálsson, F., Mottram, R., Gascoin, S. and Björnsson, H. (2017). The importance of accurate glacier albedo for estimates of surface mass balance on Vatnajökull: evaluating the surface energy budget in a regional climate model with automatic weather station observations. *The Cryosphere.* 11: 1665-1684. doi: 10.5194/tc-11-1665-2017.

Scherler, D., Bookhagen, B., & Strecker, M. R. (2011a). Spatially variable response of Himalayan glaciers to climate change affected by debris cover. *Nature Geoscience,* 4(1), 1 – 1. doi:10.1038/ngeo1059.

Scherler, D., Bookhagen, B. and Strecker, M. (2011b). Hillslope-glacier coupling: The interplay of topography and glacial dynamics in High Asia, *Journal of Geophysical Research: Earth Surface*, 116(F2). doi: 10.1029/2010jf001751

Scherler, D. and Egholm, D., (2020). Production and Transport of Supraglacial Debris: Insights From Cosmogenic 10 Be and Numerical Modeling, Chota Shigri Glacier, Indian Himalaya. *Journal of Geophysical Research: Earth Surface,* 125(10).

Schoof, C. (2005). The effect of cavitation on glacier sliding. *Proceedings of the Royal Society A*.461609–627 doi: 10.1098/rspa.2004.1350

Seko, K. (1987). Seasonal variation of altitudinal dependence of precipitation in Langtang Valley, Nepal Himalayas. *Bull. Glacier Res.*, 5: 41– 47.

Sharma, E., Molden, D., Rahman, A., Khatiwada, Y.R., Zhang, L., Singh, S.P., Yao, T., Wester, P., (2019). "Introduction to the Hindu Kush Himalaya Assessment" in *The Hindu Kush Himalaya Assessment: Mountains, Climate Change, Sustainability and People* ed. Wester, P., Mishra, A., Mukherji, A., Shrestha, A.B. (Springer International Publishing, Cham). 1: 1–16. doi: 10.1007/978-3-319-92288-1_1.

Shaw, T. E., Brock, B. W., Fyffe, C. L., Pellicciotti, F., Rutter, N., and Diotri, F. (2016). Air temperature distribution and energy-balance modelling of a debris-covered glacier. *Journal of Glaciology,* 62(231):185–198.

Shea, J. and Moore, R. (2010). Prediction of spatially distributed regional-scale fields of air temperature and vapor pressure over mountain glaciers. *Journal of Geophysical Research.* 115(D23). doi: 10.1029/2010JD014351.

Shea, J., Immerzeel, W., Wagnon, P., Vincent, C. and Bajracharya, S. (2015a). Modelling glacier change in the Everest region, Nepal Himalaya. *The Cryosphere.* 9: 1105-1128. doi: 10.5194/tc-9-1105-2015

Shea, J., Wagnon, P., Immerzeel, W., Biron, R., Brun, F. and Pellicciotti, F. (2015b). A comparative high-altitude meteorological analysis from three catchments in the Nepalese Himalaya. *International Journal of Water Resources Development.* 31(2): 174-200. doi: 10.1080/07900627.2015.1020417.

Shean, D. E., Bhushan, S., Montesano, P., Rounce, D. R., Arendt, A. and Osmanoglu, B. (2020). A Systematic, Regional Assessment of High Mountain Asia Glacier Mass Balance. *Frontiers in Earth Science*, 7. doi: 10.3389/feart.2019.00363.

Singh, D. et al. Distinct influences of land cover and land management on seasonal climate. (2018). *Journal of Geophysical Research: Atmospheres.* 123: 12017–12039.

Smith, R.B. and Barstad, I. (2004). A Linear Theory of Orographic Precipitation. *Journal of Atmospheric Science.* 61: 1377–1391. doi: 10.1175/1520-0469(2004)061<1377:ALTOOP>2.0.CO;2.

Soncini, A., Bocchiola, D., Confortola, G., Minora, U., Vuillermoz, E., Salerno, F., Viviano, G., Shrestha, D., Senese, A., Smiraglia, C., and Diolaiuti, G.. (2016). Future hydrological regimes and glacier cover in the Everest region: The case study of the upper Dudh Koshi basin. *Science of The Total Environment,* 565: 1084-1101. doi: 10.1016/j.scitotenv.2016.05.138.

Steinegger, U., L. N. Braun, G. Kappenberger, and G. Tartari (1993). Assessment of annual snow accumulation over the past 10 years at high elevations in the Langtang Region. *IAHS Publ.* 218: 155– 166. Int. Assoc. of Hydrol. Sci., Wallingford, U. K.

Takeuchi, Y., Kayastha, R. B., and Nakawo, M. (2000). Characteristics of ablation and heat balance in debris-free and debris-covered areas on Khumbu Glacier, Nepal Himalayas, in the pre-monsoon season. *IAHS PUBLICATION*, 53–62.

Thayyen, R.J. and Dimri, A.P. (2018). Slope Environmental Lapse Rate (SELR) of Temperature in the Monsoon Regime of the Western Himalaya. *Frontiers in Environmental Science*, 6: 42. doi: 10.3389/fenvs.2018.00042.

Turner, A. G. and Annamalai, H. (2012). Climate change and the South Asian summer monsoon. *Nature Climate Change,* 2(8):587.

Ueno, K., Shiraiwa, T., & Yamada, T. (1993). Precipitation Environment in the Langtang. Valley, Nepal. In: Snow and Glacier Hydrology (Proceedings of the Kathmandu Symposium, November 1992). *IAHS Publ.* 218: 207–219.

Ueno, K., Toyotsu, K., Bertolani, L. and Tartari, G. (2008). Stepwise Onset of Monsoon Weather Observed in the Nepal Himalaya. *Monthly Weather Review.* 136: 2507-2522. doi: 10.1175/2007MWR2298.1

Veh, G., Korup, O., von Specht, S., Roessner, S., and Walz, A. (2019). Unchanged frequency of moraine-dammed glacial lake outburst floods in the Himalaya. *Nature Climate Change*. 9, 379–383. 60.

Vincent, C., Wagnon, P., Shea, J. M., Immerzeel, W. W., Kraaijenbrink, P., Shrestha, D., et al. (2016). Reduced melt on debris-covered glaciers: Investigations from Changri Nup Glacier, Nepal. *The Cryosphere,* 10(4): 1845– 1858. doi: 10.5194/tc-10-1845-2016.

Vuillermoz, E., Antonella, S., Giuglielmina, S. C., Paolo, C., Angela, M., Verza, G. and Paolo, B. (2014). The Case Study of the Changri Nup glacier (Nepal, Himalaya) to Understand Atmospheric Dynamics and Ongoing Cryosphere Variations in *Engineering Geology for Society and Territory ed.* Lollino, G. et al. 1: 73-76.

Wang, Q., Fan, X., and Wang, M. (2014). Recent warming amplification over high elevation regions across the globe*. Climate Dynamics*, 43 (1–2): 87–101.

Watson, C.S., Quincey, D.J., Carrivick, J.L. and Smith, M.W. (2016). The dynamics of supraglacial ponds in the Everest region, central Himalaya, *Global Planetary Change.,* 142: 14-27. doi: 10.1016/j.gloplacha.2016.04.008.

Weidemann, S.S., Sauter, T., Malz, P., Jaña, R., Arigony-Neto, J., Casassa, G. and Schneider, C. (2018). Glacier Mass Changes of Lake-Terminating Grey and Tyndall Glaciers at the Southern Patagonia Icefield Derived From Geodetic Observations and Energy and Mass Balance Modeling. *Frontiers in Earth Science*, 6: 81. doi: 10.3389/feart.2018.00081.

Wester, A. Mishra, A. Mukherji, A. B. Shrestha (eds). 2019. The Hindu Kush Himalaya Assessment—Mountains, Climate Change, Sustainability and People Springer Nature Switzerland AG, Cham.

Whiteman, C.D. and Doran, J.C. (1993). The Relationship between Overlying Synoptic-Scale Flows and Winds within a Valley. *Journal of Applied Meteorology*. 32: 1669–1682.

Wijngaard, R. R., Steiner, J. F., Kraaijenbrink, P. D. A., Klug, C., Adhikari, S., Banerjee, A., Pellicciotti, F., van Beek, L. P. H., Bierkens, M. F. P., Lutz, A. F. and Immerzeel, W. W. (2019). Modeling the Response of the Langtang Glacier and the Hintereisferner to a Changing Climate Since the Little Ice Age, *Frontiers in Earth Science*, 7. doi: 10.3389/feart.2019.00143

Wiltshire, A. K. (2014). Climate change implications for the glaciers of the Hindu Kush, Karakoram and Himalayan region. *The Cryosphere.* 8: 941-958. doi: 10.5194/tc-8-941-2014.

Wood, L.R., Neumann, K., Nicholson, K.N., Bird, B.W., Dowling, C.B., and Sharma, S. (2020). Melting Himalayan glaciers threaten domestic water resources in the Mount Everest Region, Nepal. *Frontiers Earth Sciences.* 8. doi: 10.3389/feart.2020.00128.

Yanai, M. H., & Li, C. (1994). Mechanism of heating and the boundary layer over the Tibetan Plateau. *Monthly Weather Review,* 122, 305–323.

Yang, K., N. Guyennon, L. Ouyang, L. Tian, G. Tartari, and F. Salerno (2017). Impact of summer monsoon on the elevation-dependence of meteorological variables in the south of Central Himalaya. *International Journal of Climatology.* 5293: 1748-1759. doi:10.1002/joc.5293.

Yao, T., Thompson, L., Yang, W., Yu, W., Gao, Y., Guo, X., Yang, X., Duan, K., Zhao, H., Xu, B., Pu, J., Lu, A., Xiang, Y., Kattel, D., Joswiak, D. (2012). Different glacier status with atmospheric circulations in Tibetan Plateau and surroundings. *Nature climate change (Letter).* 2: 663-667. doi: 10.1038/nclimate1580.

Zekollari, H., Huss, M. and Farinotti, D. (2020). On the Imbalance and Response Time of Glaciers in the European Alps, *Geophysical Research Letters,* 47(2). doi: 10.1029/2019gl085578.

Zekollari, H., Huss, M. & Farinotti, D. (2019). Modelling the future evolution of glaciers in the European Alps under the EURO-CORDEX RCM ensemble*. Cryosphere* 13, 1125–1146.

Zemp, M., Frey, H., Gärtner-Roer, I., Nussbaumer, S. U., Hoelzle, M., Paul, F., Haeberli, W., Denzinger, F., Ahlstrøm, A. P., Anderson, B., Bajracharya, S., Baroni, C., Braun, L. N., Cáceres, B. E., Casassa, G., Cobos, G., Dávila, L. R., Delgado Granados, H., Demuth, M. N., Espizua, L., Fischer, A., Fujita, K., Gadek, B., Ghazanfar, A., Ove Hagen, J., Holmlund, P., Karimi, N., Li, Z., Pelto, M., Pitte, P., Popovnin, V. V., Portocarrero, C. A., Prinz, R., Sangewar, C. V., Severskiy, I., Sigurđsson, O., Soruco, A., Usubaliev, R. and Vincent, C. (2015) Historically unprecedented global glacier decline in the early 21st century, *Journal of Glaciology,* 61(228) : 745-762. doi: 10.3189/2015jog15j017.

Zhang R, Liu X D. (2010). The effects of tectonic uplift on the evolution of Asian summer monsoon climate since Pliocene. *Chinese Journal of Geophysics*, 53: 948–960.

Zhang, Y., Hirabayashi, Y., Liu, Q. and Liu, S., (2015). Glacier runoff and its impact in a highly glacierized catchment in the southeastern Tibetan Plateau: past and future trends. *Journal of Glaciology*, 61(228): 713-730.

Zoet, L. and Iverson, N. (2015) Experimental determination of a double-valued drag relationship for glacier sliding, *Journal of Glaciology,* 61(225): 1-7. doi: 10.3189/2015jog14j174.